Title
Performance Characterization of Beams with High-Strength Reinforcement

Author
To, Duy Vu

Publication Date
2018

Peer reviewed|Thesis/dissertation

Performance Characterization of Beams with High-Strength Reinforcement

by

Duy Vu To

A dissertation submitted in partial satisfaction of the requirements for the degree of

Doctor of Philosophy

in

Engineering – Civil and Environmental Engineering

in the

Graduate Division

of the

University of California, Berkeley

Committee in charge:

Professor Jack P. Moehle, Chair

Professor Khalid M. Mosalam

Professor Per-Olof Persson

Spring 2018

Performance Characterization of Beams with High-Strength Reinforcement

Abstract

Performance Characterization of Beams with High-Strength Reinforcement

by

Duy Vu To

Doctor of Philosophy in Engineering – Civil and Environmental Engineering

University of California, Berkeley

Professor Jack P. Moehle, Chair

A laboratory test and analytical research program was undertaken to characterize the performance of reinforced concrete beams with high-strength reinforcement subjected to reversed cyclic lateral loading simulating earthquake effects. The beams are representative of beams used in special moment frames. Four beams were tested in the laboratory test investigation, one with A706 Grade 60 reinforcement, one with Grade 100 reinforcement having tensile-to-yield strength ratio (T/Y) of 1.17, one with Grade 100 reinforcement with T/Y = 1.26, and one with A1035 Grade 100 reinforcement. In each beam, the noted reinforcement grade was used for both longitudinal and transverse reinforcement, except for beam with Grade 100 T/Y = 1.17 that had transverse reinforcement of Grade 100 with T/Y = 1.26. Overall, all beams achieved rotation capacity of at least 0.045 radians. The beams with A706 Grade 60 and Grade 100 (T/Y = 1.26) reinforcement failed by buckling of longitudinal bars over several hoop spacings. The other two beams with Grade 100 reinforcement failed by fracture of longitudinal bars at the maximum moment section. Strain gauges installed on longitudinal bars indicated that beams with higher T/Y achieved greater spread of plasticity compared to beams with lower T/Y.

In the analytical study, the seismic performance of tall reinforced concrete special moment resisting frames with high-strength reinforcement was investigated through nonlinear dynamic analyses. Four 20-story reinforced concrete moment frames, three reinforced with Grade 100 steel and one with Grade 60 steel were designed in accordance with ASCE 7-16 and ACI 318-14 at a hypothetical site in San Francisco, California. All four frames had the same dimensions and concrete properties, resulting in identical design drifts. Frames with Grade 100 reinforcement were designed to have reduced amount of longitudinal reinforcement to provide equivalent nominal strength as was provided in the Grade 60 reinforcement model. Tests had demonstrated that frames with higher-grade reinforcement had greater strain penetration into beam-column joints, resulting in greater slip of reinforcement from connections. This effect combined with reduced reinforcement ratios caused the frames with Grade 100 reinforcement to be more flexible than the frame with Grade 60 reinforcement. In addition, some currently available types of Grade 100 reinforcement have lower tensile-to-yield strength ratio and lower uniform elongation compared

with Grade 60 reinforcement. The reduced T/Y results in reduced strain-hardening, increased strain localization, and increased P-Delta effects. The effects of these local behaviors on overall frame performance are studied through the nonlinear dynamic analyses. The various types of reinforcement were found to result in minor differences in overall frame seismic performance.

ACKNOWDGEMENT

First and foremost, I would like to express my sincerest gratitude to Professor Jack Moehle. His patient guidance, generous support, and endless encouragement had made my doctoral endeavor a rewarding and memorable experience. I am especially grateful for his advice in both academic and professional matters. It has truly been a privilege to have you as a research advisor and a mentor.

I would like to particularly thank Professors Stephen Mahin, Khalid Mosalam, Raymond Seed, and Per-Olof Persson for serving as members in my qualifying exam and dissertation committees.

The research presented here is financially supported by Charles Pankow Foundation, the CRSI Foundation, and ACI Foundation's Concrete Research Council. CMC Commercial Metals Corporation, Nucor Corporation Seattle, and MMFX Technologies Corporation donated reinforcement used in the test specimens. Clark Construction Group and The Conco Companies constructed the test specimens as an in-kind contribution. The project benefitted greatly from discussion and advice from our Industry Advisory Committee comprising Dominic Kelly (Simpson Gumpertz & Heger), Andy Taylor (KPFF), Loring Wyllie (Degenkolb Engineers), and Ron Klemencic (Magnusson Klemencic Associates).

The study reported here was done in collaboration with Professor Wassim Ghannoum, University of Texas, San Antonio and his graduate student Drit Sokoli. The shared data and experience added considerably to the quality of the work.

The laboratory tests were conducted in the Structural Research Laboratory of the Department of Civil and Environmental Engineering, University of California, Berkeley. I would like to recognize the capable contributions of laboratory staff Phillip Wong, Matt Cataleta, Llyr Griffith, and Cruz Carlos. Several graduate and undergraduate students contributed to the construction and testing program, including Daniel Miller, Pablo Parra, Carlos Arteta, John N. Hardisty, Pablo Azcona, Edmond Yi, Monica Liu, Max Jung, Angela Tarng, Eduardo Espitia, and Juan Garcia.

The analytical work was done with much help and shared knowledge from Dr. Frank McKenna (University of California, Berkeley), Dr. Tea Visnjic (Exponent Engineering and Scientific Consulting), Dr. Yuan Lu and Dr. Robert Morris (Computers and Structures, Inc.), and Zen Hoda (Englekirk Structural Engineers). I would also like to acknowledge the expertise of Dr. Yousef Bozorgnia (University of California, Berkeley) and Dr. Silvia Mazzoni (Degenkolb Engineers) assisting in selection of ground motions.

Finally, I am eternally grateful to my parents Lang and Hanh, and my sister Hy. Without their love, support, and encouragement this achievement would not have been possible.

TABLE OF CONTENTS

LIST OF FIGURES

LIST OF TABLES

CHAPTER 1: INTRODUCTION

1.1. MOTIVATION

In the United States, reinforced concrete structures are designed primarily in accordance with requirements of ACI 318 Building Code. Current version ACI 318-14 Code provisions allow the use of Grade 60 A706 reinforcement in seismic applications. Higher grades of reinforcement are only permitted for confinement reinforcement. The use of higher grade reinforcing steel has the potential benefit of reducing material quantities, thereby leading to reduced reinforcement congestion and reduced construction costs in reinforced concrete construction. Several steel mills in the United States can produce reinforcing steel of grade 100 (nominal yield strength of 100 ksi) and higher. However, at the time of this writing, none of these higher grades can match the benchmark mechanical properties of Grade 60 A706 steel. This raises questions about the performance characteristics of reinforced concrete construction that uses the higher-grade reinforcement.

Figure 1.1.1 depicts typical stress-strain behaviors of A706 Grade 60 reinforcement and three different types of Grade 100 reinforcement. The stress-strain relations were obtained from tests of reinforcing bars used in the present study. Of note are differences in the yield point characteristics, tensile-to-yield strength ratios (T/Y), and ultimate uniform elongations (defined as the strain at the ultimate stress). The A706 Grade 60 reinforcement shows a defined yield plateau with T/Y = 1.48 and ultimate elongation of 0.114 (ASTM, 2016). Two of the Grade 100 bars also show a defined yield plateau, but with reduced T/Y (1.26 and 1.17, respectively) and reduced ultimate elongation (0.094 and 0.068, respectively). The third Grade 100 reinforcement (A1035) does not have a defined yield plateau but instead has a roundhouse curve with high T/Y and ultimate elongation around 0.056. The lower T/Y is believed to reduce the spread of plasticity in a beam after onset of yielding, and that effect combined with reduced elongation may result in lower rotational capacity of reinforced concrete members with some types of higher-grade reinforcement.

Reinforced concrete Special Moment Resisting Frames (SMRFs) are usually used as part of the seismic-force-resisting system in buildings designed to resist earthquake shaking (Figure 1.1.2). They are generally selected due to the desire of architectural feature flexibility. They comprise beams, columns, and beam-column joints. Special proportioning and detailing requirements must be satisfied to enable the frame to resist combinations of shear, moment, and axial force while safely undergoing extensive inelastic deformations as a building responds to strong earthquake ground shaking.

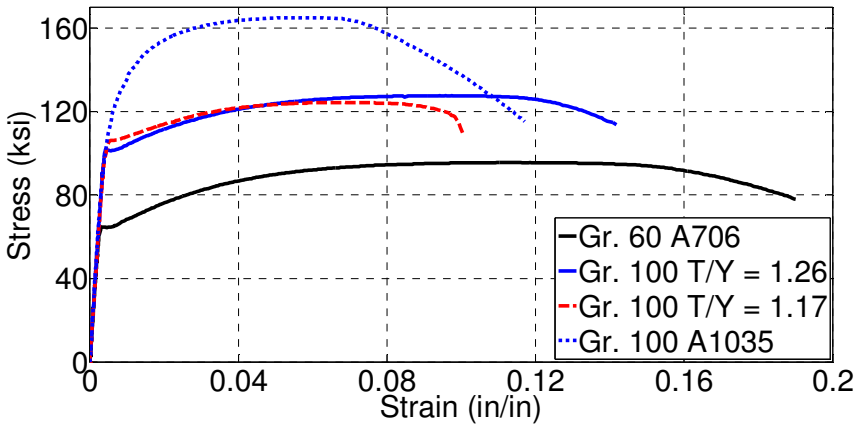

Figure 1.1.1: Mechanical Properties of Grade 60 and Grade 100 Steels

ACI 318 requires that SMRFs be designed to have columns that are flexurally stronger than the beams. The purpose of this strong-column/weak-beam design approach is to promote yielding to be primarily flexural yielding in the beams, and to force inelastic response to extend upward along the height of the building. In the idealized case where the columns provide a very stiff and strong spine over the building height, lateral drift will be more uniformly distributed and yielding will tend toward a full beam yielding mechanism (Figure 1.1.2c). If the beams are detailed for ductile response, this design approach enables the building frame to deform well into inelastic range.

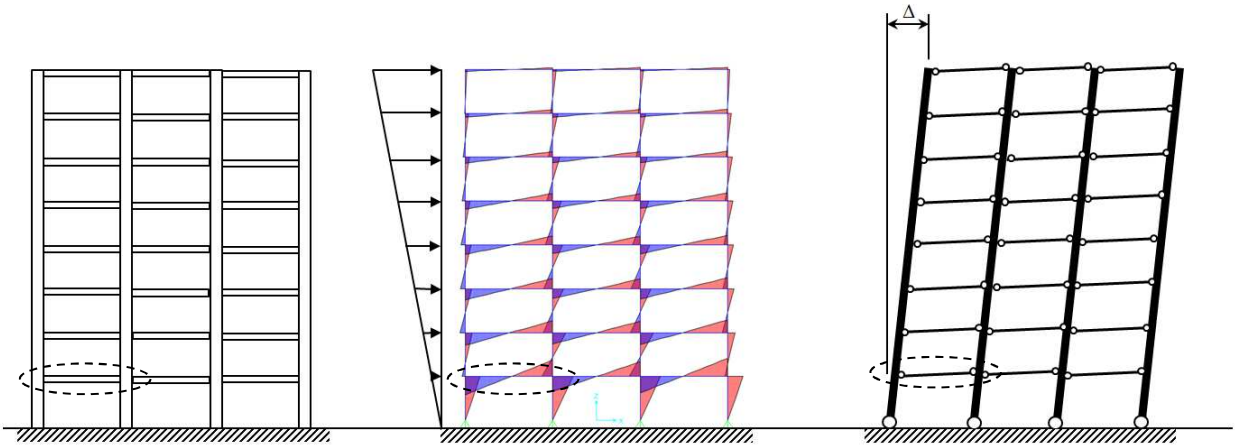

(a) (b) (c)

Figure 1.1.2: General response of special moment resisting frames (SMRFs). (a) Frame proportions. (b) Moment diagram under lateral force. (c) Deflected shape under lateral force

Considering one typical beam on the left of first floor (circled by dashed line in Figure 1.1.2), and assuming gravity load effects are negligible, the moment diagram indicates the point of inflection (zero moment) is in the mid-span of beam under lateral load. Focusing on this beam (Figure 1.1.3), it can be seen that the main flexural and shearing behaviors of the beam can be

simulated by considering only half of the beam as a cantilever with concentrated lateral load applied at tip. Consequently, behavior of typical beams in SMRFs can be investigated through laboratory tests of cantilever beams that have half the length of the beam in prototype structure. This latter geometry is adopted for the laboratory test specimens in this research program.

The primary motivation of this research is to explore the seismic performance characteristics of beams constructed of higher-grade reinforcement. The study includes both laboratory tests to characterize the beam behavior and numerical studies to understand the effects on seismic performance of multi-story frames.

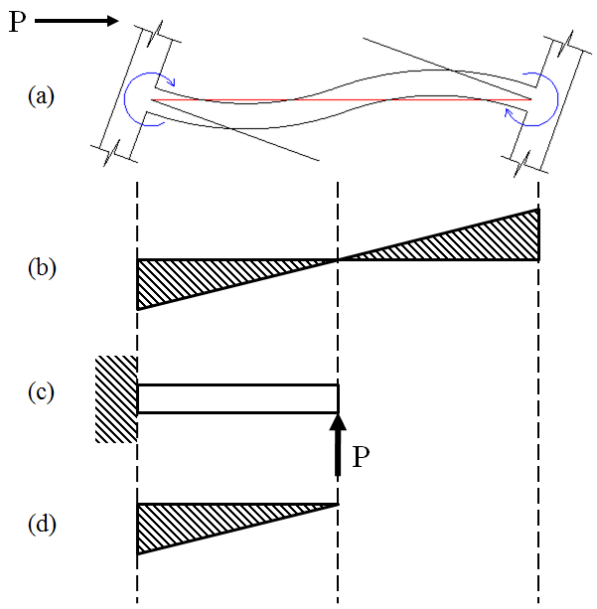

Figure 1.1.3: (a) Deformed shape of beam under lateral load. (b) Moment diagram of full-length beam. (c) Cantilever half-length beam. (d) Moment diagram of half-length beam under application of concentrated load

1.2. OBJECTIVES AND SCOPE

The objective of this study is to characterize and quantify the seismic performance of reinforced concrete beams typical of those used in special moment frames reinforced with high-strength steel bars having yield strength of 100 ksi. The scope includes both laboratory testing of representative beams and numerical modeling of archetype buildings using high-strength reinforcement.

The laboratory tests include tests on four representative beams. For an individual beam, longitudinal and transverse reinforcement uses one of the four types shown in Figure 1.1.1, except the beam with Grade 100 T/Y = 1.17 had transverse reinforcement of Grade 100 with T/Y = 1.26.

The beams are designed to have nominally identical moment strengths, with nominal shear strengths exceeding the maximum shear expected during the test. The tests specimens are instrumented to record overall load-deformation behavior, as well as spread of plasticity, inelastic rotation capacity, longitudinal reinforcement buckling characteristics and related requirements for transverse reinforcement, and local bond stress-slip relationships for reinforcement anchored in adjacent connections.

The numerical study begins with development of numerical models for each of the beams, including relatively simple models for stiffness, strength, and deformation capacity, as well as relatively complex models to represent the reversed-cyclic behavior of the beams under force reversals. Additionally, four 20-story reinforced concrete moment frames, three reinforced with Grade 100 reinforcement and one reinforced with A706 Grade 60 reinforcement, are designed in accordance with ASCE 7-16 and ACI 318-14 at a hypothetical site in San Francisco, California. Nonlinear dynamic analyses of these frames are carried out to investigate the seismic performance characteristics of tall, reinforced concrete special moment resisting frames with Grade 60 and Grade 100 reinforcement.

CHAPTER 2: LITERATURE REVIEWS

Historical development of reinforcing bar specifications dates back to the year of 1911 when ASTM A15 was first published with Structural Grade (Grades 33) and Hard Grade (Grade 55) (FEMA 273, 1997). In 1914, ASTM A15 was revised to add Intermediate Grade (Grade 40). In 1959, ASTM A432 (ASTM, 1959a) and A431 (ASTM, 1959b) were published which introduced Grade 60 and Grade 75 reinforcement, respectively (ATC 115, 2014). In response, ACI 318-63 allowed the use of reinforcement with a yield strength of 60 ksi. ASTM A15, ASTM A431, and ASTM A432 were then replaced by ASTM A615 with grades 40, 60, and 75 in the year of 1968. Since 1971 the ACI 318 has restricted the maximum specified yield strength for reinforcement in special seismic system to 60 ksi. And this limit is still in effect in the current ACI 318-14. In 1974, ASTM A706, *Standard Specification for Low-Alloy Steel Deformed and Plain Bars for Concrete Reinforcement* (ASTM, 1974), was published, and permitted in ACI 318-77. Later, in the 1983 version of ACI 318, ASTM A706 was required for special seismic system. ASTM A615 was also allowed with specified mechanical properties were met. In 2009, ASTM A615 and A706 (ASTM, 2009a; ASTM, 2009b) included specifications for Grade 80 reinforcement. Although ACI 318-11 adopted these specifications and allowed the use of Grade 80 reinforcement, it is not permitted for use in seismic applications due to insufficient test data for cyclically loaded components with this grade of reinforcement.

As early as 1975, one of the countries with the highest seismicity on the world, Japan, has seen the quick development of high-rise reinforced concrete construction (Aoyama, 2011). Owing to many factors such as large scale structural testing, advanced analysis techniques, and construction technology, the most significant and influential factor was the development of high strength materials, namely concrete and steel reinforcement. Based on such advancement, the Ministry of Construction of Japan promoted a five-year national research project entitled "Development of Advanced Reinforced Concrete Buildings using High Strength Concrete and Reinforcement" (usually referred to as the "New RC") from 1988 until 1993. The research project focused on utilizing high strength materials such as concrete having specified strength from 30 to 120 MPa (4.4 to 17.4 ksi) and steel reinforcing bars with yield strength from 400 to 1200 MPa (58 to 174 ksi) in seismic applications.

In the United States, early tests on columns with longitudinal bars having yield strengths of 72 ksi and 96 ksi were conducted in 1934 with conclusion that longitudinal bars were fully effective under axial compression (Richart and Brown, 1934). In 1965, test results on eccentrically loaded columns with reinforcement that had yield plateau up to 90 ksi were published (Todeschini et al., 1965). The Portland Cement Association (PCA) carried out a series of tests including beams, girders, and columns with reinforcement having strength ranging from 55 ksi to 120 ksi in the late 1950s and 1960s (Hognestad, 1961; Hognestad, 1962; Gaston et al., 1962; Kaar and Mattock, 1963; Pfister et al., 1963; Pfister et al., 1964; Kaar and Hognestad 1965; Kaar, 1966). These early

research efforts provided evidence and support for adoption of Grade 80 reinforcement in non-seismic applications, but not in seismic applications, in the 1971 edition of ACI 318 (ACI 318, 1971).

Cyclic tests in the early 1960s were conducted by Burns and Siess (1962) and indicated that more ductile reinforcement in structural elements resisting earthquake forces was needed. Given the tendency for material strain capacity to decrease as tensile strength increase, there is a recognized need for additional research on members reinforced with high-strength steel having yield strength in excess of 60 ksi for use in seismic applications.

2.1. MATERIALS

In the "New RC" project, several newly developed high-strength reinforcing bars were used in reinforced concrete specimens tested in laboratory including USD685A and USD685B for reinforcement of beams and columns expected to form yield hinges, USD980 for reinforcement of non-yielding elements, and USD785 and USD1275 for confinement and shear reinforcement. Typical stress-strain relationships of these higher-grade steels are displayed in Figure 2.1.1. Among these high-strength reinforcements in Japan, USD685A, USD685B, and USD785 are especially noted as they are manufactured under the same process and have comparable properties as high-strength steel currently available in the United States. Note that stress-strain curve for USD785 reinforcement is shown in Figure 2.1.1 but marked by NewRC USD780.

Currently available high-strength reinforcing steels in the United States are manufactured by several processes including cold working, micro-alloying, quenching and tempering (NIST, 2014; ATC 115, 2014). Among the three methods, cold working is not an appropriate means of producing high-strength reinforcement for members resisting earthquake forces as it eliminates a yield plateau and hardens the steel, resulting in reduction in both ductility and ratio of tensile-to-yield strength.

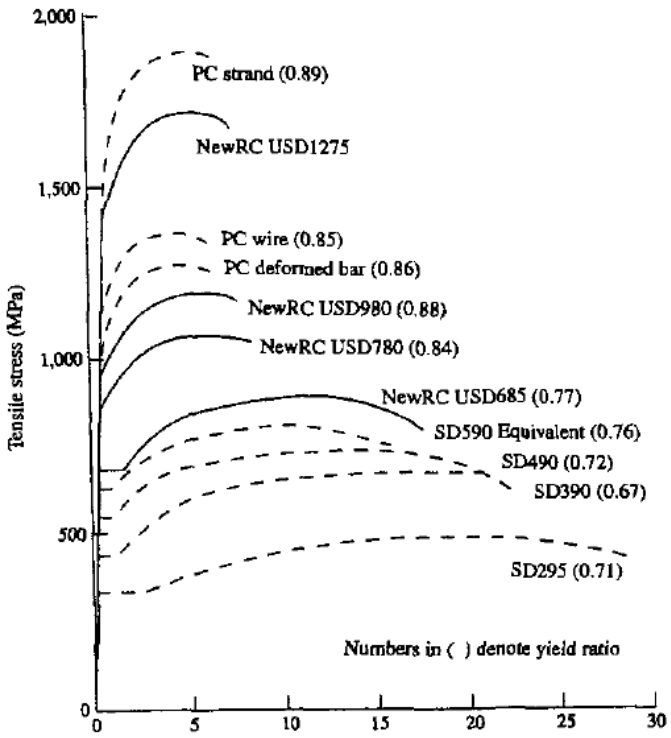

Figure 2.1.1: Stress-Strain Relationships of Steel with Different Strength (after Aoyama, 2011)

Quenching and tempering

In the quenching method, steel bars are sprayed with water to rapidly cool steel that has been heated to the austenite phase, at which solid steel recrystallizes (Dotreppe, 1997; NIST, 2014; and ATC 115, 2014). It is followed by self-tempering resulting from the gradual release of the heat that is trapped in the core of the quenched steel. As a result, remaining heat at the core of the bar modifies the microstructure to decrease the hardness and increase the ductility of the material. Therefore, this entire process of quenching and tempering typically produces steel bars with high yield strength but relatively modest tensile strength, resulting in low T/Y ratio. Nominal Grade 100 reinforcement with T/Y = 1.17 used in this research program and USD685A reinforcement used in the "New RC" project had similar properties and both were manufactured by this process.

Micro-alloying

Micro-alloying is the process, in which small amounts of titanium (Ti), Niobium (Nb), or vanadium (V) are included in the molten steel to result in higher strength due to atomic size effect or crystallization effect (Aoyama, 2001; Caifu, 2010). Micro-alloying forms intermetallic carbides that produce fine-grain strengthening and precipitation strengthening. Fine-grain strengthening occurs by pinning of planar defects (grain boundaries) during thermo-mechanical processing

(rolling), which produces a very fine grain size in the steel product. In general, the finer the grain size, the higher the yield strength, a relationship known as the Hall-Petch Effect. These intermetallic carbides are dispersed through the ferrite grains, pinning line deflects (dislocations), which further raises the yield strength of the material, a mechanism known as precipitation strengthening.

Titanium micro-alloying contributes to precipitation strengthening, but its strong tendency to combine with oxygen, sulfur, and nitrogen makes it difficult to control the strengthening effects. Niobium micro-alloying is widely used in steel sheet and strip production, in which the temperature at the end of production is relatively low and the deformation is high. Reinforcement production requires higher rolling temperatures and less deformation, making Niobium micro-alloying ineffective for high-strength reinforcement production.

Vanadium or vanadium-nitrogen micro-alloying process is used to develop high-strength weldable reinforcement around the world. Vanadium additions increase yield strength due to precipitation of carbides and nitrides. Vanadium-only micro-alloying results in 35.5% of the vanadium forming carbide and nitride precipitates, while 56.3% of the vanadium ends up as solid solution dissolved in the matrix, not improving the reinforcement yield strength. The amount of vanadium forming precipitates can be increased up to 70% with the addition of nitrogen. Another advantage of vanadium-nitrogen micro-alloyed reinforcement is that it eliminates the adverse effects of strain aging on properties of steel as it pins the soluble nitrogen (Caifu, 2010; Erasmus et al., 1978; Restrepo-Posada et al., 1994).

Therefore, micro-alloying process can produce high-strength reinforcement with T/Y ratio that is higher than that by quenching and tempering. Nominal Grade 100 reinforcement with T/Y = 1.26 in this laboratory test program and USD685B reinforcement in the “New RC” project were produced by micro-alloying and they both had comparable mechanical properties.

Combination of micro-alloying and micro-structure manipulation

Combination of chemical composition and manufacturing process produces steel that has a completely different structure at nanoscale (MMFX Technologies Corporation, 2012). MMFX’s steel bars are low-carbon, chromium alloy steel that are produced as part of a controlled-rolling production process, in which steel is rolled within a well-defined temperature range and cooled at a specific rate. These steel bars satisfy the ASTM A1035 specifications (ASTM A1035/A1035M-16a, 2016). ASTM A1035 Grade 100 steel reinforcement used in this research program and USD785 in the “New RC” were manufactured in relatively similar process and both had roundhouse stress-strain curve with high T/Y and ultimate elongation around 0.05.

2.2. COMPONENT TESTINGS

Sugano et al., 1990 and Kimura et al., 1993

Laboratory tests on reinforced concrete beams with high-strength reinforcement are reported in Sugano et al. (1990) and Kimura et al. (1993). Being part of beam-column subassemblages tested by Sugano et al., two beams were reinforced with longitudinal and transverse reinforcement both having yield strength of 85 ksi and 125 ksi. Beam cross section dimensions were 12 inches wide by 16 inches deep and shear span to effective depth ratio was 3.5. Concrete compressive strength was 12 ksi. In Kimura et al. (1993), seven of fourteen cantilever beams reinforced longitudinally and transversely with steel bars having yield strength of 115 ksi were tested. Cross section of beams was 8 inches wide by 12 inches deep with shear span to effective depth ratio of 4.7. Compressive strength of concrete was either 5.5 ksi or 11 ksi. All beams with high-strength reinforcement tested by Sugano et al. and Kimura et al. were reported to achieve drift ratio in excess of 5%.

Aoyama, 2001

In the Japan's New RC Project (Aoyama, 2001), a series of beam tests were performed under reversed cyclic loading in the laboratory. Reinforcement with yield ratio (yield strength to tensile strength ratio) ranging from 0.90 to 0.75 were used as longitudinal reinforcement in test specimens. A test beam with yield ratio of 0.75 maintained its post yield strength to a drift ratio of 5.6% while a specimen with yield ratio of 0.90 started losing strength at drift ratio of about 2.2%. Figure 2.2.1 depicts the drawing and details of beam test specimens and Figure 2.2.2 shows their Lateral Load – Deflection responses. It was observed that the beam with reinforcement having higher yield ratio sustained lower drift at a given bar strain, meaning that strain was more localized. As a result, the plastic hinge zone became more concentrated.

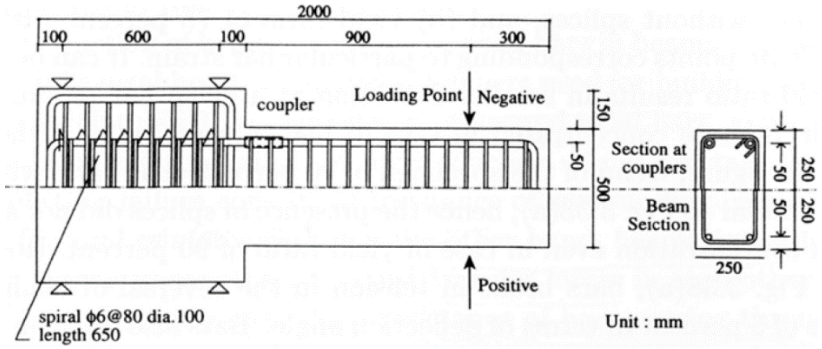

Figure 2.2.1: Test Beams in Study of the Effects of Yield Ratio (Aoyama, 2011)

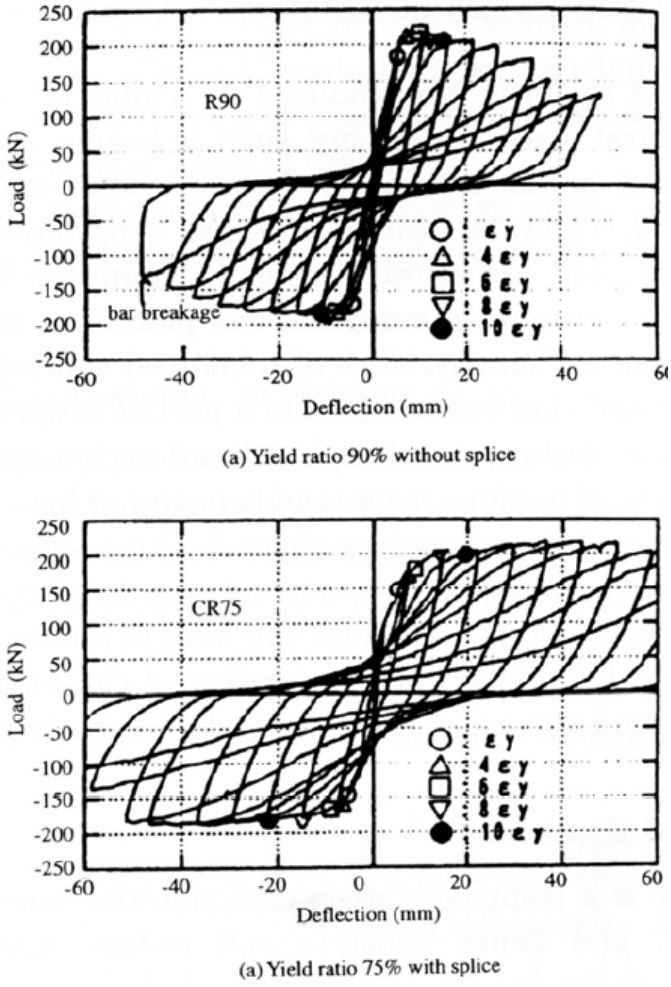

Figure 2.2.2: Load - Deflection Response of Test Beams (Aoyama, 201)

Pfund, 2012

Pfund (2012) tested four specimens reinforced with conventional ASTM A706 Grade 60, ASTM A1035 Grade 120, and Grade 97. Typical stress-strain relationship of ASTM A1035 Grade 120 is shown in Figure 2.2.3. Each specimen had two cantilever beams connected through a central stub (Figure 2.2.4). Each cantilever beam was 36-inch long with cross section dimensions of 16-inch wide by 10-inch deep (effective depth was 8 inches). Loading was applied at 24 inches away from the face of central hub, resulting to a shear span of 24 inches and shear span to effective depth ratio of 3. All specimens were designed to have similar flexural strength and high shear stress of approximately $6\sqrt{f_c'}\,(psi)$. Specified compressive strength of concrete was 6,000 psi. Test specimens were named by following convention. The first character identified type of longitudinal reinforcement, where "C" stood for conventional steel with $f_y = 60\,ksi$, "M" was for high-strength steel with $f_y = 120\,ksi$, and "U" was also for high-strength steel but $f_y = 97\,ksi$. The second character specified type of transverse steel. All specimens were reinforced transversely with conventional Grade 60. The third character described the spacing of transverse reinforcement,

4 for *d*/4 and 2 for *d*/2, where *d* is effective depth of the beam cross section. The last character was either "F" for high performance fiber reinforced concrete (HPFRC) or "X" for reinforced concrete (RC).

Figure 2.2.5 and Figure 2.2.6 display shear vs. drift ratio cyclic response while Figure 2.2.7 illustrates response envelopes of these test beams, which includes the "final push" under monotonic load until failure of specimens. It is apparent that all beams with high-strength reinforcement sustained equivalent drift capacity of 5.0% as that with conventional Grade 60 steel. It is also worth noticing that hysteretic shape of cyclic response of beams with high-strength steel $f_y = 120\ ksi$ is narrower than that of beam CC4-X, indicating lower energy dissipation capacity.

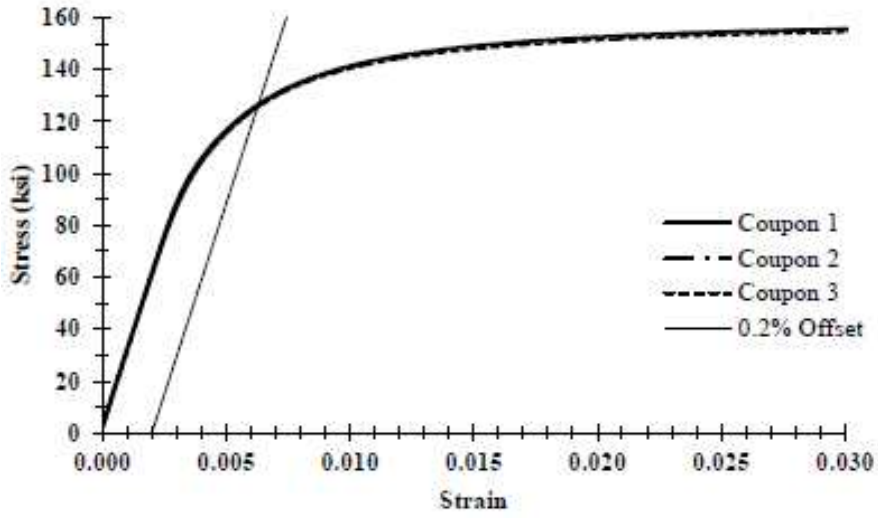

Figure 2.2.3: Stress-Strain Curve for Samples of No. 6 Grade 120 Bar (Pfund, 2012)

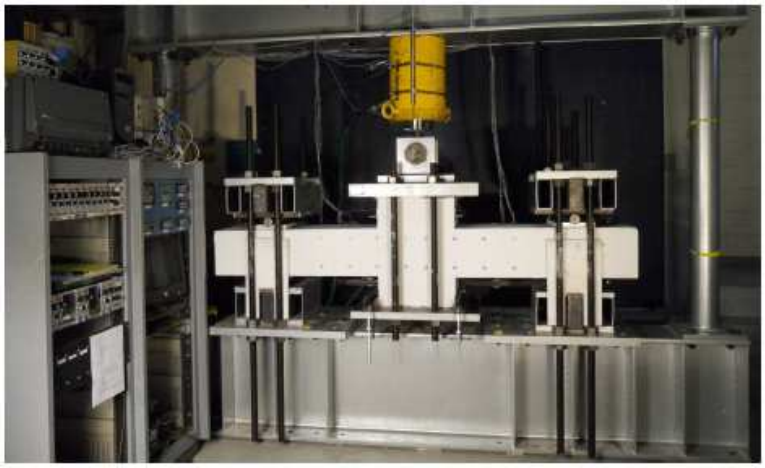

Figure 2.2.4: Test Setup (Pfund, 2012)

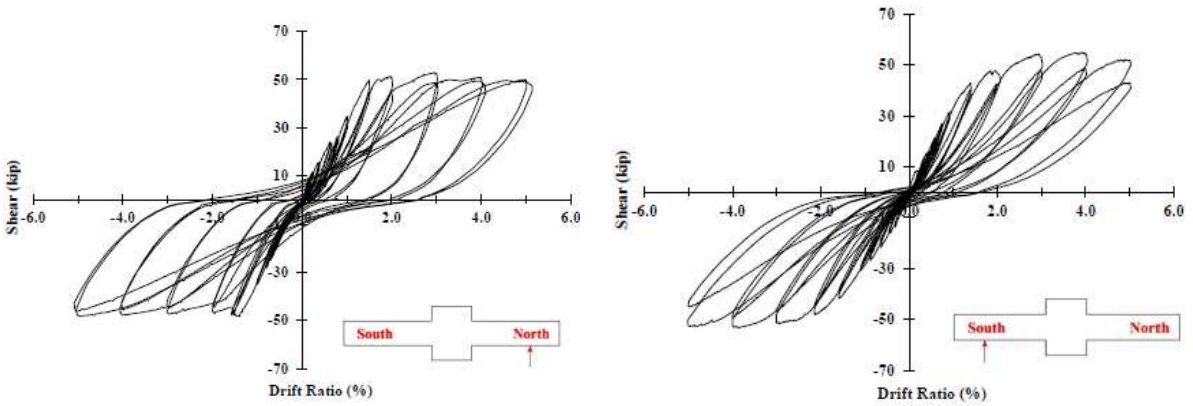

Figure 2.2.5: Shear vs. Drift Ratio - Left: CC4-X, North Beam - Right: MC4-X, South Beam (Pfund, 2012)

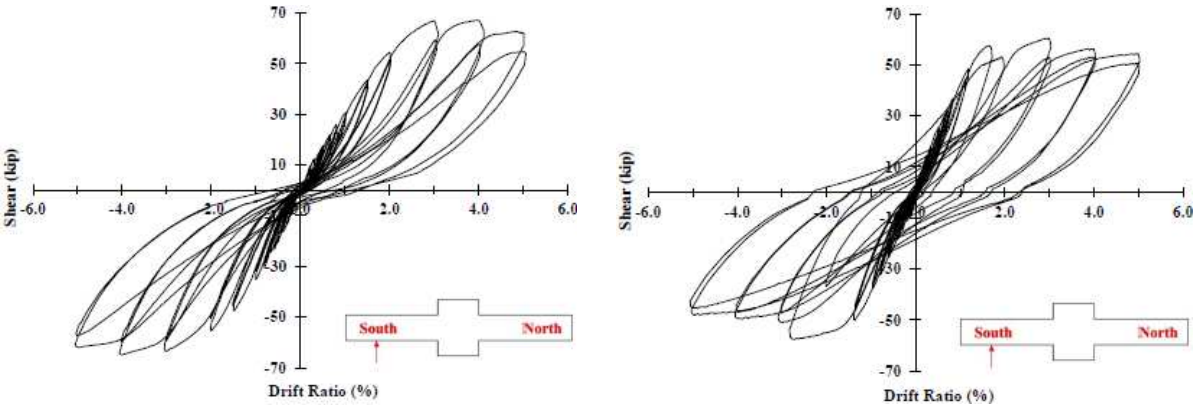

Figure 2.2.6: Shear vs. Drift Ratio - Left: MC2-F, South Beam - Right: UC2-F, South Beam (Pfund, 2012)

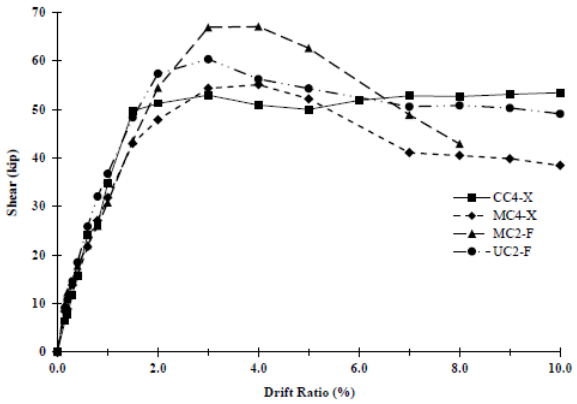

Figure 2.2.7: Comparison of Envelopes of Measure Response (Pfund, 2012)

Tavallali et al., 2014

Tavallali et al. (2014) reports seven more beam test specimens with dimensions similar to those reported in Pfund (2012). These beams were also designed to have nearly identical flexural strength and high shear stress of $6\sqrt{f_c'}\ (psi)$. Concrete compressive strength was approximately 6,000 psi. Representative mechanical properties of reinforcement used in these specimens are shown in Figure 2.2.8.

All beams were reported to achieve drift capacity of about 5.0%. It was observed in this study that reduced amount of reinforcement in combination with higher yield strain of high-strength reinforcement resulted in lower effective initial stiffness of beams with higher-grade steel bars, approximately three-quarter (3/4) of stiffness of specimen with Grade 60 bars.

It is especially of interest to examine the behavior of specimens CC4-X and UC4-X of this study (Figure 2.2.9). Beam CC4-X was reinforced with Grade 60 steel while beam UC4-X was with Grade 97 reinforcement. They were designed to provide the same $A_s f_y$, resulting in reduced amount of longitudinal bars in UC4-X. Both beams attained equivalent drift capacity of about 5.0%. It is apparent that beam UC4-X is less stiff than beam CC4-X due to its reduced amount of reinforcement. Additionally, CC4-X appeared to gain a small increase in shear resistance while UC4-X showed a nearly flat post-yield shear-drift curve. It is due to strain-hardening characteristics of two different types of steel. While Grade 60 bars typically have the tensile-to-yield strength ratio of 1.4 or larger, Grade 97 steel has that ratio of 1.2. Lastly, hysteretic-shaped cyclic response of UC4-X is narrower, indicating less energy dissipation capacity than that of CC4-X.

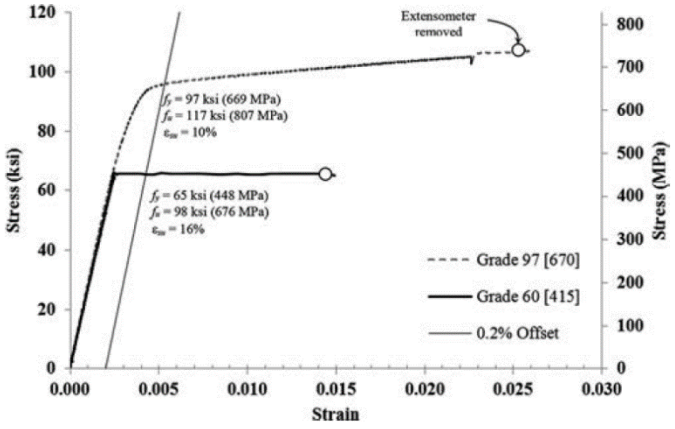

Figure 2.2.8: Representative Mechanical Properties of Reinforcement (Tavallali et al., 2014)

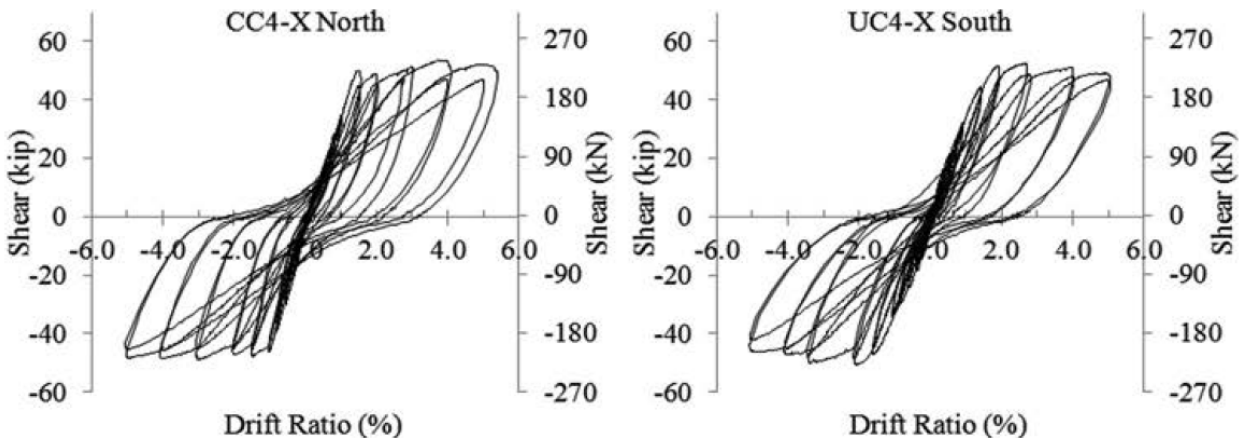

Figure 2.2.9: Measured Shear vs. Drift Ratio - Left: Beam with Grade 60 - Right: Beam with Grade 97 (Tavallali et al., 2014)

Cheng and Giduquio, 2014

Three beams reinforced with Grade 60, SD685, and A1035 and designated as SP1, SP2, and SP3, respectively, were tested in cantilever configuration by Cheng and Giduquio (2014) (Figure 2.2.11). All these beams had cross section of 10 inches wide by 24 inches deep and shear span of 71 inches, resulting in shear span to effective depth ratio of about 3.3. Actual concrete compressive strength of test beams was around 5.4 ksi. Shear stress measured during tests was relatively low at about $2\sqrt{f_c'}\ (psi)$ for all beam tests. Stress – strain relations of longitudinal reinforcement used in test beams are shown in Figure 2.2.10. Measured moment vs. drift ratio cyclic responses are displayed in Figure 2.2.12.

Specimens with high-strength reinforcement achieved comparable rotation capacity of 4.0%, which was drift when beam with Grade 60 started losing strength. It was evident that beams with high-strength reinforcement sustained larger drift at yield, meaning that they had lower effective lateral stiffness than that of beam with Grade 60. It was also noticeable that beams with A1035 had narrower hysteretic shape of cyclic response than that of beam with SD685. Beam with Grade 60 had the broadest hysteretic response shape. As a result, SP1 achieved the highest energy dissipation followed by SP2. SP3 exhibited the lowest energy dissipation capacity.

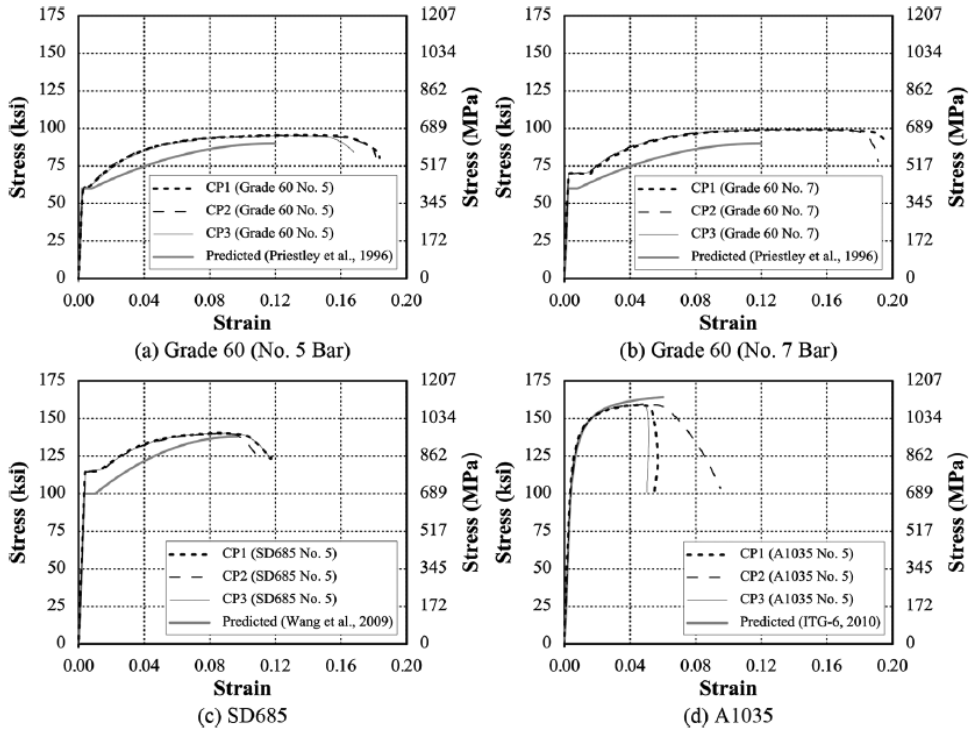

Figure 2.2.10: Stress-Strain Relationship of Longitudinal Reinforcement Used in Test Specimens (Cheng and Giduquio, 2014)

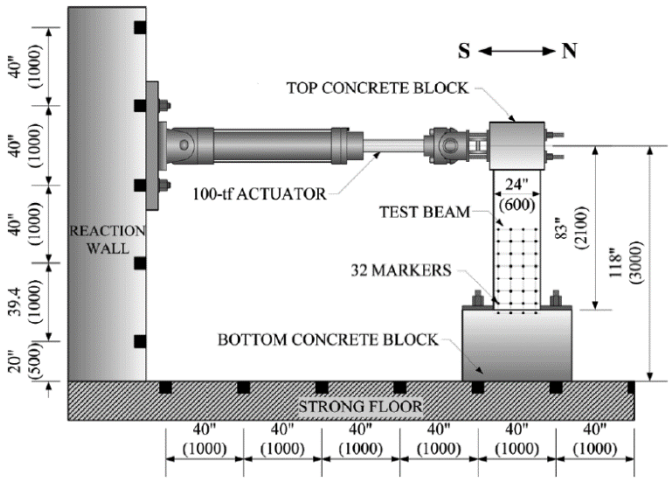

Figure 2.2.11: Test Setup (Cheng and Giduquio, 2014)

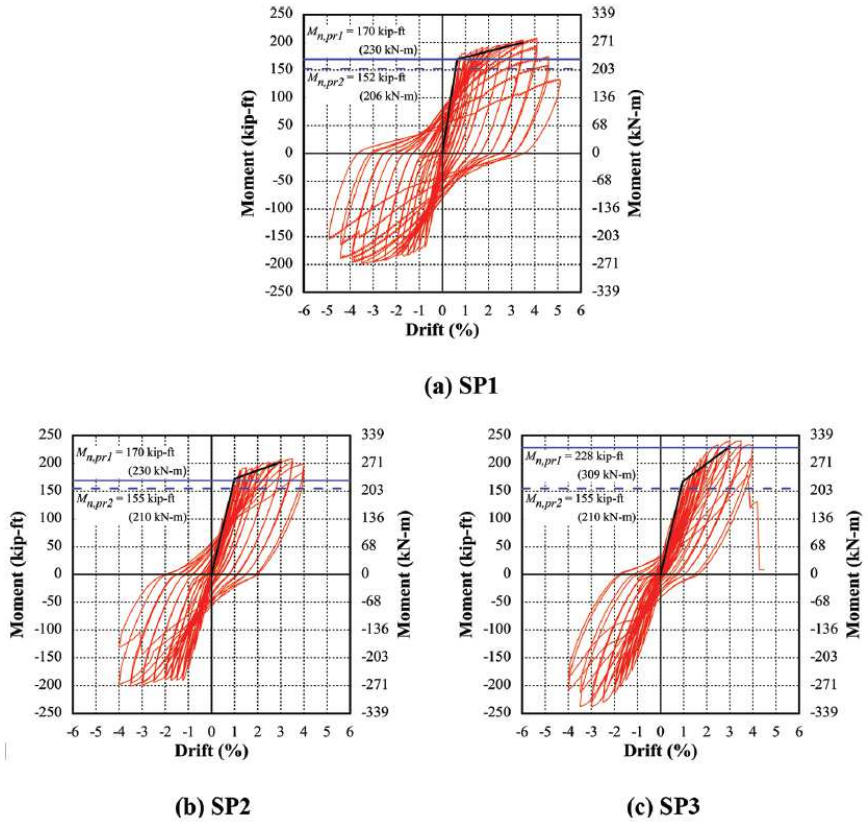

Figure 2.2.12: Measured Moment - Drift Ratio Relationships (Cheng and Giduquio, 2014)

Rautenberg et al., 2013

Rautenberg et al. (2013) reports reversed cyclic tests of eight columns reinforced longitudinally with steel ranging from Grade 60 to Grade 120. Stress-strain relationships of reinforcement used in test specimens are displayed in Figure 2.2.13. Each specimen consisted of two cantilever columns connected by a central loading stub (Figure 2.2.14). Cross section of each column was 9-inch wide by 10-inch deep with shear span-to-effective depth ratio of 3. Columns were reinforced with either four or six deformed steel bars with diameters ranging from 5/8 to 7/8 inch. Reinforcement ratio varied between 1.1 to 3.3%. Columns with Grade 60 and Grade 120 were designed to have approximately the same flexural capacity. Transverse reinforcement was 3/8-in. diameter deformed-bar hoops for all columns. Concrete compressive strength ranged from 5,000 to 8,000 psi. Applied axial load was either 10% or 20% of $A_g f_c'$. Testing configuration is illustrated in Figure 2.2.15.

In their study, moment-curvature analyses indicated that section with reduced amount of Grade 120 steel had lower effective cracked stiffness than that of section with Grade 60

reinforcement. In the laboratory tests, it was observed that columns with Grade 120 reinforcement had less cracked stiffness than those with Grade 60 (Figure 2.2.16). Nevertheless, columns with high-strength reinforcement (Grade 80 and Grade 120) achieved drift capacities between 4 and 8%, which was comparable to those of similar columns with conventional Grade 60 steel. Additionally, it was noted that columns with higher-grade reinforcement dissipated less energy than columns with Grade 60 steel.

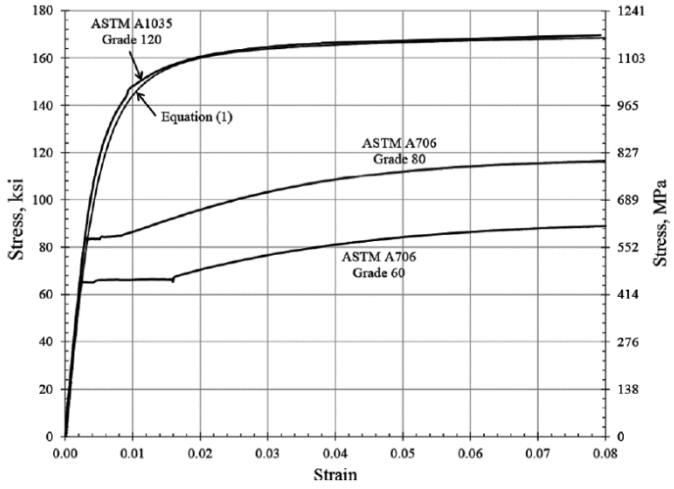

Figure 2.2.13: Stress-Strain Curves of Longitudinal Reinforcement Used in Test Specimens (Rautenberg et al., 2013)

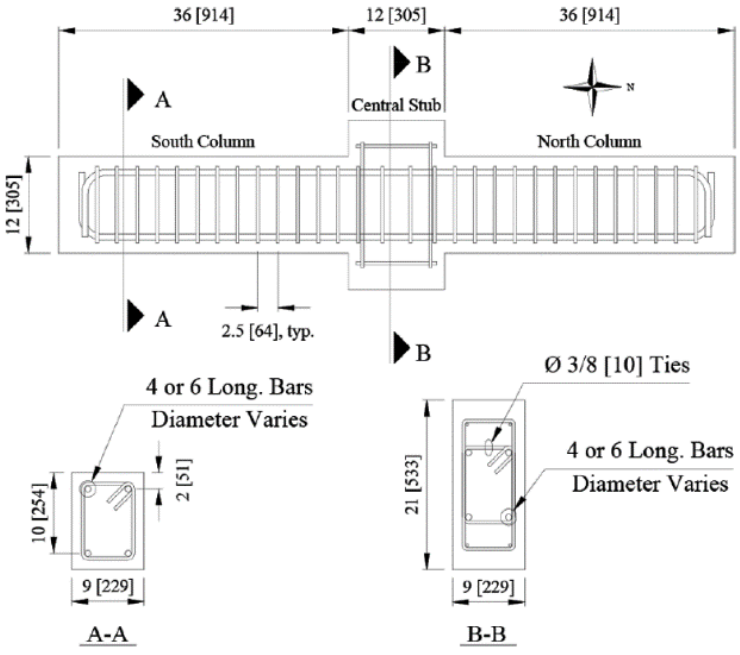

Figure 2.2.14: Drawings of Test Specimens (Rautenberg et al., 2013)

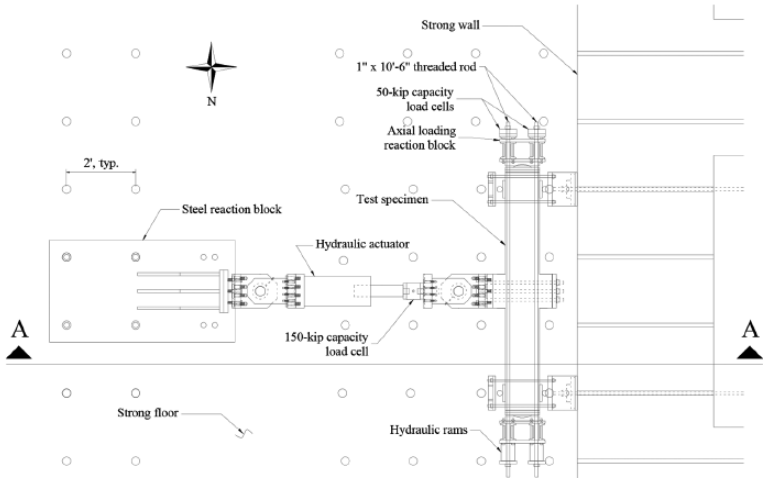

Figure 2.2.15: Test Setup (Rautenberg et al., 2013)

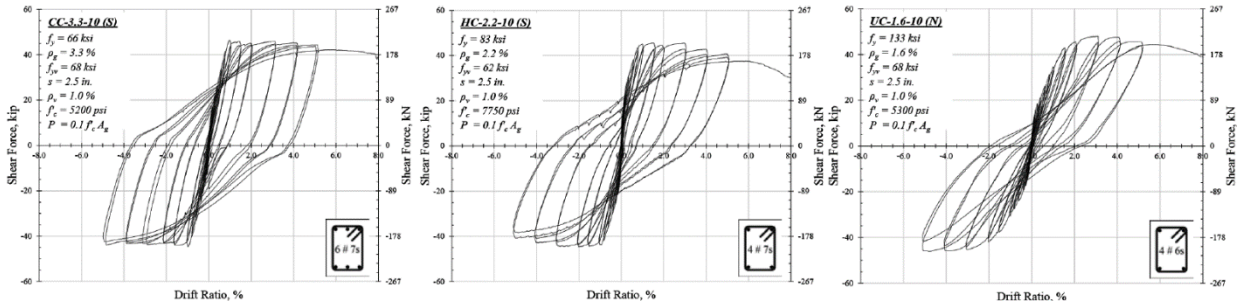

Figure 2.2.16: Measured Shear vs. Drift Ratios under Axial Load of $0.1A_g f_c'$ - Left: Gr. 60 - Middle: Gr. 80 - Right: Gr. 120 (Rautenberg et al., 2013)

Sokoli & Ghannoum, 2016

In this laboratory test investigation, three columns reinforced with Grade 60, Grade 80, and Grade 100 (designated as CS60, CS80, CS100, respectively) longitudinal reinforcement were tested under reversed cyclic loading with axial load of approximately $0.27A_g f_c'$ as well as shear stress of about $8\sqrt{f_c'}\ (psi)$. All steel bars have well-defined yield plateau in the stress-strain relationship (Figure 2.2.17). Columns with higher-grade reinforcing steel bars were designed to have reduced amount of longitudinal bars as to achieve equivalent flexural strength as that of column with Grade 60 steel.

Figure 2.2.18 illustrates the lateral load vs. drift ratio response of test specimens. CS60 and CS80 both had similar cyclic behaviors and achieved at least 5% drift capacity without significant loss in lateral strength. CS100, however, only sustained up to 3% drift ratio before starting to lose lateral strength drastically. Test results also indicated that strain demands on longitudinal bars in

CS100 and CS80 were 100% and 65% higher than that in CS60, respectively at the same drift levels.

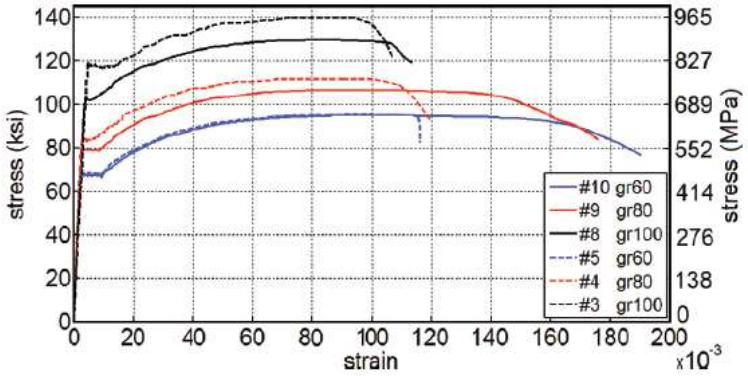

Figure 2.2.17: Typical Stress-Strain Relations of Reinforcement (Sokoli and Ghannoum, 2016)

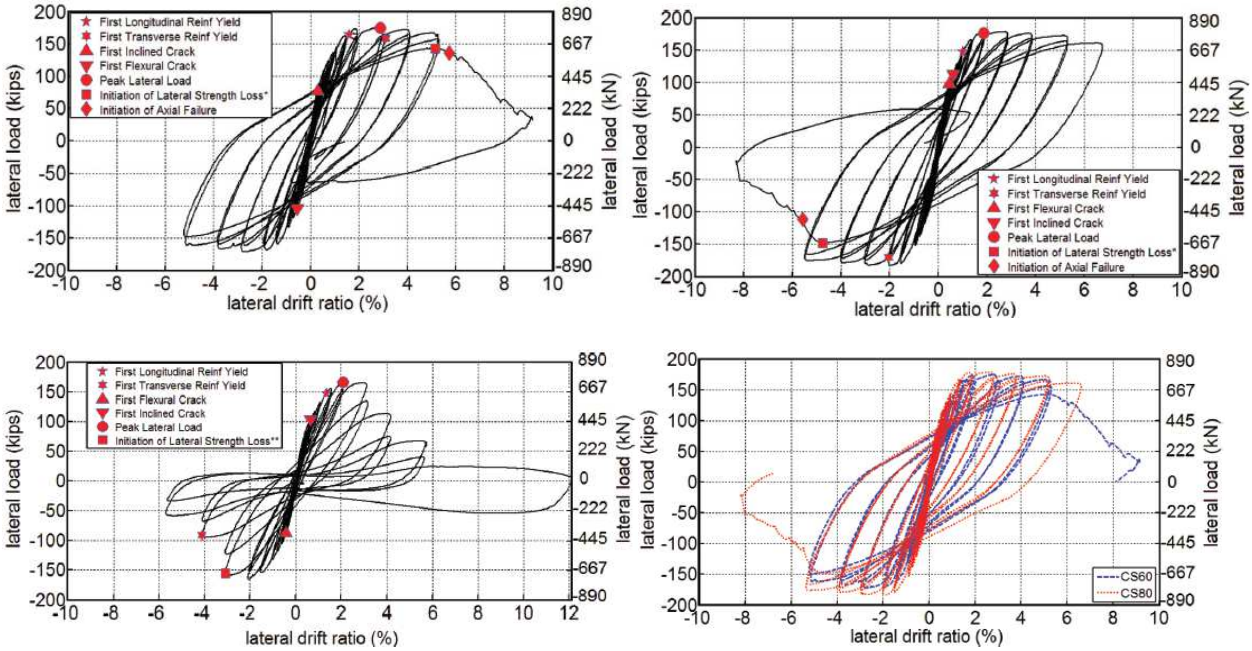

Figure 2.2.18: Lateral Load vs. Drift Ratio Response – Top Left: CS60 – Top Right: CS80 – Bottom Left: CS100 – Bottom Right: Comparison between CS60 and CS80 (Sokoli and Ghannoum, 2016)

Sokoli et al., 2017

Companion research program with laboratory tests on columns was carried out at University of Texas, Austin at the same time as this research program. Four test columns were reinforced with conventional Grade 60 (CH60), Grade 100 A1035 with round-hound stress-strain

curve (CM100), and Grade 100 T/Y = 1.16 and Grade 100 T/Y = 1.27 both having distinct yield plateau (CL100 and CH100, respectively). The specimen design resulted in low axial load of $0.15A_g f_c'$ and low shear stress of $4\sqrt{f_c'}\ (psi)$.

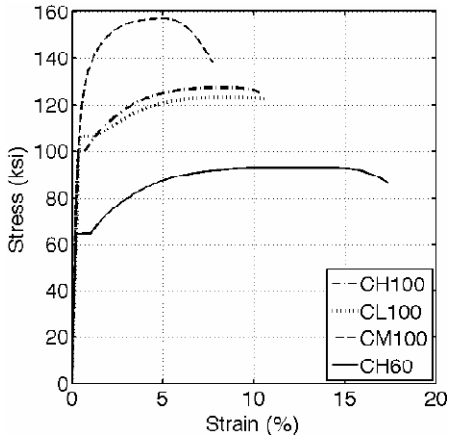

Figure 2.2.19: Stress-Strain Relations of Longitudinal Reinforcement (Sokoli et al., 2017)

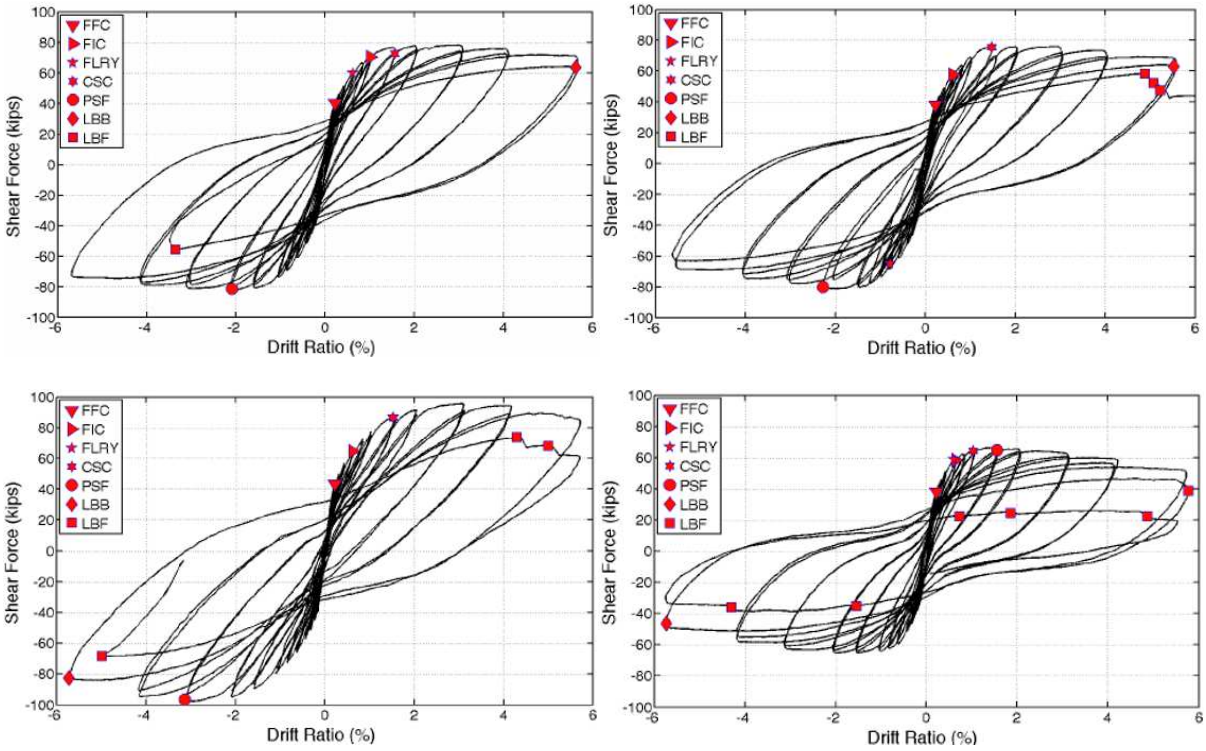

Figure 2.2.20: Lateral Load vs. Drift Response - Top Left: CH100 - Top Right: CL100 - Bottom Left: CM100 - Bottom Right: CH60

Note: FFC: First Flexural Crack – FIC: First Inclined Crack – FLRY: First Longitudinal Reinforcement Yield – CSC: Cover Splitting Crack – PSF: Peak Shear Force – LBB: Longitudinal Bar Buckling – LBF: Longitudinal Bar Fracture.

Figure 2.2.19 displays typical stress-strain relations of longitudinal reinforcement used in test columns. All columns had the same longitudinal reinforcement ratio. Lateral load vs. drift ratio responses are presented in Figure 2.2.20. It was concluded that all columns attained comparable drift capacities at about 5.5% prior to longitudinal bar fractures. They all appeared to have equivalent effective stiffness.

2.3. FRAME ELEMENT MODELS

Beam and column frame elements can be modeled by different formulations. 3-D continuum finite element models can account for discrete concrete cracking, bond-slip effects (Lowes, 1999; Girard and Bastien, 2002), and bar buckling. These models are relatively complex in their formulation and are computationally intensive.

Another category of models are the concentrated plasticity elements, in which non-linear flexural behavior is lumped in a non-linear rotational spring element at each end of frame elements (Figure 2.3.1). This approach generally does not account for flexural-axial interaction, and the possibility for hinging to occur along the length is precluded unless nonlinear springs are distributed along the length. In addition, it is unable to model beam axial elongation (Visnjic, 2014), which has been recognized to impose additional shear forces onto exterior columns (Fenwick et al., 1996; Kabeyasawa et al., 2000; Kim et al., 2004; and Visnjic et al., 2012). Furthermore, concentrated-plasticity element used in building models under nonlinear dynamic analyses has been observed to cause spurious damping force given Rayleigh damping model with initial stiffness matrix being employed (Chopra and McKenna, 2016).

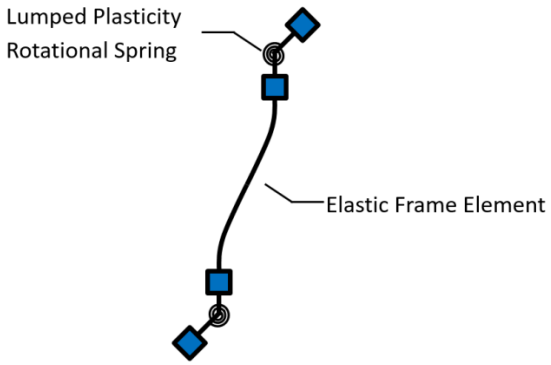

Figure 2.3.1: Typical Lumped Plasticity Model

Distributed-plasticity fiber-section elements have gained favorability in modeling beams and columns because the formulation eliminates the above-mentioned short-comings. There are currently two distributed-plasticity fiber-section element types available in OpenSees platform, which are displacement-based and force-based beam-column elements (OpenSees, 2012). Displacement-based element is formulated based on the principle of virtual displacement such that

equilibrium is satisfied "weakly." To increase accuracy of solution, the element must be divided into smaller sub-elements, which would increase number of degrees of freedom of the global system. For the force-based element, the principle of virtual force is employed in the formulation and equilibrium between element and section forces is exact. Accuracy of the solution can be improved by increasing the number of integration points, which is preferable from a computational standpoint.

Longitudinal reinforcement of reinforced concrete beams and columns anchored in a beam-column joint or foundation are expected to develop tensile strain over the development length. Tensile strain gradient causes slip of reinforcing bar relative to surrounding concrete. Consequently, the slip results in fixed-end rotation between frame members and their adjacent supports at the interface. This rotation in turn increases flexibility of the beam and column elements, which should be modeled (Sezen and Setzler, 2008) as it has been reported to account for up to 40% of total lateral deformation of frame members (Sezen and Moehle, 2006).

One method to account for fixed-end rotation due to bar slip in frame element model is to reduce the effective flexural stiffness of the frame member (Elwood and Eberhard, 2009). However, by this approach, local responses of the frame member and bar slip cannot be separated. Other researchers have proposed the addition of rotational springs at the ends of frame elements (Otani, 1974; Ibarra et al., 2005), but the absence of slip-axial-load interaction can be a drawback of this approach. Zero-length fiber-section element implemented in series with frame element (Figure 2.3.2) has been introduced and studied to model fixed-end rotation (Berry, 2006; Zhao and Sritharan, 2007; and Ghannoum and Moehle, 2012) and has gained popularity.

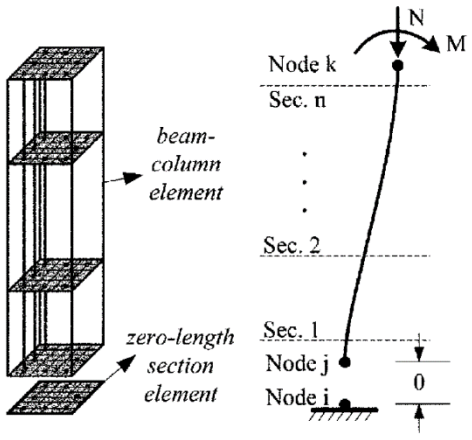

Figure 2.3.2: Zero-Length Fiber-Section Element to Model Bar Slip (Zhao and Srithanran, 2007)

Shear response can be incorporated into total response of frame elements by a separate zero-length shear spring element (Figure 2.3.3) or it can be aggregated into any section of a beam-column element. In such approach, flexure and shear are typically uncoupled within the element, which may be acceptable as the shear component generally does not contribute significantly to total deformation in typical frame members provided frame member is not shear-critical element.

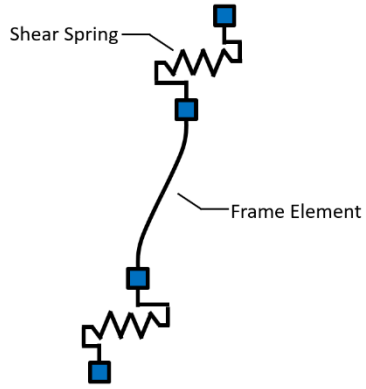

Figure 2.3.3: Shear Spring in Series with Frame Element

Beam-column joints can also be modeled based on different approaches. Joint deformation can be accounted for through calibration of flexural stiffness of frame elements (Otani, 1974; Anderson and Townsend, 1997). Another method employs the lumped-plasticity rotational hinge (Alath and Kunnath, 1995; El-Metwally and Chen, 1988). More advanced formulation involving 2-D or 3-D continuum finite element models to incorporate joints also has been proposed (Fleury et al., 2000; Elmorsi et al., 2000). Lowes and Altoontash (2003) proposed a joint model in which bond-slip springs and a shear panel are self-calibrated within the element based on results from laboratory tests (Figure 2.3.4). The main short-comings of these approaches include the inability to separate joint behavior from adjacent framing elements, the absence of interaction with axial load, intensive computation, and numerical convergence problem.

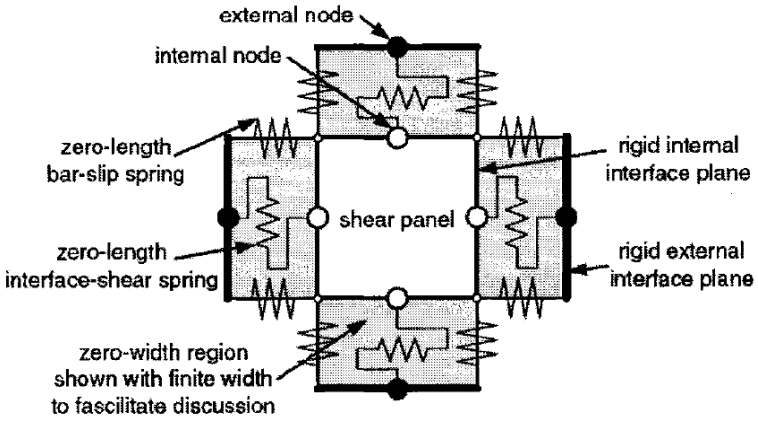

Figure 2.3.4: Joint Element (Lowes et al., 2004)

A simpler approach is to model beam-column joints as partially rigid. Through statistical analyses of laboratory test results, Birely et al. (2012) suggested to model the stiffness of the beams and columns in accordance with ASCE 41 and model the joint as partially rigid with recommended coefficient of 0.6 for beam-column connections that are compliant with the ACI 318 design requirements (Figure 2.3.5).

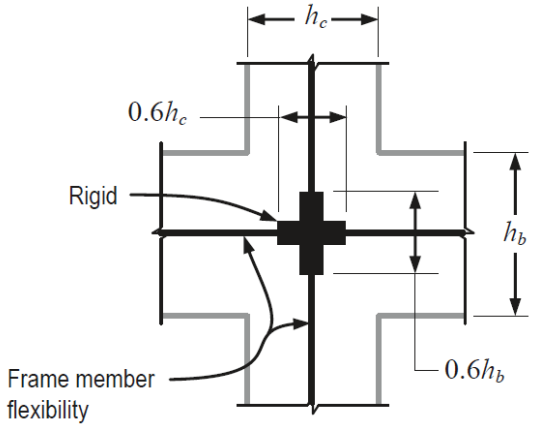

Figure 2.3.5: Partially Rigid Joint Model by Birely et al. (2012)

2.4. BUILDING RESPONSE

Rautenberg, 2011

Two sets of special moment frame buildings having three, six, twelve, and twenty stories were considered. In one set of buildings, columns were designed using conventional Grade 60 reinforcement while those in other set were designed with Grade 120 A1035 reinforcement. All beams and slabs were reinforced with Grade 60 steel. All buildings were designed following requirements by ACI 318-08 with strong-column-weak-beam design philosophy. Columns were sized such that axial loads due to gravity were between 0.10 and $0.20A_g f_c'$ for interior columns.

Typical moment-curvature and hysteretic responses of columns with different grades of reinforcement are shown in Figure 2.4.1 and Figure 2.4.2, respectively. Dynamic analyses were performed for each of the eight building models subjected to 24 unscaled strong-motion acceleration records.

The mean ratio of the roof drift ratio in models with Grade 120 reinforcement to that in models with Grade 60 reinforcement for a given number of stories was 1.03 (Figure 2.4.3). It was concluded that frame buildings with columns reinforced longitudinally with high-strength steel were not likely to experience consistently higher drift ratios than those with columns reinforced longitudinally with Grade 60 steel.

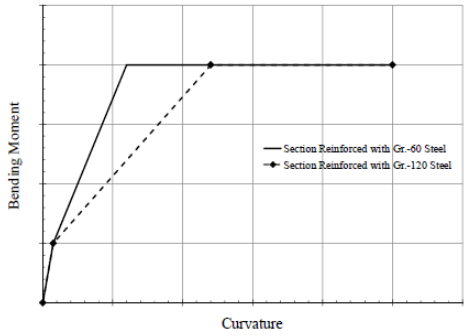

Figure 2.4.1: Moment-Curvature Relations for Column Sections (Rautenberg, 2011)

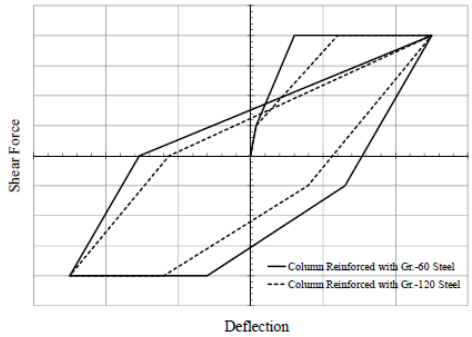

Figure 2.4.2: Hysteretic Responses for Columns (Rautenberg, 2011)

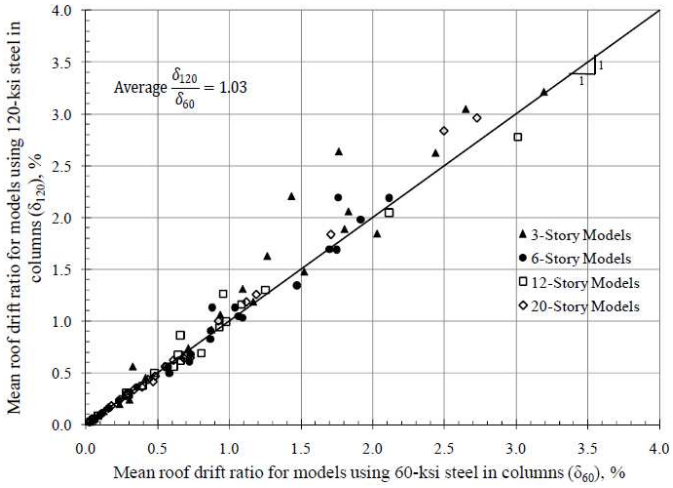

Figure 2.4.3: Comparison of Maximum Computed Mean Roof Drift Ratios of Models using Grade 60 and Grade 120 Reinforcement in Columns

Rautenberg and Pujol, 2012

Similar sets of frame buildings as in Rautenberg (2011) were used in this study to explore and compare the seismic performance between buildings with Grade 60 and Grade 120 reinforcement. Both columns and beams in all frame buildings with higher-grade reinforcement were designed with Grade 120 steel (in Rautenberg, 2011 only columns were designed with Grade 120 steel and beams were designed with Grade 60 steel). Hysteretic behavior proposed by Takeda et al. (1970) was employed to model the responses of columns. Each of the building models was subjected to a set of seven unscaled ground motions. The mean peak roof displacement computed for models with Grade 120 reinforcement was on average 15% higher than that of comparable models with Grade 60 steel (Figure 2.4.4).

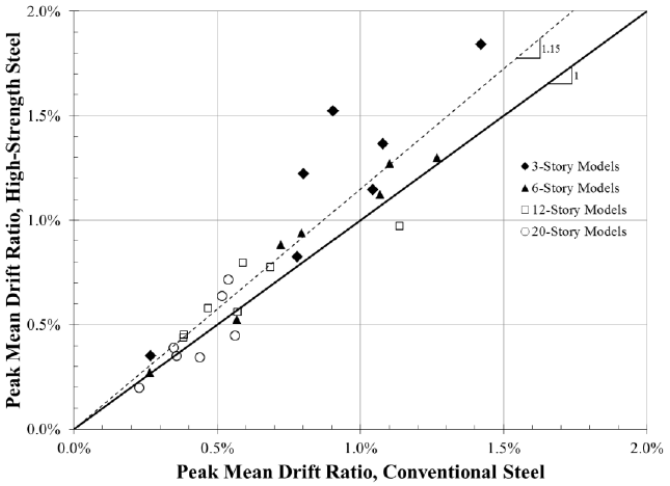

Figure 2.4.4: Comparison of Peak Computed Roof Drift Ratios of Building Models (Rautenberg and Pujol, 2012)

NIST, 2014

In this study, nonlinear analysis of buildings with conventional Grade 60 and high-strength reinforcement was carried out and seismic performance was compared between these buildings. Buildings with reinforcement other than Grade 60 were designed by reducing the area of longitudinal reinforcement detailed for the Grade 60 design by the ratio of the yield strengths of the steel grades used. Reduced amount of longitudinal reinforcement in structural components results in reduction of cracked effective stiffness of these elements. Therefore, predominant periods of these buildings are lengthened.

The archetype building was a 13-story office building. The hypothetical site was in Berkeley, California with Soil Class C, for which S_{DS} and S_{D1}were 1.17 and 0.65 second, respectively (ASCE 7-10). The building had one basement level and twelve stories above grade (Figure 2.4.5). Typical bay widths are 30 feet in the north-south direction and either 40 feet or 20 feet long in the east-west directions. The flooring system is a two-way, post-tensioned, 8-inch thick

cast-in-place slab. The lateral force-resisting system in the north-south direction was four 7-bay special moment resisting frames. In the east-west direction, a dual system composed of four special moment frames and four special walls with outrigger beams was used as the seismic system.

The building with Grade 60 reinforcement as base model was designed in accordance with ACI 318 and ASCE 7. Specified compressive strength of concrete was $f_c' = 5\ ksi$ (Barbosa, 2011). Per ASCE 7, the building was classified as Seismic Design Category D with an importance factor of 1. The seismic response modification coefficient R was 8 and 7 for the special moment frames and dual system, respectively. The design base shear coefficients were 4.1% in north-south direction and 7.6% in east-west direction. Axial load due unfactored gravity loads ranged from $0.15A_g f_c'$ to $0.35A_g f_c'$ on perimeter columns and was $0.30A_g f_c'$ on corner columns and $0.12A_g f_c'$ on walls.

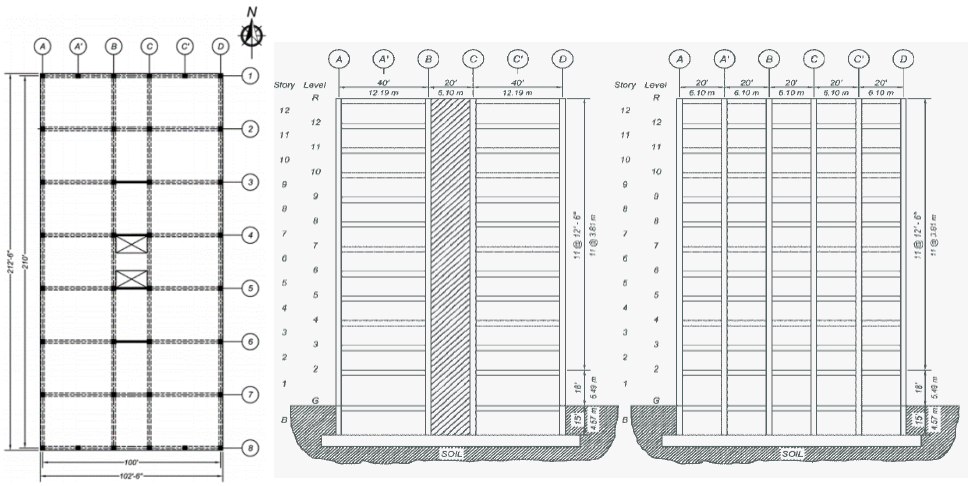

Figure 2.4.5: Archetype Building – Left: Plan View – Right: Elevation View (Barbosa, 2011)

Numerical models of these buildings were constructed and nonlinear dynamic analyses were performed using the Open System for Earthquake Engineering Simulation (OpenSees, 2011). Beams and columns were modeled using force-based beam column elements while reinforced-concrete walls were modeled by a 3-D nonlinear truss (Barbosa, 2011; Panagiotou et al., 2011; Lu and Panagiotou, 2013). Rayleigh damping proportional to stiffness after application of gravity load was incorporated with damping coefficients of 2% being set at 0.56 Hz (1.77 seconds) and 6.25 Hz (0.16 seconds). More details on modeling can be found in the NIST (2014) report.

The building models did not incorporate the effect of bond slip of longitudinal reinforcement of the beams and the wall anchored in the beam-column joints and foundation elements, respectively. Greater strain penetration of higher-grade steel, resulting in greater slip of reinforcement from connections or foundation elements, would cause the buildings with high-strength reinforcement to be even more flexible. Rayleigh damping proportional to stiffness after the application of gravity loads were employed to define damping force matrix.

A set of seven ground motion pairs with near-fault characteristics were selected for the analyses. Pseudo-acceleration spectra for the fault normal and fault parallel components of these ground motions are shown in Figure 4.1.2 and Figure 2.4.7. Nonlinear dynamic analyses were performed for design level and maximum considered level earthquakes. Fault normal and fault parallel motions were applied concurrently in each analysis. In one set of analyses, the fault normal component was applied in north-south direction and in another set of analyses in east-west direction.

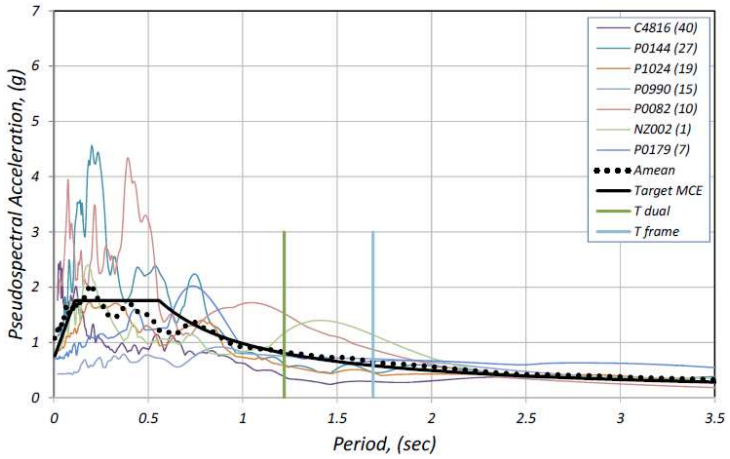

Figure 2.4.6: Spectra of Fault Normal (FN) Component of Ground Motions

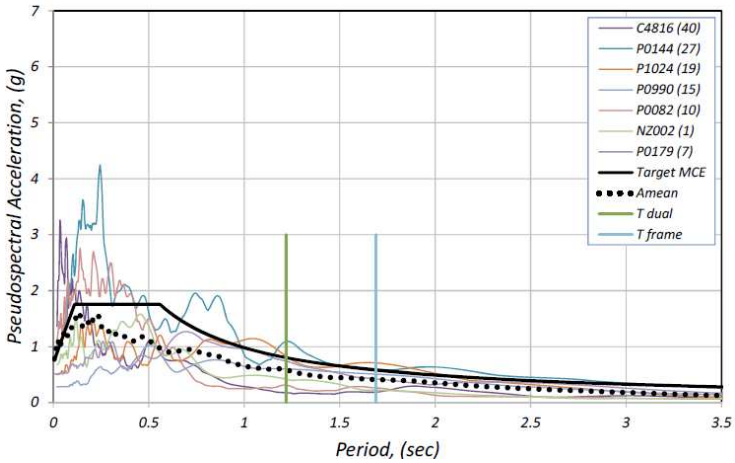

Figure 2.4.7: Spectra of Fault Parallel (FP) Component of Ground Motions

Overall results:

For the design level earthquake, mean peak roof drift ratios ranged between 1.06% and 1.25% with the lowest and highest drift ratios achieved by buildings with Grade 60 and Grade 100 reinforcement, respectively (Figure 2.4.8). Correspondingly, these ratios were 1.57% and 1.66% under maximum considered earthquake. Mean maximum story drift ratios exhibited similar trends, ranging between 2.08% and 3.40% for design level earthquake and between 2.40% and 3.45% under maximum considered earthquake (Figure 2.4.9).

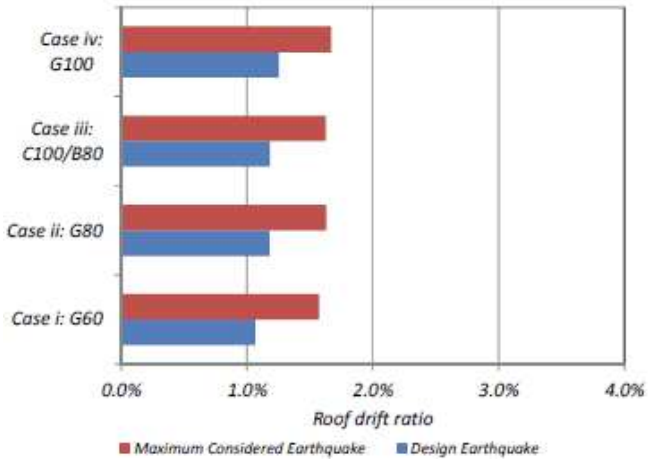

Figure 2.4.8: Mean Peak Roof Drift Ratios in Special Moment Frame - Fault Normal Component Applying in North-South Direction (ATC 98, 2014)

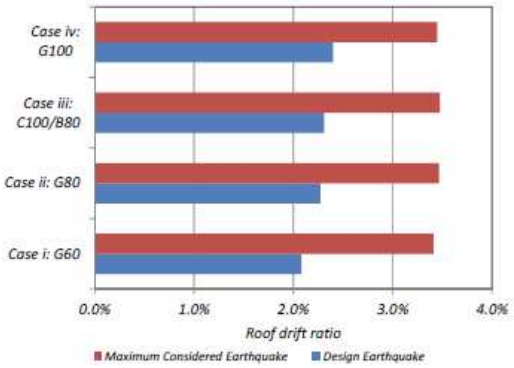

Figure 2.4.9: Mean Peak Interstory Drift Ratios in Special Moment Frame - Fault Normal Component Applying in North-South Direction (ATC 98, 2014)

For the dual system, the trends became more apparent with mean peak roof drift ratios varying from 0.88% to 0.97% and from 1.23% to 1.55% under design and maximum considered earthquakes, respectively. Mean maximum story drift ratios were between 1.08% and 1.60% at design level earthquake and between 1.17% and 1.88% under maximum considered earthquake.

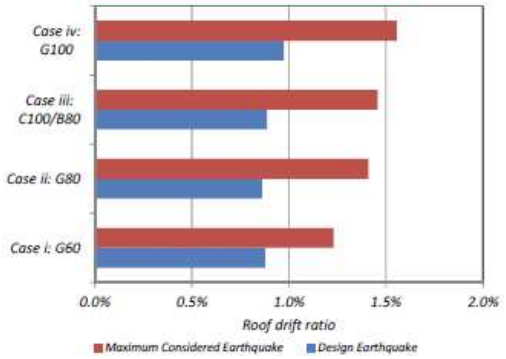

Figure 2.4.10: Mean Peak Roof Drift Ratios in Dual System - Fault Normal Component Applying in East-West Direction (ATC 98, 2014)

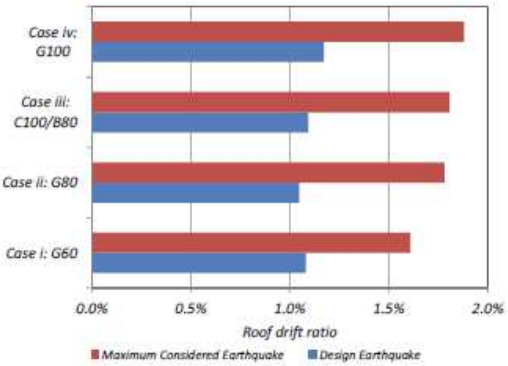

Figure 2.4.11: Mean Peak Interstory Drift Ratios in Dual System - Fault Normal Component Applying in East-West Direction (ATC 98, 2014)

Figure 2.4.12 displays reported strain response of longitudinal bars in perimeter beams, interior columns, and wall boundary elements. Mean maximum tensile strain in perimeter beams and shear wall boundary elements did not indicate any particular trend across all buildings with different reinforcement grades. Longitudinal bar strain in interior columns appeared to be larger for higher grade reinforcing steel.

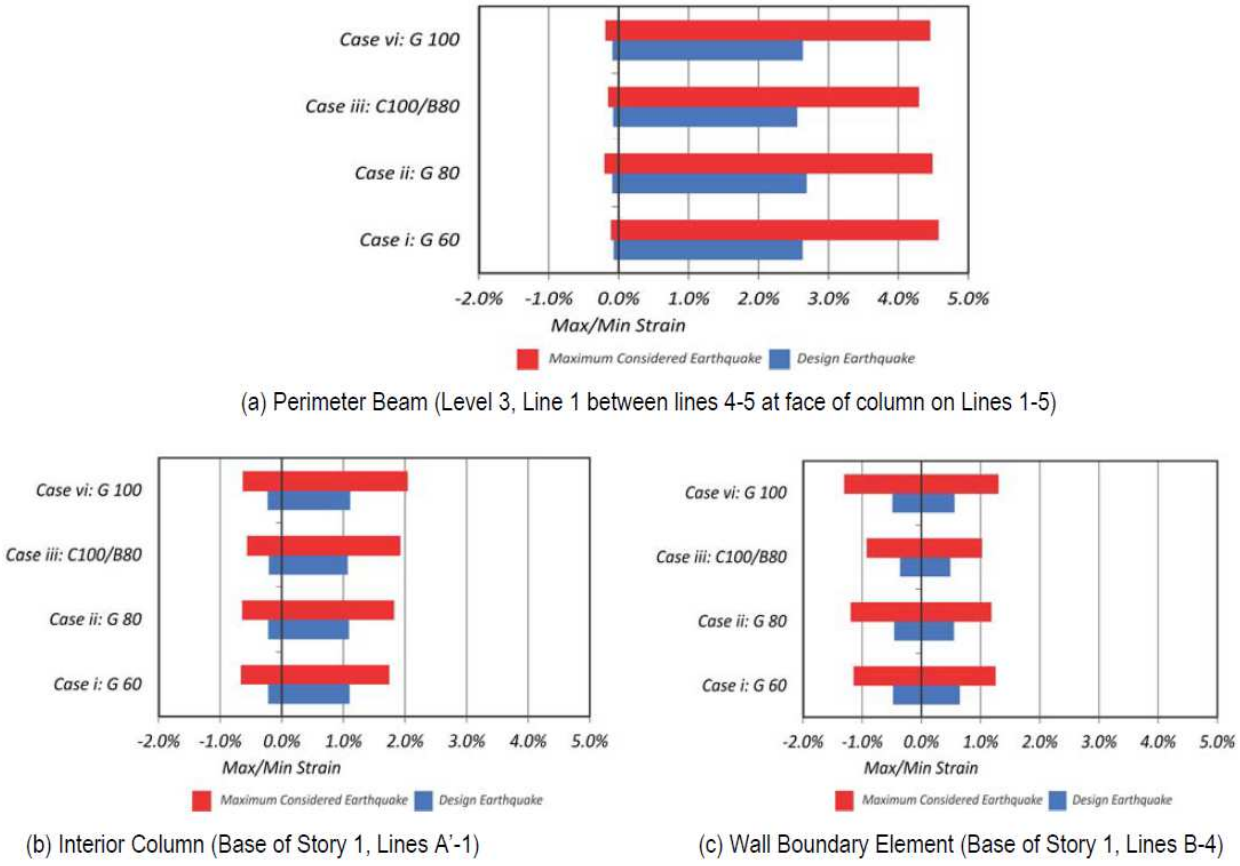

Figure 2.4.12: Mean Strains on Longitudinal Bars (NIST, 2014)

2.5. LOW-CYCLE FATIGUE

Several laboratory test studies have investigated the low-cycle fatigue performance of steel reinforcing bars. Several tests have been carried out on conventional Grade 60 with bar size ranging from No. 4 to No. 9. Most recent laboratory tests have been carried out on both A706 Grade 60 and Grade 100 (Ghannoum and Slavin, 2016). Most of these studies utilize the Coffin-Mansion relation (Manson, 1953; Coffin, 1954) to describe the relationship between strain quantity and fatigue life that is represented by number of half cycles, as

$$\varepsilon_a = M\left(2N_f\right)^m$$

ε_a: is the strain amplitude or strain range [strain amplitude is defined as half the strain range, where $strain\ range = (\varepsilon_{max} - \epsilon_{min})$]

N_f: is the number of full cycles ($2N_f$ is number of half cycles) to failure.

M and m: are material constants.

M and m are determined from laboratory tests, with values found to vary among different investigations in which different steel grades and bar sizes were used.

Mander et al., 1994

ASTM A615 Grade 40 steel reinforcing bars with nominal yield strength of 40 ksi were experimentally evaluated for low-cycle fatigue behavior under axial-strain-controlled reversed cyclic tests with strain amplitudes ranging from yield to 6%. All bars were laterally supported at spacing of six bar diameters. It was also found in the study that if $s > 8d_b$, the compressive yield strength could not be sustained under cyclic loading.

Several existing fatigue models such as Coffin-Mansion and Koh-Stephen (1991), which related plastic strain (ε_{ap}) and total strain (ε_a) amplitudes, respectively, with fatigue-life were assessed and applied on the laboratory test data to arrive at following relations

Coffin-Mansion: $\varepsilon_{ap} = 0.0777\left(2N_f\right)^{-0.486}$

Koh-Stephen: $\varepsilon_a = 0.0795\left(2N_f\right)^{-0.448}$

Brown and Kunnath (2004): Low-Cycle Fatigue Failure of Reinforcing Steel Bars

Laboratory tests were also performed in this investigation. ASTM A615 Grade 60 reinforcing steel with bar size ranging from No. 6 to No. 9 were tested under cyclic axial load with amplitudes varying between 1.5% and 3.0%. The test specimens were laterally supported with spacing of six bar diameters. Koh-Stephens model was applied on test data to give

$$\varepsilon_a = 0.09\left(2N_f\right)^{-0.45} \rightarrow No.6$$
$$\varepsilon_a = 0.11\left(2N_f\right)^{-0.44} \rightarrow No.7$$
$$\varepsilon_a = 0.08\left(2N_f\right)^{-0.36} \rightarrow No.8$$
$$\varepsilon_a = 0.07\left(2N_f\right)^{-0.31} \rightarrow No.9$$

Similarly, Coffin-Manson expression was also employed by Brown and Kunnath

$$\varepsilon_{ap} = 0.16\left(2N_f\right)^{-0.57} \rightarrow No.6$$
$$\varepsilon_{ap} = 0.13\left(2N_f\right)^{-0.51} \rightarrow No.7$$
$$\varepsilon_{ap} = 0.09\left(2N_f\right)^{-0.42} \rightarrow No.8$$
$$\varepsilon_{ap} = 0.07\left(2N_f\right)^{-0.37} \rightarrow No.9$$

Hawileh et al., 2010

ASTM A706 and A615 Grade 60 deformed reinforcing steel bars were tested in the laboratory to evaluate the low-cycle fatigue behavior in this study. All bars were No. 6 and subjected to strain-controlled cyclic axial loading with nonzero mean strains. Constant-amplitude

sinusoidal strains ranging from 2% to 8% were applied in different tests. The clear length of bar specimen was 6 inches in all tests. It was also demonstrated that the low-cycle fatigue behaviors of ASTM A706 and A615 steel bars were similar even though their monotonic ductility ratios were significantly different. Following relations were derived from the test program

$$\varepsilon_a = 0.09\left(2N_f\right)^{-0.409} \rightarrow A706$$
$$\varepsilon_a = 0.1008\left(2N_f\right)^{-0.428} \rightarrow A615$$
$$\varepsilon_{ap} = 0.103\left(2N_f\right)^{-0.54} \rightarrow A706$$
$$\varepsilon_{ap} = 0.128\left(2N_f\right)^{-0.57} \rightarrow A615$$

Ghannoum and Slavin, 2016:

Four different grades of steel were tested including Grade 60 and 80 conforming ASTM A706, Grade 80 satisfying ASTM A615, and Grade 100 having a distinct yield plateau, with bar sizes of No. 5, 8, and 11. Three clear spans of $4d_b$, $5d_b$, and $6d_b$ were applied for different tests. Only No. 8 bars of different grades were tested cyclically under axial load with two different strain ranges. Therefore, a fatigue model was only developed for this bar size with the form

$$2N_f = a \times (total\ strain\ range)^b$$

Coefficients a and b were determined experimentally for No. 8 bars of different grades from tests with varying clear spans. Revising the above form to the familiar Coffin-Manson model of $\varepsilon_a = M\left(2N_f\right)^m$ leads to the following relations

Manufacturer 1:

Grade 60:
$$\varepsilon_a = 0.0797\left(2N_f\right)^{-0.348} \rightarrow 4d_b$$
$$\varepsilon_a = 0.0785\left(2N_f\right)^{-0.361} \rightarrow 5d_b$$
$$\varepsilon_a = 0.0772\left(2N_f\right)^{-0.386} \rightarrow 6d_b$$

Grade 100:
$$\varepsilon_a = 0.0500\left(2N_f\right)^{-0.216} \rightarrow 4d_b$$
$$\varepsilon_a = 0.0492\left(2N_f\right)^{-0.246} \rightarrow 5d_b$$
$$\varepsilon_a = 0.0483\left(2N_f\right)^{-0.265} \rightarrow 6d_b$$

Manufacturer 2:

Grade 60:
$$\varepsilon_a = 0.0603\left(2N_f\right)^{-0.267} \rightarrow 4d_b$$
$$\varepsilon_a = 0.0590\left(2N_f\right)^{-0.302} \rightarrow 5d_b$$

$$\varepsilon_a = 0.0583\left(2N_f\right)^{-0.330} \rightarrow 6d_b$$

Grade 100: $$\varepsilon_a = 0.0440\left(2N_f\right)^{-0.185} \rightarrow 4d_b$$

$$\varepsilon_a = 0.0432\left(2N_f\right)^{-0.190} \rightarrow 5d_b$$

$$\varepsilon_a = 0.0423\left(2N_f\right)^{-0.224} \rightarrow 6d_b$$

CHAPTER 3: LABORATORY TEST PROGRAM

Important and general information about the laboratory test program is presented in this chapter including test specimen design, test setup and apparatus, instrumentation, preliminary estimate of load-resisting capacity, and loading procedure. More details on actual dimensions, actual material properties, instrumentation, loading protocols, data acquisition systems, and data reduction methods are described in Appendix A.

3.1. TEST SPECIMEN DESIGN

Four beams were designed to have cross section and span that are scaled up (by linear scale factor 1.5) from beam specimens tested previously by Ma, Bertero, and Popov (Ma et al., 1976). Those previous tests used conventional A615 Grade 60 reinforcing bars having T/Y = 1.45. In the present test series, one of the four test beams was reinforced longitudinally with A706 Grade 60 reinforcement. The remaining three test beams have nominal Grade 100 reinforcement, including two beams with a distinct yield plateau and one beam with a round-house-shaped stress-strain relation (Figure 1.1.1). All longitudinal steel was laterally supported by hoops and crossties of the same grade steel used in each test specimen, except beam SBL100 that had transverse reinforcement of Grade 100 with T/Y = 1.26. Specimen names and their material properties are described in Table 3.1.1.

The beams were designed such that inelastic response would occur primarily through flexural yielding. Maximum shear force was expected to be approximately $3\sqrt{f_c'}bd$, where f_c' = concrete compressive strength in psi, b = beam width, and d = beam effective depth. The relatively low shear stress was intended to avoid extensive shear cracking, thereby minimizing effects of tension shift on beam inelastic rotations (Park and Paulay, 1975). The expected shear force was estimated to be about 25% of nominal shear strength provided by transverse reinforcement for all beams (Table 3.1.1). The design also satisfied transverse reinforcement requirements of ACI 318-14 for special moment frame beams, but with longitudinal spacing of transverse reinforcement reduced to $5d_b$ as recommended (NIST, 2014) for higher strength reinforcement with smaller T/Y ratio. Spacing of transverse reinforcement for all beams was controlled by the requirement to limit spacing to $d/4$, leading to spacing of 5 in. for all beams. Concrete was normal weight with design compressive strength of 5,000 psi. Table 3.1.1 summarizes the design and material properties and Figure 3.1.1 depicts general shape and dimensions of the test beams. Figure 3.1.2 through Figure 3.1.4 display the general design drawings of the test specimens in this research program and that by Ma et al. (1976), respectively.

Table 3.1.1: Summary of Design and Material Properties of Test Specimens

Author	**Ma, Bertero and Popov**	**To and Moehle**			
Specimen name	**BEAM R-6**	**SBH60**	**SBH100**	**SBL100**	**SBM100**
Scale factor	-	1.5	1.5	1.5	1.5
Width (in.)	9	13.5	13.5	13.5	13.5
Height (in.)	16	24	24	24	24
Length (in.)	62.5	93.75	93.75	93.75	93.75
Effective depth (in.)	14	22.13	22.13	22.13	22.13
Longitudinal reinforcement					
Top reinforcement	4 No. 6	4 No. 9	3 No. 8	3 No. 8	3 No. 8
Bottom reinforcement	4 No. 6	4 No. 9	3 No. 8	3 No. 8	3 No. 8
ASTM designation	A615	A706	NA	NA	A1035
Grade	60	60	100	100	100
$f_y\ (ksi)$	65.5	64.5	101.5	106	120.0
$f_t\ (ksi)$	94.2	95.5	127.6	123.9	165.0
$T/Y = f_t/f_y$	1.44	1.48	1.26	1.17	1.38
Transverse reinforcement	4 No. 2	4 No. 4	3 No. 4	3 No. 4	3 No. 4
Hoop & crosstie spacing (in.)	3.5	5	5	5	5
ASTM designation	A615	A706	NA	NA	A1035
Grade	60	60	100	100	100
$f_y\ (ksi)$	60.0	62.5	102.0	102.0	130.0
$f_t\ (ksi)$	83.0	93.2	127.4	127.4	169.0
$T/Y = f_t/f_y$	1.38	1.49	1.25	1.25	1.30
V_s (kips)	47	206	258	258	258
M_y (kip-in.)	1375	4748	4556	4753	5530
M_{pr} (kip-in.)	1666	5886	5795	5795	5795
$V_{u,measured}$ (kips)	29.5	74.6	61.0	60.8	81.9
v_u (psi)*	$3.5\sqrt{f_c'}$	$3.6\sqrt{f_c'}$	$3.0\sqrt{f_c'}$	$3.0\sqrt{f_c'}$	$4.0\sqrt{f_c'}$

*Calculation of this quantity uses the inch-lb measurement system, in which f_c' is in units of psi.

In Table 3.1.1, yield and tensile strengths of reinforcement were measured in laboratory tests as described in the materials section in Appendix A. Shear strength provided by transverse reinforcement (V_s) was calculated in accordance with procedures defined in ACI 318-14. Yield moment strength M_y was taken to be the strength at which longitudinal reinforcement reached measured yield strength. M_{pr} was calculated with steel strength equal $1.25f_y$, where f_y is specified (nominal) yield stress of longitudinal reinforcement, and concrete reaching crushing strain of 0.003. Measured shear forces $V_{u,measured}$ were taken from test data and shear stresses were determined as

$$v_u = \frac{V_{u,measured}}{bd} \quad \text{Eq. (1)}$$

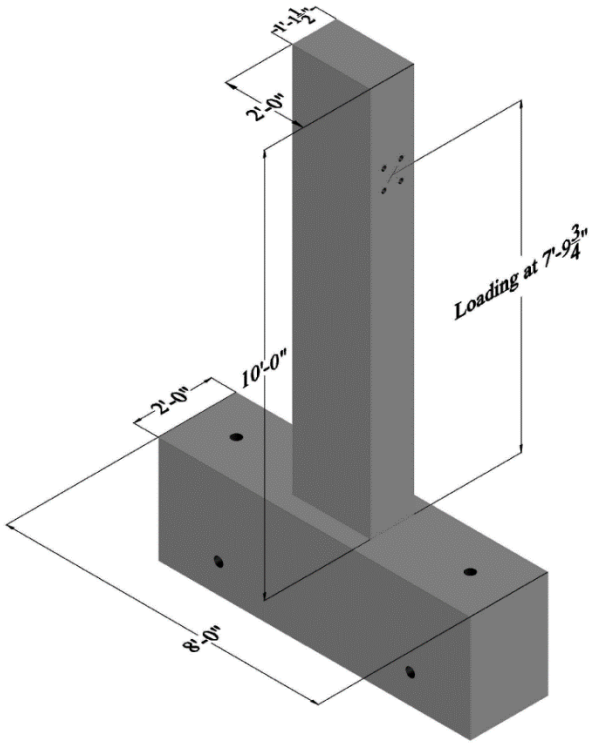

Figure 3.1.1: Geometry and Dimensions of Test Beam Designs

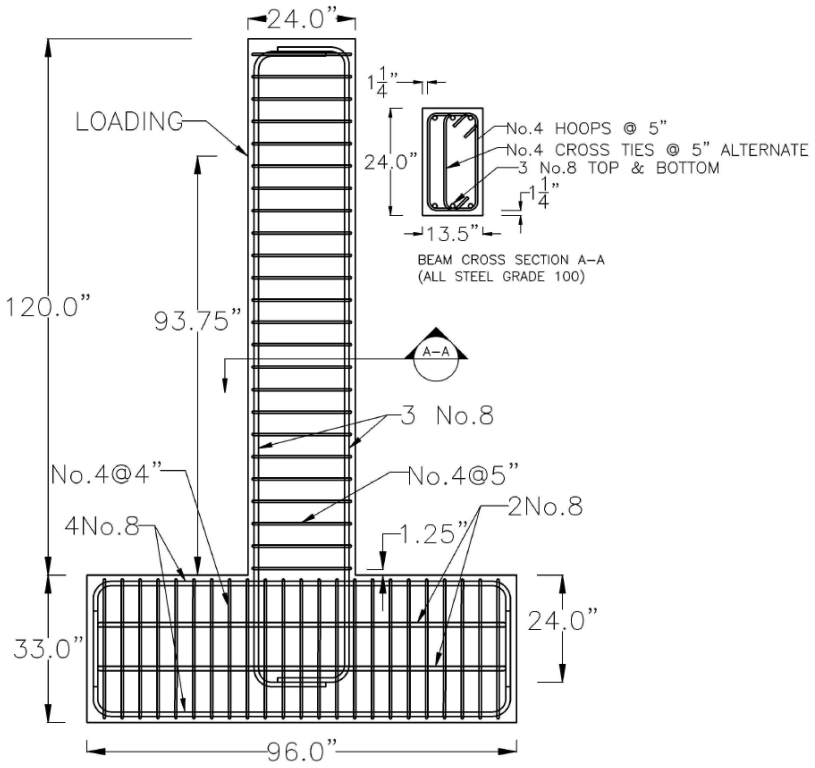

Figure 3.1.2: Reinforcement Details for Beams SBL100, SBH100, and SBM100

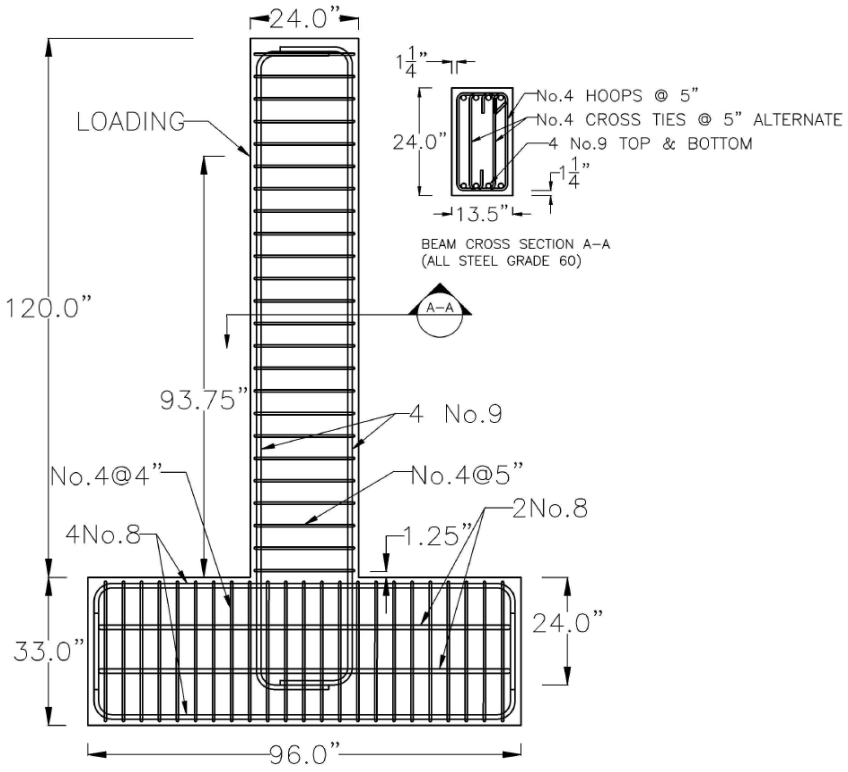

Figure 3.1.3: Reinforcement Details for Beam SBH60

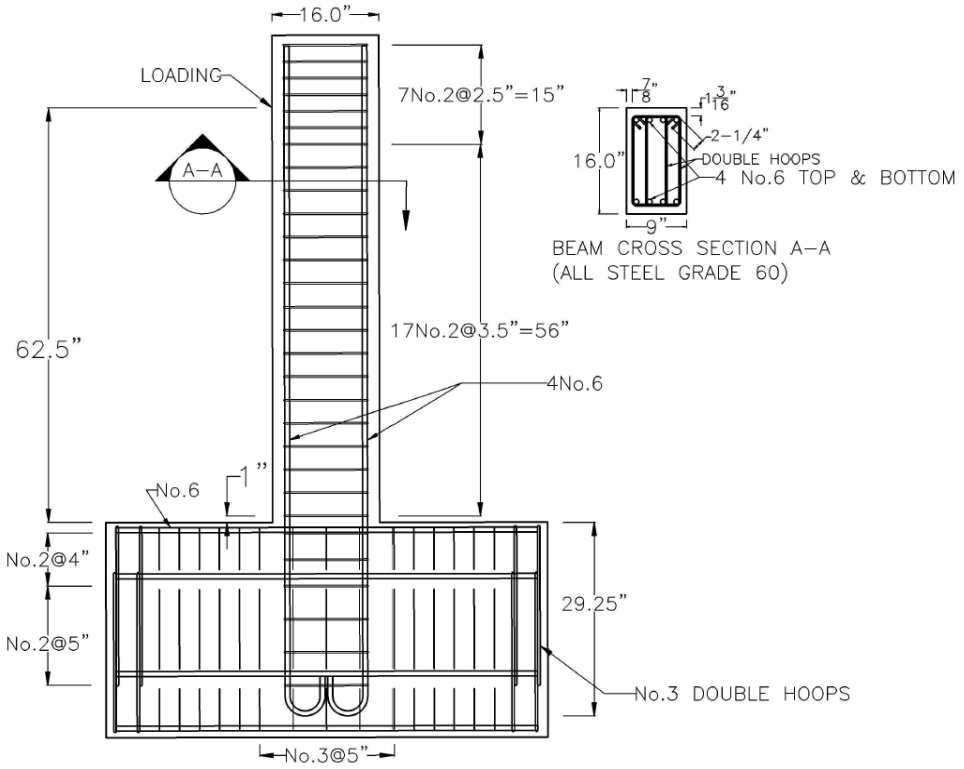

Figure 3.1.4: Reinforcement Details for Beam R-6 (Ma et al., 1976) (Drawing has been redone for clarity.)

3.2. TEST PROCEDURE

Cured specimens were oriented vertically and anchored down on the strong floor of the laboratory (Figure 3.2.1 and Figure 3.2.2). Since each hole on the strong floor has nominal capacity of 100 kips under tension, two large W-section steel beams were used to engage three holes on each side of test beam, resulting in total of 450 kips on each side (post-tensioning at the middle hole directly compressed together the concrete block and the floor, enabling a peak post-tensioning force of 250 kips). The anchorage force on both sides together created large enough friction on the interface between the test specimen and the laboratory floor to resist sliding caused by applied lateral load on top of the beam.

Two actuators were used to apply reversed cyclic lateral load on the specimen. Each of actuators formed an angle of about sixty (60) degrees with the horizontal steel beam on the reaction frame and was connected to the specimen through a loading fixture to restrain accidental out-of-plane bending of the specimen during test.

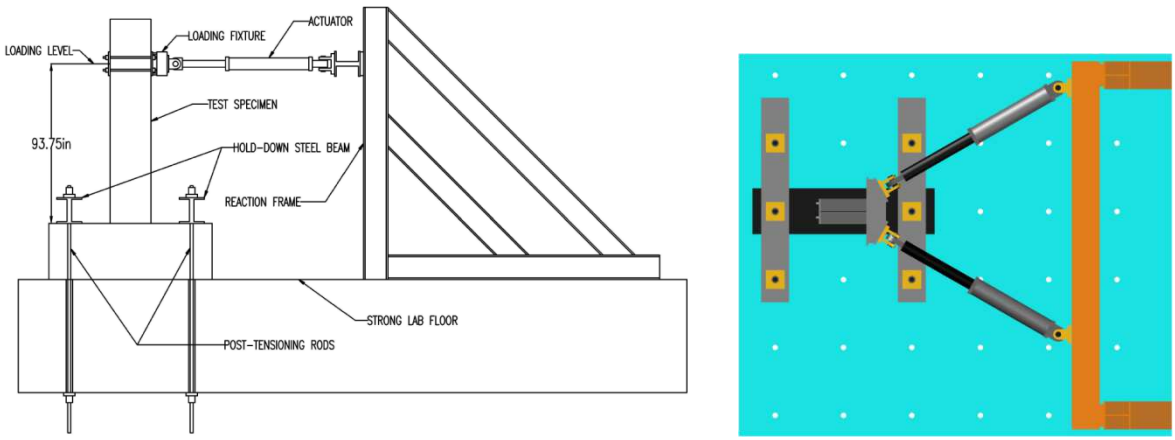

Figure 3.2.1: Schematic test setup – Left: Elevation View; Right: Plan View

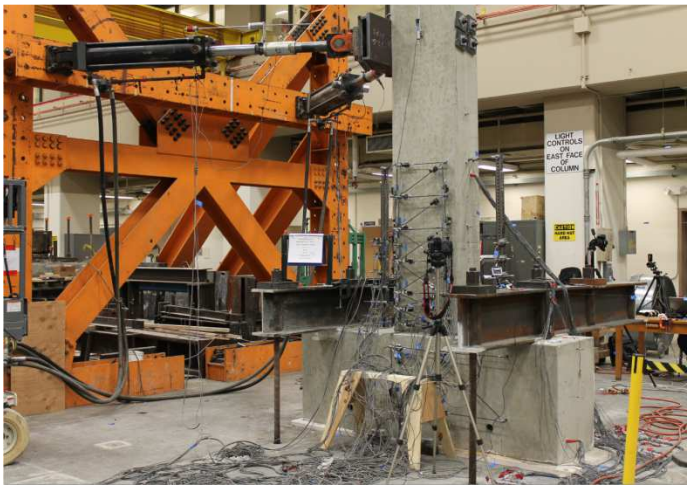

Figure 3.2.2: General Test Setup

Strain gauges were installed onto reinforcing bars as interior instrumentation. Typical locations of these strain gauges are shown in Figure 3.2.3. These strain gauges were installed to measure strain primarily along middle longitudinal bars on both sides of beam, hoops and crossties, and along the anchorage length of middle longitudinal bars.

Exterior instrumentation included displacement transducers set up to measure global deflection and local deformations along test specimen length (Figure 3.2.4). Global deflection was measured by wire potentiometers. Lateral force was measured by load cells attached on the two actuators that were used to apply force on the test specimens. The total force was the sum of the force measured by two load cells projected on the direction of loading. Local deformation was measured by LVDTs. From a truss system of LVDTs as shown in Figure 3.2.4, total deformation was computed from measurement of local deformation based on the principle of virtual force (Appendix A).

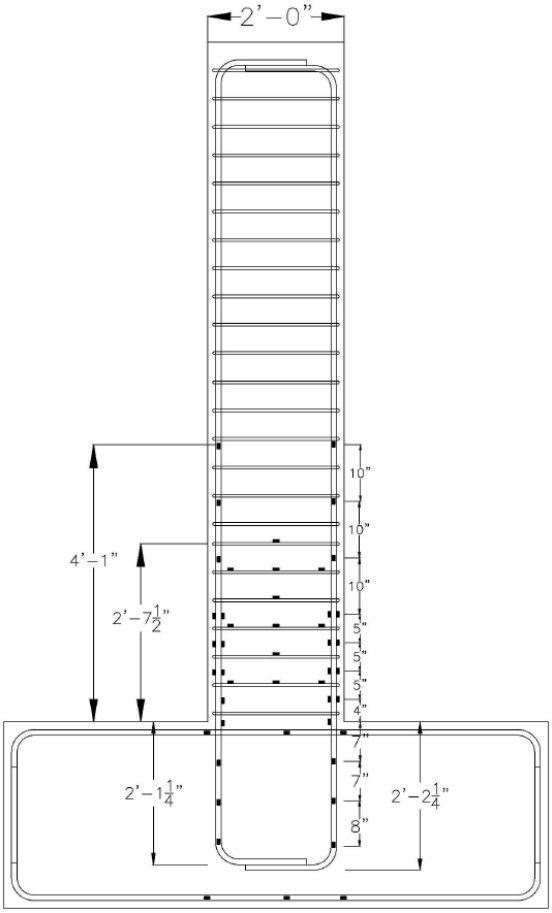

Figure 3.2.3: Interior Instrumentation – Strain Gauges

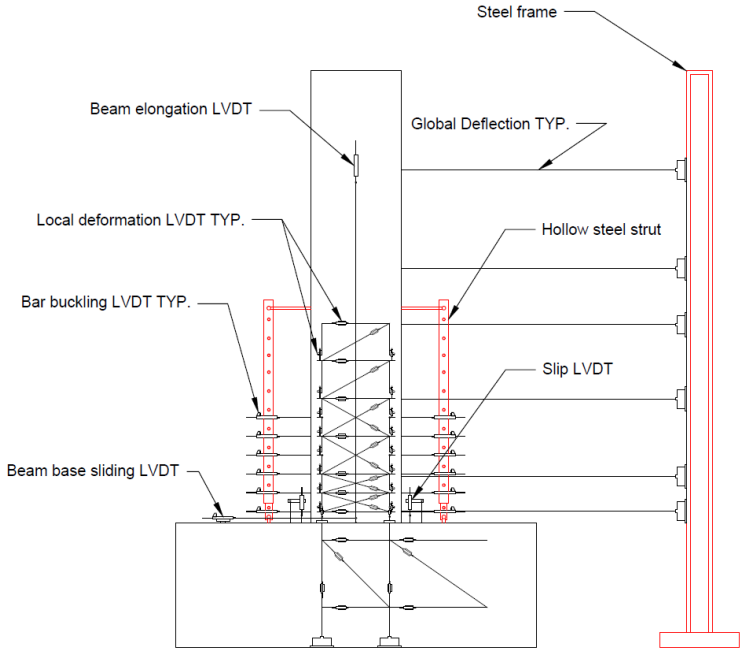

Figure 3.2.4: Schematic Drawing of Exterior Instrumentations

The loading history was developed based on recommendations of FEMA 461 (FEMA, 2007). It consists of two major loading types: load controlled and displacement controlled. Figure 3.2.5 displays a typical loading time series imposed on the test specimens. More details on loading protocol can be found in Appendix A. For each loading amplitude of either force- or displacement-controlled loading, the test beams were loaded from initial position to the peak in the east direction first, followed by another peak in the west direction, and one cycle was completed by loading the beam back to initial position. The test was stopped for marking cracks when the specimen was loaded to the peak on the east, and west direction of the first cycle and the end of loading cycles (either second or third) when the pre-determined applied load or displacement became zero.

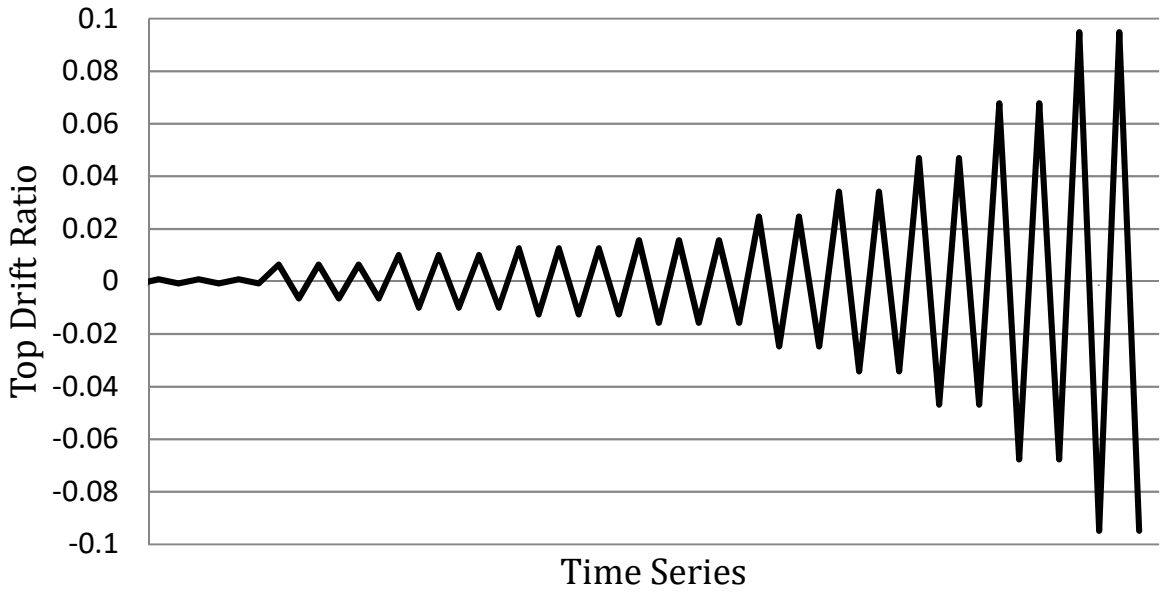

Figure 3.2.5: Loading History

CHAPTER 4: LABORATORY TEST RESULTS

4.1. GENERAL OBSERVATIONS

Main observations on both beams tests are summarized below:

1) Flexural cracks in all beams were first observed at loads of approximately 60 percent of yield force.
2) Flexural crack patterns were similar in either direction of loading.
3) From the beginning of test to the end of loading stage of 1.96Δy, curvature was visibly apparent along the length of all the beams.
4) After several loading cycles of large displacement and starting from loading stage of 2.74Δy, a couple of major cracks opened and caused relatively large shear distortion in beams SBH100 and SBL100. Also, deformations in beam SBL100 appeared to be dominated by concentrated rotation at the base, giving the appearance that the rest of the beam remained straight.
5) As test beams were loaded to pre-computed force corresponding to nominal yield stress of reinforcement, strain of longitudinal reinforcement was measured by strain gauges to be approximately 0.002 and 0.0034 for Grade 60 and Grade 100 reinforcement with a distinct yield plateau (beams SBL100 and SBH100), respectively, indicating that the beams yielded.
6) Beam SBH60 with conventional Grade 60 A706 reinforcement yielded at drift ratio of 0.008, which is lower than the yielding drift ratio of 0.013 for the beams with Grade 100 reinforcement with a distinct yield plateau (beams SBL100 and SBH100). The yield point was indistinct for beam SBM100, apparently because the longitudinal reinforcement did not have a distinct yield plateau.
7) As loading progressed beyond yield point, additional cracks developed at an angle inclined relative to the longitudinal axis. The horizontal crack at the interface between a beam and its anchorage block widened as testing progressed, and some horizontal slip was apparent between the two crack surfaces. Figure 4.1.1 to Figure 4.1.4 illustrate the deflected shape and crack pattern of the test specimens during testing.
8) Vertical crack of concrete associating with onset of concrete crushing appeared during the loading stage of 0.035 drift ratio for both specimens SBH60 and SBH100. Following the occurrence of vertical crack, concrete spalling was also first observed at the corner close to the base of these two beams.

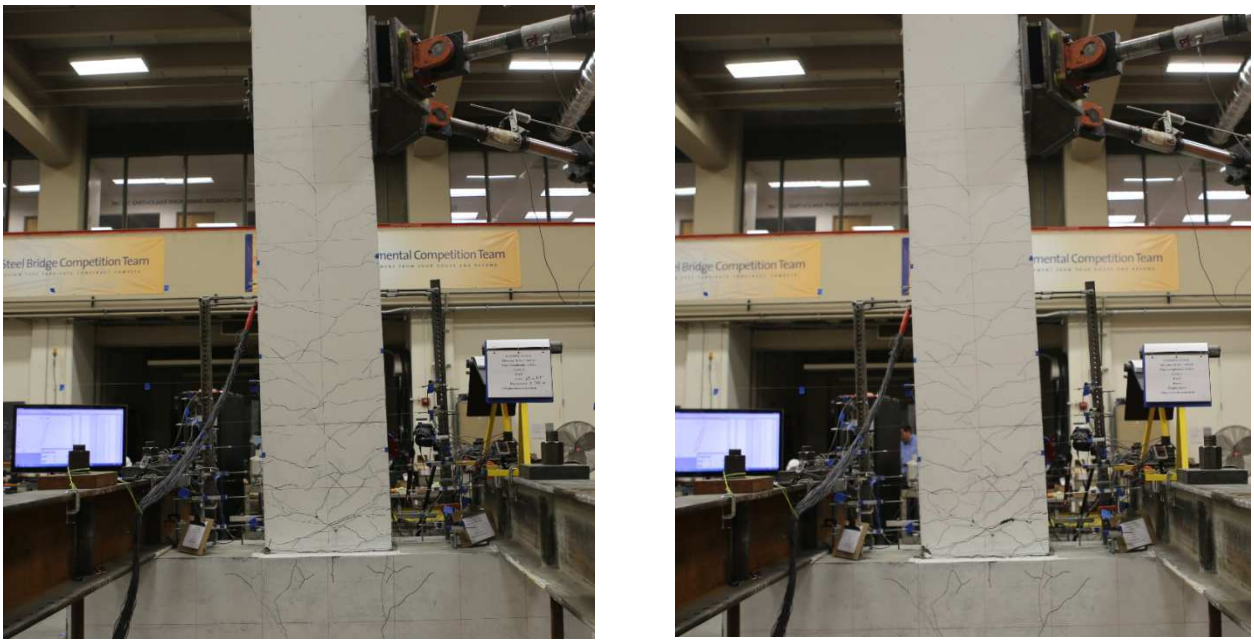

Figure 4.1.1: Deflected Shape of SBH60 at Drift Ratio 2.45% (Left) and 3.45% (Right)

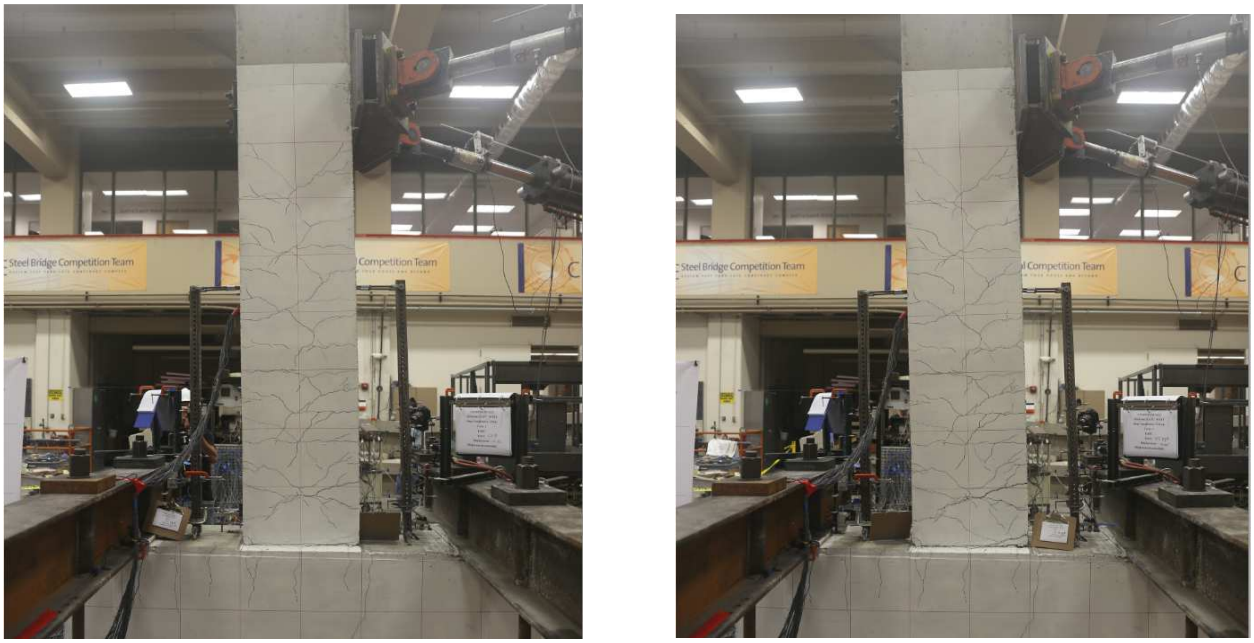

Figure 4.1.2: Deflected shape of SBH100 at Drift Ratio 2.45% (Left) and 3.45% (Right).

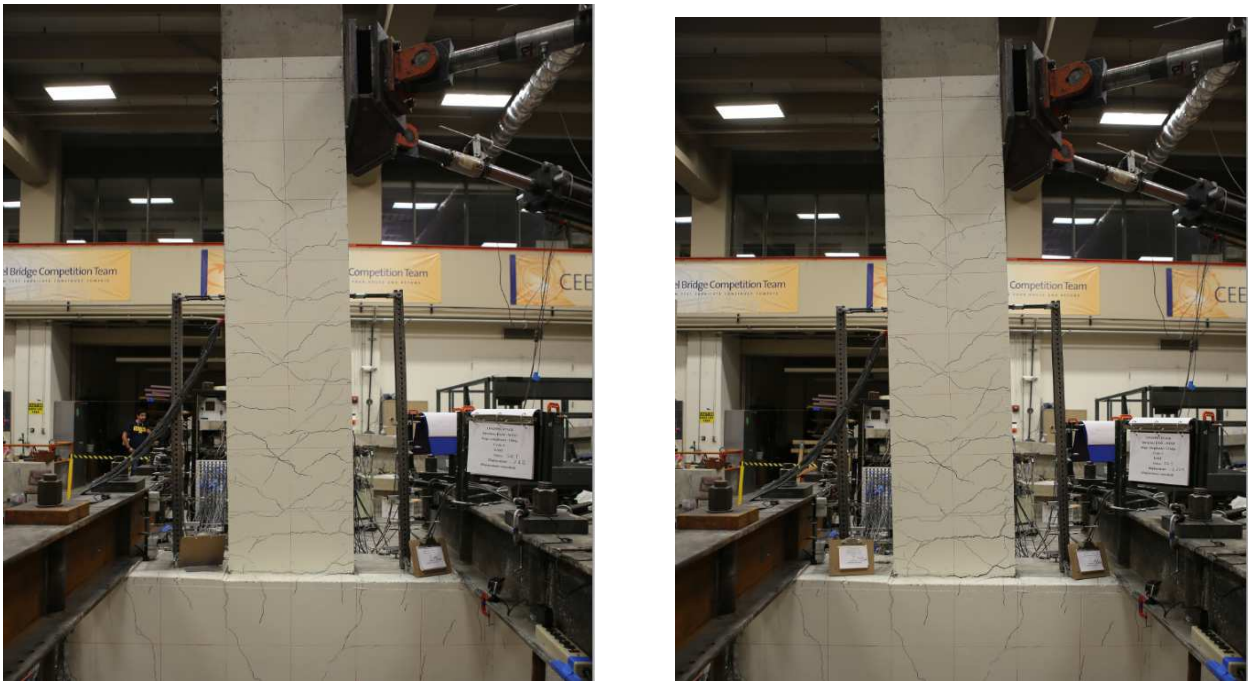

Figure 4.1.3: Deflected shape of SBL100 at Drift Ratio 2.45% (Left) and 3.45% (Right).

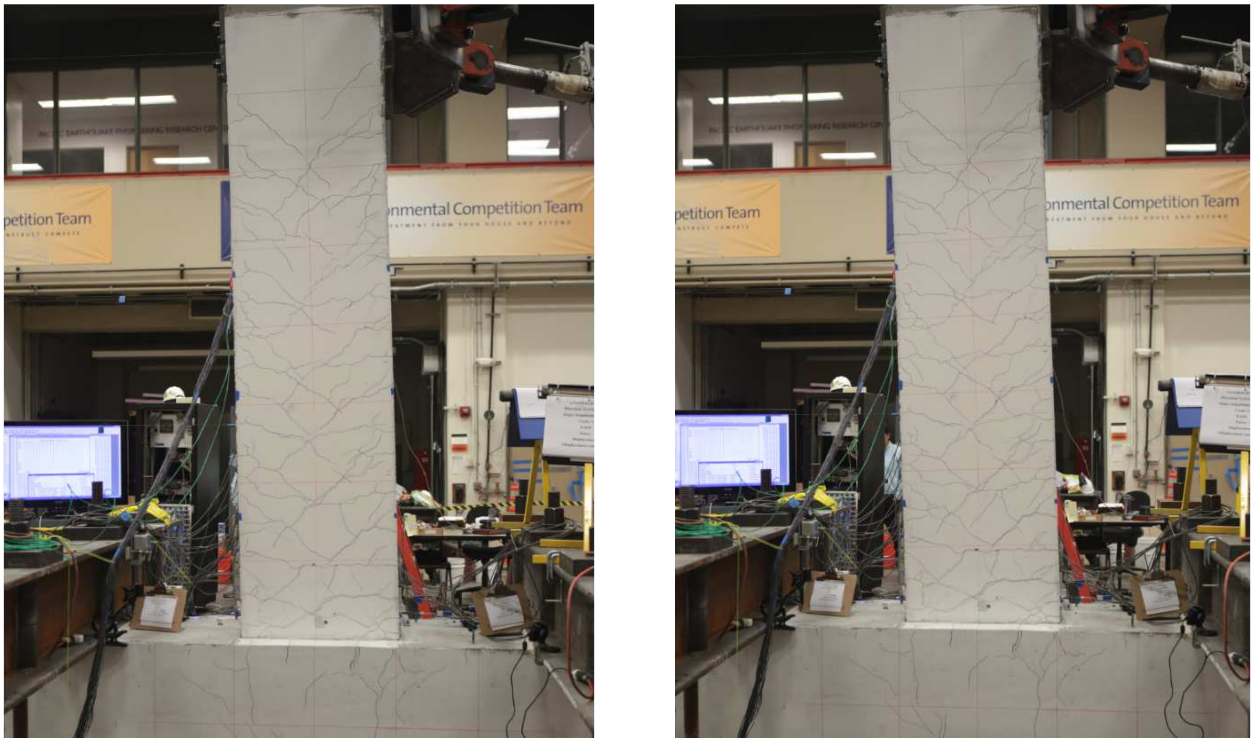

Figure 4.1.4: Deflected shape of SBM100 at Drift Ratio 2.45% (Left) and 3.45% (Right).

4.2. CRACK DEVELOPMENT

First cracks were observed to occur in the beam with Grade 60 reinforcement at drift ratio 0.0035 and in the beams with Grade 100 reinforcement at drift ratio 0.006. These cracks were primarily horizontal, consistent with expectations for flexure-dominated beams. As loading progressed, several inclined cracks appeared, consistent with expectations for combined flexure and shear. Figure 4.2.1 through Figure 4.2.4 depict development of cracks. Table 4.2.1 and Table 4.2.2 show crack widths measured on the east and west sides of test beams, respectively, while Table 4.2.3 displays crack widths measured when the beams were unloaded at the end of a cycle.

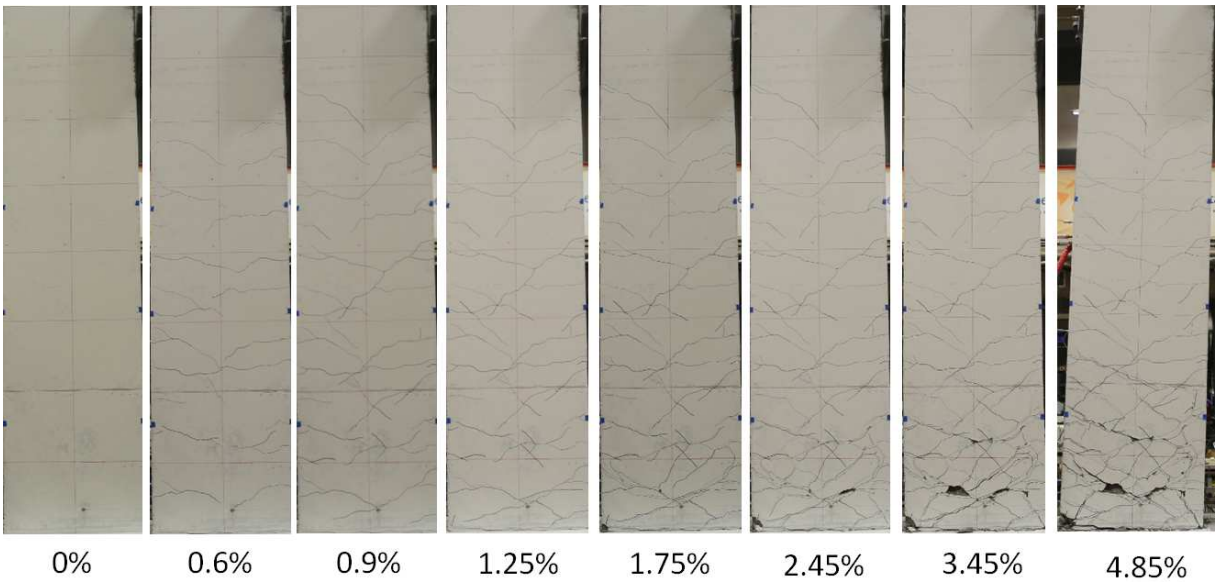

Figure 4.2.1: Crack Development on SBH60

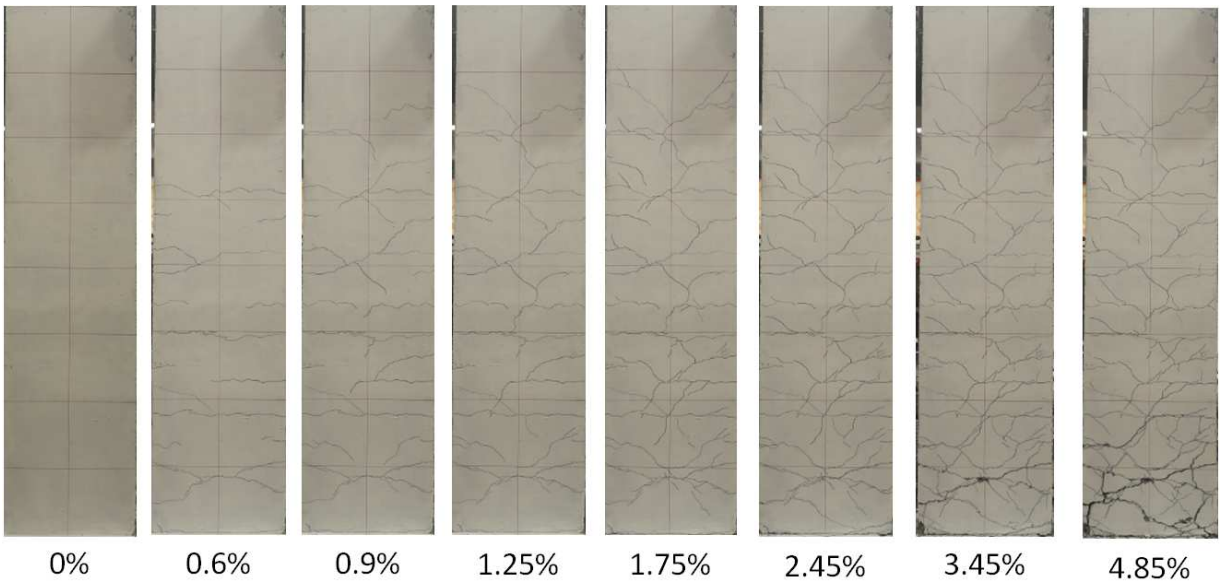

Figure 4.2.2: Crack Development on SBH100

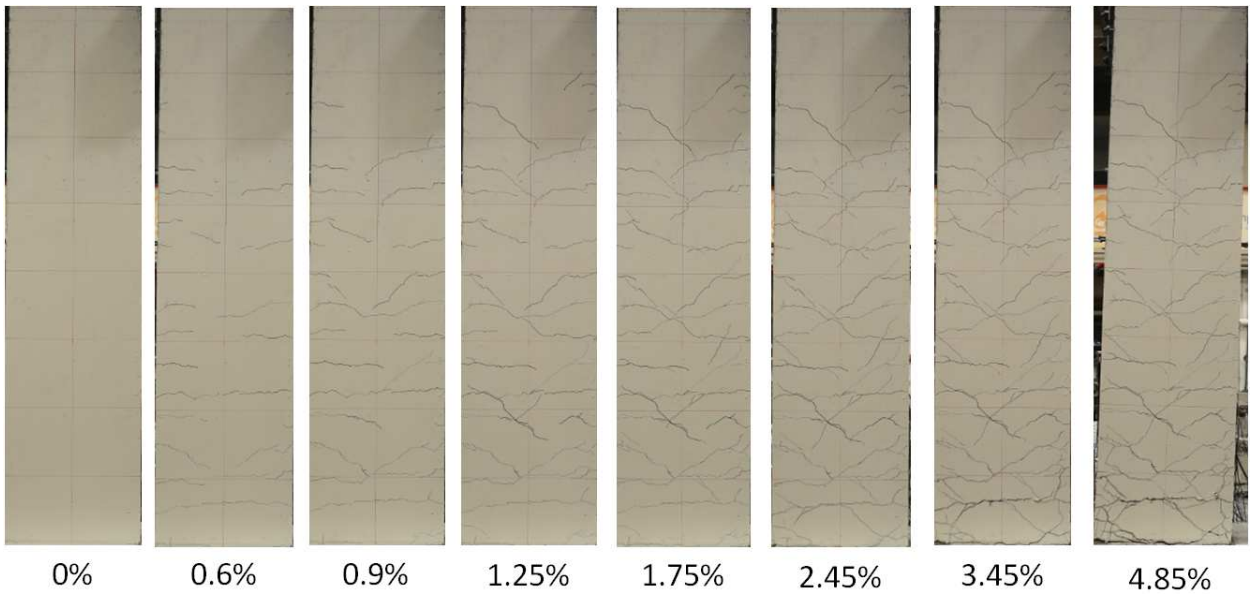

Figure 4.2.3: Crack Development on SBL100

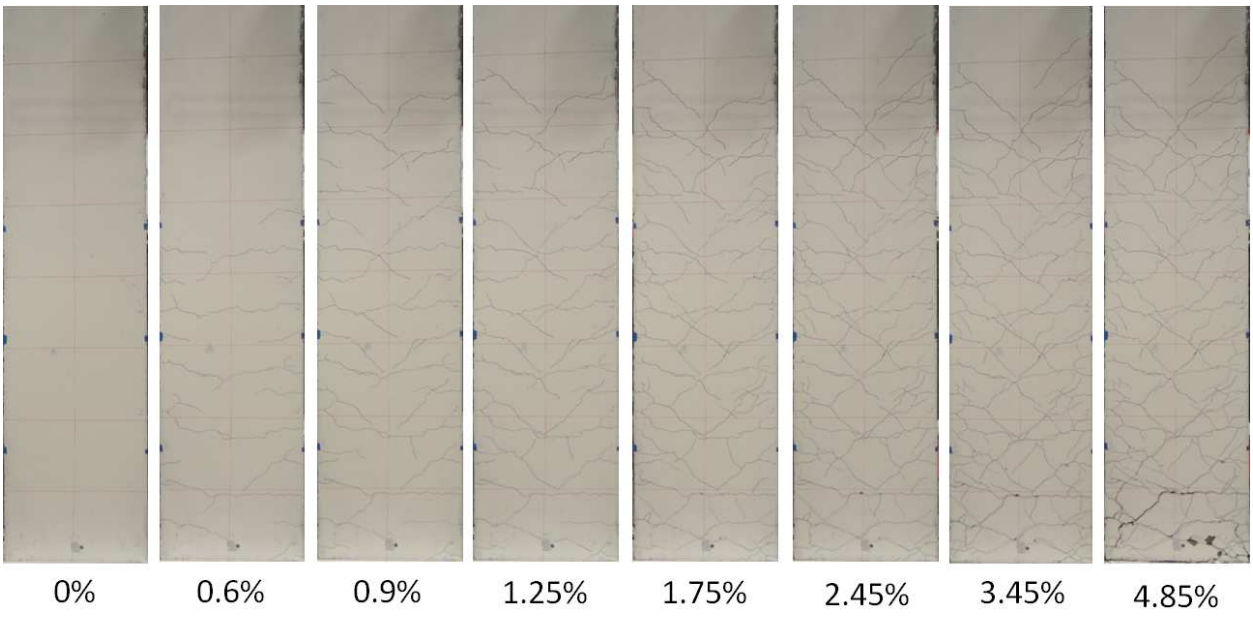

Figure 4.2.4: Crack Development on SBM100

Table 4.2.1: Measured Crack Widths on East Side (Loading to West Direction)

Drift Ratio	Location (percentage of beam length)*	**Crack Width (inch)**			
		SBH60	**SBH100**	**SBL100**	**SBM100**
0.6%	100	0.016	0.005	0.020	0.000
	80	0.008	0.010	0.010	0.008
	60	0.008	0.005	0.005	0.005
	40	0.008	0.000	0.010	0.005
0.9%	100	0.035	0.047	0.030	0.000
	80	0.012	0.015	0.015	0.012
	60	0.008	0.010	0.010	0.012
	40	0.008	0.010	0.010	0.008
1.25%	100	0.040	0.110	0.050	0.030
	80	0.012	0.025	0.025	0.020
	60	0.008	0.010	0.010	0.020
	40	0.008	0.015	0.015	0.012
1.75%	100	0.070	0.156	0.075	0.060
	80	0.012	0.030	0.030	0.020
	60	0.012	0.015	0.015	0.016
	40	0.012	0.015	0.020	0.012
2.45%	100	0.125	0.156	0.110	0.094
	80	0.035	0.075	0.040	0.040
	60	0.016	0.015	0.015	0.030
	40	0.012	0.015	0.015	0.016
3.45%	100	0.219	0.175	0.180	0.125
	80	0.070	0.140	0.050	0.060
	60	0.012	0.015	0.020	0.020
	40	0.012	0.020	0.015	0.016
4.85%	100	0.313	0.220	0.250	0.219
	80	0.125	0.188	0.075	0.094
	60	0.012	0.015	0.020	0.040
	40	0.012	0.020	0.020	0.016

* This location of the crack with measured width is at a distance as a percentage of beam length (beam length is 93.75 inches) away from application of lateral load.

Table 4.2.2: Measured Crack Widths on West Side (Loading to East Direction)

Drift Ratio	Location (percentage of beam length)	**Crack Width (inch)**			
		SBH60	**SBH100**	**SBL100**	**SBM100**
0.6%	100	0.012	0.063	0.025	0.000
	80	0.012	0.010	0.010	0.012
	60	0.008	0.010	0.005	0.012
	40	0.005	0.000	0.005	0.005
0.9%	100	0.025	0.094	0.050	0.000
	80	0.016	0.015	0.015	0.016
	60	0.008	0.015	0.00	0.016
	40	0.005	0.005	0.010	0.012
1.25%	100	0.050	0.125	0.050	0.040
	80	0.016	0.010	0.025	0.025
	60	0.008	0.020	0.010	0.020
	40	0.005	0.005	0.010	0.012
1.75%	100	0.050	0.188	0.075	0.094
	80	0.012	0.030	0.025	0.040
	60	0.008	0.020	0.010	0.020
	40	0.008	0.005	0.015	0.012
2.45%	100	0.125	0.156	0.180	0.094
	80	0.060	0.120	0.020	0.030
	60	0.008	0.025	0.010	0.016
	40	0.005	0.005	0.015	0.012
3.45%	100	0.188	0.250	0.250	0.156
	80	0.070	0.188	0.050	0.080
	60	0.012	0.030	0.005	0.020
	40	0.008	0.005	0.015	0.012
4.85%	100	NR*	0.313	0.250	0.344
	80	NR*	0.313	0.020	0.094
	60	NR*	0.025	0.000	0.040
	40	NR*	0.005	0.000	0.020

* Width was not recorded for these cracks at this loading stage as condition of test beam was deemed too dangerous to measure crack width

Table 4.2.3: Measured Cracked Widths at the End of Loading Cycles

Drift Ratio	Location (percentage of beam length)	Crack Width (inch)							
		SBH60		SBH100		SBL100		SBM100	
		West*	East*	West*	East*	West*	East*	West*	East*
0.6%	100	0.000	0.000	0.000	0.000	0.000	0.000	0.000	0.000
	80	0.000	0.000	0.000	0.000	0.000	0.000	0.000	0.000
	60	0.000	0.000	0.000	0.000	0.000	0.000	0.000	0.000
	40	0.000	0.000	0.000	0.000	0.000	0.000	0.000	0.000
0.9%	100	0.003	0.008	0.000	0.000	0.000	0.000	0.000	0.000
	80	0.000	0.003	0.000	0.000	0.000	0.000	0.030	0.000
	60	0.000	0.003	0.000	0.000	0.000	0.000	0.000	0.000
	40	0.000	0.003	0.000	0.000	0.000	0.000	0.000	0.000
1.25%	100	0.003	0.030	0.000	0.000	0.000	0.000	0.008	0.008
	80	0.000	0.003	0.000	0.000	0.000	0.000	0.005	0.003
	60	0.000	0.003	0.000	0.000	0.000	0.000	0.003	0.000
	40	0.000	0.003	0.000	0.000	0.000	0.000	0.000	0.000
1.75%	100	0.040	0.050	0.188	0.031	0.010	0.010	0.016	0.020
	80	0.005	0.008	0.000	0.000	0.000	0.000	0.008	0.008
	60	0.000	0.000	0.000	0.000	0.000	0.000	0.000	0.000
	40	0.000	0.000	0.000	0.000	0.000	0.000	0.000	0.000
2.45%	100	0.070	0.070	0.063	0.063	0.075	0.060	0.025	0.020
	80	0.040	0.016	0.030	0.000	0.000	0.010	0.016	0.016
	60	0.000	0.005	0.000	0.000	0.000	0.000	0.003	0.003
	40	0.000	0.005	0.000	0.000	0.000	0.000	0.000	0.000
3.45%	100	0.094	0.188	0.220	0.250	0.110	0.110	0.060	0.050
	80	0.060	0.040	0.035	0.015	0.020	0.020	0.025	0.025
	60	0.000	0.005	0.000	0.000	0.000	0.005	0.005	0.005
	40	0.000	0.005	0.000	0.000	0.000	0.005	0.000	0.000
4.85%	100	NR**	NR**	0.156	0.094	NR**	NR**	0.125	0.125
	80	NR**	NR**	0.094	0.010	NR**	NR**	0.080	0.070
	60	NR**	NR**	0.000	0.010	NR**	NR**	0.005	0.008
	40	NR**	NR**	0.000	0.000	NR**	NR**	0.000	0.000

* West and East indicate the west and east sides of the test specimens, respectively.

** Width was not recorded for these cracks at this loading stage as condition of test beam was deemed too dangerous to measure crack width.

4.3. FAILURE MODES

Specimen SBH60 with conventional Grade 60 A706 steel failed by twisting of the beam about its longitudinal axis after it achieved drift ratio of 0.0485. This phenomenon was associated with overall instability of the flexural compression zone (Figure 4.3.1). Beam SBH100 with Grade 100 T/Y = 1.26 also failed by beam twisting after buckling of all three longitudinal bars on one side over several hoop spacings was observed in the previous loading cycle (Figure 4.3.2).

Both beams SBL100 and SBM100 failed by fracture of longitudinal bars (Figure 4.3.3 and Figure 4.3.4). On the loading cycle to 0.0485 drift ratio, specimen SBL100 had the first bar fracture while SBM100 was observed to have bar necking. During the last loading stage to target drift ratio 0.068, the remaining two bars on the same side of first fracture in beam SBL100 ruptured at drift ratios 0.025 and 0.04, and all three longitudinal bars in SBM100 ruptured simultaneously at drift ratio 0.0555. Table 4.3.1 summarizes the failure mechanism of all test specimens. Values in Table 4.3.1 indicate the drift ratio that test specimens had achieved before failure was observed.

Table 4.3.1: Failure Mechanisms of Test Beams

	Specimen			
Failure Mode	**SBH60**	**SBH100**	**SBL100**	**SBM100**
Bar Buckling		0.0485		
Global Instability	0.0485	0.0680		
Bar Fracture			0.0485	0.0555

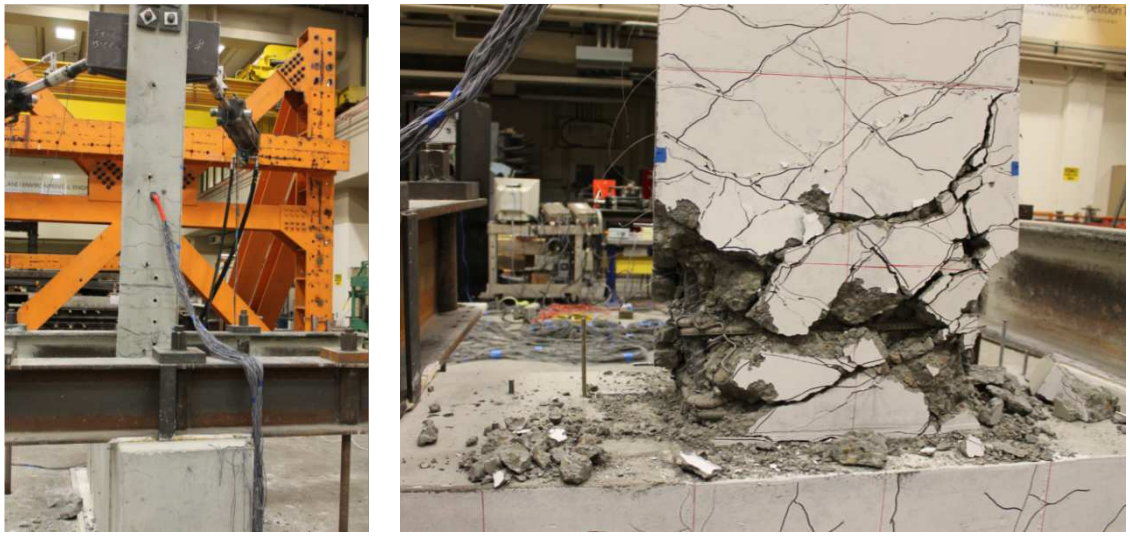

Figure 4.3.1: Failure Mechanism of SBH60 by Twisting of Beam (Global Instability)

Figure 4.3.2: Failure Mechanism of SBH100 by Buckling of Longitudinal Bars Over Several Hoop Spacings

Figure 4.3.3: Failure Mechanism of SBL100 by Fracture of Longitudinal Bars

Figure 4.3.4: Failure Mechanism of SBM100 by Fracture of Longitudinal Bars

4.4. OVERALL FORCE-DEFORMATION RELATONS

Overall force-deformation relations of all test specimens are presented in Figure 4.4.1 through Figure 4.4.4. Figure 4.4.5 shows the envelopes of these force-deformation relations and Table 4.4.1 summarizes the main laboratory test results. It is apparent that all beams have equivalent yield strength as intended (the scaled values of the quantity $A_s f_y$ were the same for all beams). The three beams with Grade 100 reinforcement are less stiff than the one with conventional Grade 60 as expected due to lower reinforcement ratio. Specimens SBH60 and SBM100 had higher peak strength than the other two Grade 100 beams because Grade 60 A706 and Grade 100 A1035 reinforcement have more strain-hardening. All test beams achieved at least 0.045 drift ratio.

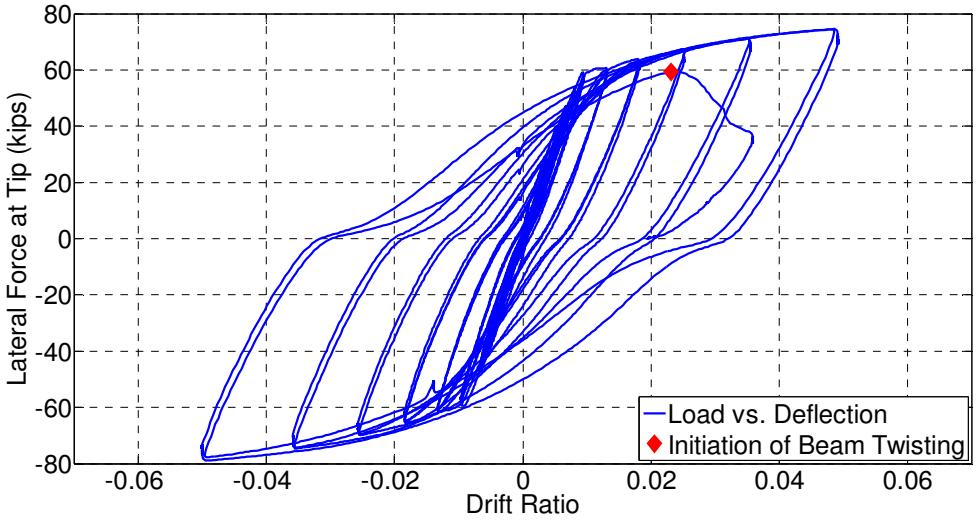

Figure 4.4.1: Lateral Force vs. Deformation – SBH60

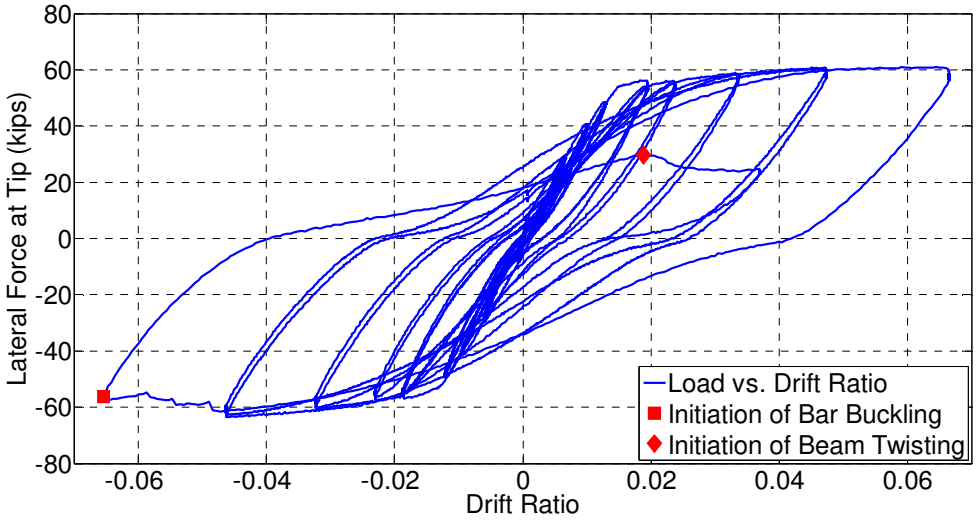

Figure 4.4.2: Lateral Force vs. Deformation – SBH100

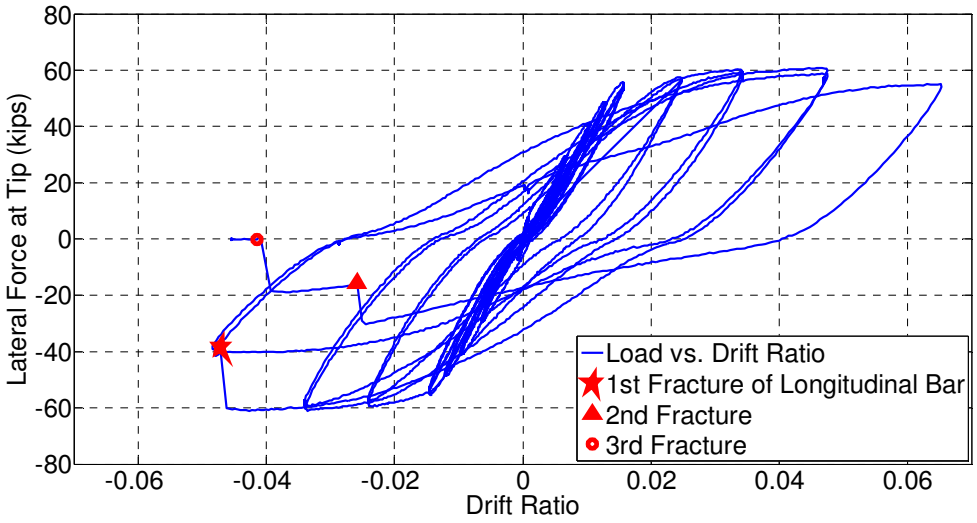

Figure 4.4.3: Lateral Force vs. Deformation – SBL100

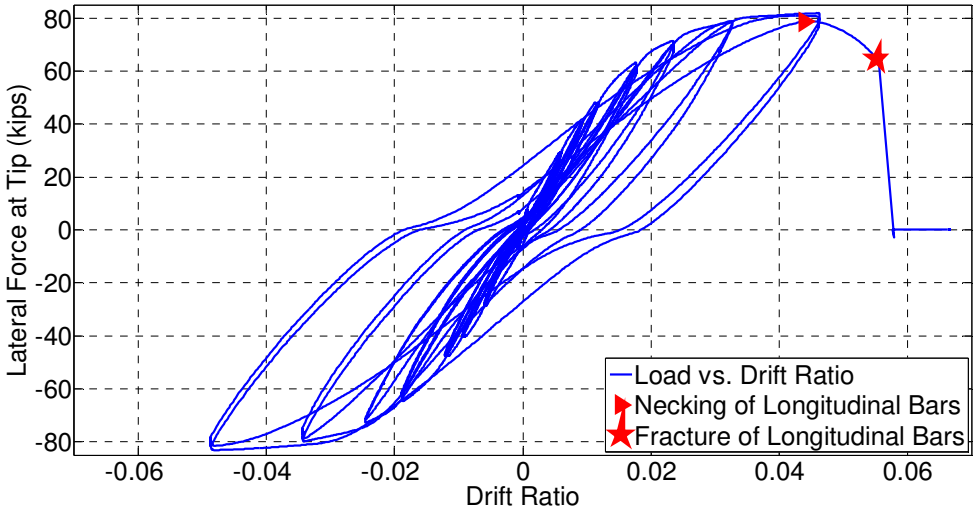

Figure 4.4.4: Lateral Force vs. Deformation – SBM100

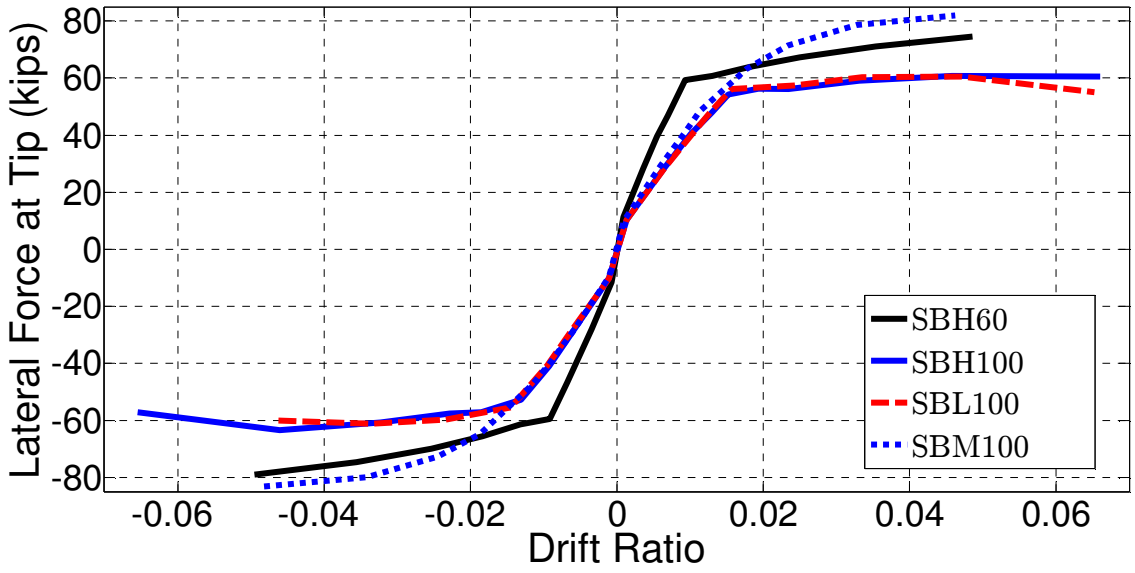

Figure 4.4.5: Force-Deformation Envelopes

Table 4.4.1: Main Laboratory Test Results

	SBH60	**SBH100**	**SBL100**	**SBM100**
$V_{cr}\ (kips)$	11.5	10.0	10.0	10.0
$V_y\ (kips)$	52.0	48.0	49.0	60.0
$V_{max}\ (kips)$	74.6	61.0	60.8	81.9
$v_u\ (psi)$	$3.6\sqrt{f_c'}$	$3.0\sqrt{f_c'}$	$3.0\sqrt{f_c'}$	$4.0\sqrt{f_c'}$
$DR_{cr}\ (radian)$	0.0008	0.0013	0.0012	0.0010
$DR_y\ (radian)$	0.008	0.013	0.013	0.018
$DR_{max}\ (radian)$	0.0485	0.065	0.048	0.046
$M_{cr}\ (kips-in)$	1078	938	938	938
$M_y\ (kips-in)$	4875	4500	4594	5625
$M_{max}\ (kips-in)$	6994	5719	5700	7678

In Table 4.4.1, V_{cr} was the shear force measured at the instance the lateral stiffness of test beams was observed to decrease for the first time, which was associated with cracking of concrete. V_y was the shear force measured at the moment the strain of the longitudinal reinforcement of the test specimens first reached measured yield strain, which was defined by measured yield stress divided by Young's modulus of elasticity ($E = 29{,}000\ ksi$). V_{max} was the ultimate measured shear force. Corresponding drift ratios (DR) and moments (M) are also reported in this table.

4.5. DEFORMATION COMPONENTS

Total deformation of all test specimens was separated into three major components including flexure, shear, and slip by applying the principle of virtual forces to the grid of displacement transducers affixed to the side face of each beam (Appendix A). For beam SBL100, only one instrument was installed to measure slip of longitudinal reinforcement out of the concrete block on one side of specimen. Therefore, slip and flexure deformations could not be separated and were plotted together in Figure 4.5.7.

Figure 4.5.1 through Figure 4.5.11 present hysteretic response of each of major deformation components of the test beams. These plots do not show all measured data as instruments started to provide peculiar data in the last large loading cycles toward the end of the tests due to concrete cracking, bulging, and spalling.

Percentage contribution of these three major components of deformation are plotted in Figure 4.5.12 through Figure 4.5.15 for all four beams. It is worth noting that the contribution of flexural deformations was slightly greater for beam SBH60 with Grade 60 reinforcement than for the other beams with Grade 100 reinforcement. This may be partly attributable to the higher T/Y ratio for the Grade 60 reinforcement, which tends to spread inelastic flexural deformations along a greater length of the beam. It may also be partly due to the greater contribution of slip in the beams with Grade 100 reinforcement. In all the beams, shear deformation provided as much as 5-8% of the total deformation.

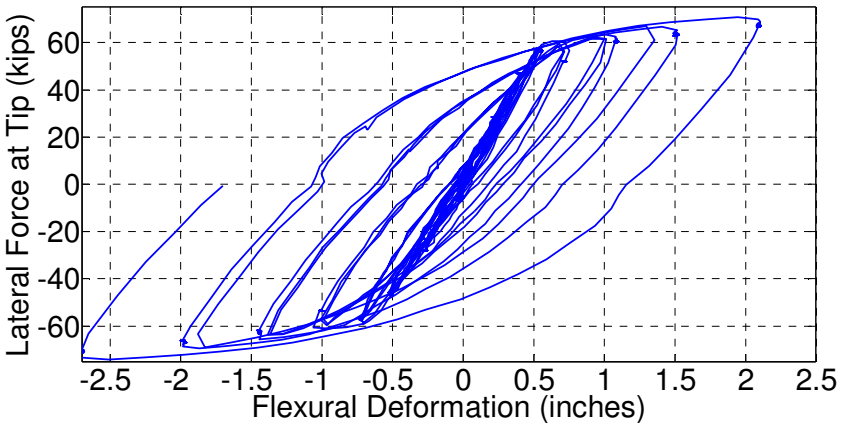

Figure 4.5.1: Lateral Force vs. Flexural Deformation Hysteretic Response of Beam SBH60

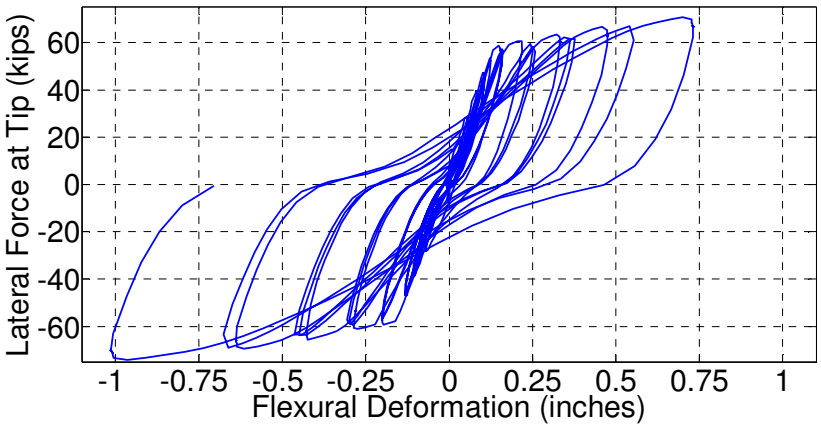

Figure 4.5.2: Lateral Force vs. Slip Deformation Hysteretic Response of Beam SBH60

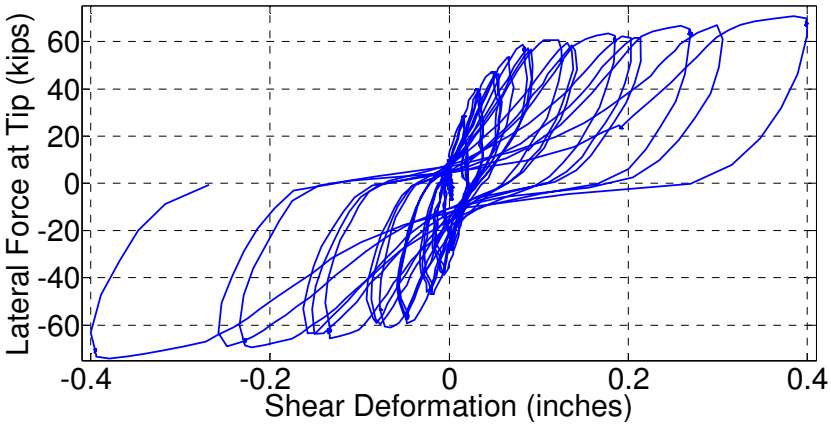

Figure 4.5.3: Lateral Force vs. Shear Deformation Hysteretic Response of Beam SBH60

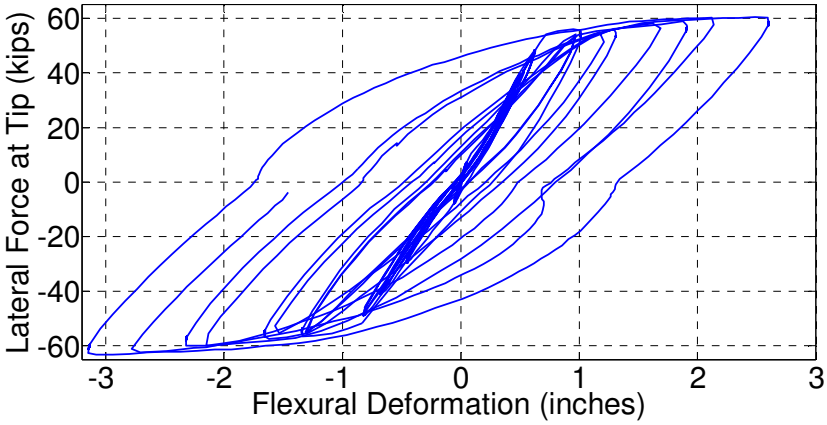

Figure 4.5.4: Lateral Force vs. Flexural Deformation Hysteretic Response of Beam SBH100

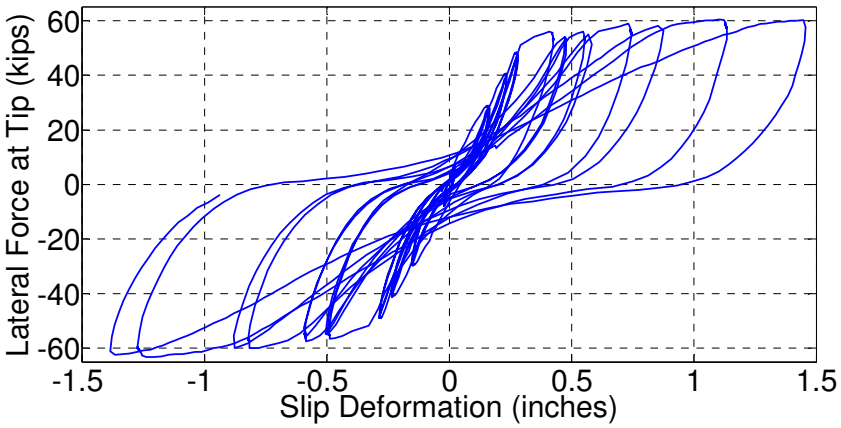

Figure 4.5.5: Lateral Force vs. Slip Deformation Hysteretic Response of Beam SBH100

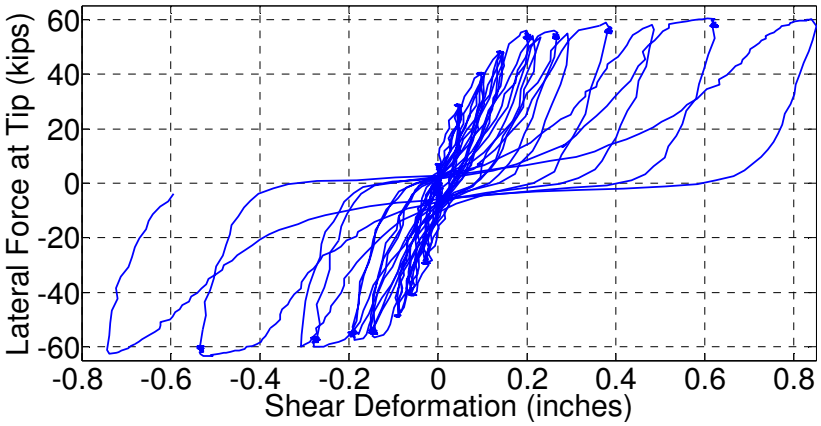

Figure 4.5.6: Lateral Force vs. Shear Deformation Hysteretic Response of Beam SBH100

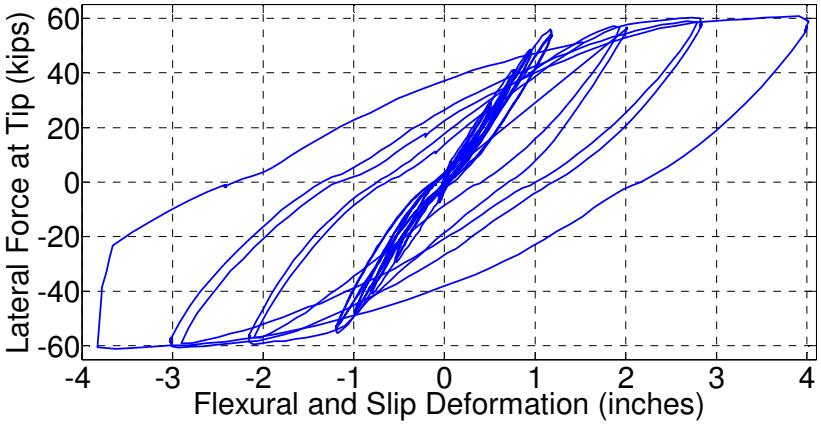

Figure 4.5.7: Lateral Force vs. Flexural and Slip Deformation Hysteretic Response of Beam SBL100

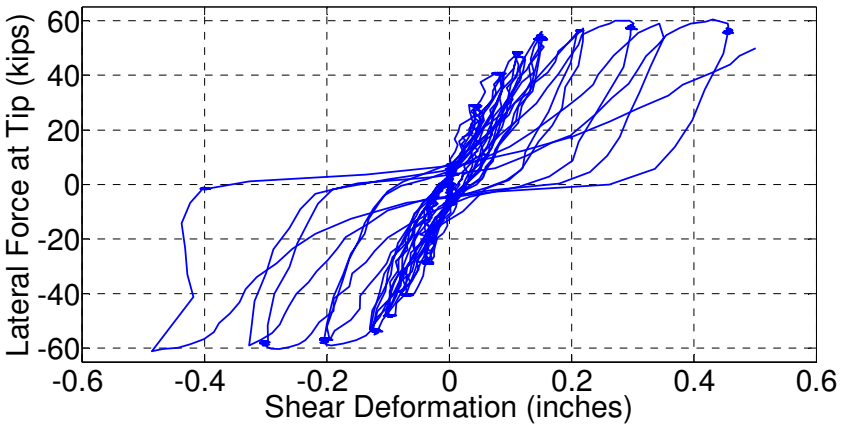

Figure 4.5.8: Lateral Force vs. Shear Deformation Hysteretic Response of Beam SBL100

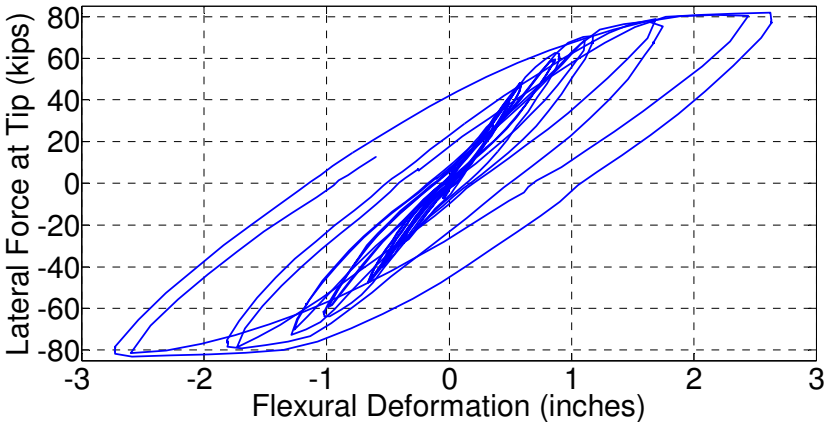

Figure 4.5.9: Lateral Force vs. Flexural Deformation Hysteretic Response of Beam SBM100

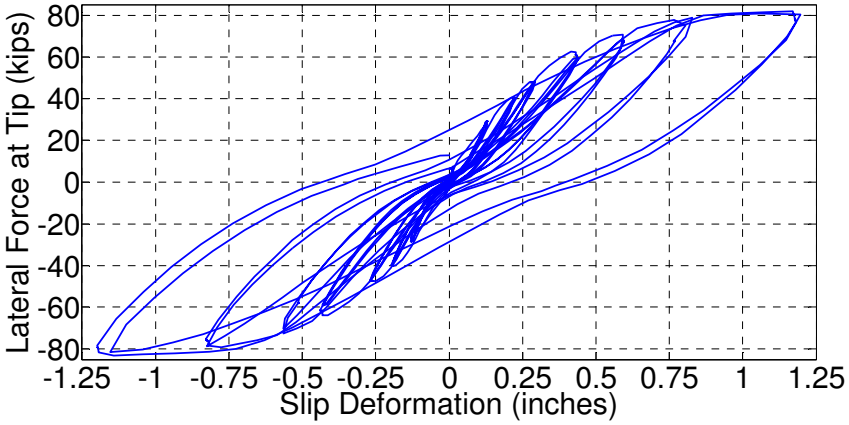

Figure 4.5.10: Lateral Force vs. Slip Deformation Hysteretic Response of Beam SBM100

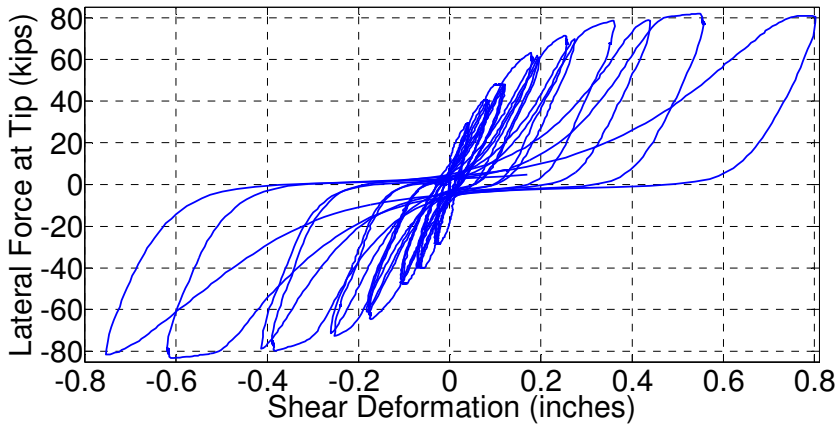

Figure 4.5.11: Lateral Force vs. Shear Deformation Hysteretic Response of Beam SBM100

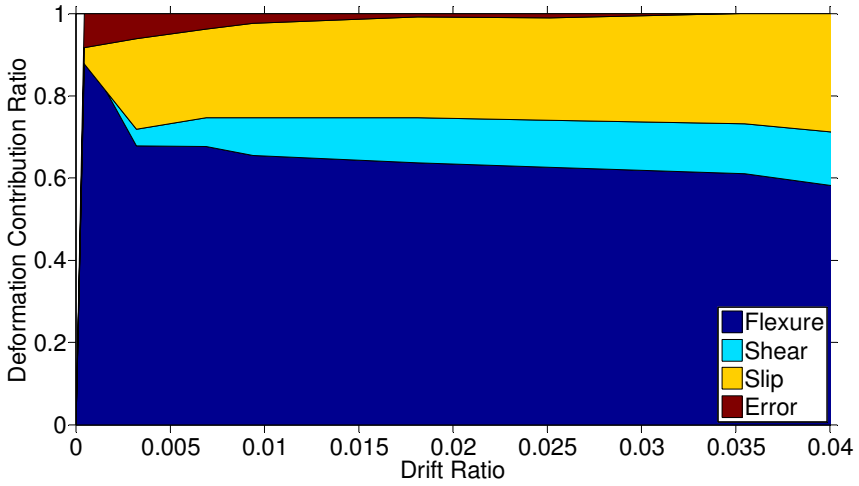

Figure 4.5.12: Deformation Components – SBH60

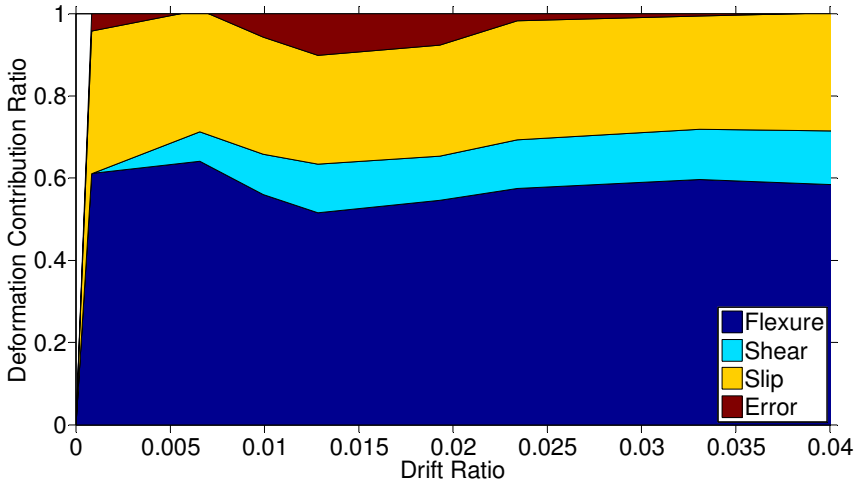

Figure 4.5.13: Deformation Components – SBH100

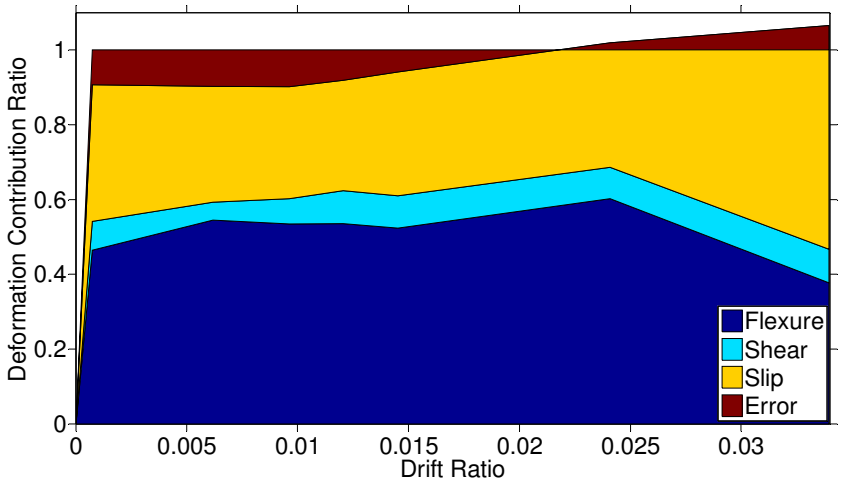

Figure 4.5.14: Deformation Components – SBL100

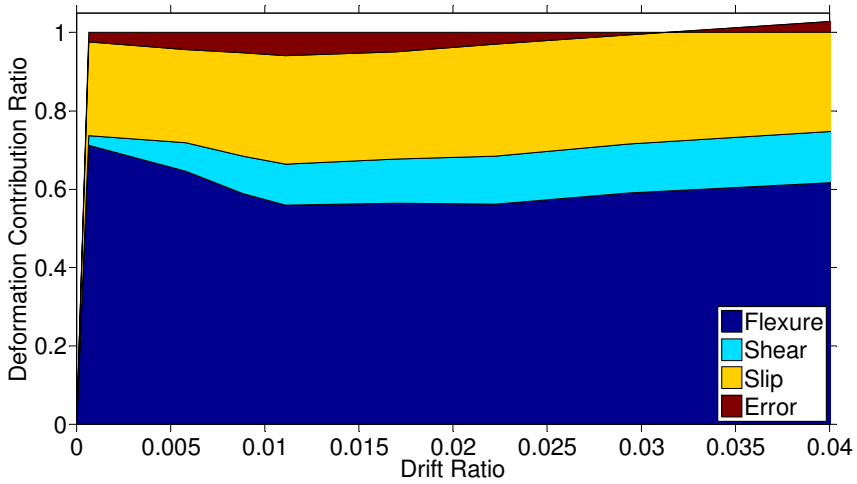

Figure 4.5.15: Deformation Components – SBM100

4.6. SPREAD OF PLASTICITY

Strain profile of the longitudinal reinforcement along the height of a beam was examined to identify if there was a trend for varying types of reinforcement. Figure 4.6.1 presents typical results, in this instance for the 1st loading cycle to drift ratio of 0.0485 in the east direction. Comparing the profiles of beams SBH100 and SBL100, it is evident that strain is more localized and concentrated at the base of the beam having lower T/Y. A direct consequence of the localized strains is that the beam having lower T/Y has higher maximum strain under the same drift demand. It is also observable that the peak strain at the base is almost the same for beams SBH60 and SBH100 even though conventional Grade 60 A706 has higher T/Y or more strain hardening. This result likely is influenced by greater slip of reinforcement from the anchorage for the beam with higher-grade steel (SBH100), leading to more slip deformation to achieve the same drift as SBH60.

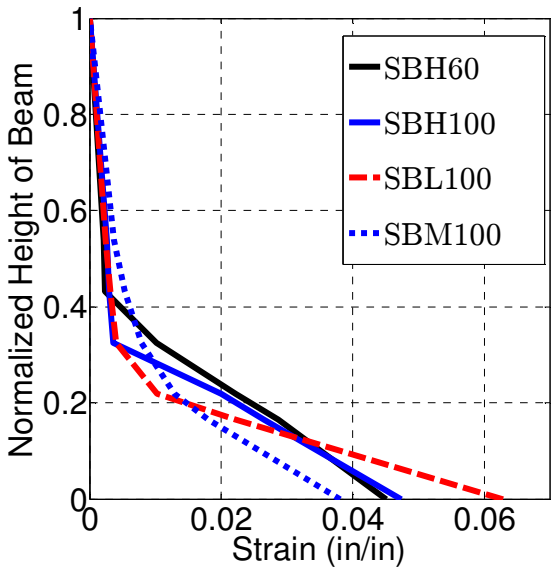

Figure 4.6.1: Strain Profiles along Length of Test Beams at Drift Ratio 0.0485.

4.7. DEVELOPMENT OF STRAIN AT BASE

Progression of peak longitudinal reinforcement strain with increasing lateral drift ratio is plotted in Figure 4.7.1. Grade 60 A706, Grade 100 T/Y = 1.17, and Grade 100 T/Y = 1.26 all exhibit a jump in strain after yielding, apparently because they all have distinct yield plateau in their stress-strain relation. In contrast, Grade 100 A1035 reinforcement with a round-house stress-strain relation experiences a more gradual increase in strain as drift ratio increases.

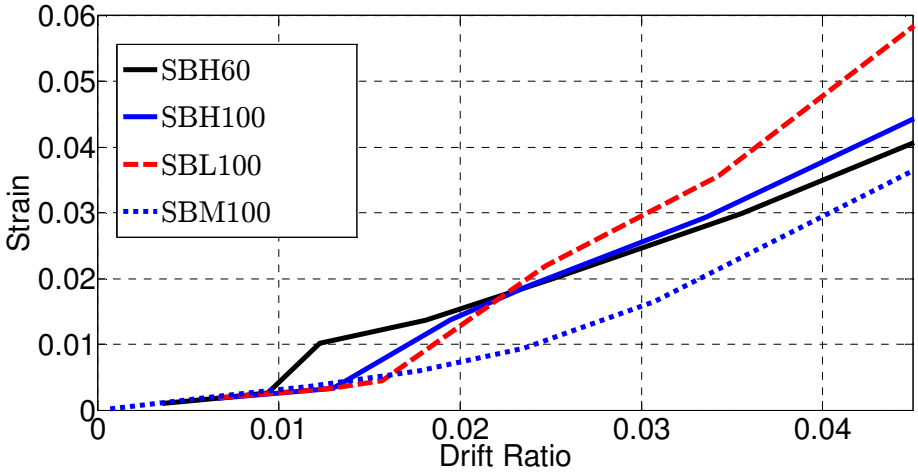

Figure 4.7.1: Strain Development of Longitudinal Bars at Base

4.8. BEAM ELONGATION

It has been observed in past research that reversed cyclic loading causes axial elongation in reinforced concrete beams (Fenwick and Fong, 1979; Qi and Patazopoulou, 1991; and Visnjic, 2014). Beam axial elongation is related to residual tensile strain in longitudinal bars even though they were subjected to flexural compression under cyclic loading as shown in Figure 4.8.1 through Figure 4.8.4 for all four test beams.

The phenomenon of positive residual strain of longitudinal bars in reinforced concrete beams under cyclic loading has been observed in many experiments. Several explanations have been proposed by previous researchers. One of them is due to the presence of loosened concrete granules entrapped in the cracks (Ma et al., 1976). As loading is reversed, the granules bridge the cracks and provide a path for transmission of compressive force. The early transfer of compression can also be caused by relative shear deformation between the faces of the cracks, leading to earlier contact of concrete. As a result, compression steel bars experience positive residual strain.

Residual elongation can also be attributed partially to the material behavior, that is, steel loaded in compression has strength slightly larger than strength in tension. For a beam with equal top and bottom reinforcement, assuming buckling does not occur, the initial yielding cycle will be due to yielding of the flexural tension reinforcement. When load is returned to zero, the yielded reinforcement will have some residual tensile strain. Upon reversed loading, this reinforcement is subjected to flexural compression, but yielding in compression will be delayed until the flexural tension side of the beam is strained past the yield point (this is because reinforcement in compression is slightly stronger than the reinforcement in tension). This delay continues through reversed cyclic loading and leads to a build-up of positive residual strain in the longitudinal reinforcement that results in axial elongation in the beam.

Figure 4.8.5 and Figure 4.8.6 display the relationship between lateral displacement and beam axial elongation of all beam specimens measured during the present tests. Beam axial elongation was measured by a displacement transducer attached to the beam at the location of applied lateral load along the centerline of the beam (Figure A-25). A target was fixed on the concrete block at the center of the beam.

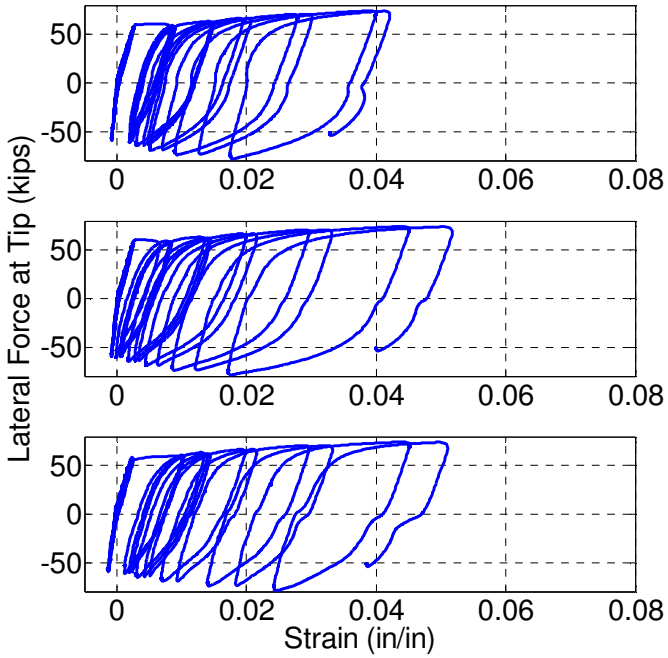

Figure 4.8.1: SBH60 - Lateral Force vs. Strain - Strain Gauge Distance from the Base - Top: 10 inches - Middle: 5 inches - Bottom: 0 inches

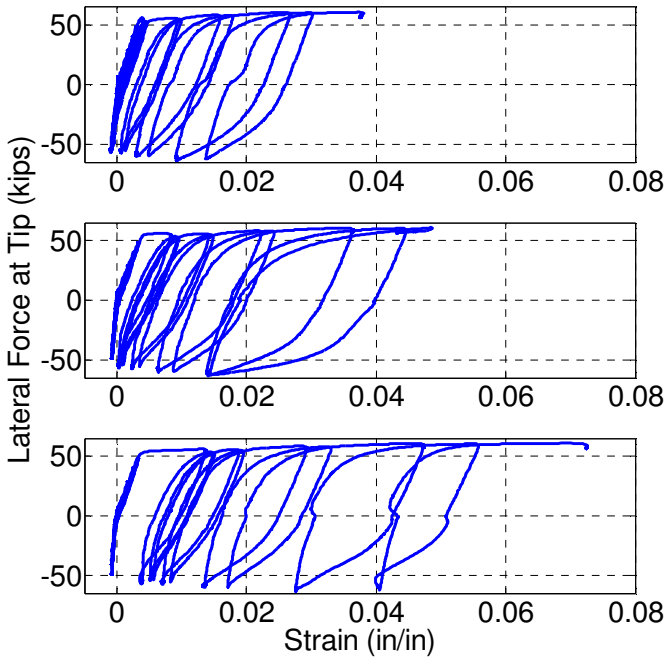

Figure 4.8.2: SBH100 - Lateral Force vs. Strain - Strain Gauge Distance from the Base - Top: 10 inches - Middle: 5 inches - Bottom: 0 inches

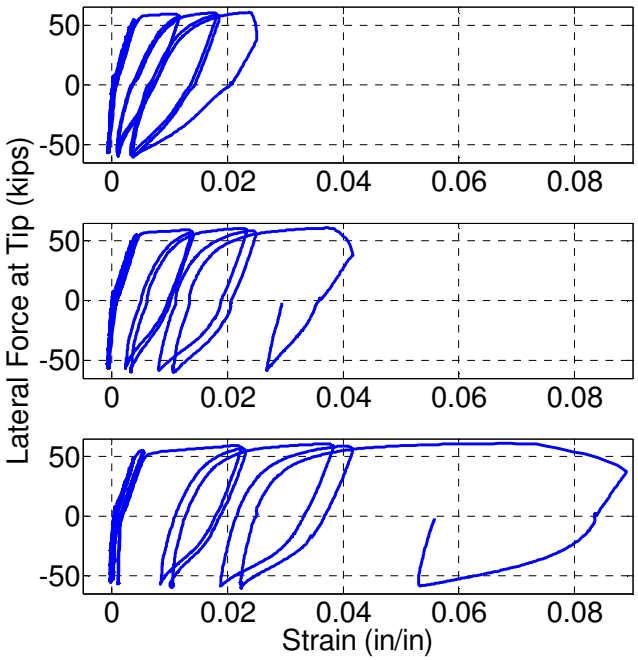

Figure 4.8.3: SBL100 - Lateral Force vs. Strain - Strain Gauge Distance from the Base - Top: 10 inches - Middle: 5 inches - Bottom: 0 inches

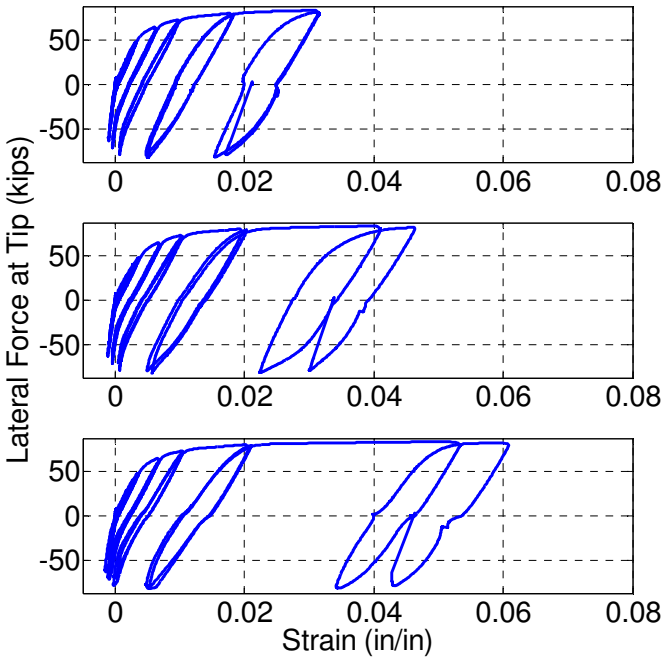

Figure 4.8.4: SBM100 - Lateral Force vs. Strain - Strain Gauge Distance from the Base - Top: 10 inches - Middle: 5 inches - Bottom: 0 inches

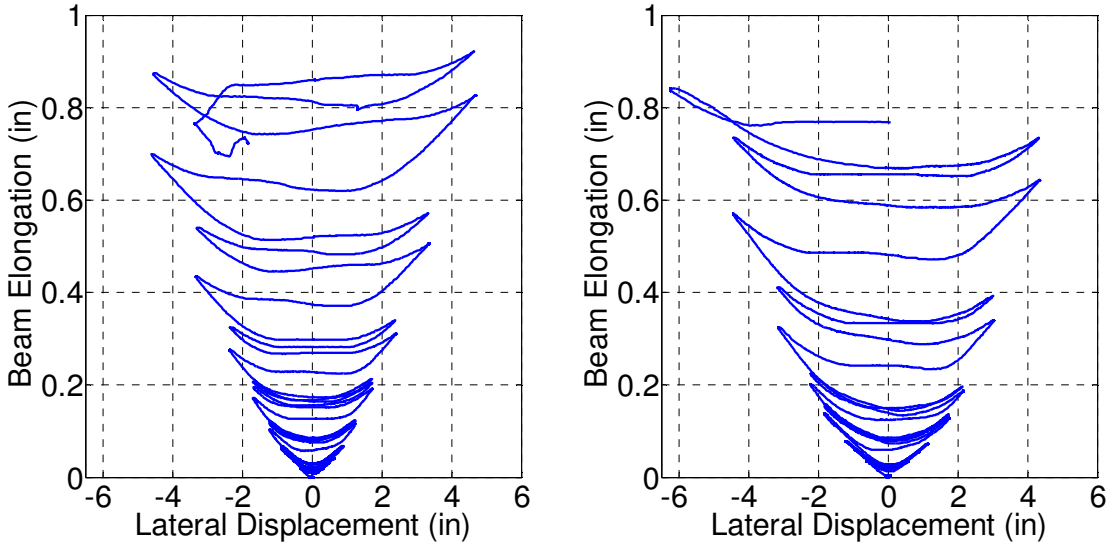

Figure 4.8.5: Beam Elongation - Left: SBH60 - Right: SBH100

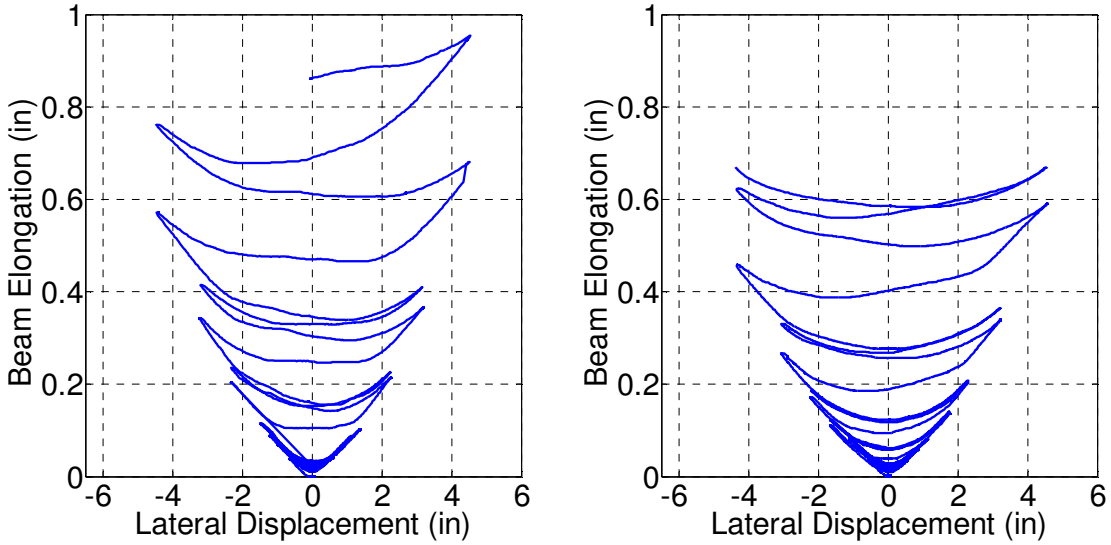

Figure 4.8.6: Beam Elongation - Left: SBL100 - Right: SBM100

CHAPTER 5: COMPARISON WITH DESIGN MODELS

5.1. STIFFNESS

Effective stiffness for design under earthquake loads is generally taken as the effective stiffness near the yield point of the longitudinal reinforcement. ACI 318 permits calculation of effective stiffness using detailed analysis considering the effects of cracking on member stiffness. The stiffness with cracked section moment of inertia, $E_c I_{cracked}$, was calculated to be approximately $0.52E_cI_g$ and $0.34E_cI_g$, where I_g = gross section moment of inertia and E_c = elastic modulus of concrete, which may be taken as $57{,}000\sqrt{f_c'}$ (psi), for beams with Grade 60 A706 and Grade 100 reinforcement, respectively. This calculated stiffness overestimates the effective stiffness for the test beams as it ignores slip of reinforcement out of the anchorage block. Alternatively, it is permitted to approximate effective flexural rigidity as a fraction of the gross-section flexural rigidity. In different code sections, both $0.35E_cI_g$ and $0.5E_cI_g$ are permitted. ASCE 41 (2013) recommends using $0.3E_cI_g$ for beams with $P/A_gf_c' \leq 0.1$. Figure 5.1.1 compares these stiffness models with measured stiffnesses obtained from the envelopes of load-deflection relations of the test beams. Shear stiffness calculated by $0.4E_cA_g$ is also examined but its contribution to total effective flexibility is negligible.

The effective stiffness values of $0.35E_cI_g$ and $0.3E_cI_g$ compare well with the measured effective stiffness of beam SBH60 with conventional Grade 60 A706 steel, while $0.5E_cI_g$ overestimates effective stiffness for that beam. All the other beams with higher-grade reinforcement and reduced amount of longitudinal reinforcement are less stiff, with effective stiffness closer to $0.2E_cI_g$.

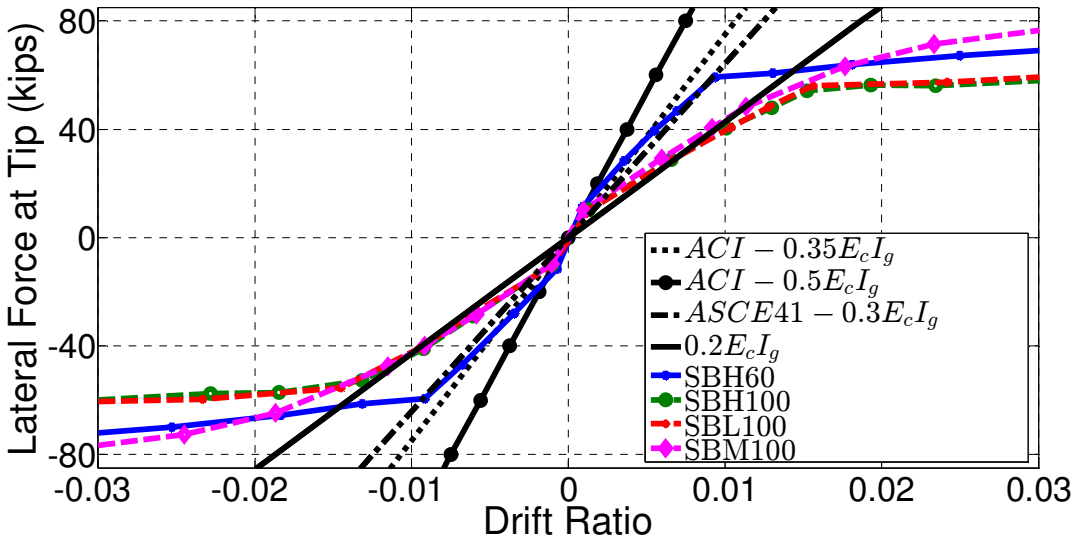

Figure 5.1.1: Lateral Stiffness Comparison

5.2. STRENGTH IN MOMENT AND SHEAR

Moment strength: Nominal flexural strength M_n and probable flexural strength M_{pr} for all test specimens were calculated in accordance with ACI 318-14 and compared with test data (Table 5.2.1 and Figure 5.2.1 through Figure 5.2.4). By ACI 318, M_n is calculated using nominal (specified) concrete strength $f_c' = 5{,}000\, psi$ and nominal yield strength of reinforcing steels, which are 60 ksi and 100 ksi for Grade 60 and Grade 100, respectively. The moment strength is taken as concrete reaches crushing strain of 0.003. Similarly M_{pr} is calculated using nominal concrete compressive strength of 5,000 psi and elasto-plastic stress-strain relation for steel with yield strength equal to 1.25 times the nominal yield strength, which are $1.25 \times 60 = 75\ (ksi)$ and $1.25 \times 100 = 125\ (ksi)$ for Grade 60 and Grade 100, respectively. By design, all four test specimens are expected to have equivalent nominal strength. Therefore, M_{pr} calculated by ACI 318 is the same for all test beams.

As shown in Figure 5.2.1 through Figure 5.2.4, the probable moment strength by ACI 318 underestimates the ultimate flexural strength of beams SBH60 and SBM100. This is due to material overstrength and high strain-hardening of Grade 60 A706 and Grade 100 A1035 reinforcement. ACI 318 M_{pr}, however, slightly overestimates moment strength of beams SBH100 and SBL100.

Table 5.2.1: Strength Comparison

	SBH60	**SBH100**	**SBL100**	**SBM100**
$V_y\ (kips)$	52.0	48.0	49.0	60.0
$V_{max}\ (kips)$	74.6	61.0	60.8	81.9
$M_y\ (kips - in)$	4875	4500	4594	5625
$M_{max}\ (kips - in)$	6994	5719	5700	7678
$M_{n\_ACI}\ (kips - in)$	4755	4694	4694	4694
$M_{pr\_ACI}\ (kips - in)$	5886	5795	5795	5795
$\frac{M_{max}}{M_{pr\_ACI}}$	1.19	0.99	0.98	1.32

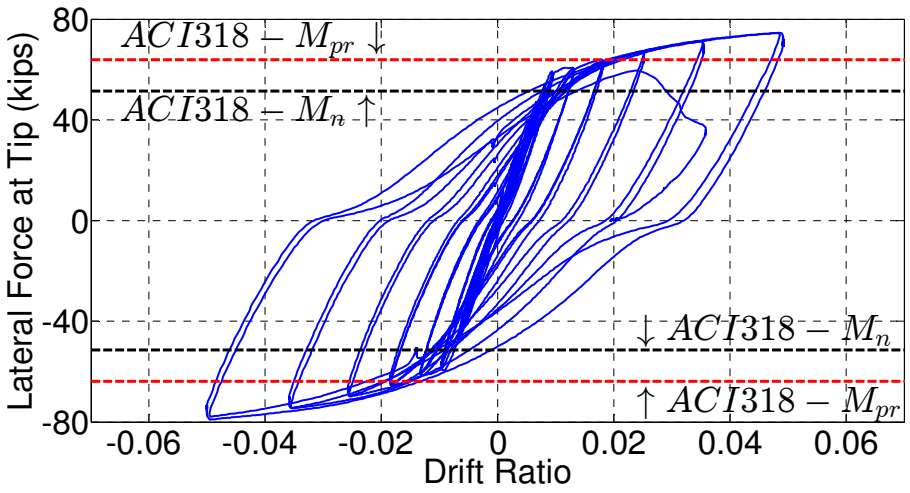

Figure 5.2.1: Lateral Force – Drift Ratio Relation of Beam SBH60

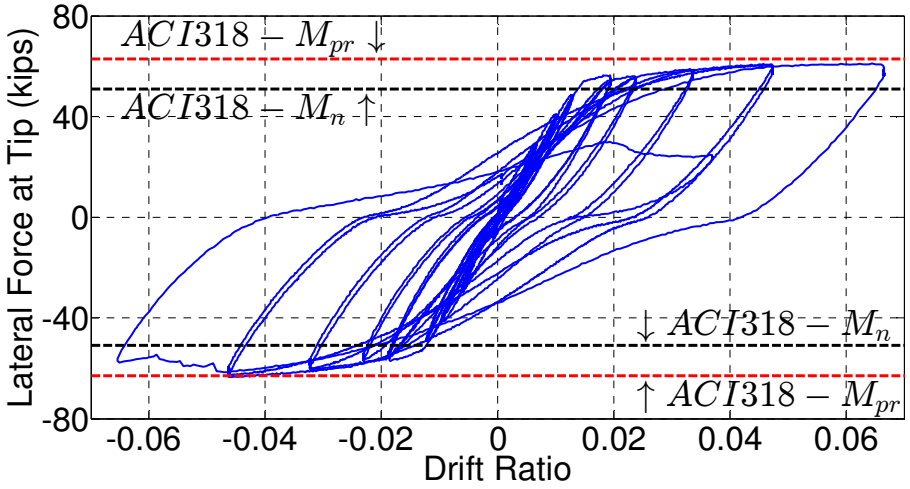

Figure 5.2.2: Lateral Force – Drift Ratio Relation of Beam SBH100

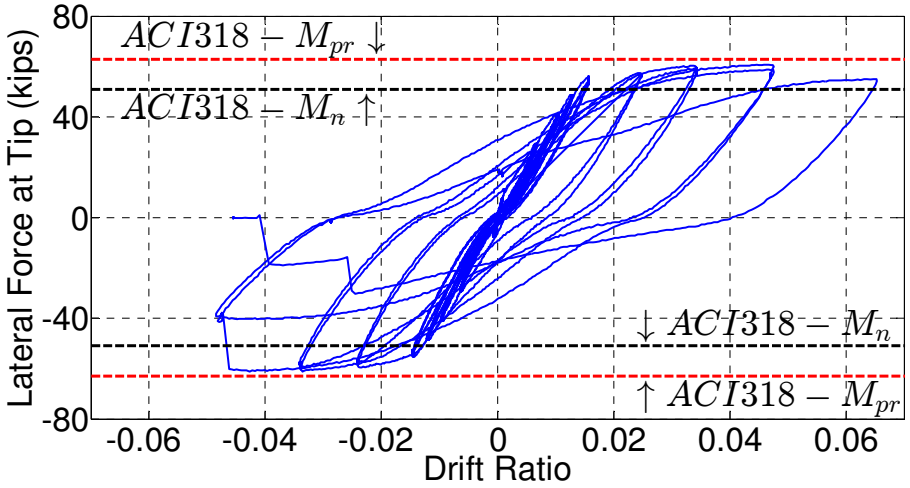

Figure 5.2.3: Lateral Force – Drift Ratio Relation of Beam SBL100

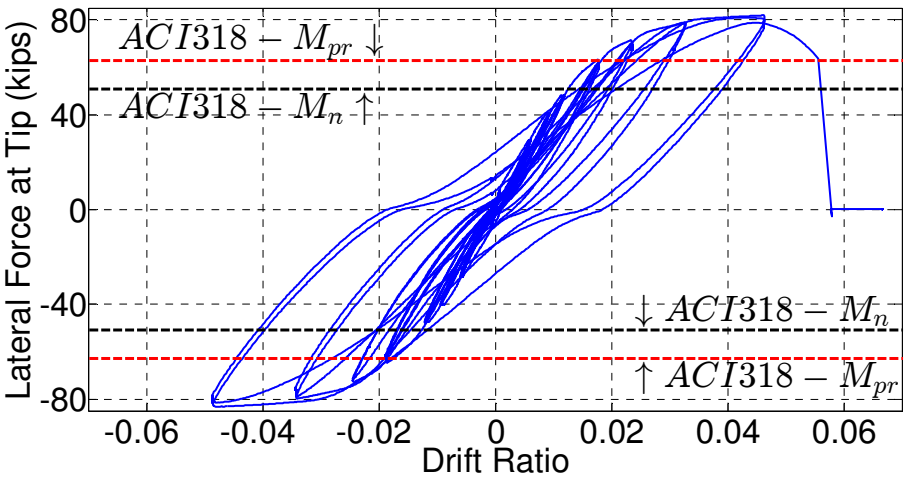

Figure 5.2.4: Lateral Force – Drift Ratio Relation of Beam SBM100

Shear strength: According to ACI 318, nominal shear strength is calculated as follows:

$$V_n = V_c + V_s \qquad \text{Eq. (2)}$$

$$V_c = 2\sqrt{f_c'}\, b_w d \qquad \text{Eq. (3)}$$

$$V_s = \frac{A_v f_{yt} d}{s} \qquad \text{Eq. (4)}$$

To accommodate shear strength decay that can occur within plastic hinge regions, ACI 318 specifies $V_c = 0$ within twice the member depth of intended critical sections. Table 5.2.2 summarizes calculated shear strength of the test specimens. As designed, all the test beams have low shear demand of about $3\sqrt{f_c'}\ (psi)$ to minimize the tension shift effect. As measured, shear stress demand on all specimens is below $4\sqrt{f_c'}\ (psi)$ or 40% of the shear capacity provided by transverse reinforcement only (Figure 5.2.5 and Figure 5.2.6).

Table 5.2.2: Shear Strength of Test Specimens

	SBH60	**SBH100**	**SBL100**	**SBM100**
$V_c\ (kips)$	41	41	41	41
$V_s\ (kips)$	206	258	258	258
$V_{measured}\ (kips)$	74.6	61.0	60.8	81.9
$V_{measured}/(b_w d\sqrt{f_c'})$	3.6	3.0	3.0	4.0
$V_{measured}/V_s$	0.36	0.24	0.24	0.32

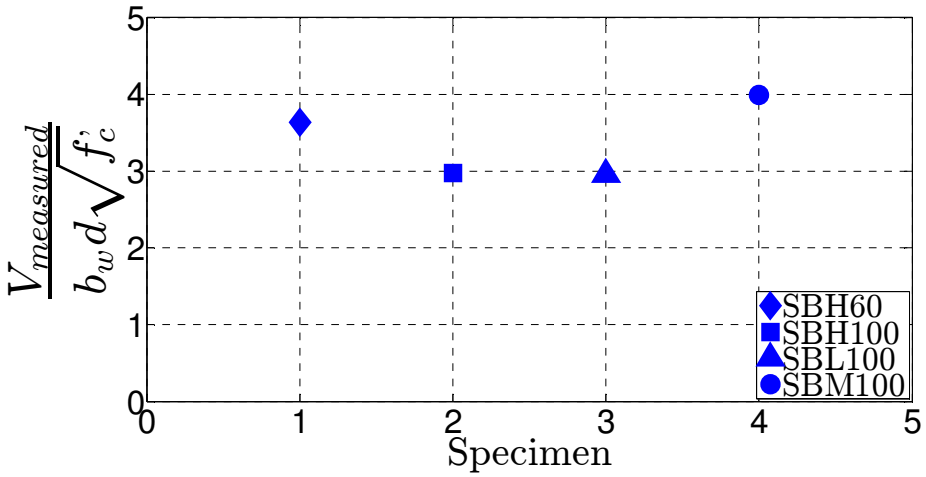

Figure 5.2.5: Normalized Shear Demand

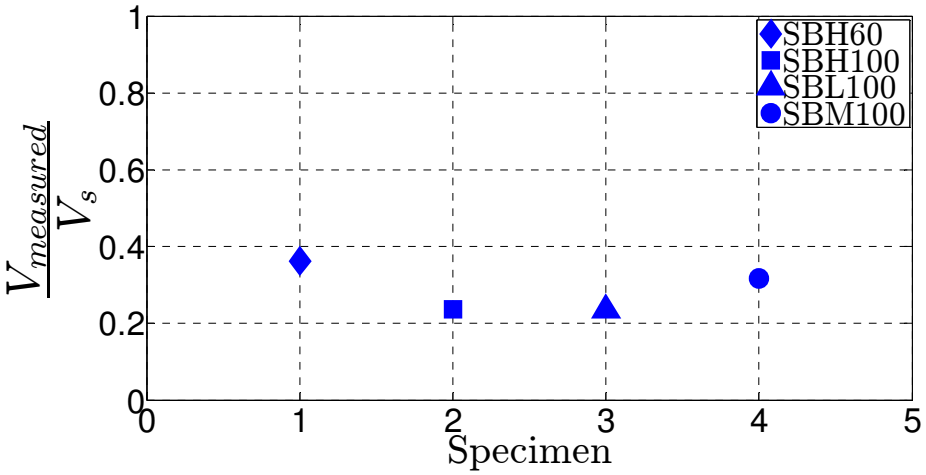

Figure 5.2.6: Shear Demand Normalized by Transverse Reinforcement Capacity

5.3. DEFORMATION CAPACITY PER ASCE 41

The monotonic load-deformation relation is calculated in accordance with ASCE 41-13 and compared against those response envelopes of beam test data in Figure 5.3.1 to Figure 5.3.4. Deformation at B is calculated by taking nominal flexural strength of the cross section divided by effective stiffness $0.30E_cI_g$ suggested by ASCE 41. Nominal flexural strength is taken as strength when concrete strain reaches 0.003 and estimated by using expected concrete compressive strength f'_c of approximately 5,000 psi for all test specimens, and expected yield stresses (f_y) of 69 ksi and 100 ksi for Grade 60 A706 and Grade 100 reinforcement, respectively. Plastic rotation recommended by ASCE 41, which is 0.025 radians for all test beams, is added to deformation at B to obtain ultimate deformation at C. Strength at C is defined as strength when concrete strain

reaches 0.003 and ultimate steel stresses (f_u) are $1.25 \times 69 = 86\ ksi$ and $1.25 \times 100 = 125\ ksi$ for Grade 60 A706 and Grade 100 reinforcement, respectively.

The ASCE 41-13 load-deformation relations agree well with test data for beam SBH60 with conventional Grade 60 reinforcement even though the ultimate rotation is slightly underestimated. The correlation is less agreeable for the beams with Grade 100 steel. The larger effective stiffness suggested by ASCE 41-13 as discussed in the previous section results in much lower deformation at B. Secondly, M_{pr} calculated according to ACI 318-14 using overstrength factor of 1.25 to account for reinforcement strain-hardening results in overestimation of the ultimate strength for beams SBH100 and SBL100 with higher-grade reinforcement having T/Y = 1.26 and 1.17, respectively. On the other hand, this M_{pr} underestimates the ultimate strength of specimen SBM100 as discussed in previous section. Disagreement in effective stiffness and ultimate strength results in poor correlation of load-deformation between model and test data for beams with higher-grade reinforcement. Results would be improved using a reduced effective stiffness of $0.2E_cI_g$ for beams with Grade 100 reinforcement.

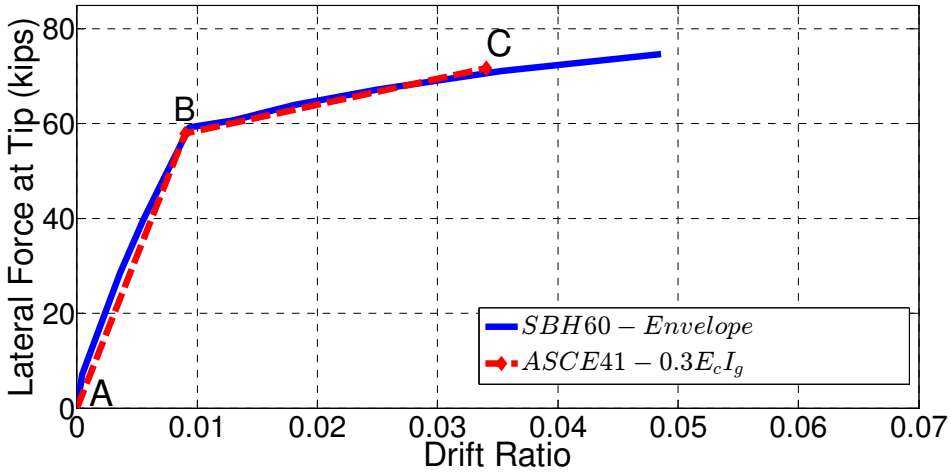

Figure 5.3.1: Monotonic Load-Deformation Comparison for Specimen SBH60

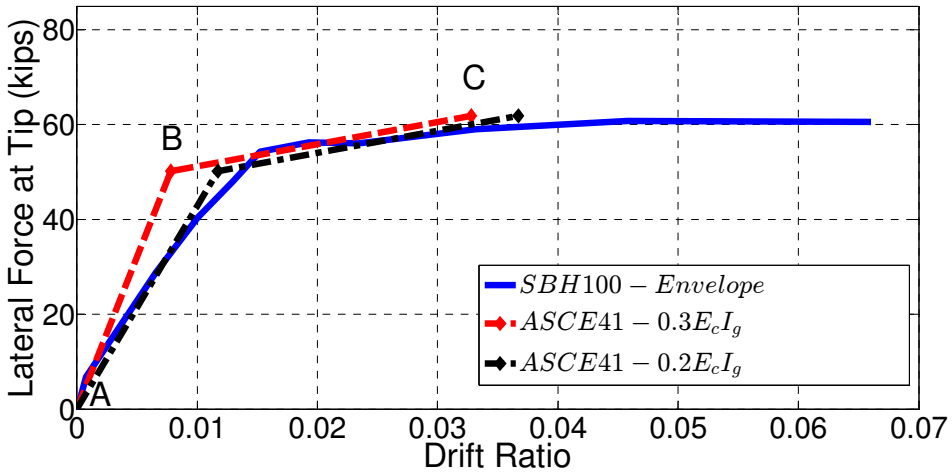

Figure 5.3.2: Monotonic Load-Deformation Comparison for Specimen SBH100

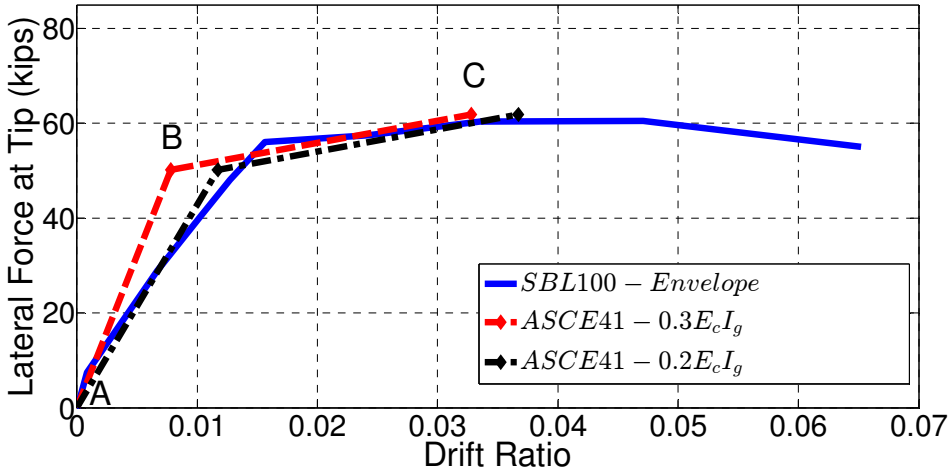

Figure 5.3.3: Monotonic Load-Deformation Comparison for Specimen SBL100

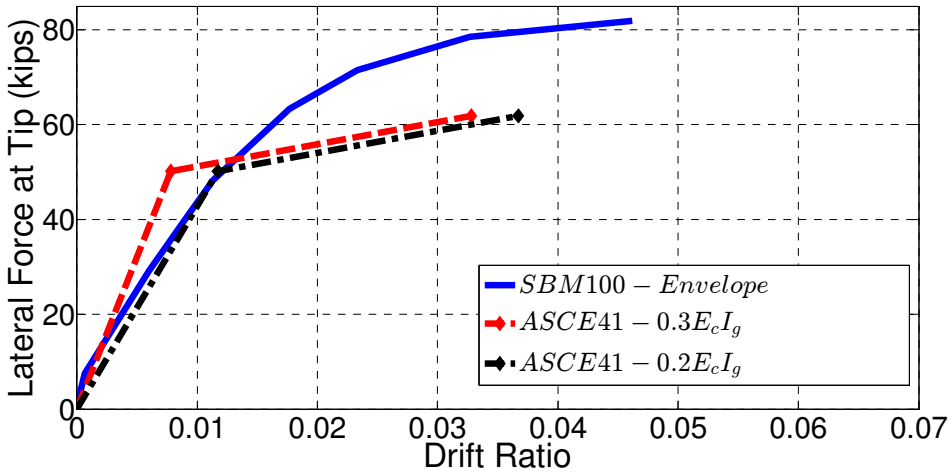

Figure 5.3.4: Monotonic Load-Deformation Comparison for Specimen SBM100

5.4. EFFECTIVE PLASTIC HINGE LENGTH

The plastic-hinge model utilizes the idealized elasto-plastic moment-curvature relation with a plastic hinge length to estimate displacement capacity. The member is assumed to develop linear-elastic curvature along its length. The inelastic curvature of magnitude $\left(\emptyset_u - \emptyset_y\right)$ is assumed to extend over the plastic hinge length l_p (Figure 5.4.1). According to the model, plastic rotation is

$$\theta_p = (\phi_u - \phi_y) l_p \qquad \text{Eq. (5)}$$

The displacement at the tip of a flexural member resisting a concentrated load at its tip is

$$\delta_u = \frac{\phi_y l^2}{3} + \left(\emptyset_u - \emptyset_y\right) l_p \left(l - \frac{l_p}{2}\right) \qquad \text{Eq. (6)}$$

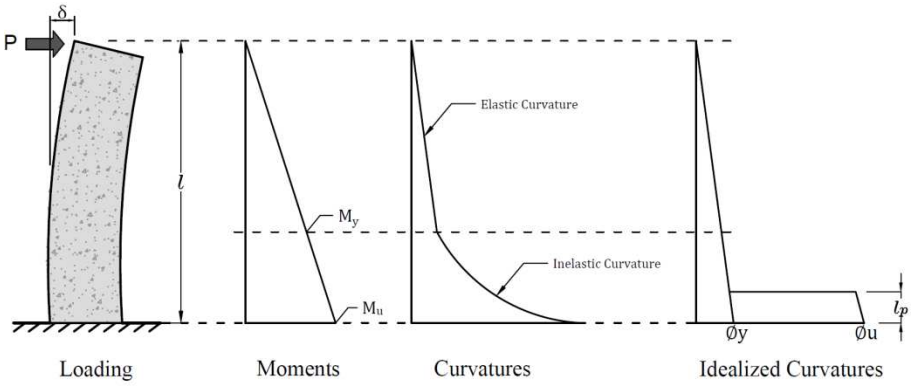

Figure 5.4.1: Conventional Plastic Hinge Model

In the plastic-hinge model, the plastic hinge length has been determined empirically. The tip displacement δ_u, and curvatures ϕ_u and ϕ_y are measured from laboratory experiment. The plastic hinge length l_p is then computed to satisfy Eq. (6). As a result, deformations contributed from shear and slip are accounted for implicitly in the plastic hinge length.

Several researchers have proposed expressions for calculating the plastic-hinge length. Priestley and Park (1987) recommended

$$l_p = 0.08l + 0.00015 d_b f_y, psi$$

Berry et al. (2008) suggested

$$l_p = 0.05l + 0.008 d_b f_y / \sqrt{f_c'}, psi$$

In practice, a simpler expression that provides reasonable accuracy is

$$l_p = 0.5h$$

These expressions for calculating the plastic-hinge length had been developed from laboratory tests of column specimens reinforced with conventional Grade 60 steel. Consequently, the expressions do not consider the effect of tensile-to-yield strength ratio (T/Y), which has been shown to significantly affect the spread of plasticity from the test results of this research program.

Applying the plastic hinge model with measured test data on tip deflection and curvatures at yield and ultimate, the plastic-hinge length is back-calculated for loading cycles with target drift ratio of 3% for all beam tests and presented in Table 5.4.1 and Figure 5.4.2 and Figure 5.4.3. Measured strain used to calculate curvatures are taken from the strain gauge reading on longitudinal reinforcement at the base of the beam during the tests. In Table 5.4.1, yield curvature is also calculated by moment-curvature analysis for the beam cross-section under monotonic loading, and strain at yielding is taken as the corresponding nominal yield stress (60 ksi or 100 ksi) divided by Young's modulus of elasticity (E = 29000 ksi). Curvatures at yield measured during tests agree well with that from moment-curvature analysis, providing confidence on performance of the strain gauges and accuracy of strain data.

Under the same drift demand, SBL100 with higher-grade reinforcement has more slip deformation, but its flexural deformation is more localized close to its base than in SBH60 with conventional Grade 60 A706 steel. As a result, comparable plastic hinge length may be expected for beams SBL100 and SBH60. Plastic hinge lengths of both specimens SBH100 and SBM100 are approximately 1.5 times the beam cross-sectional height, which is longer than that of SBH60. Plastic hinge lengths of all test beams are longer than half of beam cross-sectional height that is widely used in practice.

Table 5.4.1: Plastic Hinge Length at 3% Drift Ratio

	SBH60	**SBH100**	**SBL100**	**SBM100**
Computed Yield Curvature $(1/in.)$	0.00014	0.00022	0.00022	0.00022
Measured Yield Curvature $(1/in.)$	0.00015	0.00021	0.00022	0.00026
Measured Curvature at 3% Drift Ratio $(1/in.)$	0.0014	0.00097	0.0014	0.00097
Plastic Hinge Length l_p $(in.)$	30	48	27	46
l_p/h	1.25	2.00	1.13	1.92
l_p/l	0.32	0.51	0.29	0.49

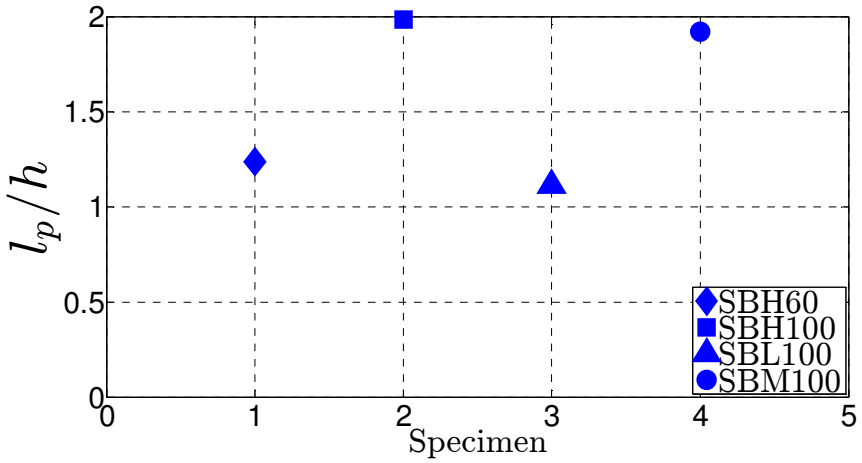

Figure 5.4.2: Plastic Hinge Length Normalized by Beam Cross-Sectional Height

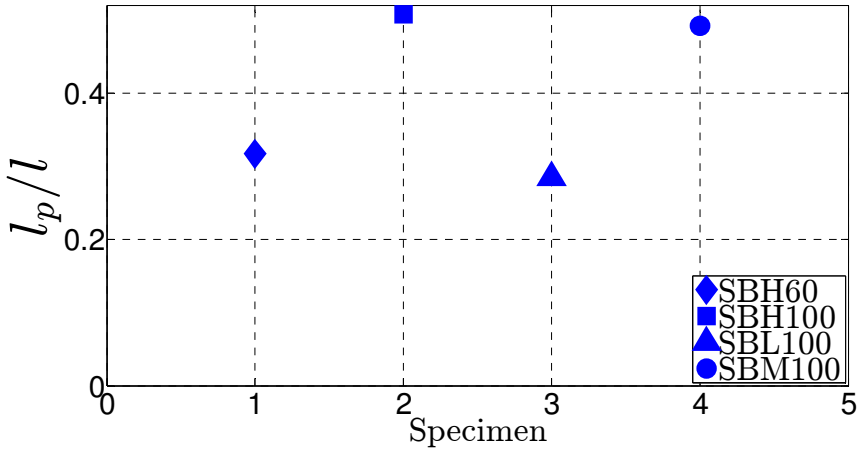

Figure 5.4.3: Plastic Hinge Length Normalized by Beam Length

CHAPTER 6: NUMERICAL MODELING OF REINFORCED CONCRETE BEAMS AND COLUMNS

6.1. BEAMS

The load-deflection response of the test beams can be calculated using conventional mechanics approaches. The total displacement is the sum of three components (Figure 6.1.1):

$$\delta = \delta_f + \delta_v + \delta_s \qquad \text{Eq. (7)}$$

where δ_f = displacement due to flexural curvature
δ_v = displacement due to conventional shear distortion
δ_s = rigid-body displacement due to reinforcement slip from anchorage zone

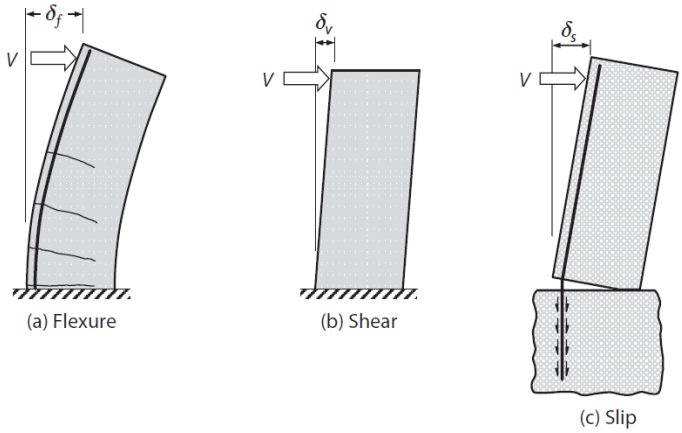

Figure 6.1.1: Components of Displacement in Beam (used with permission from Moehle, 2014)

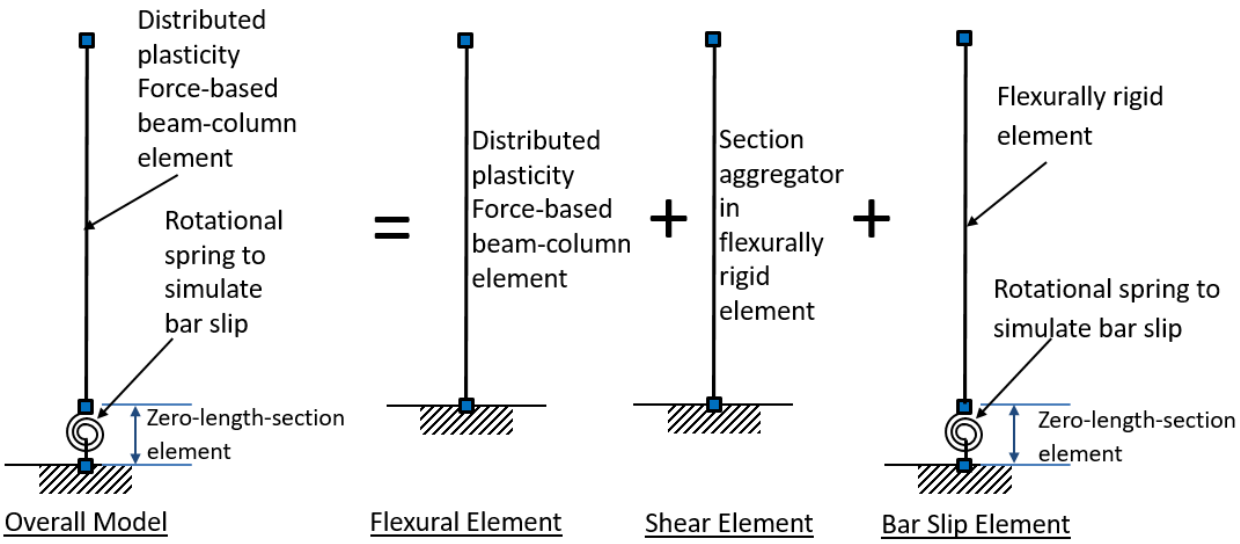

Figure 6.1.2: Overall OpenSees Model of Test Beams

Each of displacement components can be modeled separately with sufficient accuracy within the linear range of response. The nonlinear inelastic range of response, however, poses challenges because of interaction between flexure and shear. To simplify the calculations, a common practice is to model shear with a linear elastic spring that is implicitly accounted for within the flexural element through a section aggregator.

The test beams were modeled in the computer software package OpenSees (McKenna et al., 2000) and analyzed for cyclic response by displacement control with input displacement values taken from measured test data.

The overall model has a distributed plasticity force-based beam-column element and zero-length section element to simulate the response of flexure and bar slip, respectively (Figure 6.1.2). Both elements have a fiber cross section with concrete and steel fibers having properties as described in the next section on materials. Shear behavior is modeled by imposing its properties onto flexural element through a section aggregator.

a. Materials

Concrete

A simple model of stress-strain relationship is adopted here for cover (unconfined) concrete with peak strength f_c' taken from the cylinder tests of 5 ksi (Figure 6.1.3). A linearly descending branch is assumed after reaching f_c' until complete loss of strength at strain of 0.006. Core (or confined) concrete properties were modeled by the algebraic form proposed by Mander et al. (1988a). The resulting confined concrete properties and stress-strain relation of the test beams are shown in Figure 6.1.4.

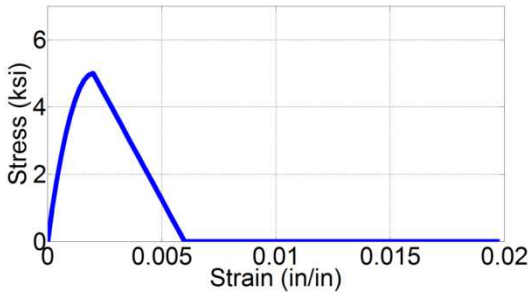

Figure 6.1.3: Cover (Unconfined) Concrete Stress-Strain Relation

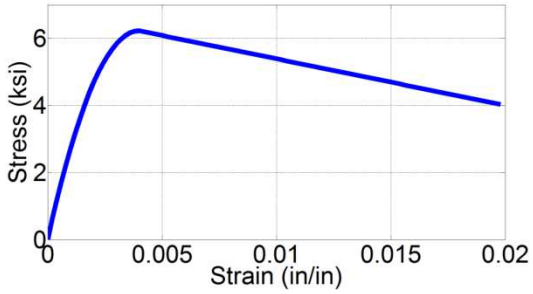

Figure 6.1.4: Core (Confined) Concrete Stress-Strain Relation

Steel

Uniaxial material ReinforcingSteel (Kunnath et al., 2009) based on Chang and Mander (1994) hysteretic behavior is used to model cyclic properties of reinforcement used in test beams SBH60, SBH100, and SBL100. Table 6.1.1 lists all the parameters used in ReinforcingSteel material.

Grade 100 A1035 steel has distinctly different stress-strain properties as evident in the round-shaped stress-strain relationship without a yield plateau. A new mathematical model has been developed in OpenSees platform for this research program to simulate the behavior of Grade 100 A1035. This new uniaxial material model has the behavior under loading in tension described by the Ramberg-Osgood equation (Ramberg and Osgood, 1943). When the loading is reversed in direction to compression after the material has yielded in tension under large strain, the material responds following the Bauschinger effect. For response in the large strain region (greater than 0.02), this material behaves according to the Bauschinger effect in both tension and compression loading conditions (Figure 6.1.8).

All the parameters shown in Table 6.1.1 were selected to obtain the best correlation with the stress-strain relations of steel bars used in the test beams. Steel specimens were taken from the same batch used to construct test beams and tested in the laboratory under cyclic loading. Grip spacing was five times the bar diameter, which was also the transverse reinforcement spacing in the test beams. The strain histories measured during beam tests were imposed onto the steel specimens under displacement control. The stress-strain relationship of the steel models and actual steel bar tests are shown in Figure 6.1.5 through Figure 6.1.8.

Table 6.1.1: Steel Material Model Parameters

			Steel used in			
Steel Model	Parameters	Description	SBH60	SBH100	SBL100	SBM100
Reinforcing Steel	f_y	Yield stress (ksi)	64.5	101.5	106	
	f_u	Ultimate stress (ksi)	95.5	127.6	123.9	
	E_s	Young's modulus (ksi)	29000	29000	29000	
	E_{sh}	Tangent stiffness at initiation of strain hardening	950	950	750	
	ε_{sh}	Strain at initiation of strain hardening	0.0055	0.007	0.007	
	ε_{su}	Strain at ultimate stress	0.15	0.08	0.08	
	l_{SR}, β, r, γ	Parameters for buckling model based on Gomes and Appleton (1997)	5, 1.0, 0.75, 0.0	5, 1.0, 0.85, 0.0	5, 1.0, 0.75, 0.0	
	a1, limit	Parameters for controlling isotropic hardening	4.3, 0.01	4.3, 0.01	4.3, 0.01	
	R1, R2, R3	Parameters for controlling transition from elastic to plastic branches	0.333, 20, 6	0.333, 25, 4	0.5, 40, 1	
New Steel Model	f_y	Yield stress (ksi)				160
	E_s	Young's modulus (ksi)				29,000
	β_{steel}	Strain hardening ratio				0.001
	Ro, cR1, cR2	Parameters for controlling transition from elastic to plastic branches				25, 0.925, 0.15
	a1, a2, a3, a4	Parameters for controlling isotropic hardening				0.0, 1.0, 0.0, 1.0
	a	Yield offset in Ramberg Osgood's model				0.015
	n	Parameter for controlling transition from elastic to plastic branches in Ramberg Osgood's model				10

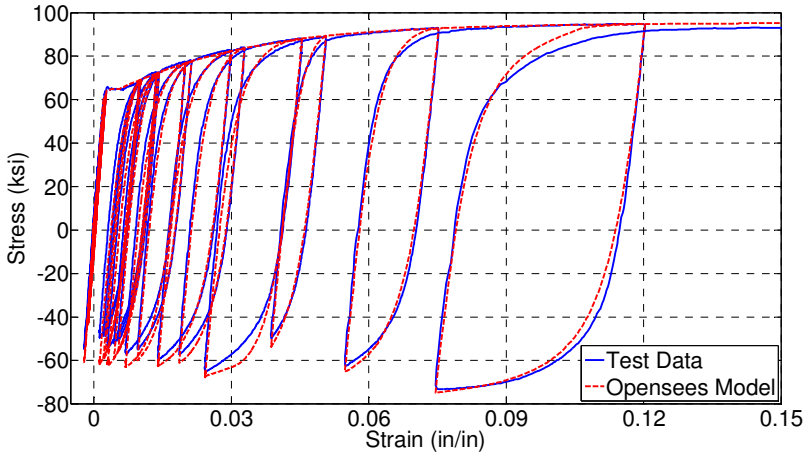

Figure 6.1.5: Stress-Strain Relationship for No. 9 Grade 60 A706 Steel Model

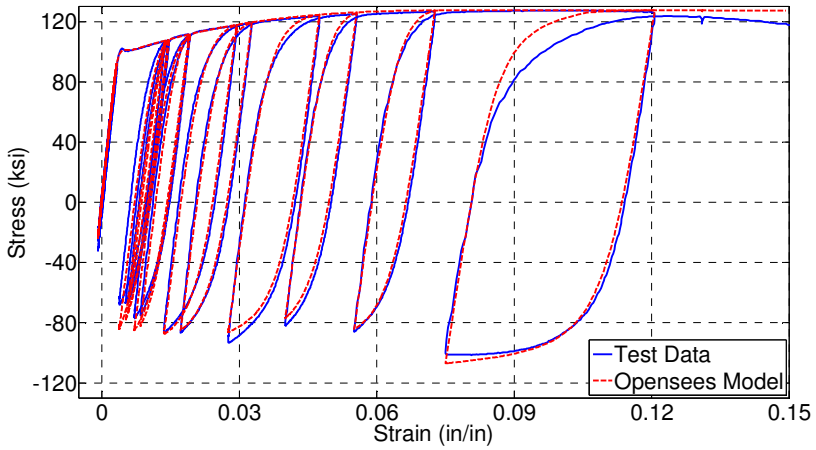

Figure 6.1.6: Stress-Strain Relationship for No. 8 Grade 100 T/Y = 1.26 Steel Model

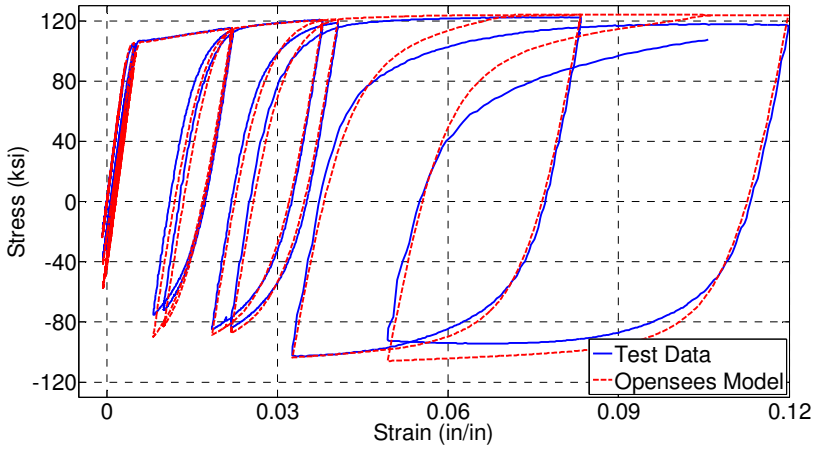

Figure 6.1.7: Stress-Strain Relationship for No. 8 Grade 100 T/Y = 1.17 Steel Model

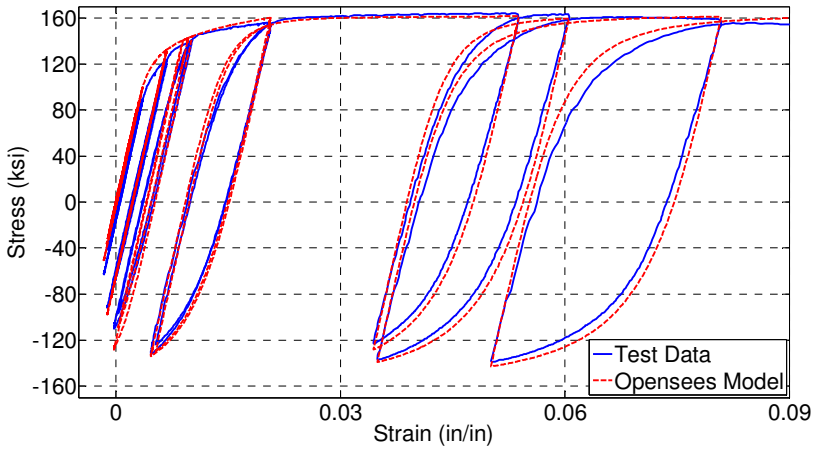

Figure 6.1.8: Stress-Strain Relationship for Grade 100 A1035 Steel Model

b. Flexural Element – Force-Based Beam-Column Element

Flexural response of the test beams can be modeled by using a distributed plasticity force-based beam-column element in OpenSees. The force-based beam-column element is formulated based on interpolation of force so that equilibrium between element and section forces is satisfied exactly, which holds in the range of constitutive nonlinearity. Section forces are determined from the element forces by interpolation within the element that comes from static equilibrium with constant axial force and linear distribution of bending moment in absence of distributed element loads (Figure 6.1.9).

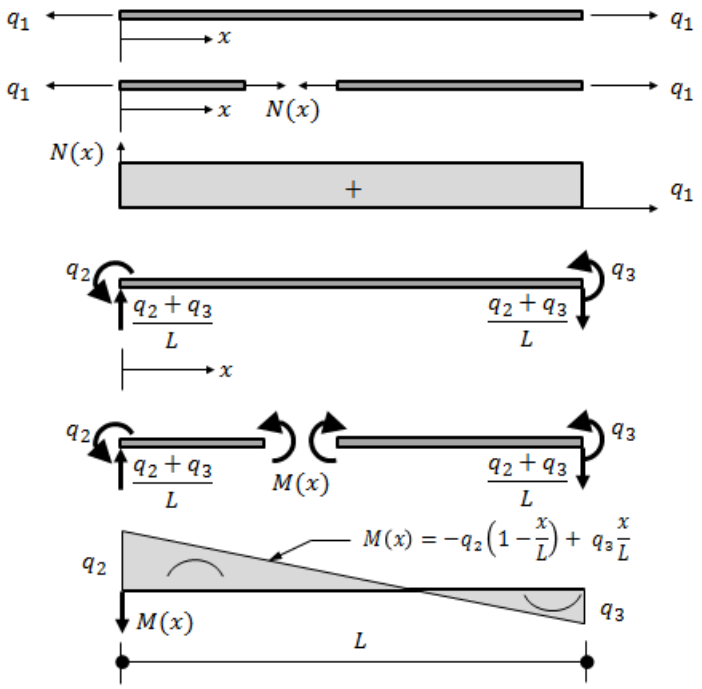

Figure 6.1.9: Element Force Diagram of Force-Based Beam-Column Element

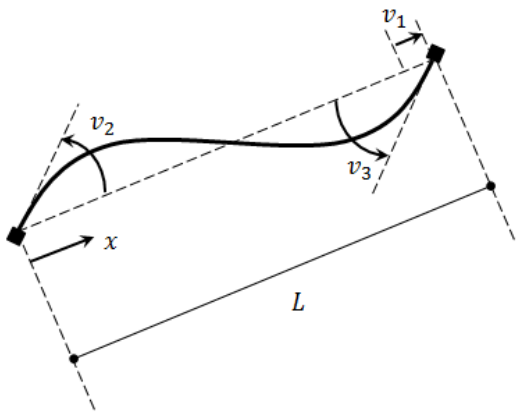

Figure 6.1.10: Deformation of Force-Based Beam-Column Element

From equilibrium in the undeformed configuration of the element's free body, the section forces at x in absence of distributed element load are:

$$\boldsymbol{s}(x) = \begin{bmatrix} N(x) \\ M(x) \end{bmatrix} = \begin{bmatrix} 1 & 0 & 0 \\ 0 & -\left(1 - \frac{x}{L}\right) & \frac{x}{L} \end{bmatrix} \begin{bmatrix} q_1 \\ q_2 \\ q_3 \end{bmatrix}$$

$$\boldsymbol{s}(x) = \boldsymbol{b}(x)\boldsymbol{q}$$

$where\ \boldsymbol{b}(x) - matrix\ of\ force\ interpolation\ functions$

Applying the principle of virtual force, the compatibility (Figure 6.1.10) between section and element deformation is

$$\boldsymbol{v} = \begin{bmatrix} v_1 \\ v_2 \\ v_3 \end{bmatrix} = \int_0^L \boldsymbol{b}^T(x)\boldsymbol{e}(x)dx = \sum_{i=1}^{N_p} \boldsymbol{b}^T(x_i)\boldsymbol{e}(x_i)w_i$$

$where\ \boldsymbol{e}(x) = \begin{bmatrix} \epsilon_a(x) \\ \kappa(x) \end{bmatrix} = \begin{bmatrix} Axial\ strain \\ Curvature \end{bmatrix}\ of\ the\ section$

$w_i = weight\ of\ integration\ point$

$N_p = number\ of\ integration\ points\ along\ length\ of\ element$

The tangent flexibility matrix of the element is

$$\boldsymbol{f} = \frac{\partial \boldsymbol{v}}{\partial \boldsymbol{q}} = \int_0^L \boldsymbol{b}^T(x)\boldsymbol{f_s}(x)\boldsymbol{b}(x)dx = \sum_{i=1}^{N_p} \boldsymbol{b}^T(x_i)\boldsymbol{f_s}(x_i)\boldsymbol{b}(x_i)w_i$$

$$where\ \boldsymbol{f_s}(x_i) - sectional\ flexibility$$

Gauss-Lobatto quadrature is used in force-based elements because it places integration points at the element ends, where bending moments and associating curvatures are largest in absence of element load. To represent accurately the nonlinear material response of a force-based beam-column element, four to six Gauss-Lobatto integration points are typically used (Neuenhofer and Filippou, 1997). A four-point Gauss-Lobatto quadrature rule applied to evaluate the compatibility relationship is depicted in Figure 6.1.11.

Flexural response of the test beams is modeled by using a distributed plasticity force-based beam-column element with four Gauss-Lobatto integration points including two points at the ends of a beam to account for locations of largest moment and curvature (Figure 6.1.12). A fiber section is used for the beam-column element with cover and core concrete, and steel fibers having similar properties as described in Section 6.1.a. An iterative procedure is required for the solution as shown in Figure 6.1.13 since the materials have nonlinear properties and the loading is displacement control.

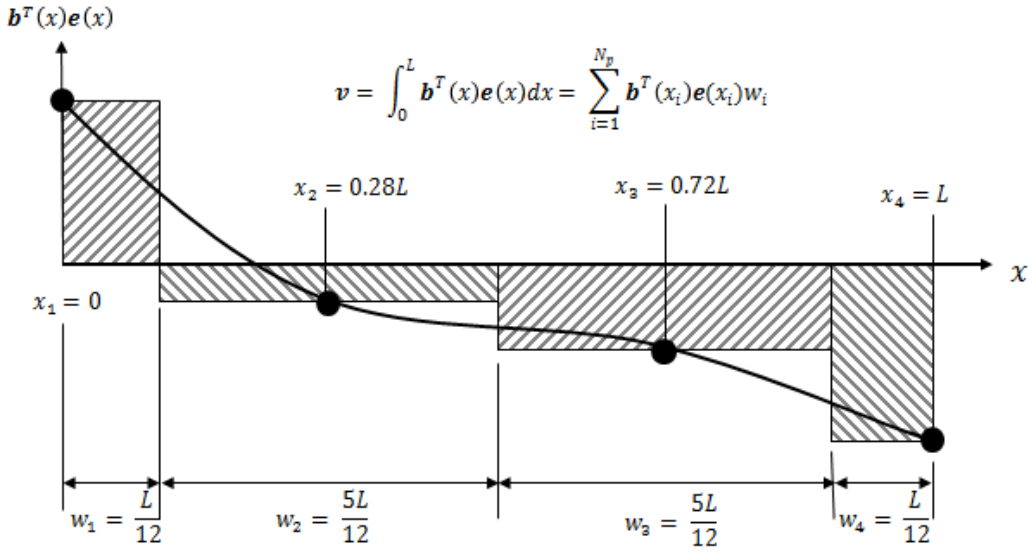

Figure 6.1.11: Four-point Gauss Lobatto quadrature rule applied to force-based element compatibility relationship

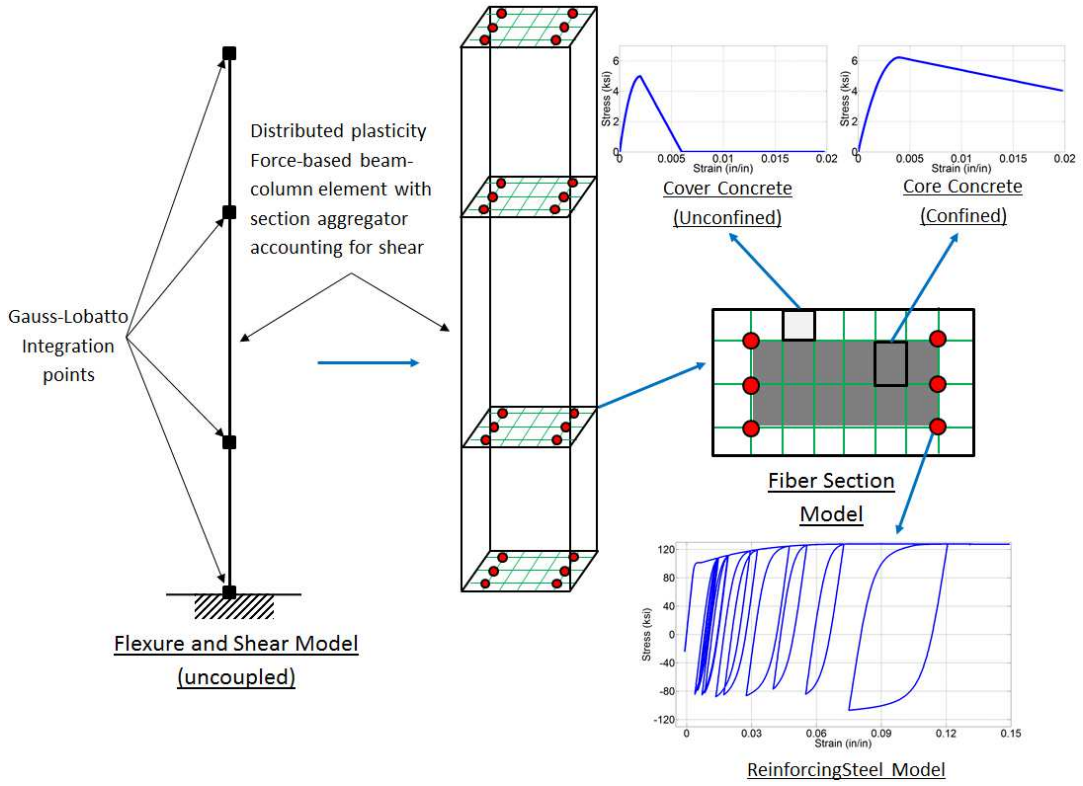

Figure 6.1.12: Force-Based Beam-Column Element with Fiber Section to Model Flexural Response of Test Beam

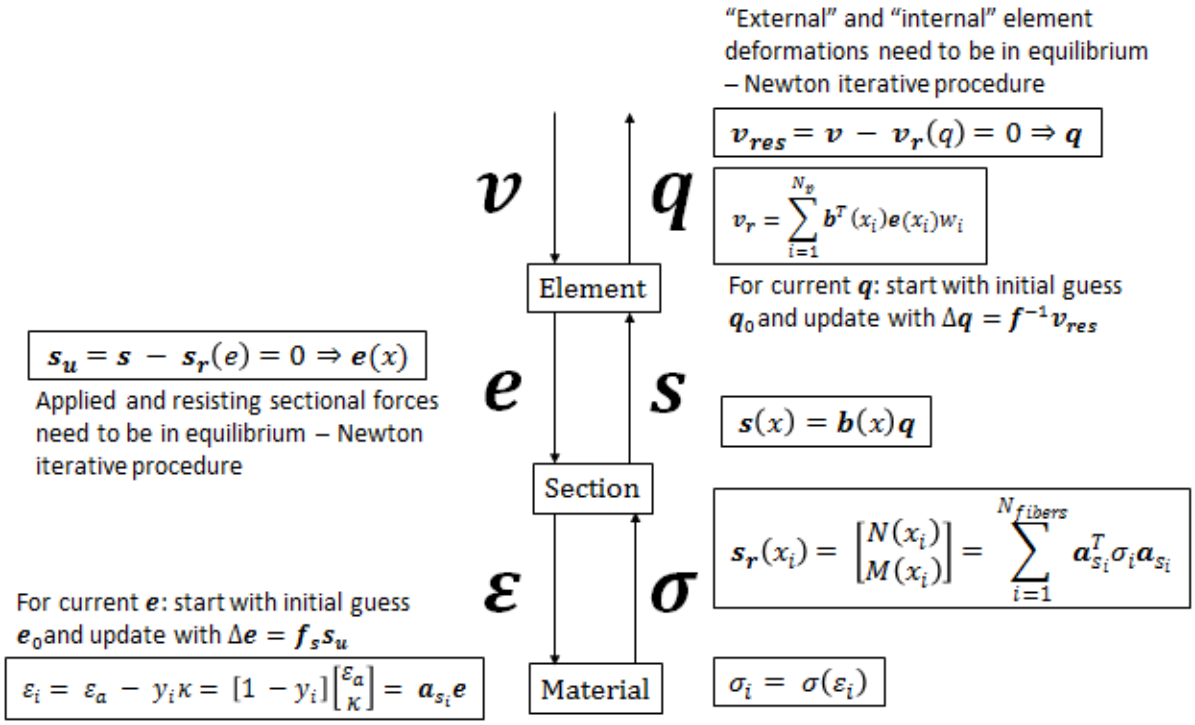

Figure 6.1.13: Iterative Procedure for Solution of Response

The measured flexural component of the displacement was derived from a test using the procedure outlined in Section 4.5 and Appendix A. This displacement history was then imposed on the analytical model of a beam. The lateral load vs. flexural displacement relations for both analytical model and test data of specimen SBH100, SBH60, and SBM100 are plotted in Figure 6.1.14, Figure 6.1.15, and Figure 6.1.16, respectively. In beam SBL100, there was only one instrument installed to measure slip of longitudinal bar out of anchorage block on one side of the specimen. Therefore, full hysteretic responses of flexure and slip could not be separated for this test beam.

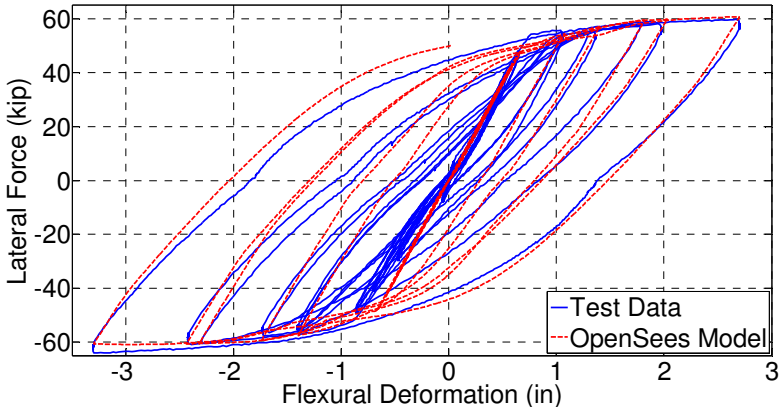

Figure 6.1.14: Flexural Hysteretic Response – SBH100

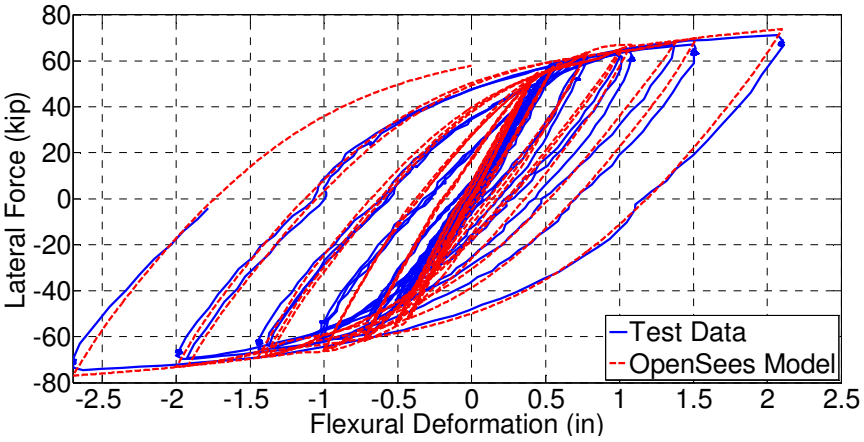

Figure 6.1.15: Flexural Hysteretic Response – SBH60

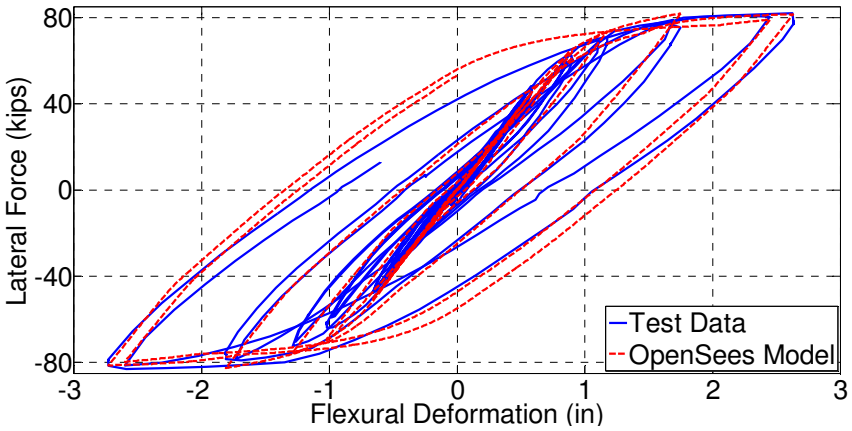

Figure 6.1.16: Flexural Hysteretic Response – SBM100

c. Shear Element – Section Aggregator

It is common in practice that linear elastic shear behavior is incorporated in the flexural element through a section aggregator to model overall response of reinforced concrete beams. In this case, flexure and shear are uncoupled within the element. A simple force-based beam-column element is again used with very large flexural stiffness to model shear behavior only for the test beams (Figure 6.1.17). Two types of shear properties are presented in this figure including linear elastic behavior typically used in design office practice and the Modified Ibarra-Medina-Krawinkler Deterioration Model with Pinched Hysteretic Response (MIMK) (Ibarra et al., 2005). Figure 6.1.18 presents the shear behavior of the two models using these two types of shear properties (specimen SBH100). Measured shear deformation was deduced from the truss system of displacement transducers as described in Section 4.5 and Appendix A.

Incorporating these two shear responses into the flexural element developed in the preceding section, the overall responses of the beam model for two cases of shear properties are computed and shown in Figure 6.1.19. Apparently, using MIMK gives better overall hysteretic response as it results in more accurate post-yield strength and unloading behavior compared to the elastic shear model. However, neither yields accurate initial lateral stiffness of the beam.

Similarly, shear response of other test specimens SBL100, SBH60, and SBM100 is also modeled and plotted in Figure 6.1.20, Figure 6.1.21, and Figure 6.1.22, respectively. Table 6.1.2 displays the value of parameters used in MIMK material model and their description can be found on OpenSees website.

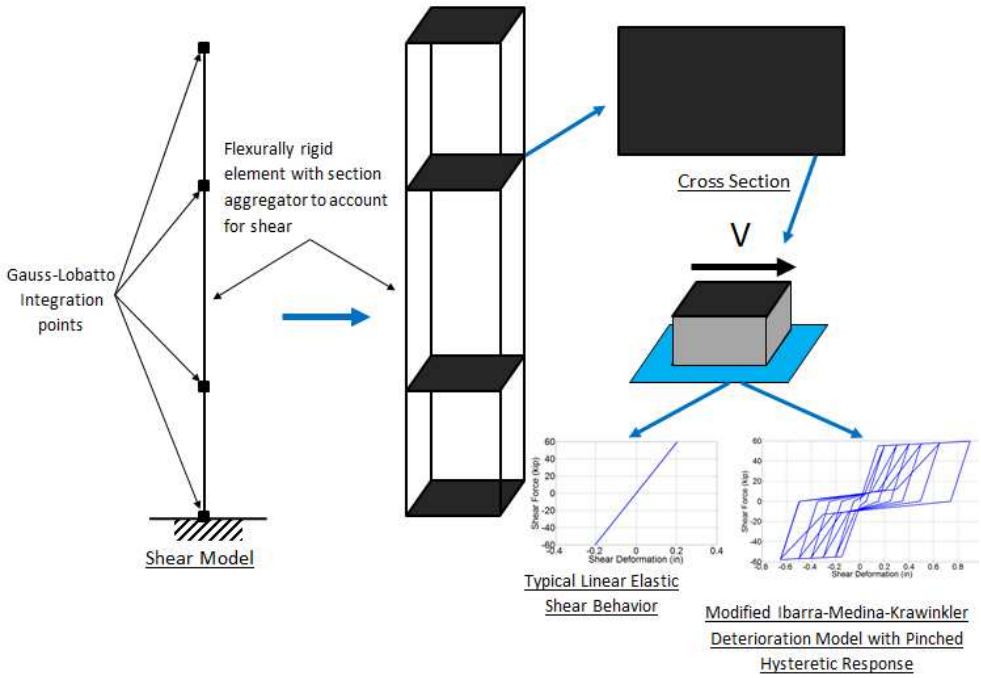

Figure 6.1.17: Shear Model

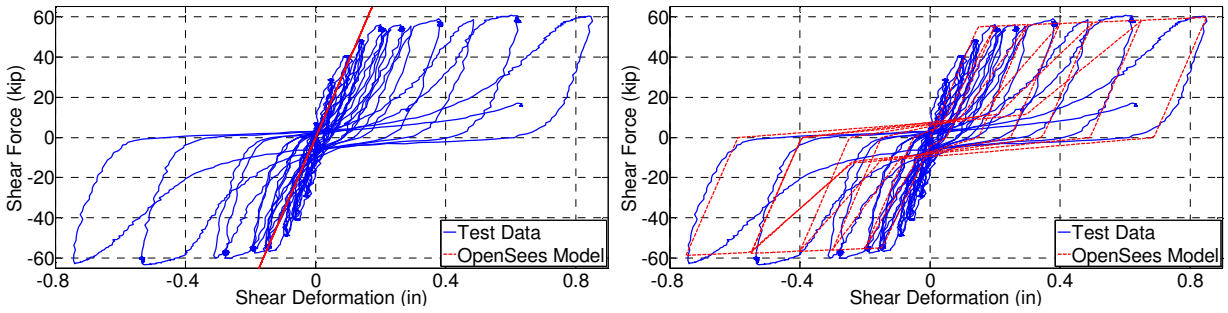

Figure 6.1.18: Shear Behavior – Left: Linear Elastic – Right: Ibarra-Medina-Krawinkler Model

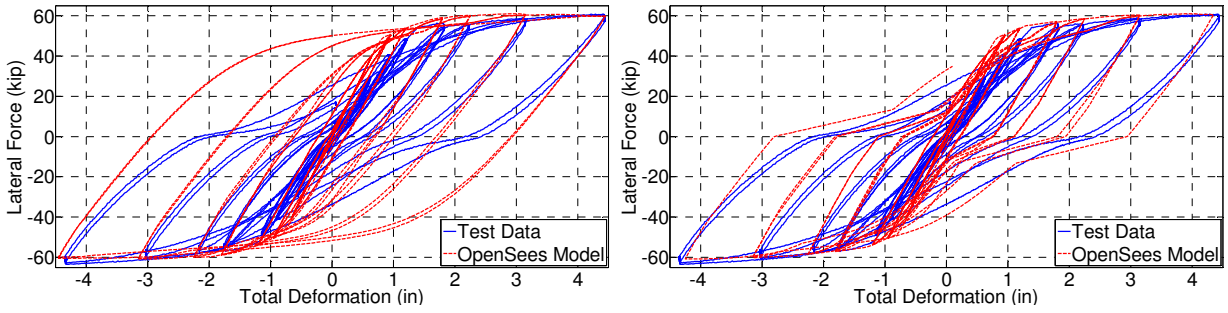

Figure 6.1.19: Overall Response with Flexure and Shear Models Combined – Left: Linear Elastic – Right: Ibarra-Medina-Krawinkler Model

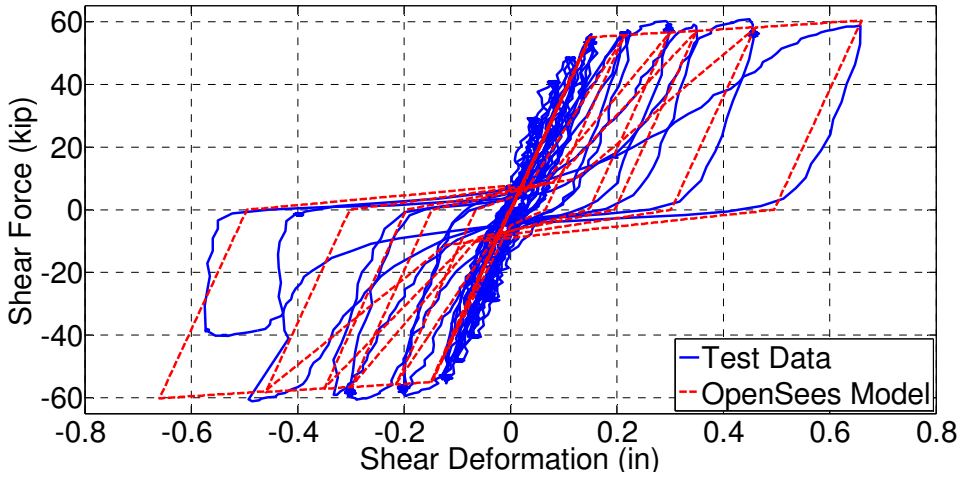

Figure 6.1.20: Shear Behavior – SBL100

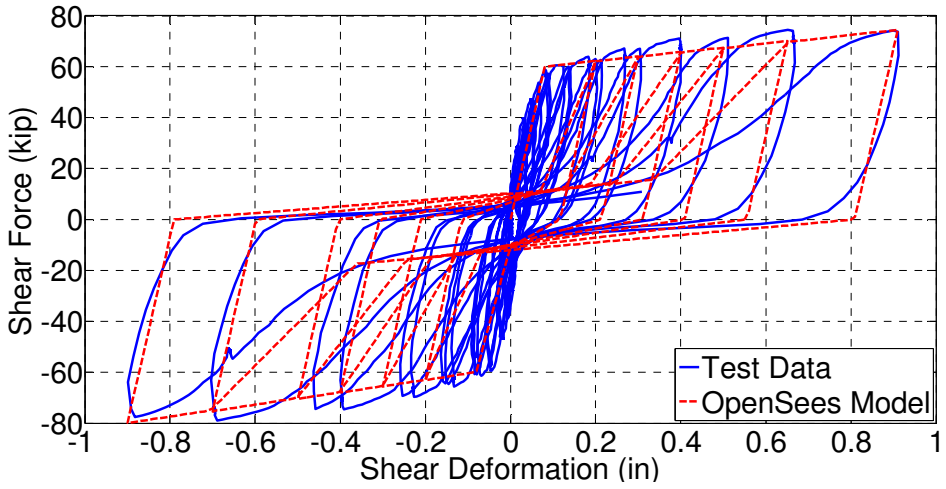

Figure 6.1.21: Shear Behavior – SBH60

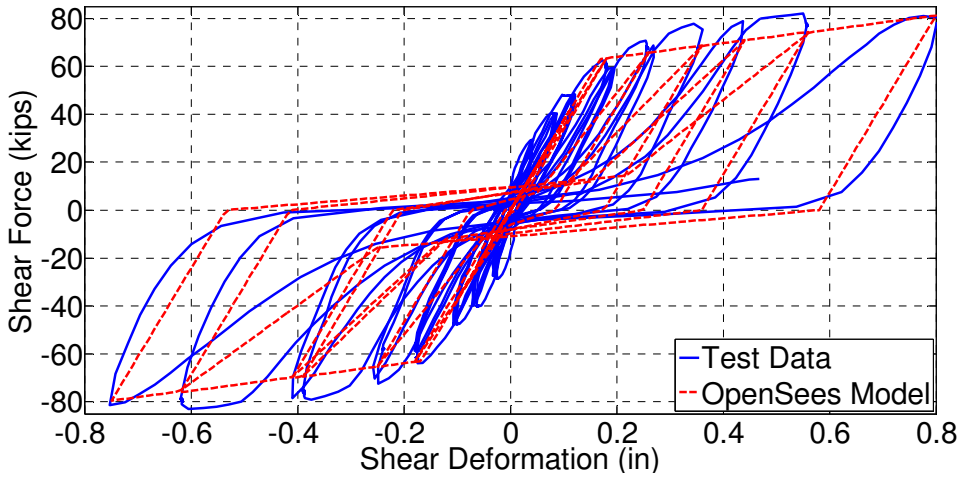

Figure 6.1.22: Shear Behavior – SBM100

Table 6.1.2: Parameters Used in ModIMKPinching Material for Shear Response Modeling

Parameters	SBH60	SBH100	SBL100	SBM100
$K0 (kips/in.)	70000	35000	35000	35000
$as_Plus	0.03	0.03	0.03	0.08
$as_Neg	0.03	0.03	0.03	0.08
$My_Plus (kips)	60	55	55	63
$My_Neg (kips)	-60	-55	-55	-63
$FprPos	0.3	0.3	0.3	0.3
$FprNeg	0.3	0.3	0.3	0.3
$A_Pinch	0.6	0.6	0.6	0.6
$Lamda_S, $Lamda_C, $Lamda_A, $Lamda_K	0, 0, 0, 0	0, 0, 0, 0	0, 0, 0, 0	0, 0, 0, 0
$c_S, $c_C, $c_A, $c_K	1, 1, 1, 1	1, 1, 1, 1	1, 1, 1, 1	1, 1, 1, 1
$theta_p_Plus, $theta_p_Neg	1, 1	1, 1	1, 1	1, 1
$theta_pc_Plus, $theta_pc_Neg	1, 1	1, 1	1, 1	1, 1
$Res_Pos, $Res_Neg	1, 1	1, 1	1, 1	1, 1
$theta_u_Plus, $theta_u_Neg	1, 1	1, 1	1, 1	1, 1
$D_Plus, $D_Neg	1, 1	1, 1	1, 1	1, 1

d. Slip Element – Zero-Length Section Element

Slip deformation was due to rigid-body rotation of the beam relative to the foundation block because of slip of the longitudinal reinforcement on the tension side of the beam under applied bending moment (Figure 6.1.23). It was computed as follows

$$\delta_s = \theta_{slip} L$$

$$\theta_{slip} = \frac{s_a}{d - c}$$

$$s_a = s_{a_e} + s_{a_{in}} + s_{a_h}$$

where s_{a_e} = elastic slip deformation of straight part of longitudinal bar

$s_{a_{in}}$ = inelastic slip deformation of straight part of longitudinal bar

s_{a_h} = slip deformation of the hook of longitudinal bar

Bond stress between concrete and steel bars provides resistance for the bars against flexural tensile force due to bending of the beam. Thus, it helps prevent the bars from pull-out of anchorage block and results in axial strain gradient along the bars. Integrating the axial strain over the anchored bar length gives the amount of slippage of the bar out of foundation.

Mathematically, the slippage phenomenon can be treated as a one-dimensional model (Figure 6.1.23) and the governing differential equation expressing equilibrium along an infinitesimal segment of steel bar is as follow:

$$\frac{d\sigma}{dx} - \alpha u(x) = 0$$

where $u(x)$ = bond stress over anchored length of the bar

$$\alpha = \frac{\pi d_b}{\mu d_b^2/4} = \frac{4}{d_b} = \frac{bar\ cross\ sectional\ circumference}{bar\ cross\ sectional\ area}$$

d_b = bar diameter

Solving above differential equation for stress $\sigma(x)$ along the anchored length of the bar for a given bond stress $u(x)$, the strain $\varepsilon(x)$ can be obtained through the steel material constitutive relationship. The amount of slippage is then computed by:

$$s_a = \int_0^{L_a} \varepsilon(x)dx$$

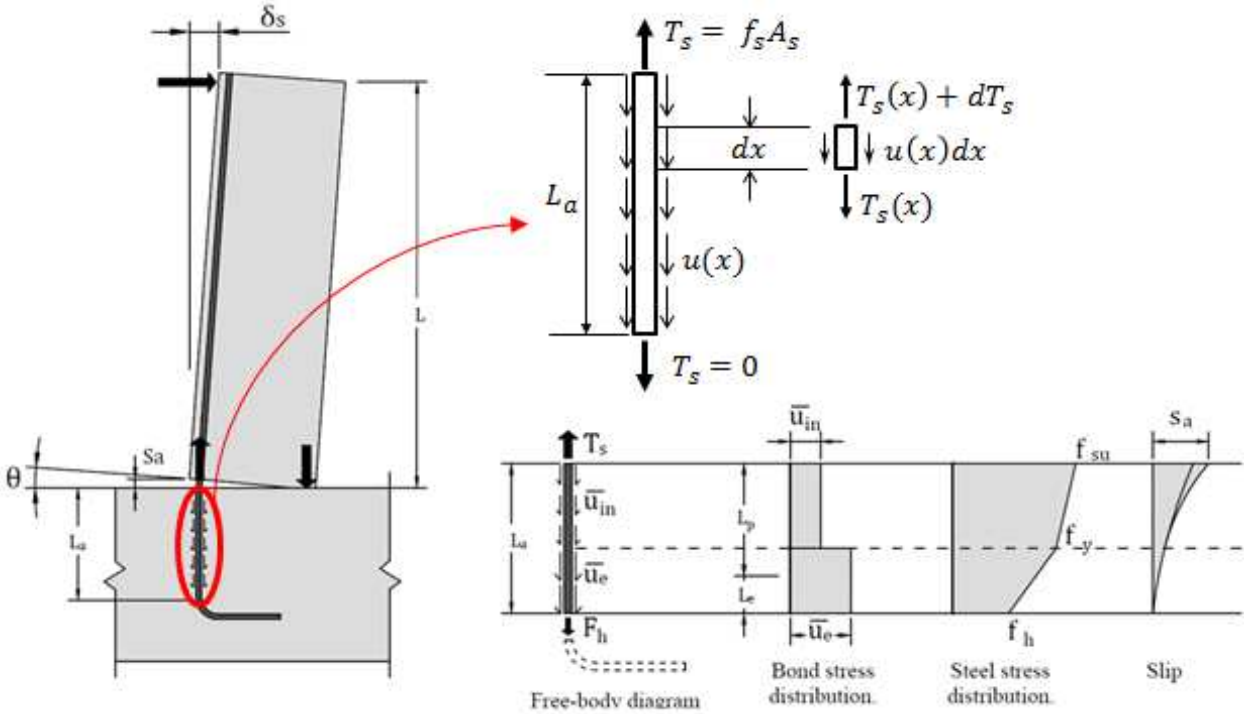

Figure 6.1.23: Bond-Slip Model for Straight Part of Bar Anchorage

Many researchers have carried out experimental study to develop bond-slip models. In such studies, the slip and bar stress (or strain) were measured by instruments and bond stress was then back-calculated. The bond stress is recommended to be $12\sqrt{f_c'}(psi)$ for the portion of the bar remaining elastic and $6\sqrt{f_c'}(psi)$ for the portion of bar being stressed into inelastic range (Lehman and Moehle, 2000). This bond stress model has been developed based on tests of conventional Grade 60 steel bars. No recommendations are currently available for Grade 100 reinforcement.

One approach for modeling bar slip from the anchorage is to introduce a zero-length linear elastic rotational spring at the base of the beam element. An improved model to estimate hysteretic response of bar slip involves constructing a fiber section and assigning its properties to the zero-length section element (Figure 6.1.27). The fiber section has cover and core concrete properties similar to those described in the fiber section of the flexural element. The hysteretic model (Bond_SP01) by Zhao and Sritharan (2007) is adopted to describe the cyclic response of the steel fiber in the fiber section (Figure 6.1.24 and Figure 6.1.25). In this model, stress and slip at yielding and ultimate were taken from test data. A zero-length section element, which actually has unit length implicitly, is used for section analysis to calculate the moment-rotation response.

Further refinement of the bond-slip model was introduced as it was recognized that the model lacked the ability to adjust the center of fixed-end rotation based on the changing neutral axis depth in the adjacent flexural element. A modification of the fiber-section spring that results in the fixed-end rotations caused by bar-slip being centered at the location of neutral axis of the flexural element was proposed (Ghannoum and Moehle, 2012) and illustrated in Figure 6.1.26. This can be achieved by using the same fiber discretization of steel and concrete in the zero-length section as in the frame section, and scaling material strain in this bar-slip element by the same factor r_y:

$$r_y = \frac{E_s}{E_{slip}} = \frac{S_y}{\varepsilon_y} \qquad E_{slip} = \frac{f_y}{S_y}$$

where: E_s = Young's modulus of steel (ksi)
f_y = yield stress of steel (ksi)
ε_y = strain at yield of steel (in/in)
S_y = amount of slip of steel out of anchorage at yield stress (in)

Based on test data, the behavior of the rotational spring is calibrated to have similar stiffness as the slip response of the test beams for the elastic rotational spring and as well as reasonably close hysteretic response for the fiber section rotational spring. The behavior of slip from models and test data of specimen SBH100 are presented in Figure 6.1.28.

Slip deformation responses for the other three beams were also modeled similarly and illustrated in Figure 6.1.29, Figure 6.1.32, and Figure 6.1.33. Table 6.1.3 presents the value of

parameters used in Bond_SP01 uniaxial material. It should be pointed out that there was only one instrument installed to measure slip of longitudinal reinforcement on one side of specimen SBL100. The full hysteretic response of slip deformation (Figure 6.1.29) was computed by assuming that the amount of slip on the other side of this beam was the same as on the side with the instrument. In Figure 6.1.30, the amount of slip on one side of beam SBL100 measured during the test was compared against that calculated by OpenSees model. In Figure 6.1.31, OpenSees model provides acceptable correlation of combination of flexure and slip responses with measured test data of beam SBL100.

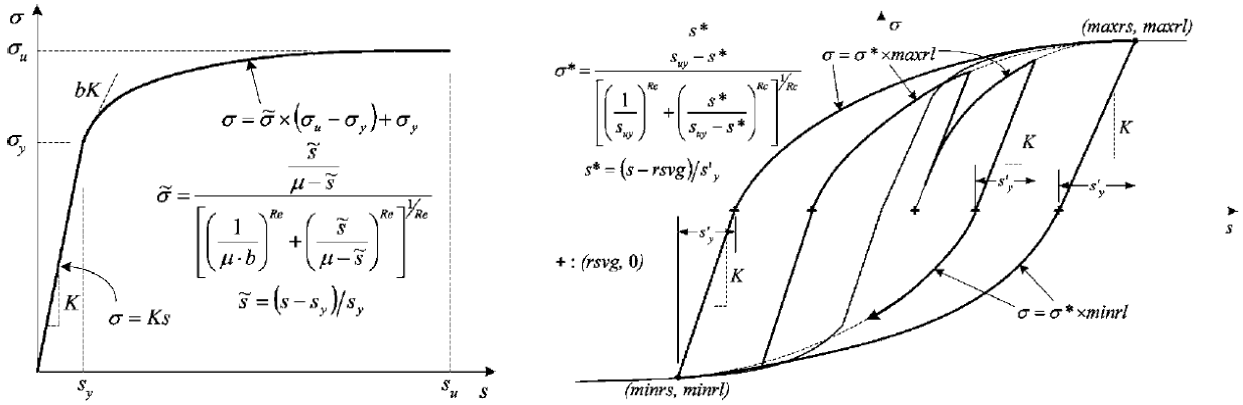

Figure 6.1.24: *Bond_SP1* Hysteretic Model Proposed by Zhao and Shritharan (2007)

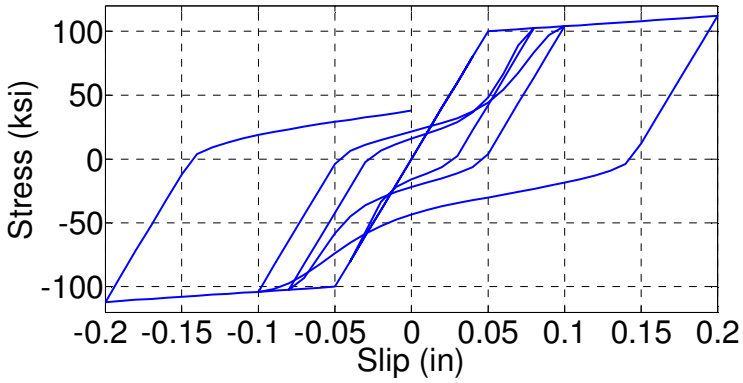

Figure 6.1.25: Cyclic Behavior of Steel in Fiber Section of Zero Length Section Element

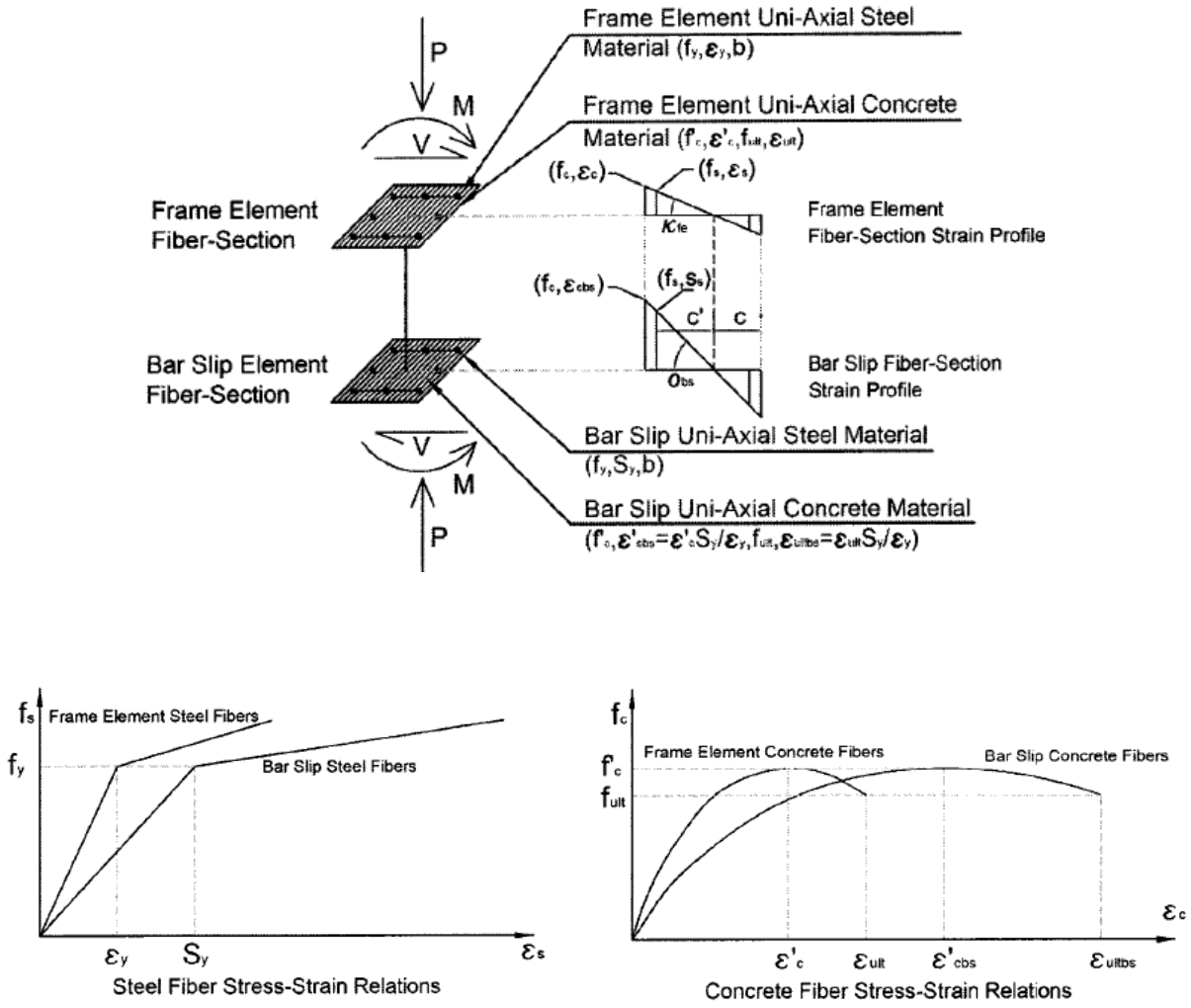

Figure 6.1.26: Bar-Slip Section Equilibrium, Strain Profiles, and Materials (Ghannoum and Moehle, 2012)

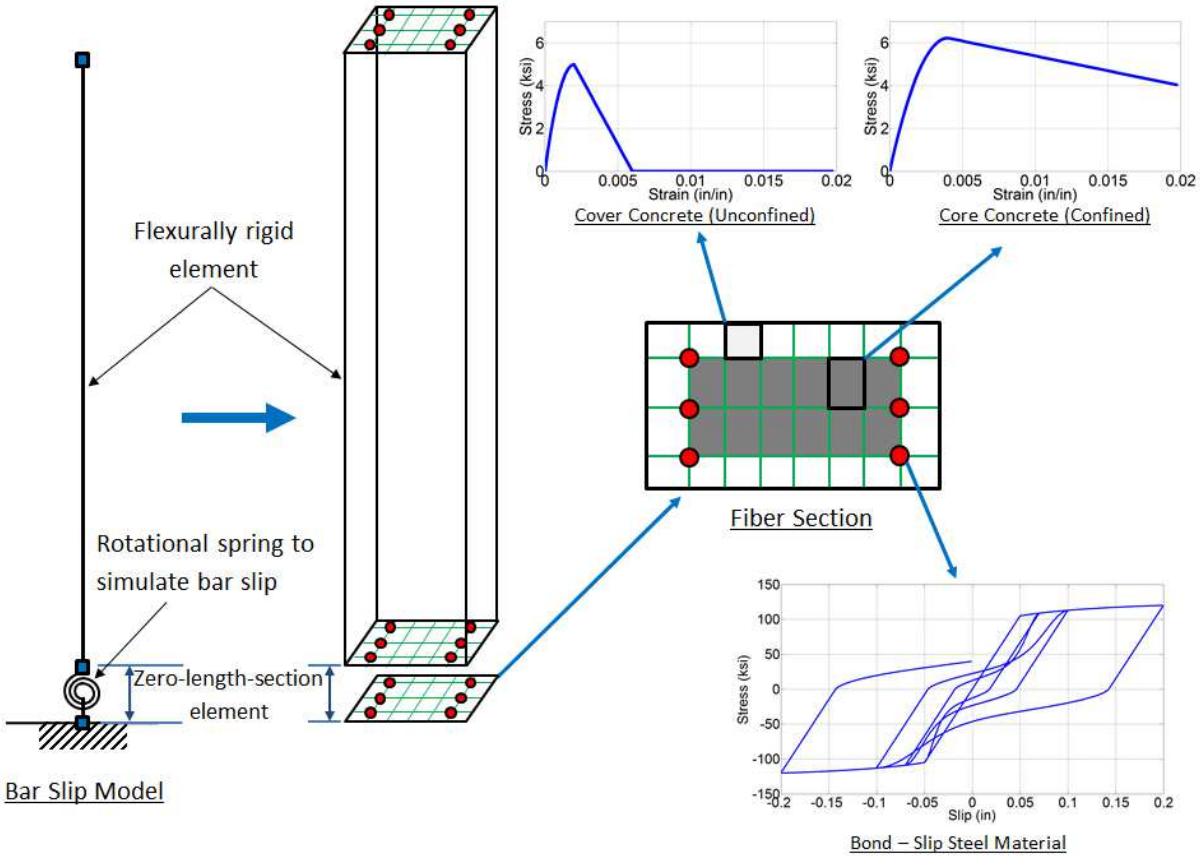

Figure 6.1.27: Bar Slip Model

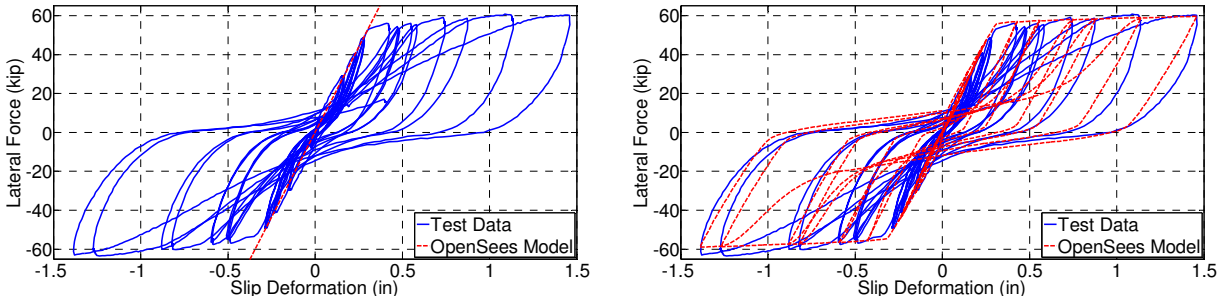

Figure 6.1.28: Slip Behavior – SBH100 – Left: Linear Elastic – Right: Fiber Section

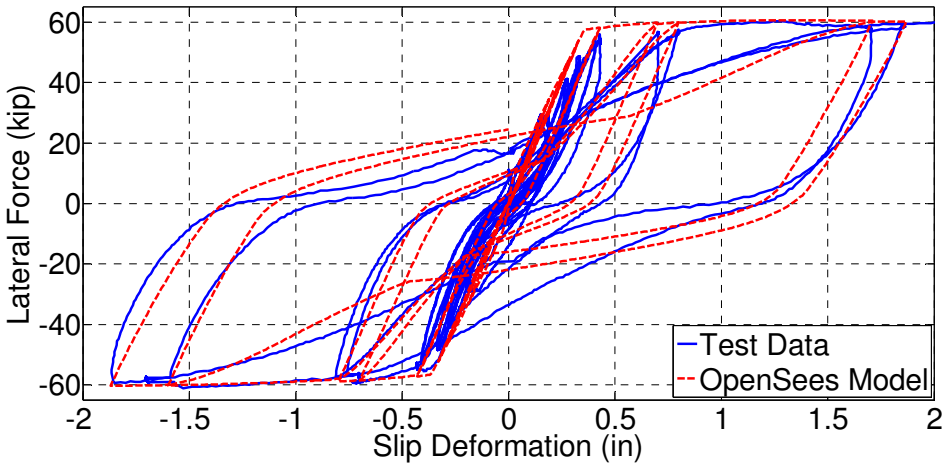

Figure 6.1.29: Slip behavior – SBL100

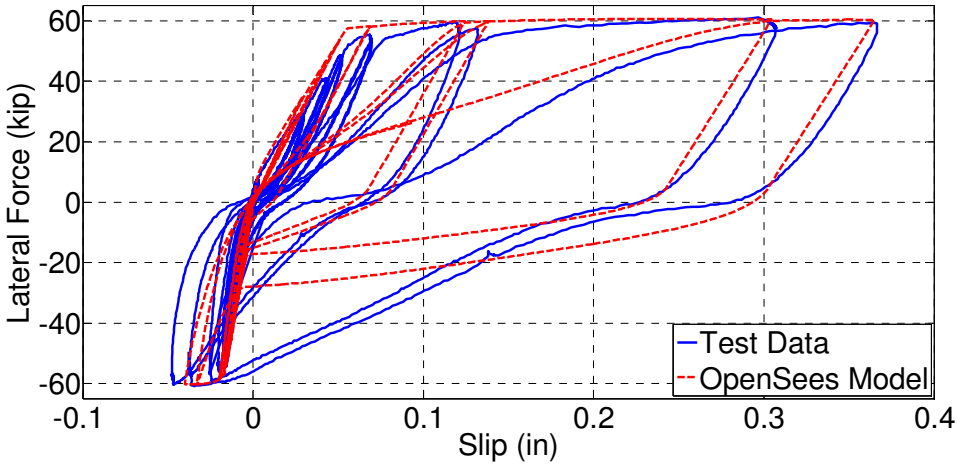

Figure 6.1.30: Amount of Slip – SBL100

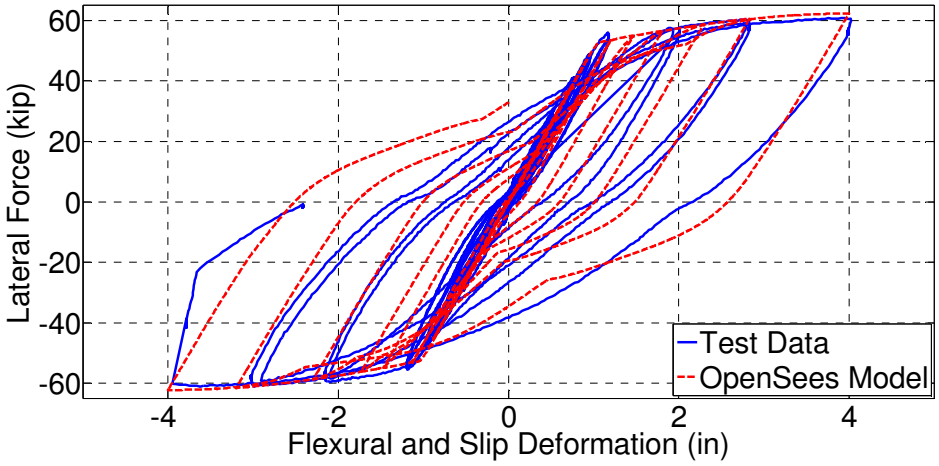

Figure 6.1.31: Flexure and Slip Deformation – SBL100

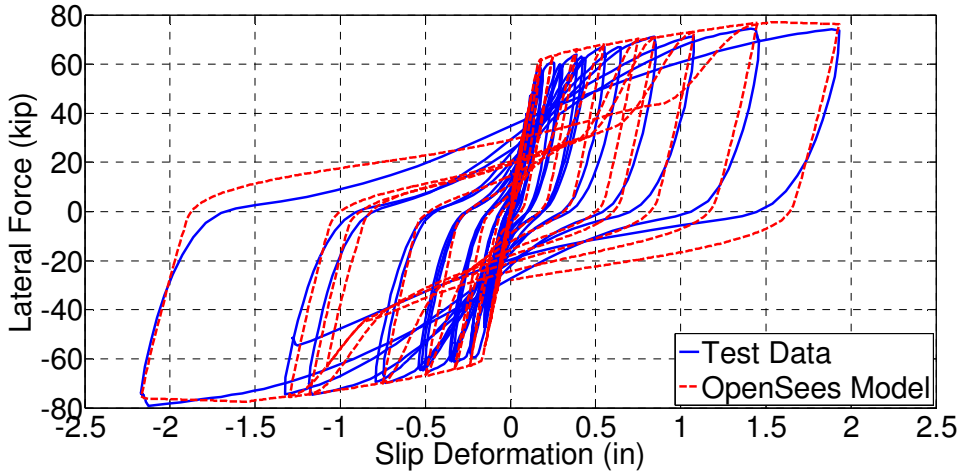

Figure 6.1.32: Slip behavior – SBH60

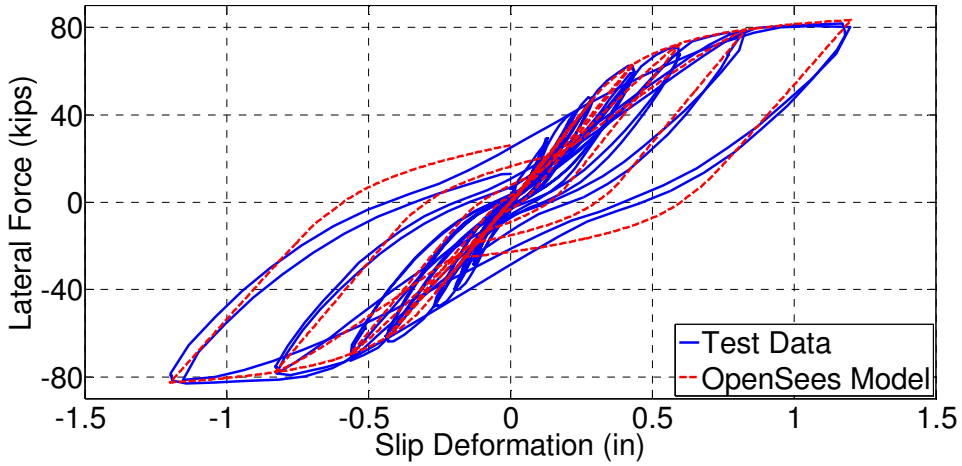

Figure 6.1.33: Slip behavior – SBM100

Table 6.1.3: Parameters Used in Bond_SP01 Material to Model Slip of Reinforcement

Parameter	Description	SBH60	SBH100	SBL100	SBM100
$Fy (ksi)	Yield strength of reinforcing steel	64.5	101.5	106.0	100.0
$Sy (in.)	Slip under yield stress	0.025	0.045	0.055	0.055
$Fu (ksi)	Ultimate strength of reinforcing steel	95.5	127.6	123.9	165.0
$Su (in.)	Slip under ultimate strength	0.35	0.25	0.35	0.30
$b	Initial hardening ratio	0.1	0.15	0.15	0.7
$R	Pinching factor	0.4	0.4	0.4	0.4

e. Overall Model Response

Three versions of the analytical model were developed and subjected to the displacement history measured during the test of specimen SBH100. The comparison of the calculated and measured load-displacement relations provides information on the importance of including various components in the overall analytical model (Figure 6.1.34).

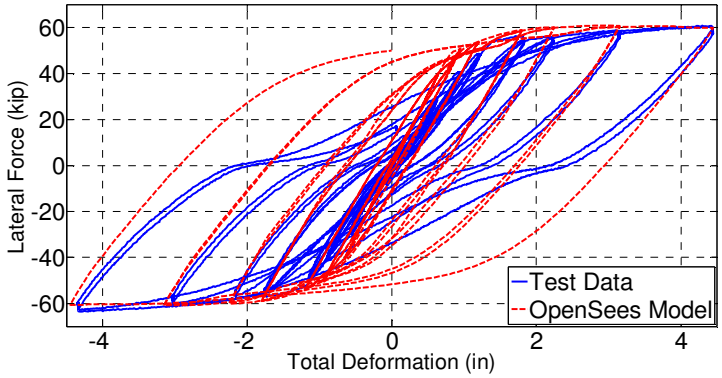

(a)

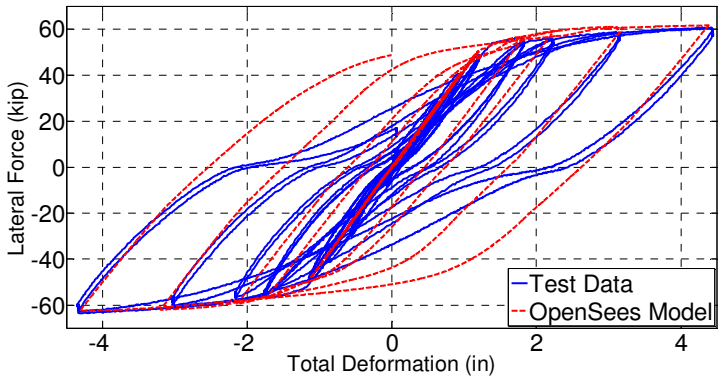

(b)

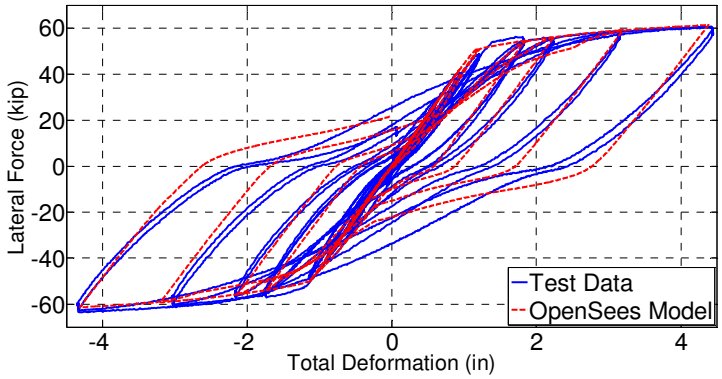

(c)

Figure 6.1.34: Overall Response of OpenSees Models. (a): Inelastic Flexure and Elastic Shear; (b): Inelastic Flexure, Elastic Shear and Slip; (c): Inelastic Flexure, Shear by IMK Model, and Slip by Fiber Section with Bond-Slip Steel Model by Zhao and Sritharan

Figure 6.1.34a presents results for an analytical model that considers inelastic flexure and elastic shear. Although the strength (which is limited by flexural strength) is well modeled, the initial stiffness is overestimated and the shapes of the load-displacement loops are wider than those of the test beam, which indicates excessive energy is being dissipated by the analytical model.

Figure 6.1.34b presents results for an analytical model that considers inelastic flexure, elastic shear, and elastic slip. By including slip, the analytical model produces a better match to the measured stiffness. However, the shape of the load-displacement relation is still too wide.

Figure 6.1.34c presents results for an analytical model that considers inelastic flexure, shear, and slip, as described previously. This model produces the best hysteretic response as it matches the initial stiffness, inelastic lateral strength, and load reversal behavior of the test beam reasonably well throughout the entire deformation history.

f. All Beam Models

Modeling elements described in preceding sections are implemented and calibrated for all other test beams. Overall model responses are plotted and compared against those measured during all beam tests in Figure 6.1.35 to Figure 6.1.38.

Beam elongations were also simulated in OpenSees models and compared against those measured during beam tests (Figure 6.1.39 and Figure 6.1.40). Analytical beam models produce reasonable agreement with test data.

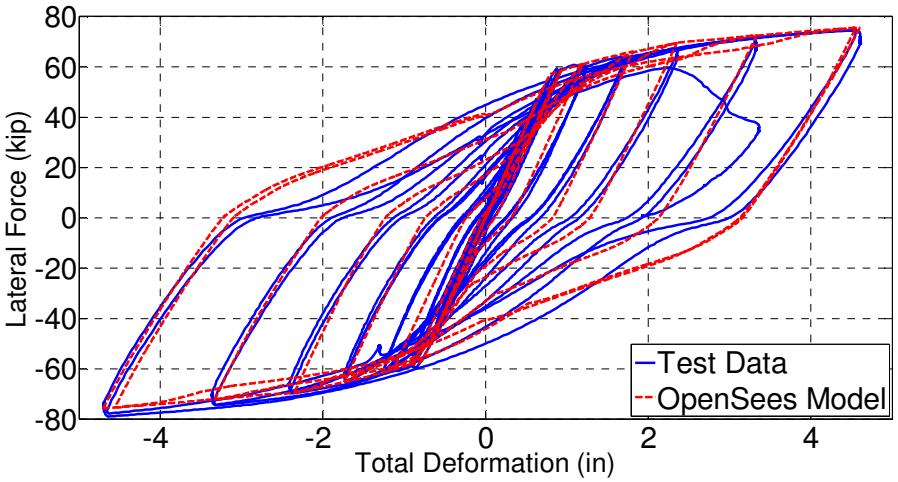

Figure 6.1.35: Overall Response of SBH60

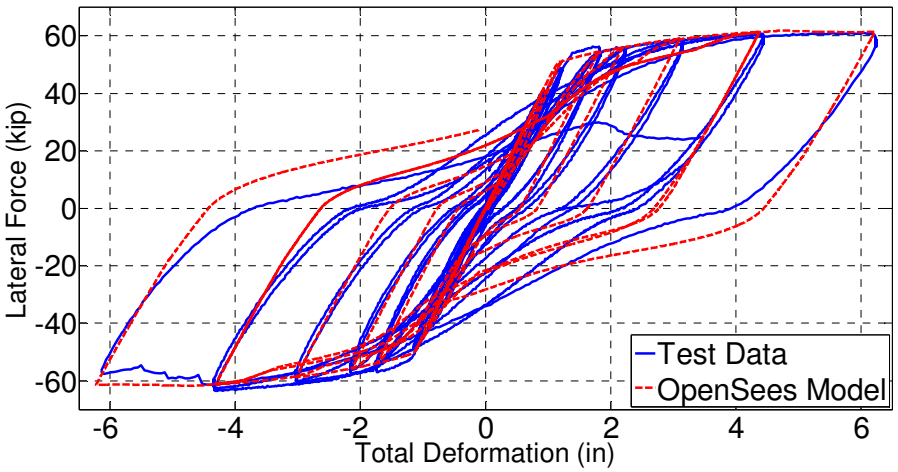

Figure 6.1.36: Overall Response of SBH100

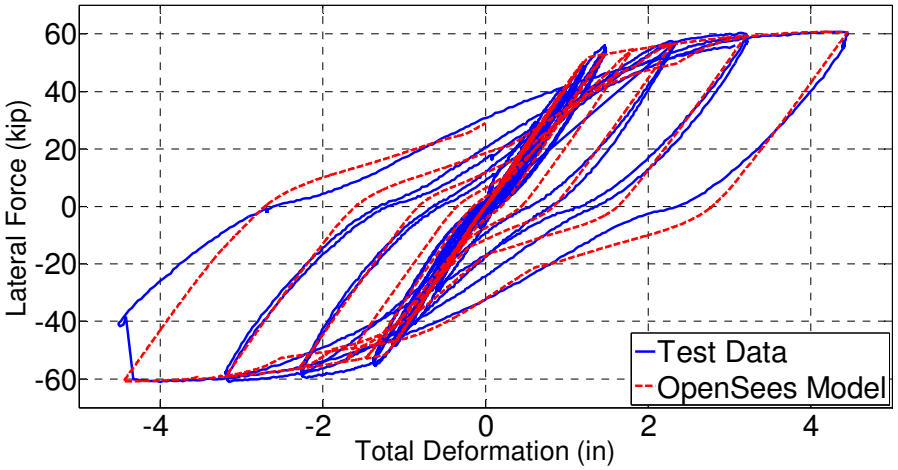

Figure 6.1.37: Overall Response of SBL100

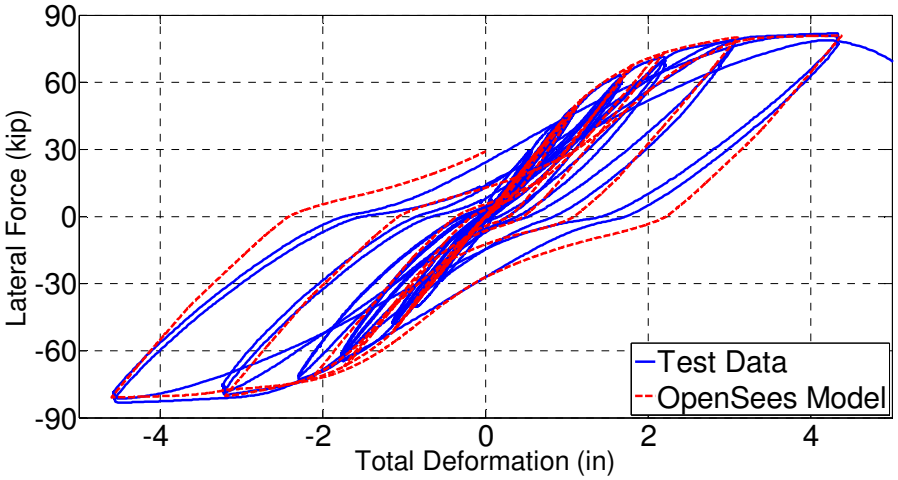

Figure 6.1.38: Overall Response of SBM100

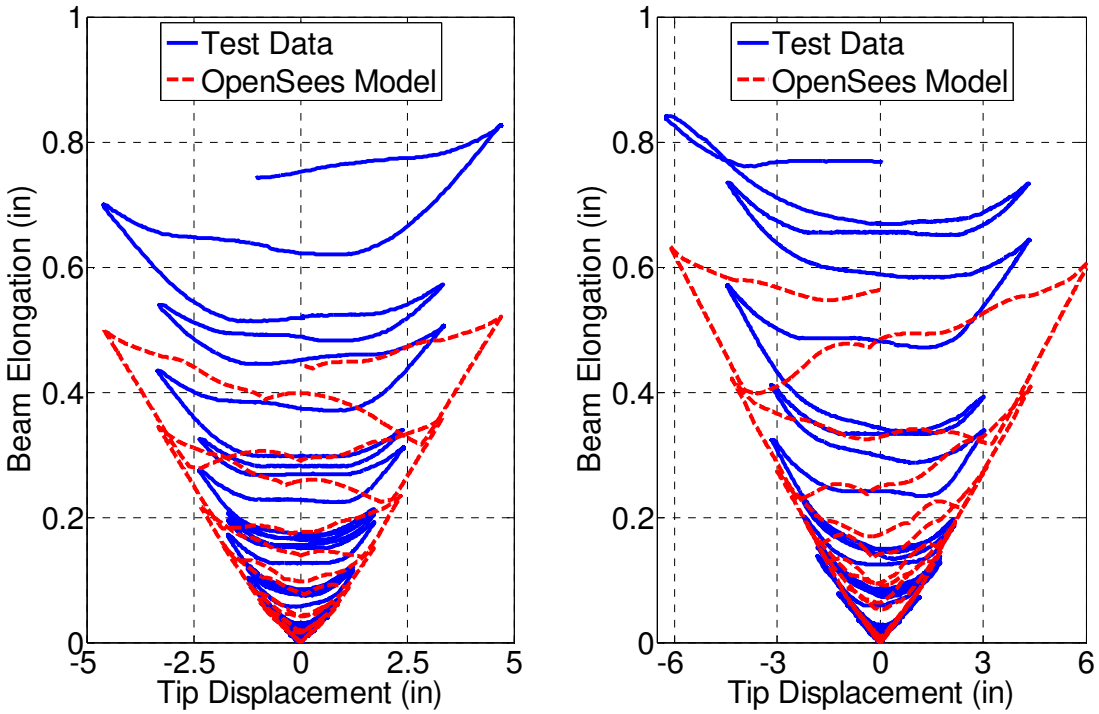

Figure 6.1.39: Beam Elongation Response - Left: SBH60 - Right: SBH100

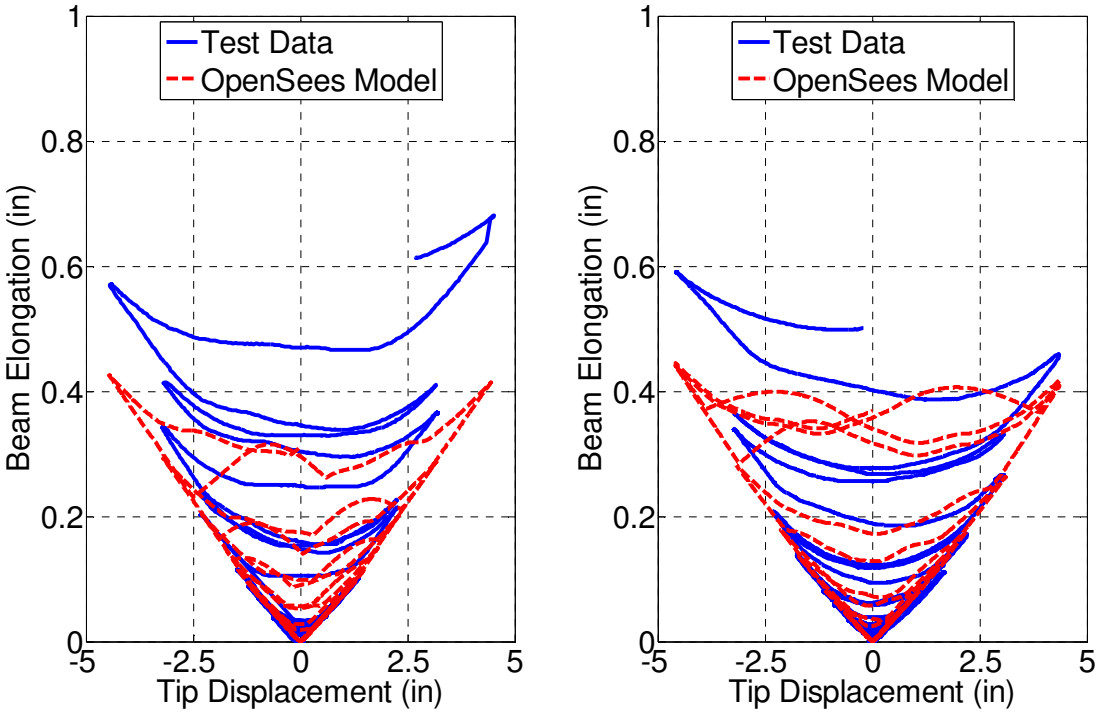

Figure 6.1.40: Beam Elongation Response - Left: SBL100 - Right: SBM100

Cyclic strain responses of the longitudinal reinforcement at the base of test beams were also simulated in the analytical models and compared with those measured during the tests in Figure 6.1.41 and Figure 6.1.42. Apparently, longitudinal bar strain at zero lateral drift ratio, which is associated with beam elongation, computed by OpenSees model had comparable magnitude compared to test data. Therefore, beam elongation was reasonably modeled as observed in Figure 6.1.39 and Figure 6.1.40. This is important as axial elongation of reinforced concrete beams has been recognized to impose additional shear forces and deformation demands onto exterior columns in frame buildings (Fenwick et al., 1996; Kabeyasawa et al., 2000; Kim et al., 2004; Visnjic et al., 2012).

In addition, computed maximum strain agrees relatively well with that measured in tests for beams SBH60, SBH100, and SBL100. The model overestimates peak strain for beam SBM100. The amount of peak strains obtained for each cycle of loading is essential in evaluating low-cycle fatigue performance of longitudinal reinforcement in reinforced concrete beams and columns in frame buildings. In all beams, the cyclic response of strain is not well modeled. In the laboratory tests, longitudinal bars under flexural compression due to reversed cyclic loading continued to show tensile strain, indicating that the cracks did not close. This also contributes to beam elongation. This tensile strain under compression is consistently underestimated by the analytical models. The change in strain of longitudinal bars loaded in tension to compression is associated to the strain amplitude for each cycle of loading. Thus, larger strain amplitude produced by the OpenSees model is expected to provide conservative low-cycle fatigue evaluation of the longitudinal bars.

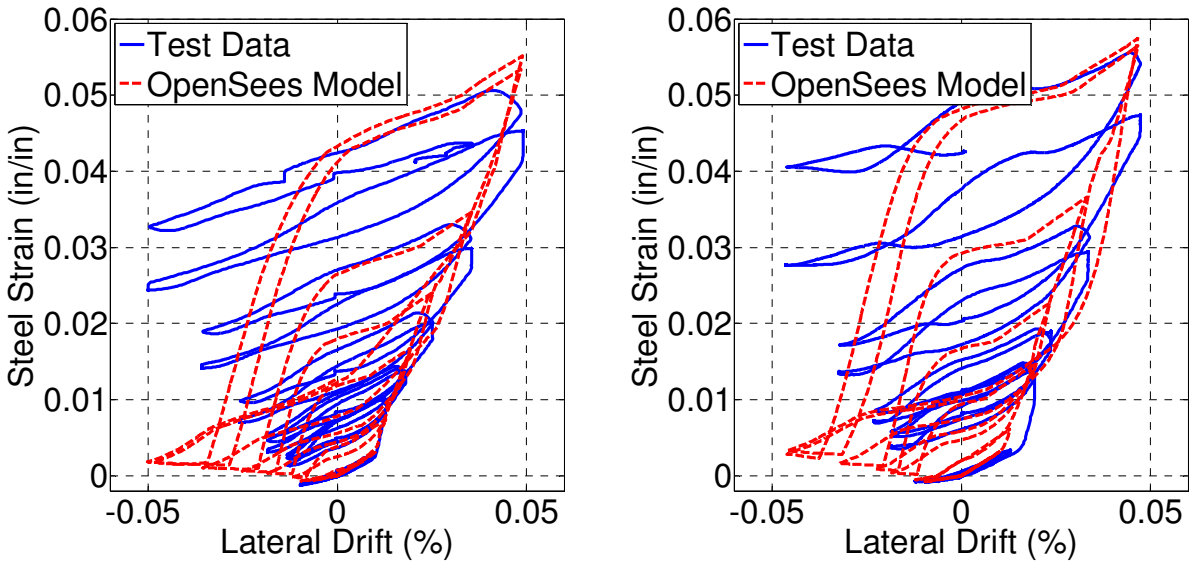

Figure 6.1.41: Cyclic Steel Strain vs. Lateral Drift Relations - Left: SBH60 - Right: SBH100

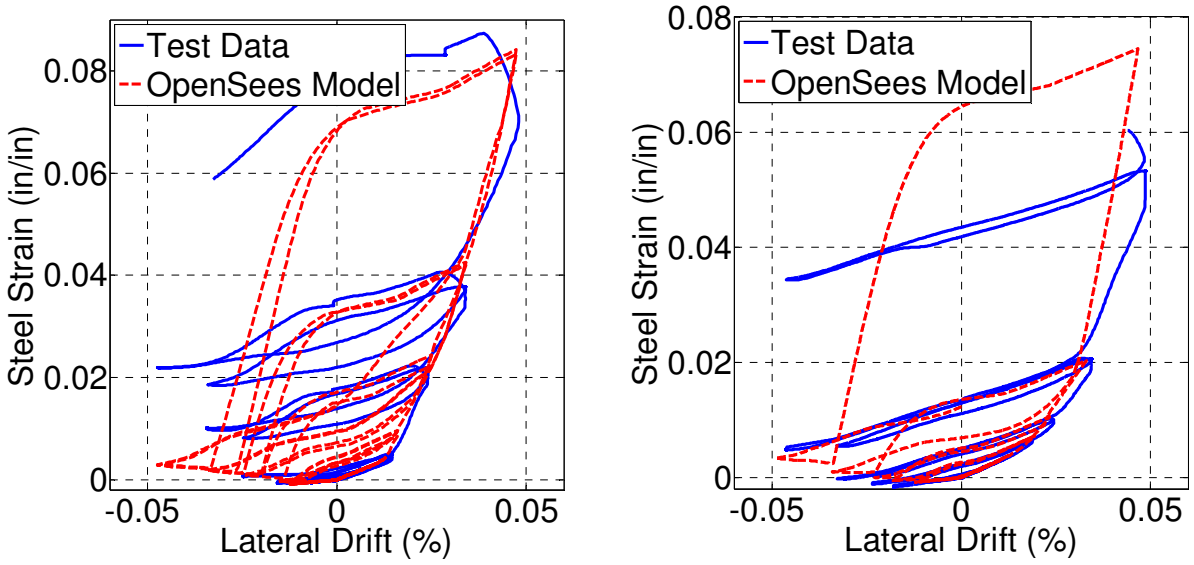

Figure 6.1.42: Cyclic Steel Strain vs. Lateral Drift Relations - Left: SBL100 - Right: SBM100

6.2. COLUMNS

Opensees models were also developed to simulate the response of columns that were tested in a companion laboratory test program at the University of Texas, Austin. The test data for those tests indicate that the contribution of shear deformation to total deformation was very small (Sokoli et al., 2017). This is thought to be due to the effect of axial load applied on the columns during the tests, resulting in fewer cracks and ultimately less deformation caused by shear. Therefore, the analytical model of the columns does not have a section aggregator to model shear deformation. The overall model includes only force-based beam-column and zero-length section elements to model flexure and slippage of longitudinal bars, respectively. The amount of slip is scaled linearly proportionally from the measured slip in the beam tests with the same grade of reinforcement by the ratio $d_b/\sqrt{f_c'}$ of the columns divided by that of the beams, where d_b (inch) is the longitudinal bar diameter and f_c'(psi) is the concrete compressive strength, and is listed in Table 6.2.1. Responses of Opensees models and column test data are presented in Figure 6.2.1 through Figure 6.2.4.

Table 6.2.1: Slip Parameters in Column Models

Parameter	Description	CH60	CH100	CL100	CM100
$Fy (ksi)	Yield strength of reinforcing steel	64.4	100.0	106.4	100.0
$Sy (in.)	Slip under yield stress	0.018	0.034	0.041	0.041
$Fu (ksi)	Ultimate strength of reinforcing steel	93.3	127.2	123.4	157.4
$Su (in.)	Slip under ultimate strength	0.26	0.18	0.26	0.22
$b	Initial hardening ratio	0.1	0.15	0.15	0.7
$R	Pinching factor	1.0	1.0	1.0	1.0

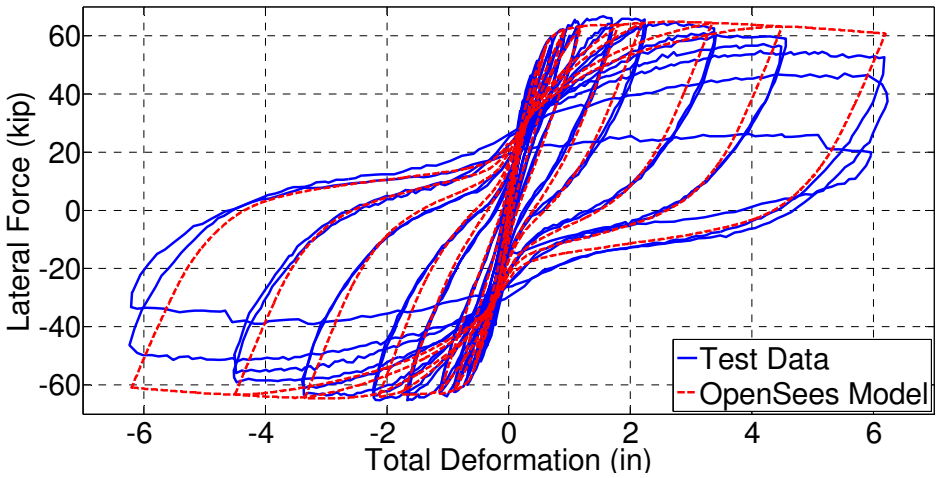

Figure 6.2.1: Overall Response of CH60

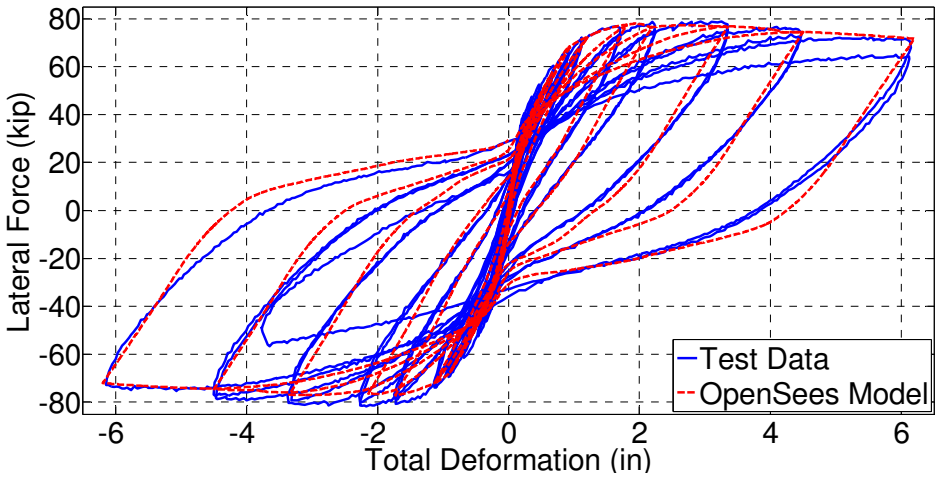

Figure 6.2.2: Overall Response of CH100

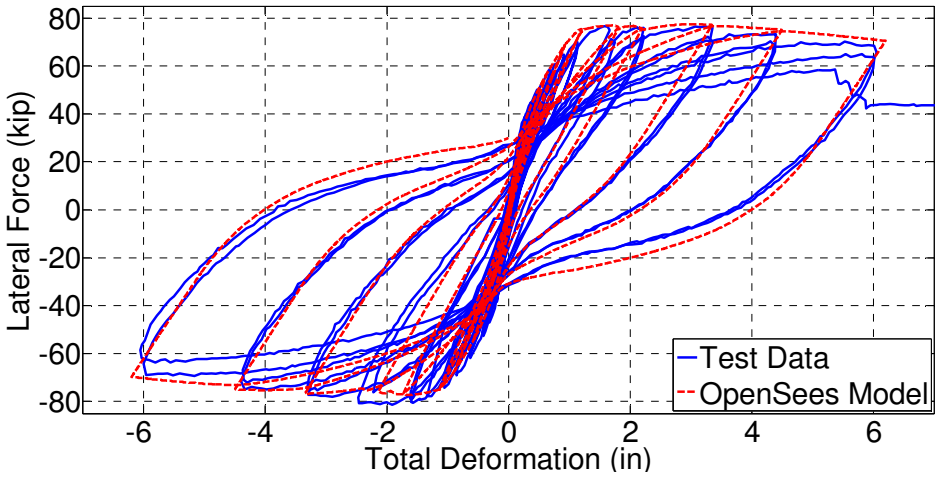

Figure 6.2.3: Overall Response of CL100

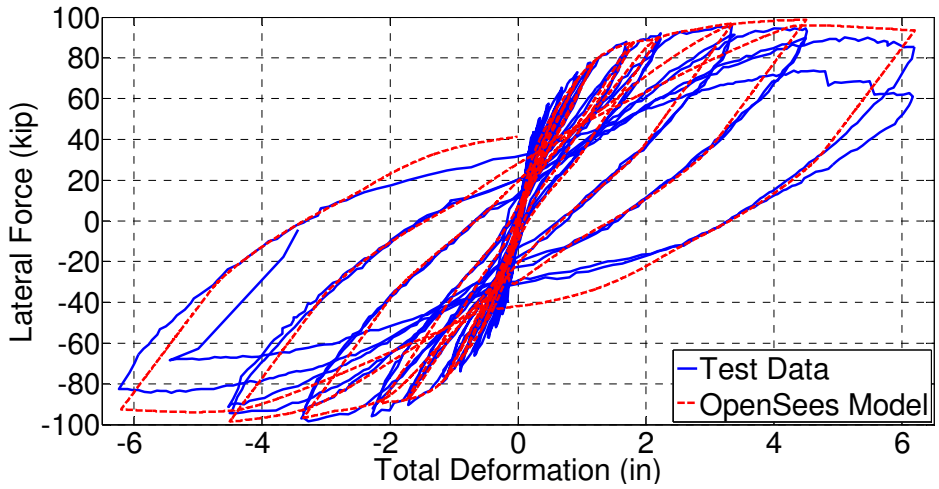

Figure 6.2.4: Overall Response of CM100

CHAPTER 7: SEISMIC PERFORMANCE OF 20-STORY REINFORCED CONCRETE SPECIAL MOMENT RESISTING FRAMES

With the representative analytical models developed for beams and columns (Chapter 6), representative frame buildings were designed and studied to explore the effects of high-strength reinforcement on seismic performance of frame buildings through nonlinear dynamic analyses.

7.1. BUILDING DESCRIPTION

Previous studies completed at UC Berkeley investigated seismic response of 20-story tall reinforced concrete office buildings with special moment resisting frames and conventional Grade 60 reinforcement (Visnjic, 2014). The same archetype building, shown in Figure 7.1.1, is re-designed with Grade 100 reinforcement based on design requirements per ASCE-7-16 and detailing requirements per ACI 318-14. As a result, there are total of four building models being studied including one building with conventional Grade 60 A706 (SBH60), one with Grade 100 having T/Y = 1.26 (SBH100), one with Grade 100 having T/Y = 1.17 (SBL100), and the last one with Grade 100 A1035 (SBM100). The naming convention of test beams is adopted for these archetype buildings.

These buildings have two reinforced concrete special moment resisting frames (SMRFs) as the seismic-force-resisting system in each of the two principal directions of the buildings. The special moment frames are located on the perimeter. They have four 21-ft long bays and twenty 12-ft tall stories to result in building height of 144 ft.

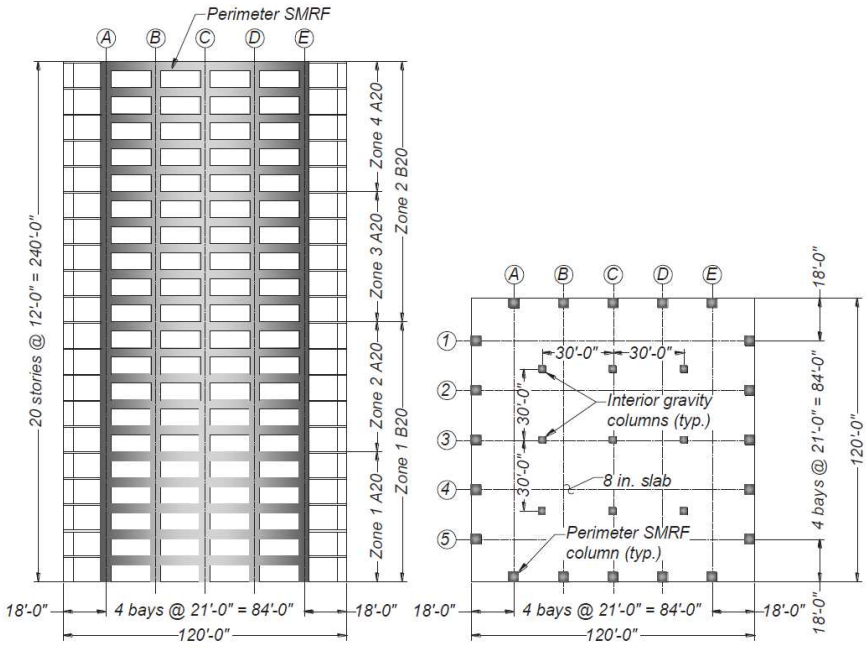

Figure 7.1.1: Elevation (Left) and Floor Plan (Right) of Archetype Buildings (Visnjic, 2014)

7.2. SEISMIC HAZARD

All four archetype buildings are hypothetically located in the financial district of downtown San Francisco, California (Figure 7.2.1). The soil condition at the selected location is categorized as stiff soil (site class D, ASCE 7). From the USGS seismic design map, the ordinates of pseudo-acceleration spectrum at short- and 1s-periods are $S_{DS} = 1.0g$ and $S_{D1} = 0.6g$, respectively, where g is gravitational acceleration, for a design earthquake level and 5% damping. For the maximum considered earthquake hazard, the corresponding spectral ordinates are $S_{MS} = 1.5g$ and $S_{M1} = 0.9g$. Based on these spectral ordinates, the design and maximum considered earthquake spectra are constructed according to ASCE 7 and plotted in Figure 7.2.2. In this figure, the RotD50 component of the design spectrum is also plotted. Determination of the RotD50 spectrum as described in ASCE 7-16 is only applicable for the site-specific case. Therefore, in this study the RotD50 spectrum is calculated by a slightly different approach. An intersecting period is found where the constant acceleration and constant velocity branches of the RotD50 spectrum intersect. The RotD50 spectrum is calculated by dividing S_{MS} by 1.1 for period less than the intersecting period and dividing the spectral ordinate S_{M1} by 1.3 times period $\left(\frac{S_{M1}}{1.3T}\right)$ otherwise.

Figure 7.2.1: Hypothetical Location of Archetype Buildings (marked with a bull's-eye)

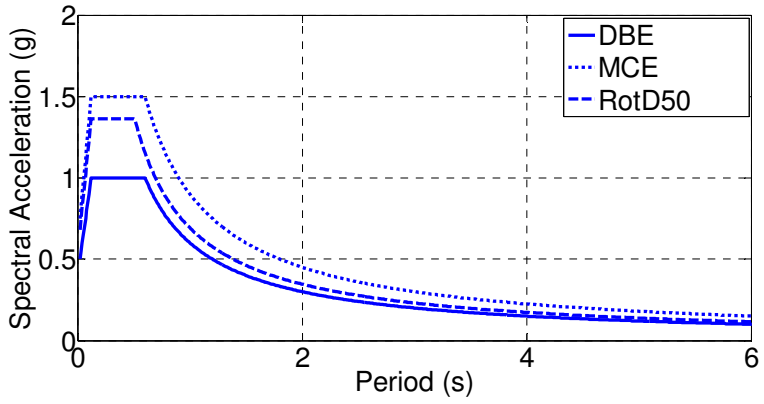

Figure 7.2.2: Pseudo-Acceleration Spectra for DE, RotD50, and MCE Hazard Level at 5% Damping

7.3. DESIGN OF BUILDINGS

The designs of four archetype buildings conform to the ASCE 7-16 and ACI 318-14 provisions. The design with conventional Grade 60 reinforcement serves as the base model. From this base design, the dimensions of all structural members are kept the same and all reinforcement is replaced with Grade 100 steel. Thus, the amount of reinforcement in all structural members is reduced appropriately to provide equivalent nominal strengths. By code-based design with linear elastic analysis, the designs of all four archetype frame buildings with normal and higher-grade steel are similar except for the amount of reinforcement. All three buildings with Grade 100 are identical in design. The reason for this design approach is that most frames are designed near the building code design drift limit and, consequently, the gross cross sections cannot be decreased without violating the drift limit.

According to ASCE 7-16, the archetype buildings have Risk Category II, Seismic Importance Factor $I_e = 1.0$, and Seismic Design Category D. The design floor live load is 60 psf. Gravity loads include self-weight of the structure and permanent non-structural components and contents.

The seismic weight of the archetype buildings includes 100% of dead load and 25% of live load. In each principal direction of the building, there are two special moment resisting frames that are symmetric over the center line of building plan. Therefore, half of the total seismic weight is assigned to each frame and each frame is assumed to resist half of the total seismic force. Note that this analysis sets aside the complication of accidental torsion.

The nominal concrete compressive strengths in design are 5.0 ksi for all beams, 8.0 ksi for all columns from the base to the 10th floor, and 7.0 ksi for all columns above the 10th floor. High-strength concrete is used in columns so as to follow the recommendation on column axial load that $P_u \leq 0.40 f_c' A_g$(LATBSDC, 2017), where A_g (in^2) is the frame element cross-sectional area and f_c'(psi) is the concrete compressive strength. During the design procedure, there are two types of reinforcement used including Grade 60 and Grade 100 with nominal yield strengths of 60 ksi and 100 ksi, respectively.

The load combinations considered in the design are the following:

1. $1.2D + 1.6L$
2. $1.2D + 0.5L \pm 1.0E + 0.2S_{DS}D$
3. $0.9D \pm 1.0E - 0.2S_{DS}D$

where:

D = dead load,
L = live load,
E = earthquake load,
S_{DS} = design spectral acceleration parameter at short periods (ASCE 7).

The design procedure follows guidance provided in a technical brief NIST GCR 16-917-40 document (Moehle and Hooper, 2016) and LATBSDC (2014). In design, the effective stiffnesses (cracked stiffnesses) used for beams and columns are $0.35E_cI_g$ and $0.5E_cI_g$, respectively, where I_g = gross section moment of inertia and $E_c = 57{,}000\sqrt{f_c'}\ (psi)$ = elastic modulus of concrete. Beam-column joints are modeled as partially rigid using the assumptions shown in Figure 7.3.1 (Birely et al., 2012). Columns at the base are fixed to the foundation at the ground level in the model as permitted by ASCE 7 §12.7.1 (Foundation Modeling).

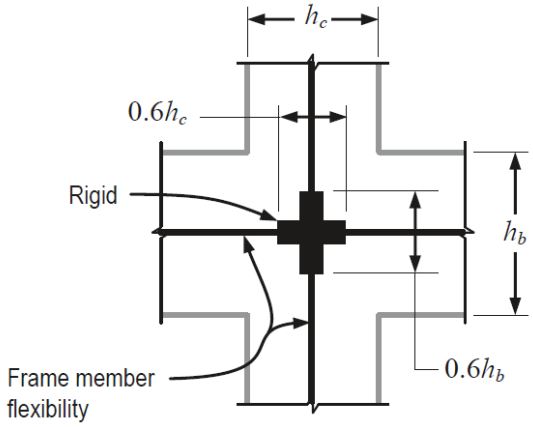

Figure 7.3.1: Partially Rigid Joint Model

The design model of the archetype frame is constructed in the computer software ETABS 2016 (Computers and Structures, Inc.) with all modeling recommendations described in the preceding paragraph implemented. The code-prescribed Modal Response Spectrum Analysis (MRSA) procedure was used for seismic design. The complete quadratic combination (CQC) was used as the modal combination rule for the first twenty (20) translational modes in the MRSA, which accounted for more than 98% of the modal mass. The applicable response modification factor was $R = 8$. ASCE 7-16 requires that design base shear given by MRSA procedure must be scaled to 100% of calculated base shear using the Equivalent Lateral Force procedure.

From the linear elastic frame model in ETABS, the design flexural strength in beams is governed by the load combinations considered. Beam shear strength demand is computed using probable moment strength of the beams M_{pr} plus appropriate gravity loads. Design axial force in columns is determined assuming an all-beams yielding mechanism with reduction factor of 0.8. Gravity load is also included in column axial demands in accordance with the controlling load combination. Column flexural strength is governed by the design principle of strong columns and weak beams, as specified by the requirement $\sum M_{nc} \geq \frac{6}{5}\sum M_{nb}$ (ACI 318-14).

Peak story drifts were calculated in the MRSA procedure with the design spectrum being scaled such that modal base shear is equal to base shear determined in accordance with Eq. 12.8-6 in ASCE 7-16. They are then multiplied by appropriate deflection amplification factor $C_d = 5.5$ for reinforced concrete frame buildings. All four buildings satisfy the story drift limit of $0.02h_{sx}$ per ASCE 7-16 (h_{sx} = story height).

Table 7.3.1 summarizes important design criteria and Table 7.3.2 presents the dimensions and longitudinal reinforcement. Note that beams and interior columns have constant cross section in the lower ten stories, with reduced sections in stories 11-20. Exterior columns were constant in stories 1-5, 6-10, and 11-20. Table 7.3.3 displays design drift ratio of the archetype frames determined by linear elastic analysis under design level hazard.

Table 7.3.1: Summary of Design Criteria

Building	**Grade 60**	**Grade 100**
Name	**SBH60**	**SBH100, SBL100, SBM100**
Risk Category	II	II
Seismic Importance Factor, I_e	1.0	1.0
Seismic Design Category	D	D
Seismic Response Modification Factor, R	8	8
Drift Amplification Factor, C_d	5.5	5.5
Live load (psf)	60	60
Seismic Weight per Frame, W $(kips)$	23,000	23,000
Design Base Shear Coefficient, V_b/W	0.044	0.044
Base Shear Coefficient for Scaling of Drift	0.038	0.038
Concrete strength in beams, f_c' (ksi)	5.0	5.0
Concrete strength in columns (1^{st}-10^{th} floors), f_c' (ksi)	8.0	8.0
Concrete strength in columns (11^{th} -20^{th} floors), f_c' (ksi)	7.0	7.0
Steel yield strength, f_y (ksi)	60	100
Beam effective stiffness	$0.35E_cI_g$	$0.35E_cI_g$
Column effective stiffness	$0.5E_cI_g$	$0.5E_cI_g$

Table 7.3.2: Dimensions and Reinforcement of Design Frames

Design		Grade 60				Grade 100			
Zone		1	2	3	4	1	2	3	4
Story		1-5	6-10	11-15	16-20	1-5	6-10	11-15	16-20
Beam	b (in.)	24	24	24	24	24	24	24	24
	h (in.)	40	40	40	40	40	40	40	40
	Top & Bottom Reinforcement	7 No. 10	7 No. 10	7 No. 9	7 No. 9	5 No. 9	5 No. 9	5 No. 8	5 No. 8
Ext. Col	b (in.)	42	42	36	36	42	42	36	36
	h (in.)	42	42	36	36	42	42	36	36
	Perimeter Reinforcement	28 No. 10	20 No. 9	20 No. 9	20 No. 9	24 No. 9	16 No. 8	16 No. 8	16 No. 8
Int. Col	b (in.)	42	42	36	36	42	42	36	36
	h (in.)	42	42	36	36	42	42	36	36
	Perimeter Reinforcement	20 No. 9	20 No. 9	20 No. 9	20 No. 9	16 No. 8	16 No. 8	16 No. 8	16 No. 8

Table 7.3.3: Design Drift of Archetype Frames

Story	Design Level Drift Ratio
20	0.005
19	0.007
18	0.008
17	0.010
16	0.011
15	0.012
14	0.013
13	0.013
12	0.014
11	0.014
10	0.014
9	0.014
8	0.014
7	0.015
6	0.015
5	0.015
4	0.016
3	0.016
2	0.014
1	0.008

7.4. NUMERICAL MODEL

A two-dimensional numerical model of a single special moment frame in the archetype building was constructed and nonlinear history analysis (NRHA) was performed using the Open System for Earthquake Engineering Simulation software platform (McKenna et al., 2007; OpenSees, 2016).

Mass and load: seismic mass is lumped and gravity load is applied at the joints. Both seismic mass and gravity load include 100% of dead load and 25% of live load in accordance with ASCE 7.

Gravity framing and foundation: gravity framing is assumed to have sufficient strength and stiffness to resist $P-\Delta$ effects under its own tributary gravity load. It is also assumed to not provide lateral resistance (Haselton et al., 2008). Foundation flexibility is not modeled and all columns at base level are fixed to the "ground."

Frame elements and joints: all beams and columns are modeled as described in Chapter 6. Force-based Euler-Bernoulli nonlinear fiber-section frame elements with five Gauss-Lobatto integration points and $P-\Delta$ geometric transformation are used to model flexural behavior. Axial force – bending moment interaction is modeled but shear force – bending moment and/or axial force interaction is not considered. Slab effects are not considered in the numerical model.

Rotational springs (slip of reinforcement): strain penetration of beam longitudinal reinforcement into joints and column longitudinal reinforcement into the foundation are modeled through nonlinear rotational springs by using a zero-length section element as described in Chapter 6 (Figure 7.4.1). For different frame elements, the amount of slip is scaled linearly proportionally from the measured slip in beam tests with the same grade of reinforcement by the ratio $d_b/\sqrt{f_c'}$ of the frame elements divided by that of the test beams, where d_b (inch) is the longitudinal bar diameter and f_c'(psi) is the concrete compressive strength.

Beam-column joints: beam-column joints are modeled with rigid end zones in both columns and beams (Figure 7.4.1). As the floor level is defined on top of the beams in the frame models, column rigid links are only implemented below the primary nodes with the length being the height of the connected beams. Between frame elements and rigid links or primary nodes at the base are the rotational springs and rigid shear links. The rigid shear links are required to connect the rigid links and frame elements in the transverse direction (direction of shear force) because rotational springs are modeled by the zero-length section elements, which only provide resistance axially and flexurally.

Section aggregator (shear): shear behavior in beams is only modeled by linear elastic properties. The reason is that, under ground motion excitation, the effect of beam elongation and kinematics with different column elements results in development of axial force in beams, and

moment strength of a beam constantly changes as a result. The Ibarra-Medina-Krawinkler model for shear response through the use of a section aggregator does not model shear-moment interaction. Since deformation contribution from shear to the total deformation of a beam is very little as observed in the beam tests and discussed in Chapter 4, shear response modeled only by the linear elastic property is deemed sufficient and overall behavior of beam models remains very similar to that shown in Chapter 6. Elastic stiffness of shear in frame elements is proportionally scaled from the measured one in beam tests by the product $A_g\sqrt{f_c'}$ of the frame elements divided by that of the test beams, where A_g (in^2) is the frame element cross-sectional area and f_c'(psi) is the concrete compressive strength. Shear flexibility is not modeled in columns.

Material properties: expected material properties are used in the frame models (TBI, 2016). Yield strength of Grade 60 A706 is taken to be 65 ksi, the value measured in the coupon tests for specimen SBH60. Expected yield strengths of Grade 100 with distinct yield plateau (SBH100 and SBL100) are both 106 ksi in the frame model but frame SBH100 has Grade 100 steel with higher strain hardening ratio as an intent of dynamic analysis study is to explore this effect on the seismic performance of two archetype frames with different types of reinforcement. Concrete strength is 1.3 times specified compressive strength of 5.0 ksi for all beams, 8.0 ksi for all columns from the base to the 10th floor, and 7.0 ksi for all columns above the 10th floor.

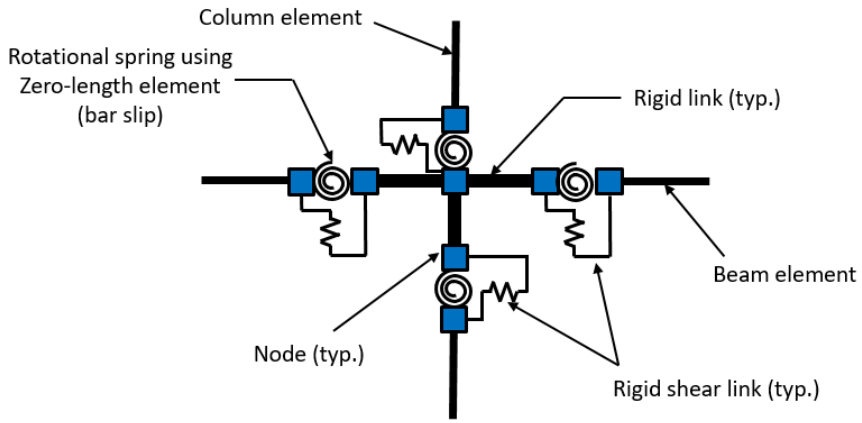

Figure 7.4.1: Typical Model at the Joint

Damping forces: as studied by many researchers, initial stiffness Rayleigh damping has been recognized to cause spurious forces in the system and equilibrium is not maintained (Charney, 2008; Chopra and McKenna, 2016; Lu and Morris, 2017). Therefore, tangent stiffness Rayleigh damping is implemented in the frame model such that equilibrium is satisfied everywhere in the system. The damping matrix is defined as a linear combination of mass matrix and tangent stiffness matrix Rayleigh damping with 2% damping ratio applied in modes 1 and 3. Damping coefficients calculated from 1st and 3rd modal properties of frame SBH60 are used to define the damping matrix in analyses of all frames studied here.

Cyclic response of typical beams and columns in the studied frames is presented in Figure 7.4.2 through Figure 7.4.7. Figure 7.4.2 displays cyclic behavior of a typical beam in frames SBH60 and SBL100. The beam in frame SBH60 is apparently stiffer and has higher peak strength than the beam in frame SBL100 because of greater longitudinal reinforcement area and material strain hardening. They both have similar yield strength as expected in the design. Figure 7.4.3 shows comparison of response between beams of frames SBH100 and SBL100. They both have equivalent stiffness and strength at yield. The beam in SBH100 is stronger after yielding as its longitudinal reinforcement has higher strain hardening ratio. In Figure 7.4.4, it is also apparent that the beam in frame SBH60 is stiffer than the beam in frame SBM100.

Similar trends can be observed for response of typical exterior columns in the frame models (Figure 7.4.5 to Figure 7.4.7). The column in frame SBH60 shows higher initial stiffness than other columns in frames with high-strength steel. It also has slightly higher strain hardening behavior after yielding. In Figure 7.4.6, the column in frame SBH100 obviously responds better after yield than that in frame SBL100 due to higher strain hardening ratio. The column in frame SBM100 has the higher peak strength but its strength degrades quicker than the column in SBH60 (Figure 7.4.7). Cyclic response of column models illustrated in Figure 7.4.5 to Figure 7.4.7 were computed under axial load of approximately $0.35A_g f_c'$.

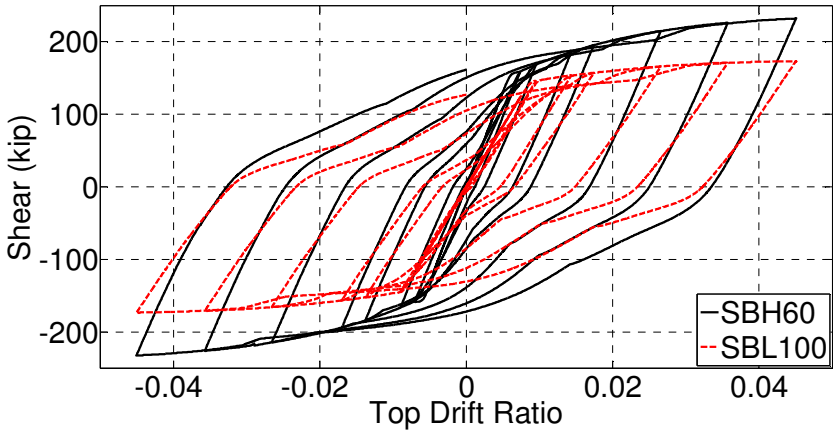

Figure 7.4.2: Cyclic Response of Typical Beams in Frames SBH60 and SBH100

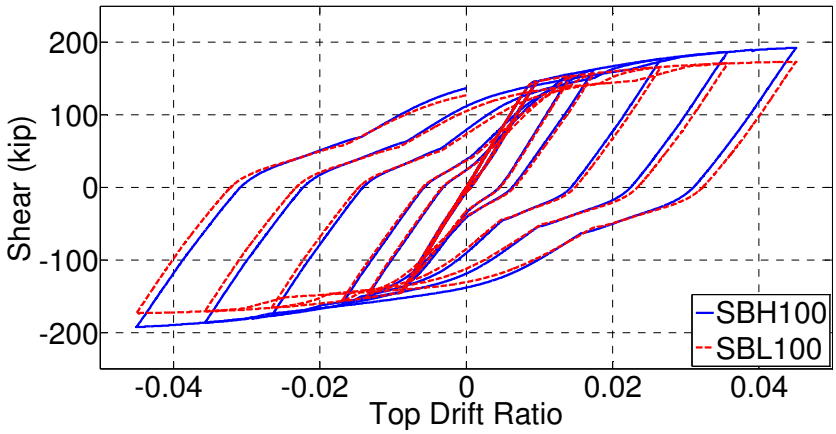

Figure 7.4.3: Cyclic Response of Typical Beams in Frames SBH100 and SBL100

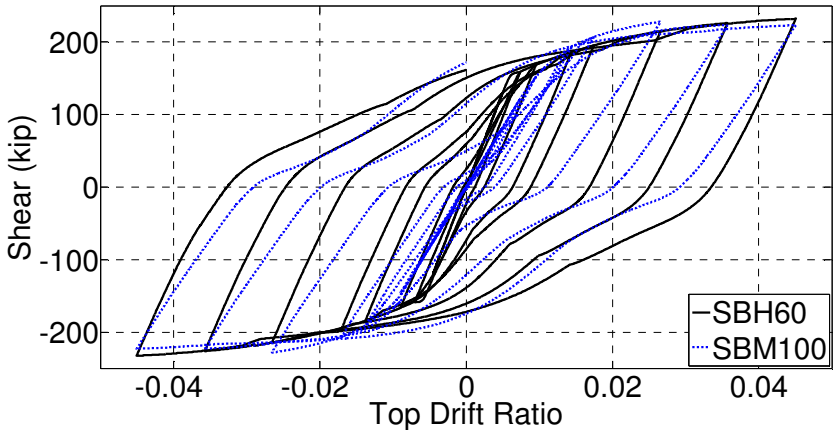

Figure 7.4.4: Cyclic Response of Typical Beams in Frames SBH60 and SBM100

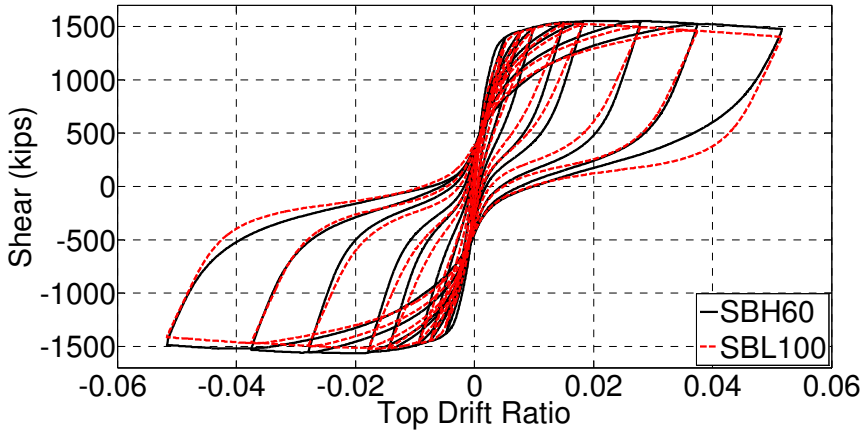

Figure 7.4.5: Cyclic Response of Typical Exterior Column in Frames SBH60 and SBH100

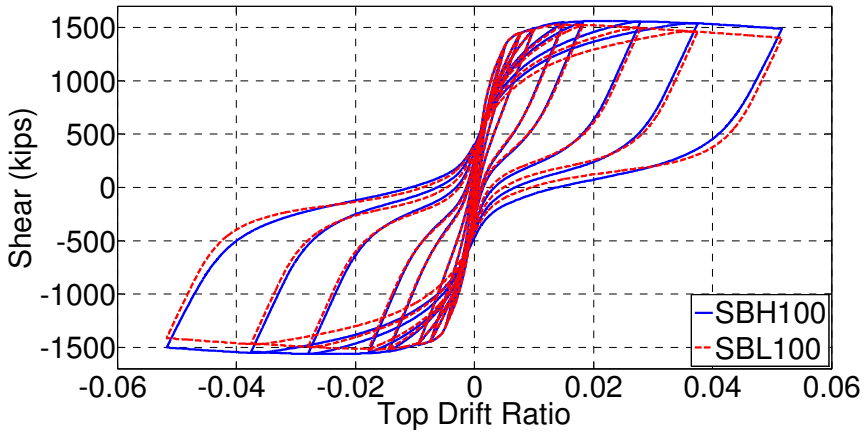

Figure 7.4.6: Cyclic Response of Typical Exterior Column in Frames SBH100 and SBL100

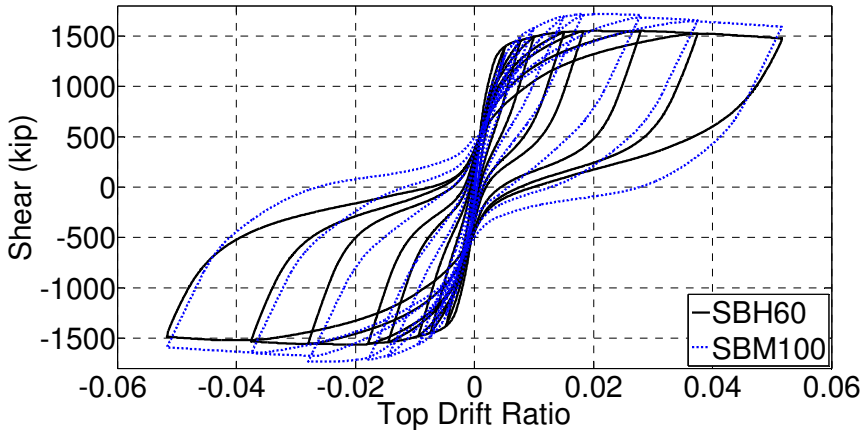

Figure 7.4.7: Cyclic Response of Typical Exterior Column in Frames SBH60 and SBM100

7.5. VIBRATION PROPERTIES AND STRENGTH

Modal periods of the first three translational modes of the planar models based on cracked section properties are listed in Table 7.5.1. In the ETABS model, cracked-section properties are modeled by applying effective stiffness for beams and columns of $0.35E_cI_g$ and $0.5E_cI_g$, respectively. In the OpenSees model with fiber sections, modal periods are computed after gravity load is applied onto the frame.

A nonlinear static push-over analysis under lateral load pattern that is similar to the ASCE 7 Equivalent Lateral Force is performed for all frame models after application of gravity loads. The results are plotted in Figure 7.5.1. It is worth noting that frame SBH60 reinforced with conventional Grade 60 A706 steel and larger amount of longitudinal reinforcement is stiffer than the other three frames with Grade 100 reinforcement. All frames with higher-grade steel have the same initial stiffness. Additionally, frame SBH100 is stronger than SBL100 after yielding as its reinforcement has higher strain hardening. Similar observation is made for SBH60 as compared with the response of SBH100 and SBL100. SBM100 has the highest peak strength as expected because Grade 100 A1035 has the highest ultimate stress of the four types of steels.

Table 7.5.1: Period of First Three Translational Modes of Archetype Buildings

Building	Mode	ETABS Period (s)	OpenSees Period (s)
SBH60	1	3.41	3.18
	2	1.16	1.07
	3	0.65	0.60
SBH100, SBL100, SBM100	1	3.41	3.82
	2	1.16	1.29
	3	0.65	0.71

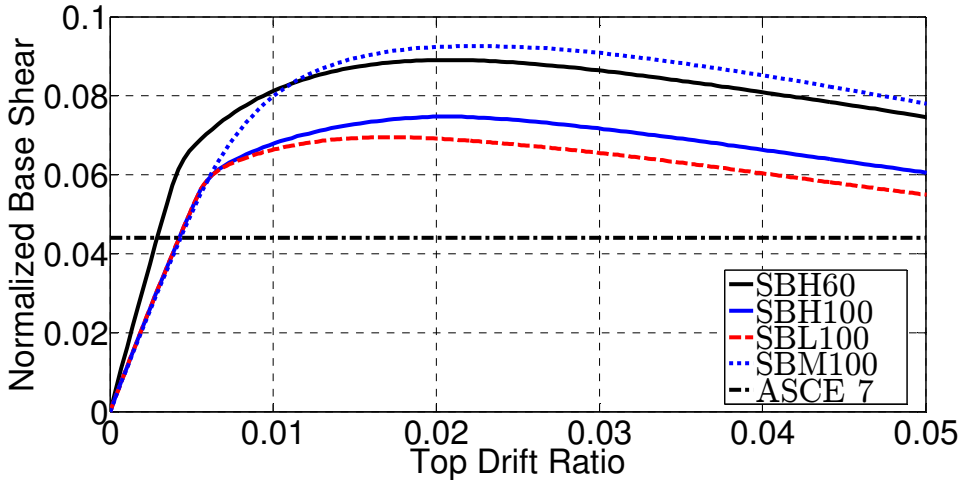

Figure 7.5.1: Push-Over Curves for All Frame Models under ASCE 7 Lateral Load Pattern

7.6. GROUND MOTION SELECTION

Dynamic analyses are performed at two levels of shaking intensities: maximum considered earthquake (MCE) and the average RotD50. Ground motions are selected using a Matlab routine developed by the Baker Research Group (Jayaram et al., 2011).

Twenty ground motions are selected such that the average spectrum of fault-normal (FN) component spectra of all ground motions approximates the MCE response spectrum defined in Section 7.2. From these selected motions, the individual fault-parallel (FP) components are scaled to agree with the RotD50 response spectrum. The selection restrictions are: 1) magnitude of the earthquake is between 6.5 and 8.0; 2) distance to site is within 20 kilometers; and 3) the scale factor is from 0.5 to 5.0. The set of 20 selected ground motions also contains about 10 near-fault pulse-like motions that have distinct velocity pulses due to directivity effects.

Table 7.6.1 lists the individual ground motion information and their scale factors. Their FN- and FP-component pseudo-acceleration spectra are plotted in Figure 7.6.1 and Figure 7.6.2. The average spectrum of FN and FP components are also shown and compared with the target MCE and RotD50 spectra in these plots, respectively.

Table 7.6.1: Selected Ground Motions and Scale Factors

GM No.	Record Sequence Number	Earthquake Name	Year	Station Name	Scale Factor FN	Scale Factor FP
1	6	Imperial Valley-02	1940	El Centro Array #9	3.60	2.20
2	126	Gazli, USSR	1976	Karakyr	1.50	1.30
3	174	Imperial Valley-06	1979	El Centro Array #11	3.50	2.00
4	182	Imperial Valley-06	1979	El Centro Array #7	0.80	1.50
5	184	Imperial Valley-06	1979	El Centro Differential Array	1.50	1.40
6	495	Nahanni, Canada	1985	Site 1	2.30	3.50
7	721	Superstition Hills-02	1987	El Centro Imp. Co. Cent	2.10	3.00
8	725	Superstition Hills-02	1987	Poe Road (temp)	3.60	2.00
9	728	Superstition Hills-02	1987	Westmorland Fire Sta	2.80	2.30
10	779	Loma Prieta	1989	LGPC	0.80	1.20
11	802	Loma Prieta	1989	Saratoga - Aloha Ave	1.80	2.40
12	803	Loma Prieta	1989	Saratoga - W Valley Coll.	1.80	1.60
13	827	Cape Mendocino	1992	Fortuna - Fortuna Blvd	3.20	3.80
14	1045	Northridge-01	1994	Newhall - W Pico Canyon Rd.	1.00	1.70
15	292	Irpinia, Italy-01	1980	Sturno (STN)	1.75	1.50
16	6906	Darfield, New Zealand	2010	GDLC	1.20	0.70
17	8119	Christchurch, New Zealand	2011	Pages Road Pumping Station	0.85	2.50
18	1605	Duzce, Turkey	1999	Duzce	1.40	1.00
19	2655	Chi-Chi, Taiwan-03	1999	TCU122	2.80	5.00
20	2658	Chi-Chi, Taiwan-03	1999	TCU129	3.60	5.00

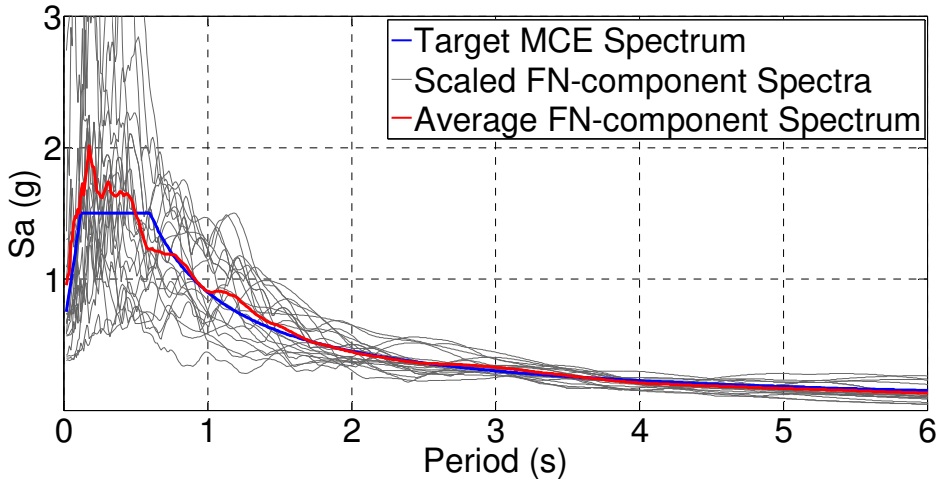

Figure 7.6.1: Pseudo-Acceleration Spectra for FN Components

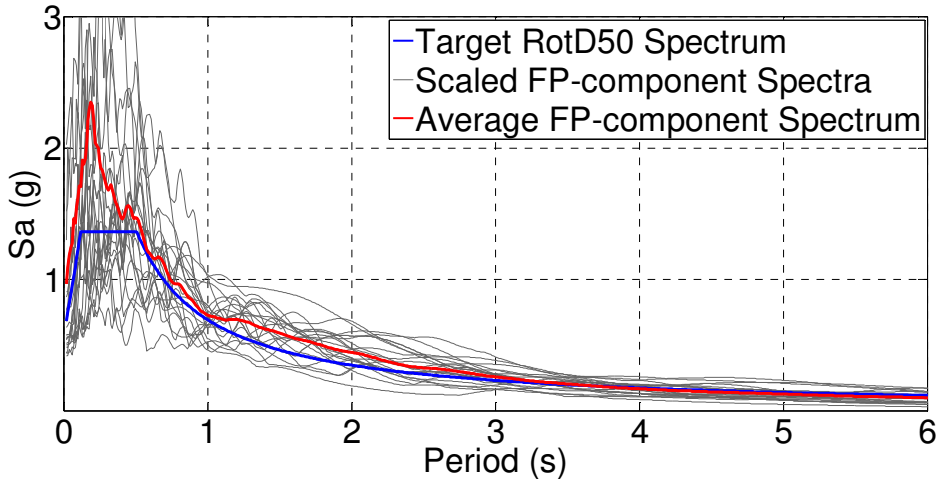

Figure 7.6.2: Pseudo-Acceleration Spectra for FP Components

7.7. RESULTS FROM NONLINEAR RESPONSE HISTORY ANALYSIS

Damping Forces

As mentioned in the numerical model section, tangent stiffness Rayleigh damping was employed in the frame models rather than modal damping as suggested by Chopra and McKenna (2016). The reason was that implementing modal damping was observed to pose additional difficulty on solution convergence and cause the analyses to take much longer to finish. Several nonlinear dynamic analyses were performed on frame model SBH60 employing three different damping models including initial stiffness Rayleigh damping (RI), tangent stiffness Rayleigh damping (RT), and modal damping (MODAL) to compare and provide judgement for the damping model selected for dynamic analyses in this study.

For both models with Rayleigh damping, the damping matrix was defined as a linear combination of mass matrix and stiffness matrix Rayleigh damping with 2% damping ratio applied in modes 1 and 3, where the stiffness matrix was for the initial stiffness matrix or the tangent stiffness matrix. Lastly, in the model with modal damping, 1.8% damping ratio was applied to the first twenty modes with additional 0.2% Rayleigh damping applied in mode 10 to the tangent stiffness matrix only without contribution from the mass matrix.

Figure 7.7.1 and Figure 7.7.2 display drift response histories and floor drifts, respectively, of frame model SBH60 with the three different damping models subjected to the ground motion recorded at Poe Road station in the event of Superstition Hills earthquake in 1987. The models RT and MODAL provide similar roof drift histories as well as peak values of floor drift. This finding was also illustrated by Chopra and McKenna (2016) and Lu and Morris (2017). The model RI shows relatively lower roof drift.

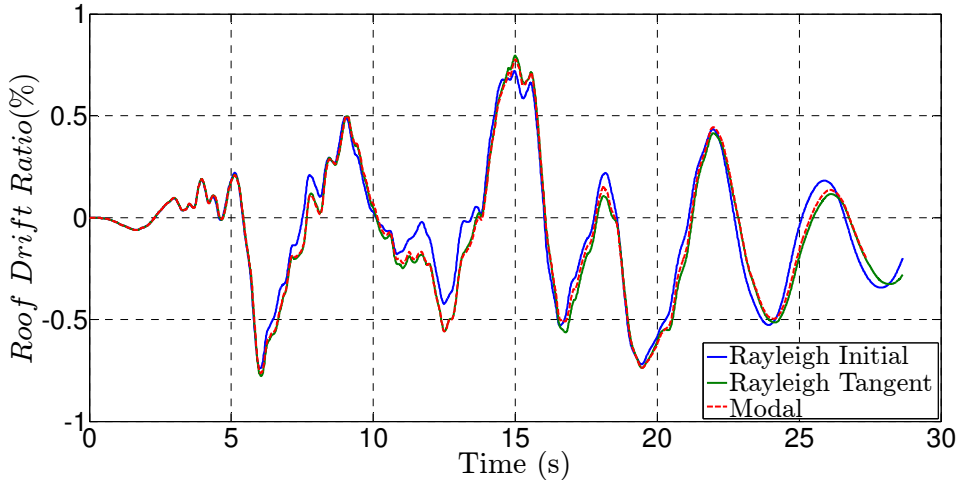

Figure 7.7.1: Roof Drift Response under Different Damping Models - Earthquake: Superstition Hills 1987 - Station Name: Poe Road - FN Component

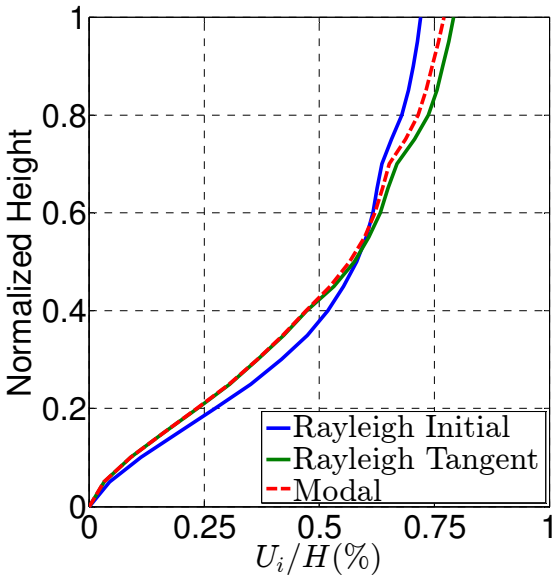

Figure 7.7.2: Peak Values of Floor Drifts under Different Damping Models - Earthquake: Superstition Hills 1987 - Station Name: Poe Road - FN Component

According to Charney (2008) and Chopra and McKenna (2016), the initial stiffness Rayleigh damping would result in unintended spurious damping forces at the location of beam-column joints in multistory buildings with structural elements being modeled using concentrated plasticity. This spurious damping forces can be significantly reduced if the structural elements are modeled as force-based elements with distributed plasticity in OpenSees (Chopra and McKenna, 2016). In the present study, all frame models use force-based elements with distributed plasticity, but these frame elements are connected at beam-column joints through concentrated rotational springs that are implemented to model effect of strain penetration of longitudinal reinforcement at the joint (Figure 7.7.3).

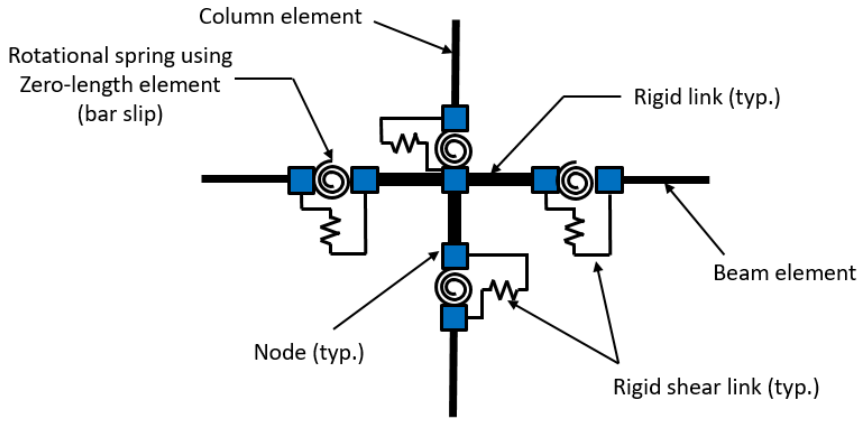

Figure 7.7.3: Typical Model at the Beam-Column Joint

Study of the analysis results in the present study identified existence of spurious damping forces at the locations of the rotational springs and rigid shear links adjacent to beam and column elements in the frame model with initial stiffness Rayleigh damping. As an example, consider the locations identified in Figure 7.7.4. Figure 7.7.5 and Figure 7.7.6 plot the normalized spurious moments and axial forces, respectively, at the interface of the beam and the adjacent rotational spring on the 2nd floor. Note the difference in scale on the y-axis of these plots. The model RI with initial stiffness Rayleigh damping clearly exhibits spurious damping moment and axial force as much as 20% of yield moment and 5% of the quantity $A_g f_c'$, respectively. The model RT with tangent stiffness Rayleigh damping substantially reduced the amount of these spurious damping forces. The model MODAL with modal damping further reduces these spurious forces to nearly eliminate them completely.

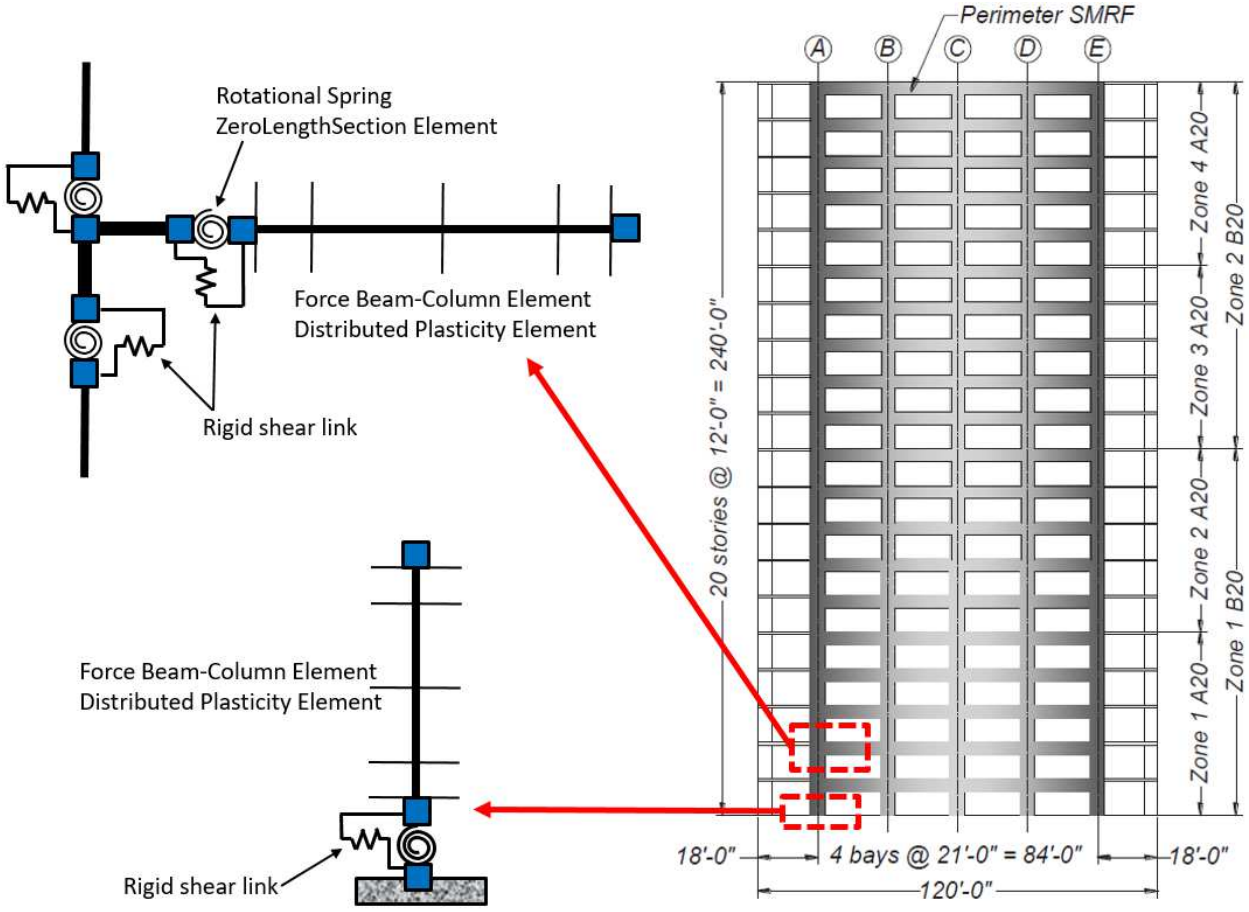

Figure 7.7.4: Location of Occurrence of Spurious Damping Force

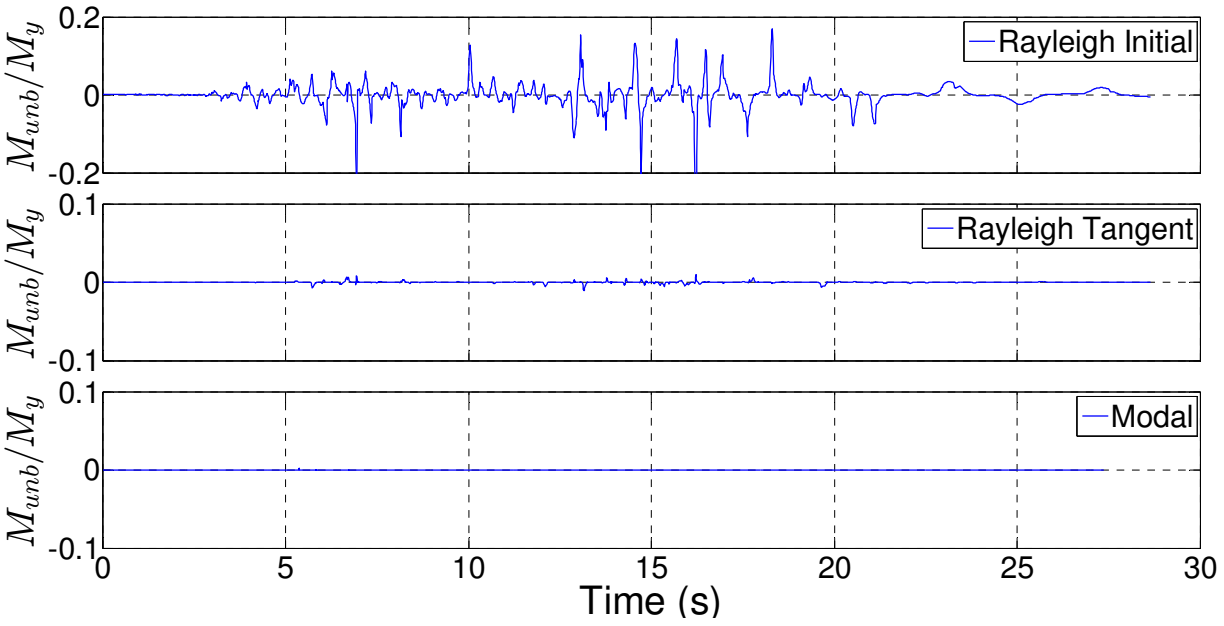

Figure 7.7.5: Unbalanced Moment at Interface of Beam and Rotational Spring at Exterior Joint on 2nd Floor

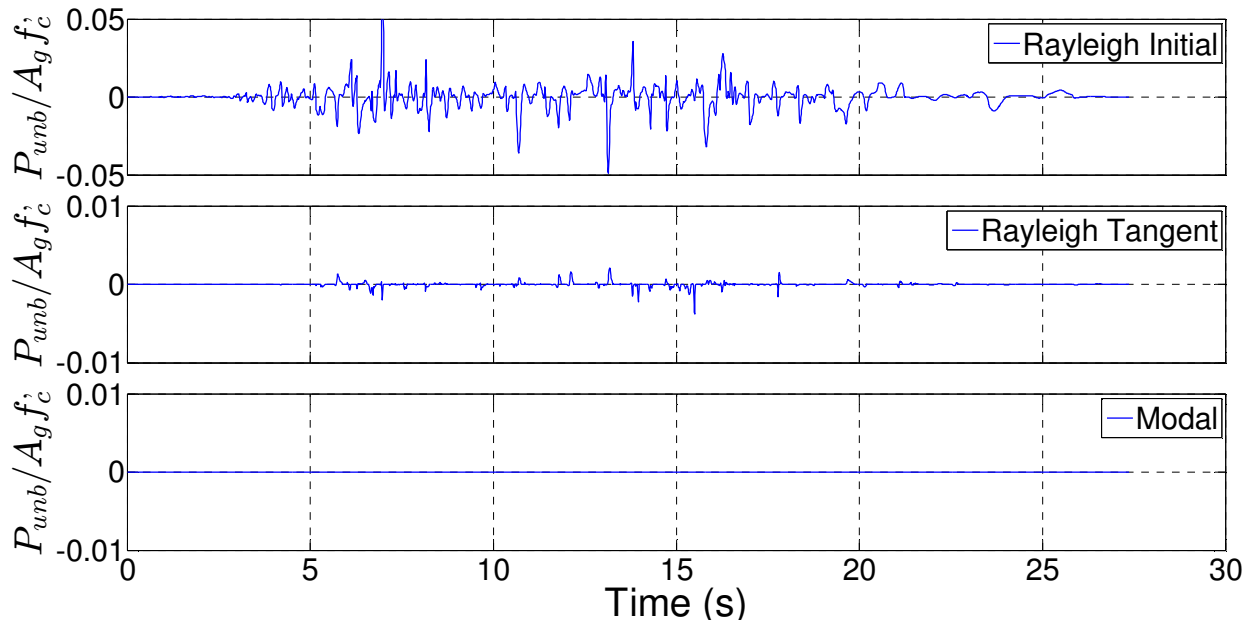

Figure 7.7.6: Unbalanced Axial Force at Interface of Beam and Rotational Spring at Exterior Joint on 2nd Floor

Figure 7.7.7 illustrates the unbalanced shear force acting between the beam element and the rigid shear link. The model RI produced discrepancy in shear force of about $0.3A_g\sqrt{f_c'}(psi)$,

which was about 10% of the average shear force acting on this beam. Model RT reduced the unbalanced shear to about $0.1A_g\sqrt{f_c'}(psi)$ and model MODAL eliminated this spurious shear.

Similar observation can be made for the exterior column at the base of the frame model. Figure 7.7.8 through Figure 7.7.10 present the spurious forces between the exterior column and the connecting rotational spring and rigid shear link. Figure 7.7.11 through Figure 7.7.13 display discrepancy between forces in the exterior column and the reaction forces of the adjacent node at the base. It is apparent that spurious forces occur between columns and their connecting elements (rotational springs and rigid shear links). These connecting elements and their adjacent nodes at the base level are in equilibrium as demonstrated in Figure 7.7.14 for the difference in force in rigid shear link and horizontal component of reaction of the node at base.

Although the modal damping model demonstrates the superior capability of reducing unintended spurious damping forces, it posed difficulty in solution convergence and caused considerably more time to complete the same analysis than the model with tangent stiffness Rayleigh damping. More importantly, both models with tangent stiffness Rayleigh damping and modal damping were demonstrated to provide relatively similar response results. Therefore, tangent stiffness Rayleigh damping was selected to implement in the remaining nonlinear dynamic analyses in this study.

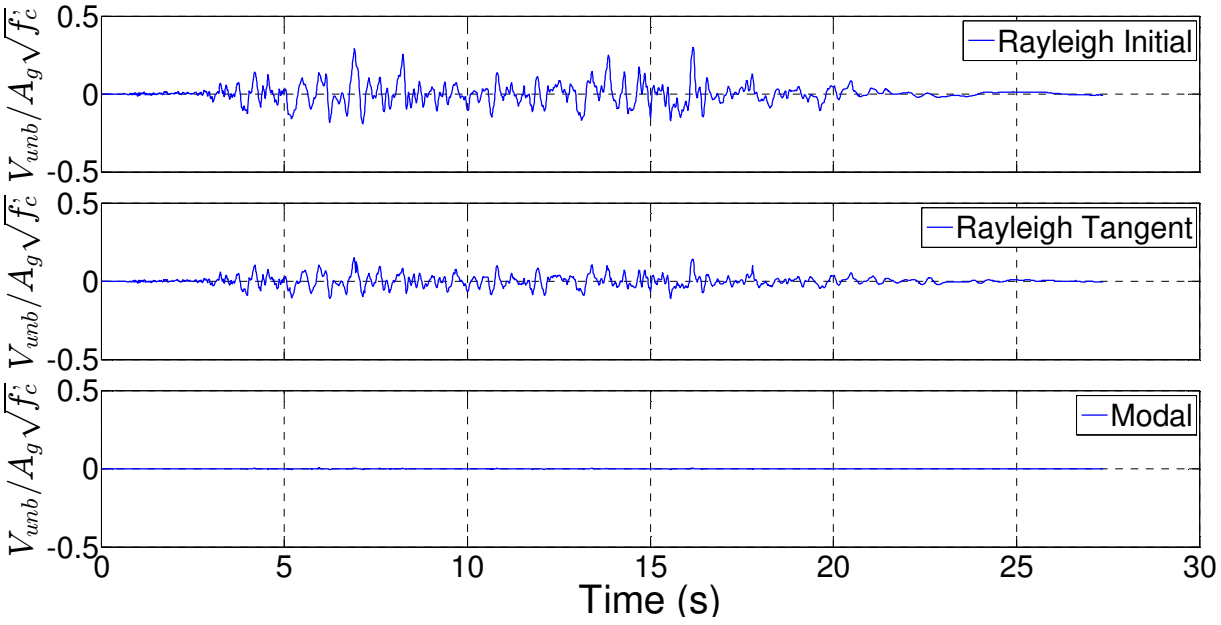

Figure 7.7.7: Unbalanced Shear Force at Interface of Beam and Rigid Shear Link at Exterior Joint on 2nd Floor

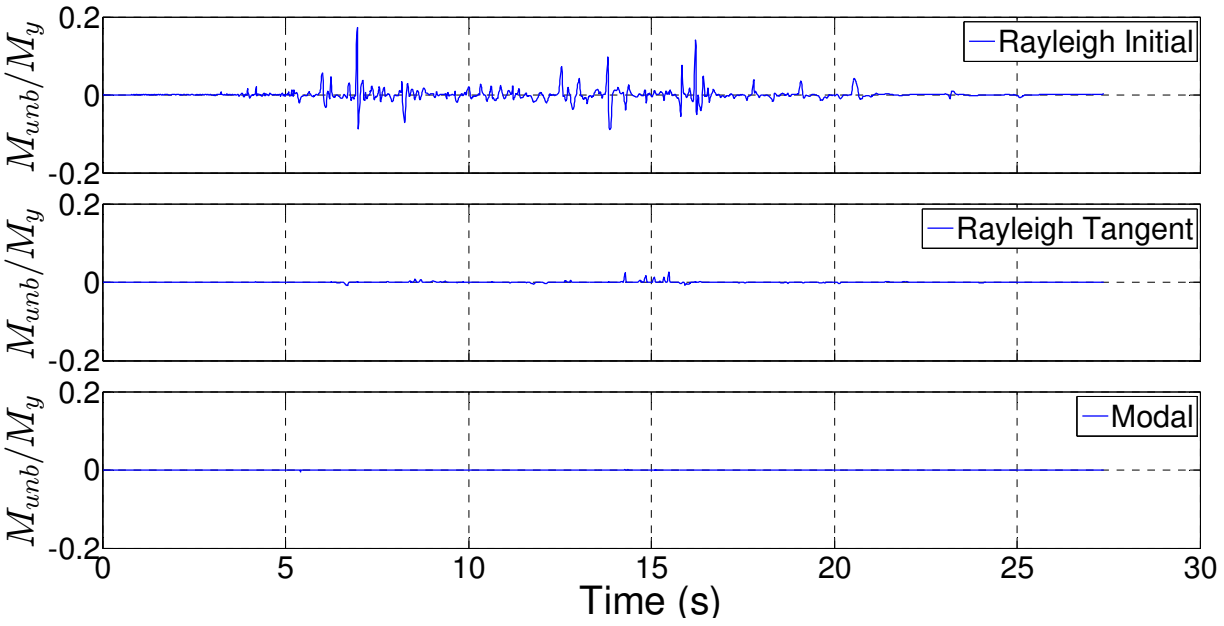

Figure 7.7.8: Unbalanced Moment at Interface of Exterior Column and Rotational Spring at Base of Frame

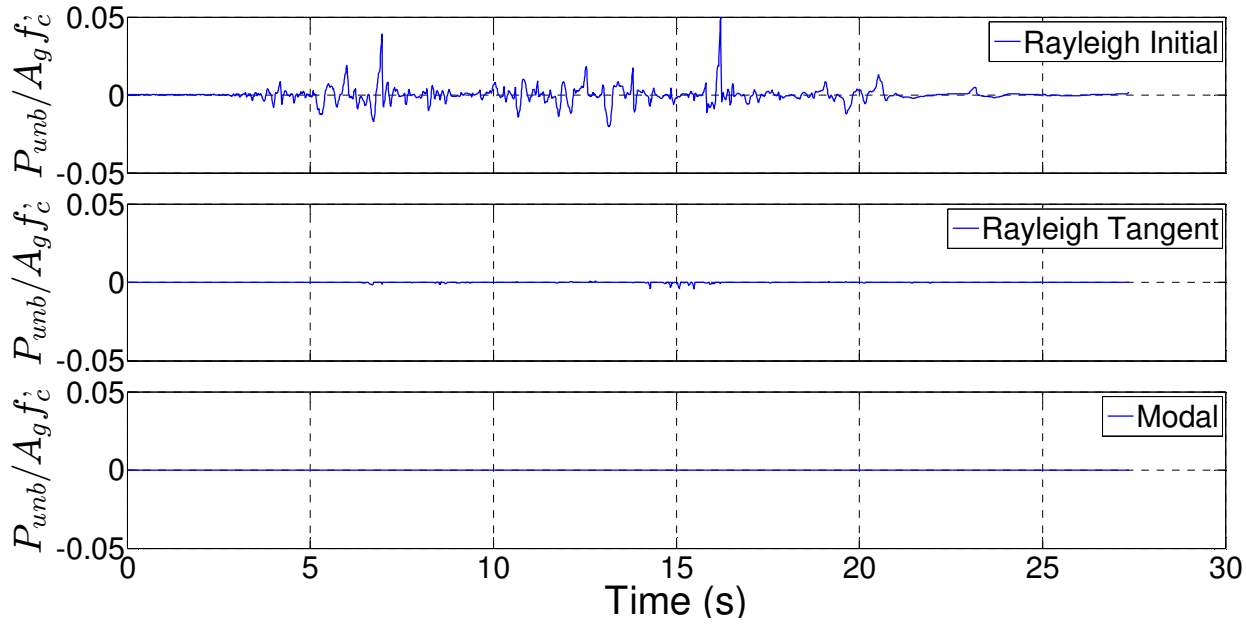

Figure 7.7.9: Unbalanced Axial Force at Interface of Exterior Column and Rotational Spring at Base of Frame

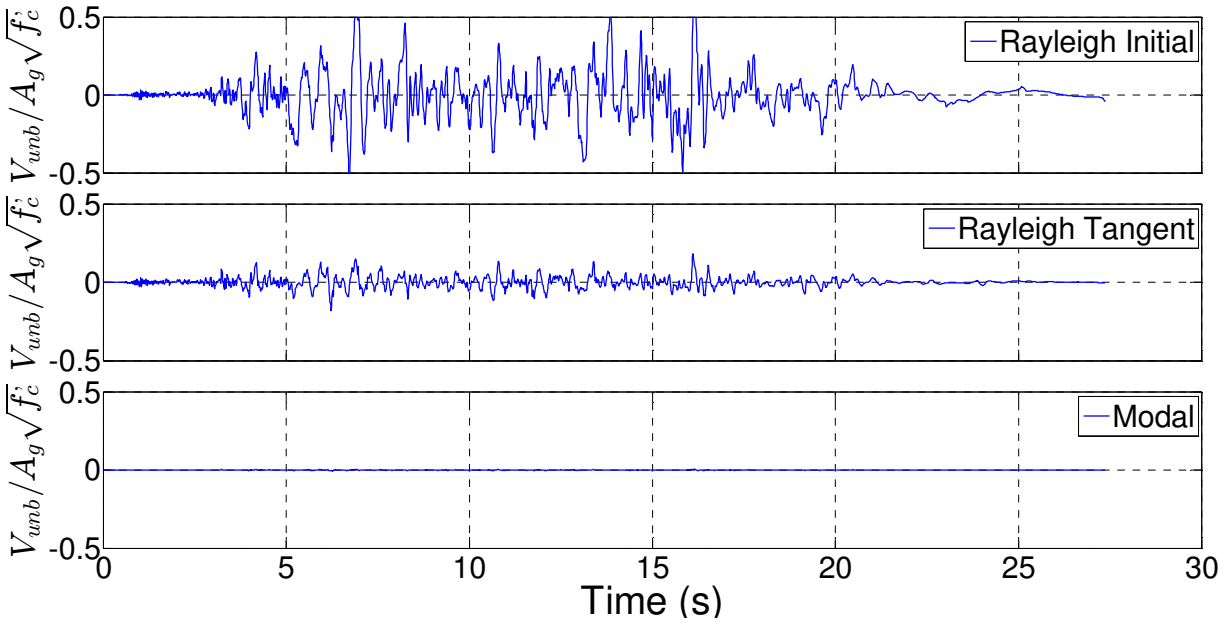

Figure 7.7.10: Unbalanced Shear Force at Interface of Exterior Column and Rigid Shear Link at Base of Frame

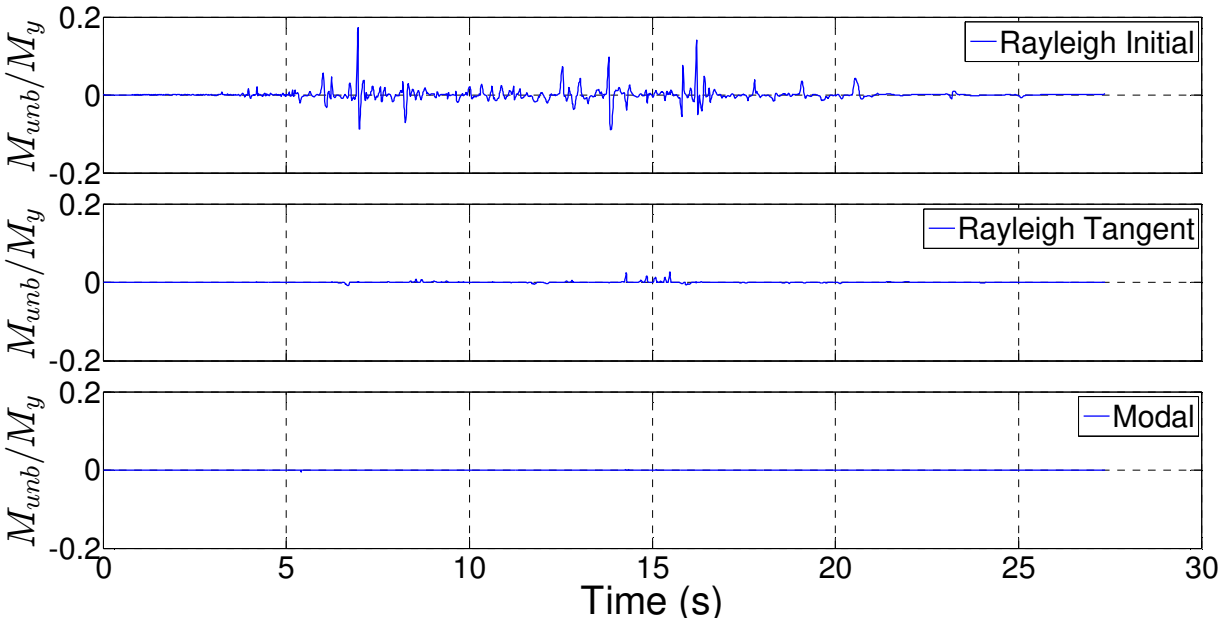

Figure 7.7.11: Unbalanced Moment at Interface of Exterior Column and Moment Reaction of Node at Base of Frame

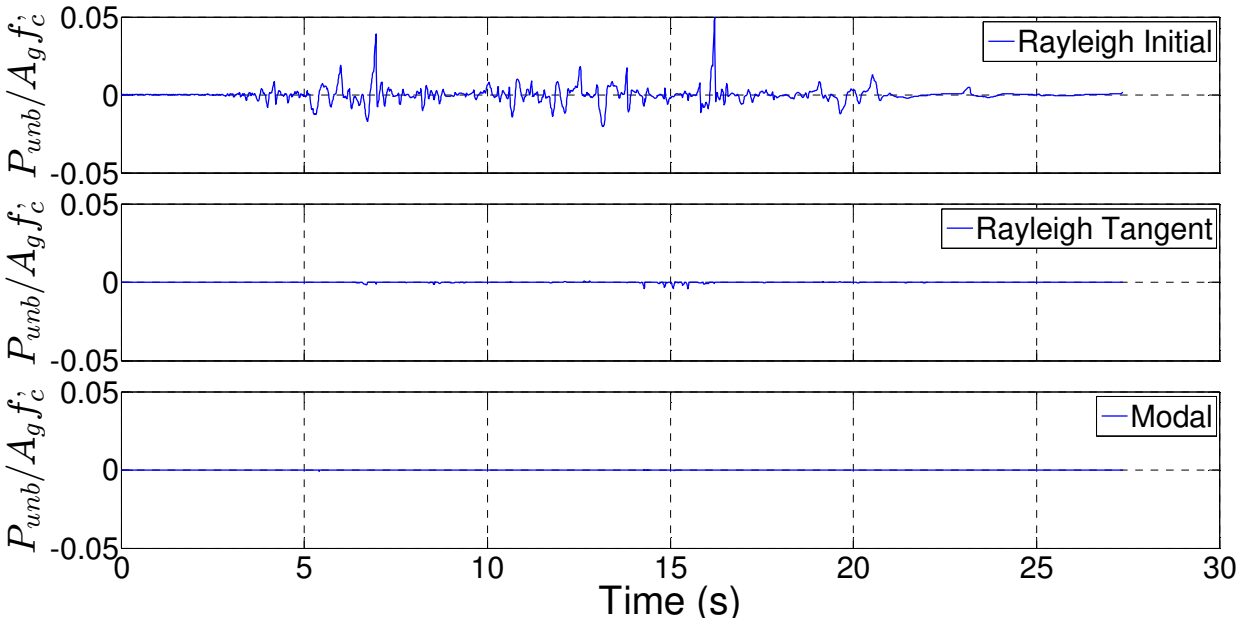

Figure 7.7.12: Unbalanced Axial Force at Interface of Exterior Column and Vertical Reaction Force of Node at Base of Frame

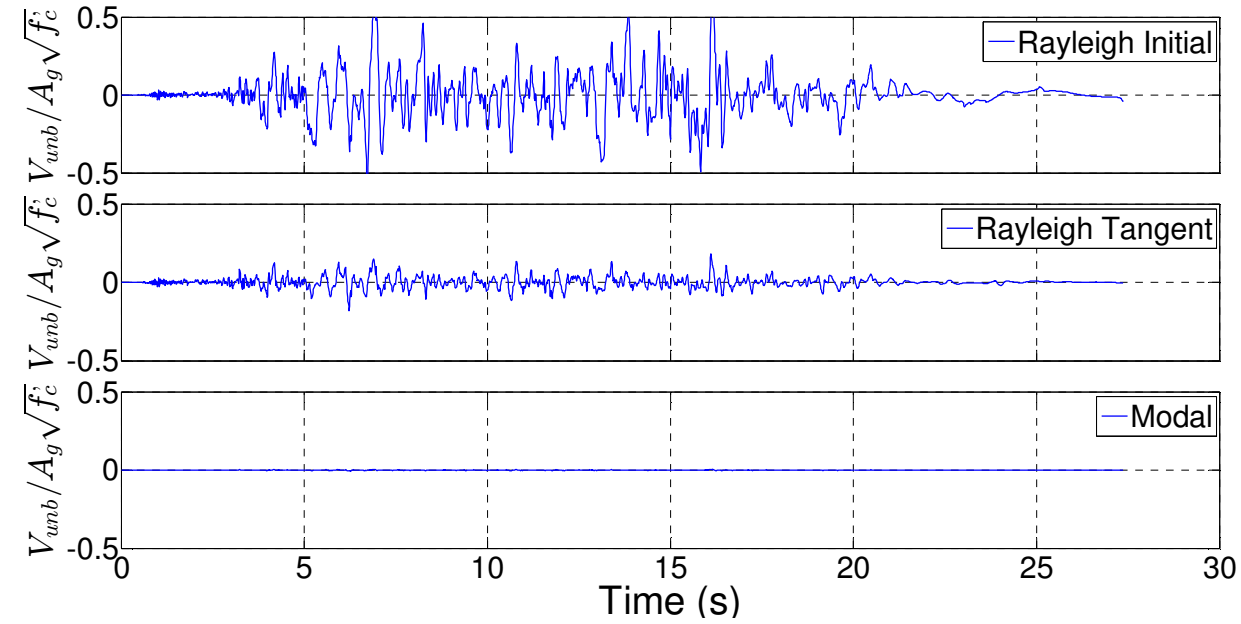

Figure 7.7.13: Unbalanced Shear Force at Interface of Exterior Column and Horizontal Reaction of Node at Base of Frame

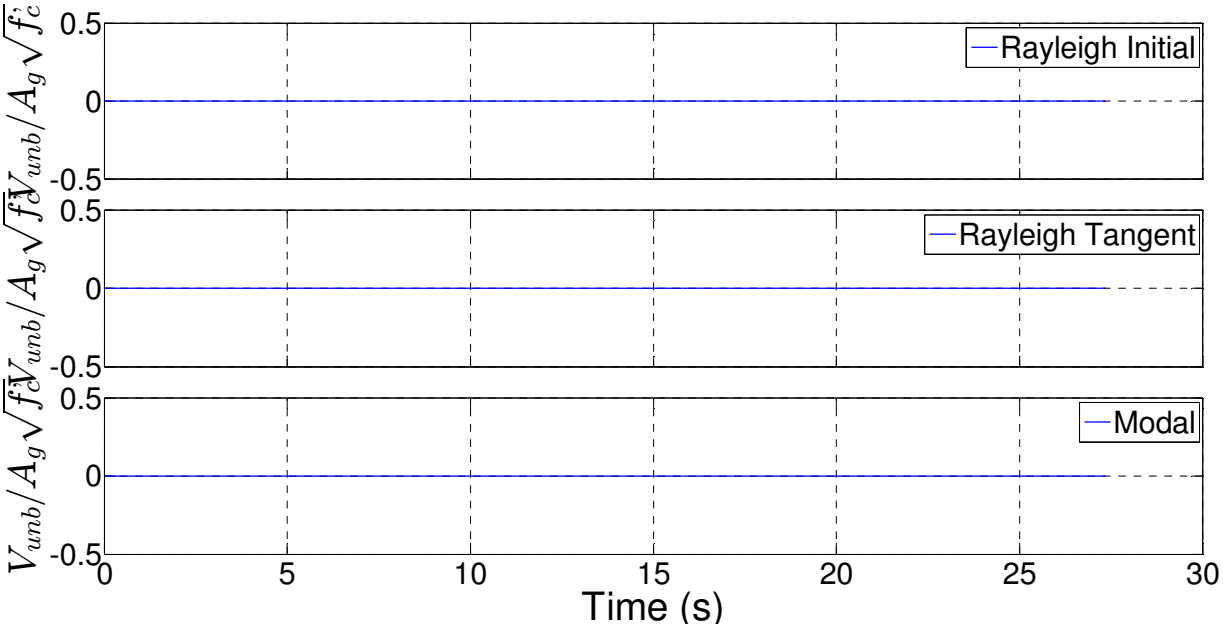

Figure 7.7.14: Unbalanced Shear Force between Rigid Shear Link and Horizontal Reaction of Node at Base of Frame

Overall Responses

Figure 7.7.15 shows the history of roof displacement of all four frames subjected to the fault-normal (FN) component of the ground motion recorded at station TCU 129 during the Chi-Chi earthquake in Taiwan 2003. Frame SBH60 with conventional Grade 60 A706 reinforcement achieved the least roof displacement of all the studied buildings as expected due to its greater stiffness. Frames SBH100 and SBL100 are both identical in all aspects except the strain-hardening property of the longitudinal reinforcement, resulting in almost the same roof response history. Lastly, frame SBM100 produces the largest roof displacement of all frames. It is also worth pointing out that roof level residual deflection for all three frames with Grade 100 reinforcement is slightly higher than that of the frame with conventional Grade 60 steel.

Zooming in on the history of the roof displacement as shown in Figure 7.7.15, it can be observed that frame SBH60 has a shorter period than the other three frames. Frame SBH60 responds mainly at period about 4.5 seconds while the other frames respond at period of approximately 5.0 seconds.

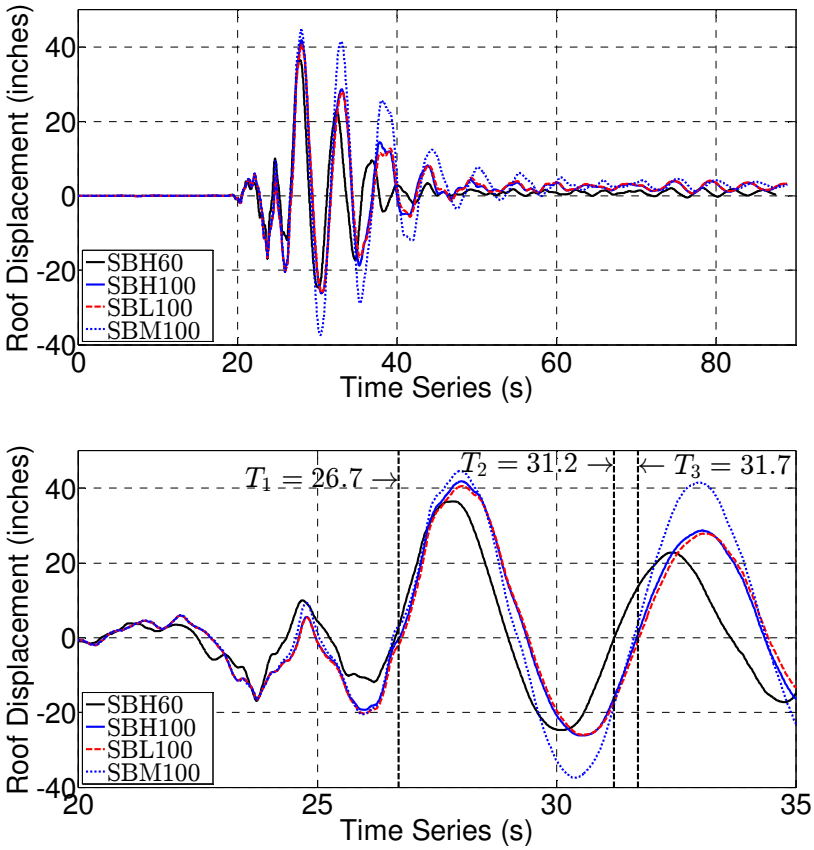

Figure 7.7.15: Roof Displacement Response History of All Frames under Record Number 2658 – Earthquake: Chi-Chi, Taiwan-03 – Station Name: TCU 129 – FN Component

Figure 7.7.16 plots calculated roof displacement histories of the four buildings under the FN component of ground motion recorded at station El Centro Imp. Co. Cent from the Superstition

Hills-02 earthquake. Figure 7.7.17 plots calculated stress-strain behavior of a representative beam element for the four buildings. In response under this motion, the beam element in frame SBH60 sustained the least calculated strain demand, mainly because the roof deflection is the least among the four buildings. Grade 100 A1035 steel used in frame SBM100 sustains the largest strain. Frames SBH100 and SBL100 have very similar calculated strains that are between strains calculated for Frames SBH60 and SBM100.

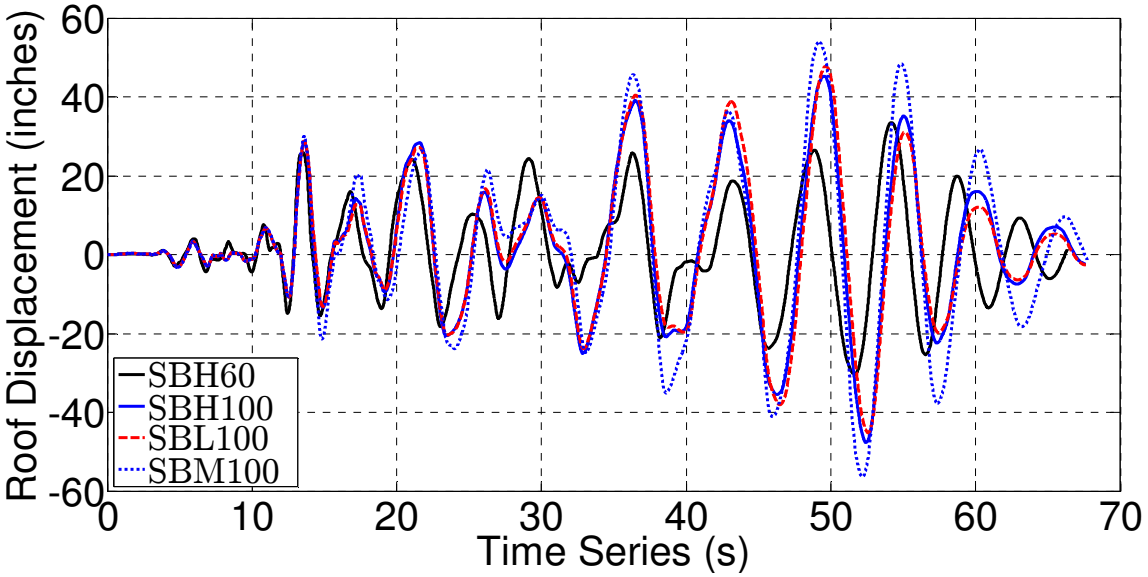

Figure 7.7.16: Roof Displacement Time Series of All Frames Subjected to Record Number 721 – Earthquake: Superstition Hills-02 – Station Name: El Centro Imp. Co. Cent – FN Component

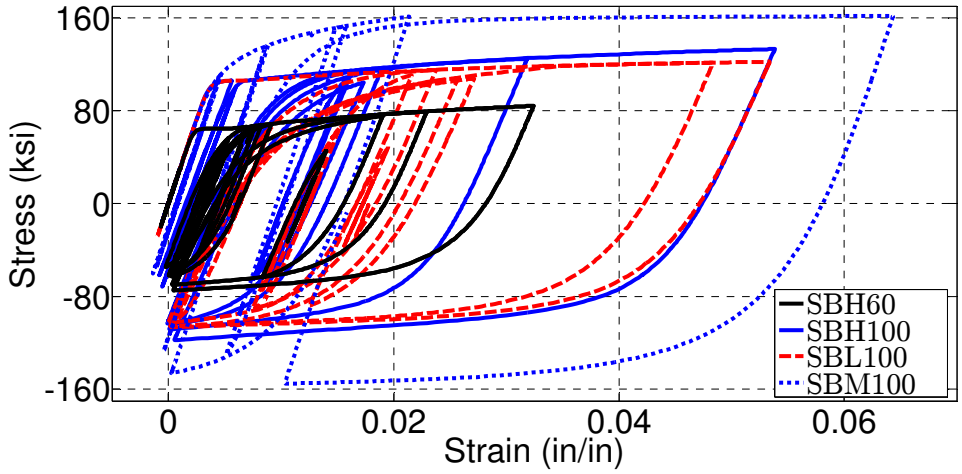

Figure 7.7.17: Stress-Strain Responses of One of the Beams in Frames Subjected to Record Number 721 – Earthquake: Superstition Hills-02 – Station Name: El Centro Imp. Co. Cent – FN Component

To study further into the difference in behavior between frames SBH100 and SBL100, analysis data of these two frames subjected to the ground motion measured at station El Centro

Array #9 from the Imperial Valley-02 earthquake is plotted in Figure 7.7.18. Despite the slight discrepancy in roof displacement response in the positive direction, the peak roof deflections are comparable for both frames. Longitudinal reinforcement in a typical beam in frame SBH100 attains lower peak strain than that in SBL100 as shown in Figure 7.7.19, most likely due to higher-strain hardening property of reinforcement. However, this higher-strain hardening increases moment strength in beams in frame SBH100, which in turn results in higher moment demand on the columns. Therefore, stress demand in longitudinal reinforcement in the columns is higher for frame SBH100, resulting in larger strain and rotation in the columns.

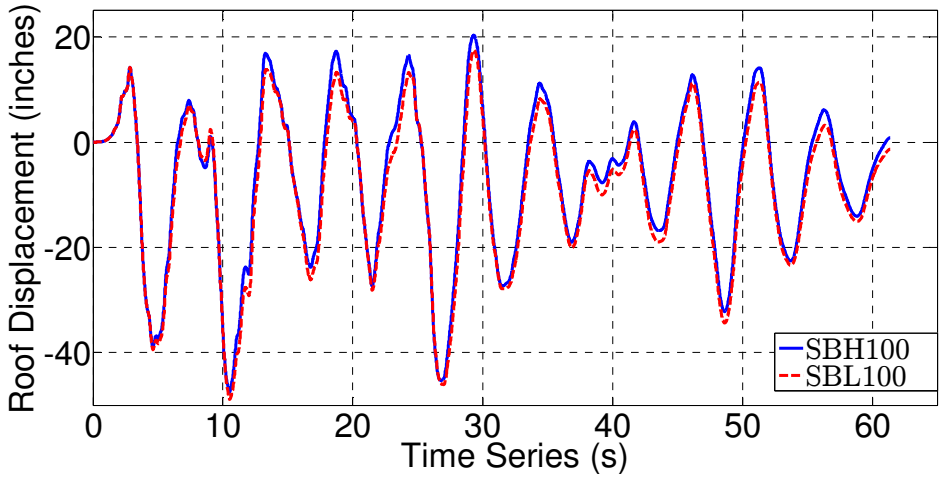

Figure 7.7.18: Roof Displacement Time Series of Frames SBH10 and SBL100 Subjected to Record Number 006 – Earthquake: Imperial Valley-02 – Station Name: El Centro Array #9

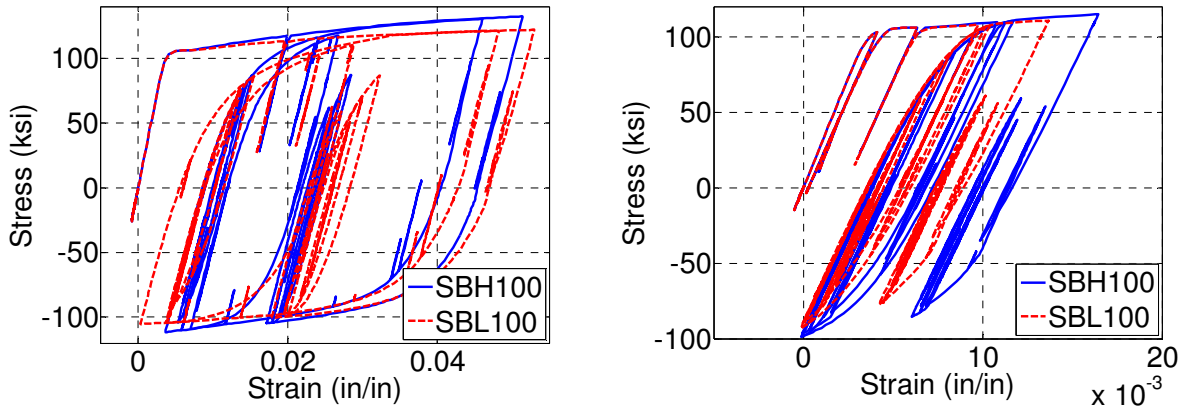

Figure 7.7.19: Stress-Strain Response of Frame Elements in SBH10 and SBL100 Subjected to Record Number 006 – Earthquake: Imperial Valley-02 – Station Name: El Centro Array #9 – Left: One of Beams – Right: Exterior Column at Base

Individual ground motion response quantities can be found in Appendix B. Average envelopes of all analyses including FN and FP components are presented in Figure 7.7.20 through Figure 7.7.23. Several representative response quantities computed from the analyses are summarized in Table 7.7.1. These values are the mean of peak responses calculated from the 20 ground motions including: roof drift ratio (roof displacement normalized by the height of the building), maximum story drift ratio along the building height, frame base shear normalized by half of building seismic weight, frame base moment normalized by the product of half the building seismic weight and two-third the height of the building, shear of exterior and interior columns at base level normalized by $A_g\sqrt{f_c'(psi)}$, and tensile and compressive force of exterior column at base level normalized by $A_g f_c'$. The FN and FP components are corresponding to MCE and RotD50 hazard levels as described in Section 7.6.

Table 7.7.1: Mean Values of Representative Response Quantities of Four Buildings Subjected to 20 Ground Motions

Response Quantity	**SBH60**		**SBH100**		**SBL100**		**SBM100**	
	FN	**FP**	**FN**	**FP**	**FN**	**FP**	**FN**	**FP**
Roof drift ratio (%)	1.15	0.90	1.30	1.07	1.30	1.07	1.46	1.20
Maximum story drift ratio (%)	2.02	1.50	2.20	1.90	2.20	1.90	2.30	2.13
Frame Base Shear, V/W	0.110	0.106	0.100	0.099	0.099	0.098	0.114	0.111
Frame Base Moment M/WH	0.079	0.075	0.069	0.064	0.067	0.063	0.084	0.076
Exterior base column shear, $V_{ext}/A_g\sqrt{f_c'(psi)}$	4.81	4.40	4.34	4.18	4.28	4.12	4.94	4.71
Interior base column shear, $V_{int}/A_g\sqrt{f_c'(psi)}$	3.60	3.50	3.34	3.31	3.30	3.29	3.85	3.76
Exterior base column tension, $T/A_g f_c'$	0.133	0.120	0.109	0.093	0.104	0.090	0.141	0.114
Exterior base column compression, $C/A_g f_c'$	0.308	0.297	0.279	0.264	0.272	0.260	0.330	0.304

In Figure 7.7.20, drift along height of the buildings is normalized by building height. It is apparent that frame SBH60 with conventional Grade 60 A706 reinforcement achieves the least roof drift of 1.15% while frame SBM100 with Grade 60 A1035 produces the largest roof drift of all frames at about 1.46%. Buildings SBH100 and SBL100 both obtain equivalent roof drift of 1.30%. Similar observation is made for story drift ratios plotted in Figure 7.7.21.

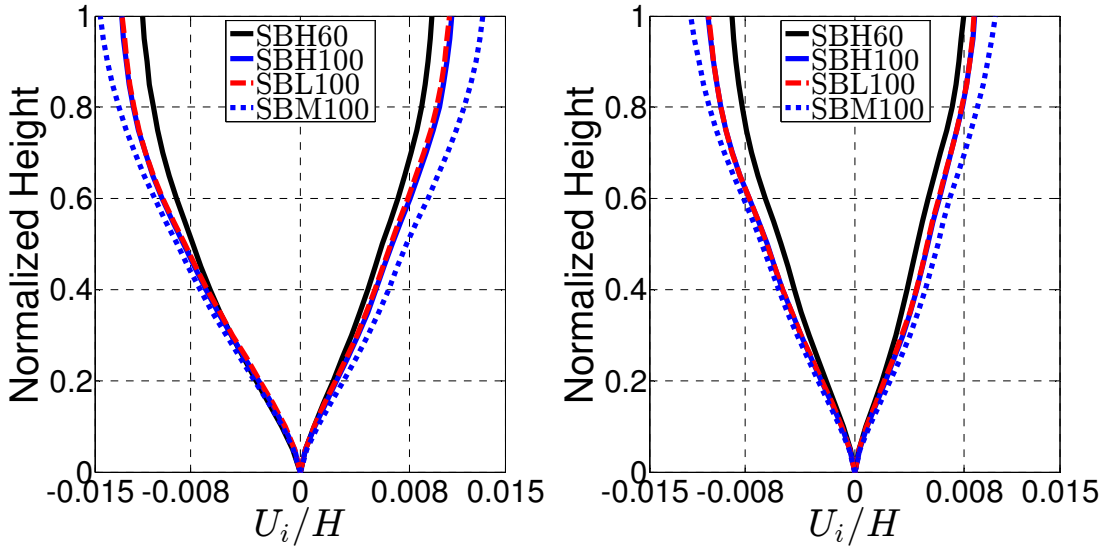

Figure 7.7.20: Average Displacement Envelopes – Left: FN Component – Right: FP Component

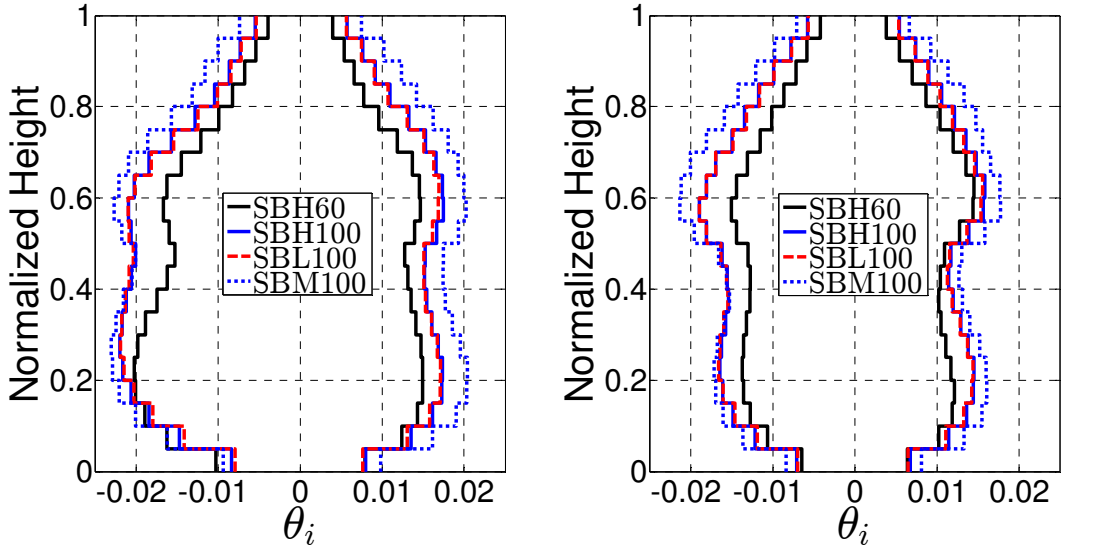

Figure 7.7.21: Average Story Drift Envelopes – Left: FN Component – Right: FP Component

Story shear is shown in Figure 7.7.22. Frame SBL100 attracts the least amount of story shear (approximately 10% of seismic weight) as expected since its longitudinal reinforcement of Grade 100 T/Y = 1.17 is the type of steel with lowest strain-hardening ratio. SBH100 with Grade 100 having slightly higher strain-hardening (T/Y = 1.26) attracts a little more shear force. Frame SBH60 attracts larger story shear force than SBL100 and SBH100. This may be attributable to larger amount of reinforcement and therefore greater stiffness, as well as higher strain-hardening ratio than both Grade 100 steels with distinct yield plateau. Frame SBM100 develops the most story shear of about 11.4% of the seismic weight, an increase of 14% compared to SBL100 and SBH100. This result is not unexpected, as Grade 100 A1035 has the highest ultimate stress of all higher-grade reinforcement and SBM100 is the strongest frame by the push-over analysis.

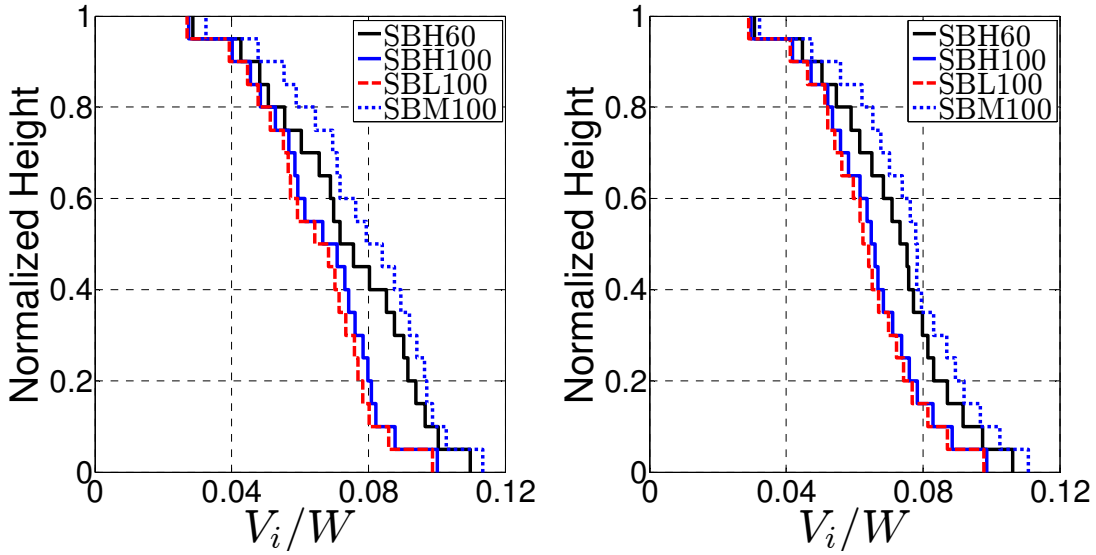

Figure 7.7.22: Average Story Shear Envelopes – Left: FN Component – Right: FP Component

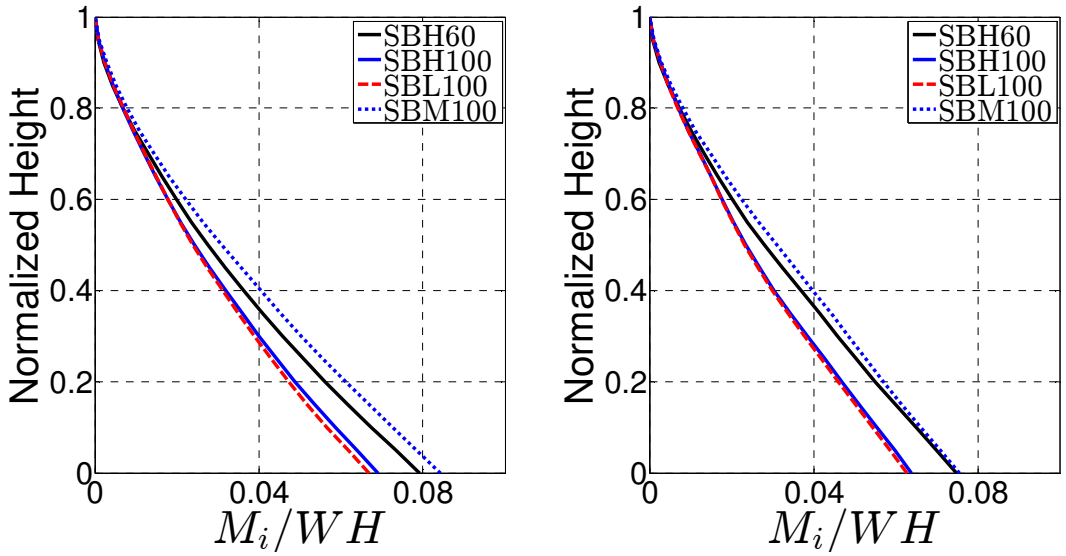

Figure 7.7.23: Average Story Moment Envelopes – Left: FN Component – Right: FP Component

Column Forces

Axial forces: axial forces in exterior columns of special moment frames subjected to earthquake excitation come from shear forces applied by moment frame beams responding at or near probable moment strengths plus column self-weight. Dead loads plus some portion of live loads may also result in additional vertical inertial forces if vertical ground motion component is present. In the present study, the effect of vertical ground motions was not included. Column axial force for design at level *i* can be estimated by:

$$P_{u,i} = P_{g,i} \pm \gamma_P \sum_{j=i}^{N} V_{pr,j} \qquad \text{Eq. (9)}$$

where $P_{u,i}$ = design axial force at level *i*,

$P_{g,i}$ = design axial force at level *i* due to gravity loads (1.0D + 0.25L)

$V_{pr,j}$ = shear due to M_{pr} at both levels of the beam at level *j* under zero gravity

γ_P = reduction factor to recognize that not all beams develop M_{pr} simultaneously, taken as 0.8 in this report as supported by Visnjic et al. (2014).

According to ACI 318-14, M_{pr} is calculated by using nominal (specified) concrete compressive strength $f_c' = 5000\ psi$ and elasto-plastic stress-strain relation for steel with yield stress equal to 1.25 times specified yield stress.

Comparison between external column axial forces calculated by the above equation and the average of those computed from dynamic analyses is presented in Figure 7.7.24 to Figure 7.7.27. For design purposes, one might choose to design for a force exceeding the average because of the critical nature of column axial performance relative to overall building performance. That aspect of design is not pursued here.

In Figure 7.7.24, it is observed that above equation marginally overestimates axial forces in columns in upper stories and underestimates those on lower stories for frame SBH60. The equation slightly overestimates axial loads for columns in all floors of frame SBL100, probably because of the lower hardening ratio of Grade 100 T/Y = 1.17 reinforcement used in frame SBL100.

In Figure 7.7.25, it is apparent that the equation considerably underestimates axial forces in column in frame SBM100. This occurs mainly because the ultimate strength of Grade 100 A1035 is about 1.6 times its specified nominal yield strength of 100 ksi, which is much higher than the factor 1.25 in calculation of M_{pr} in beams.

In tension, the equation consistently overestimates the tensile force in columns in all frames except those columns on the lowest stories in frame SBM100. The abrupt change in normalized axial load ratios at mid-height of buildings is due to the difference in sizes and concrete strength used in column design.

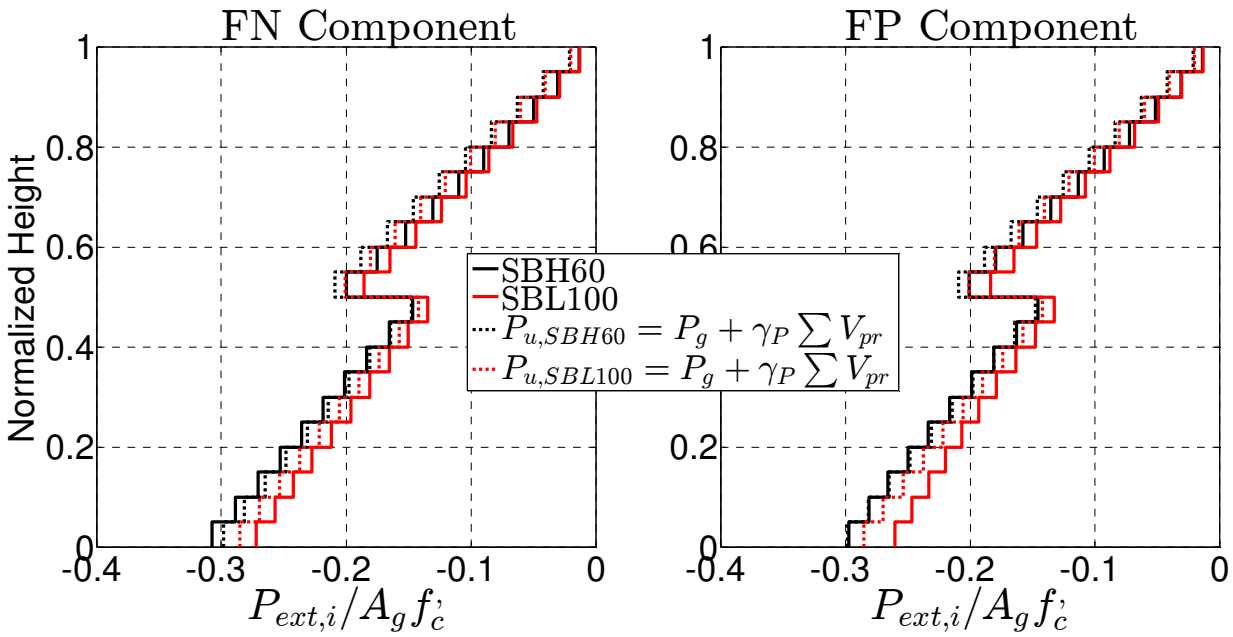

Figure 7.7.24: Exterior Column Compression in Frames SBH60 and SBL100

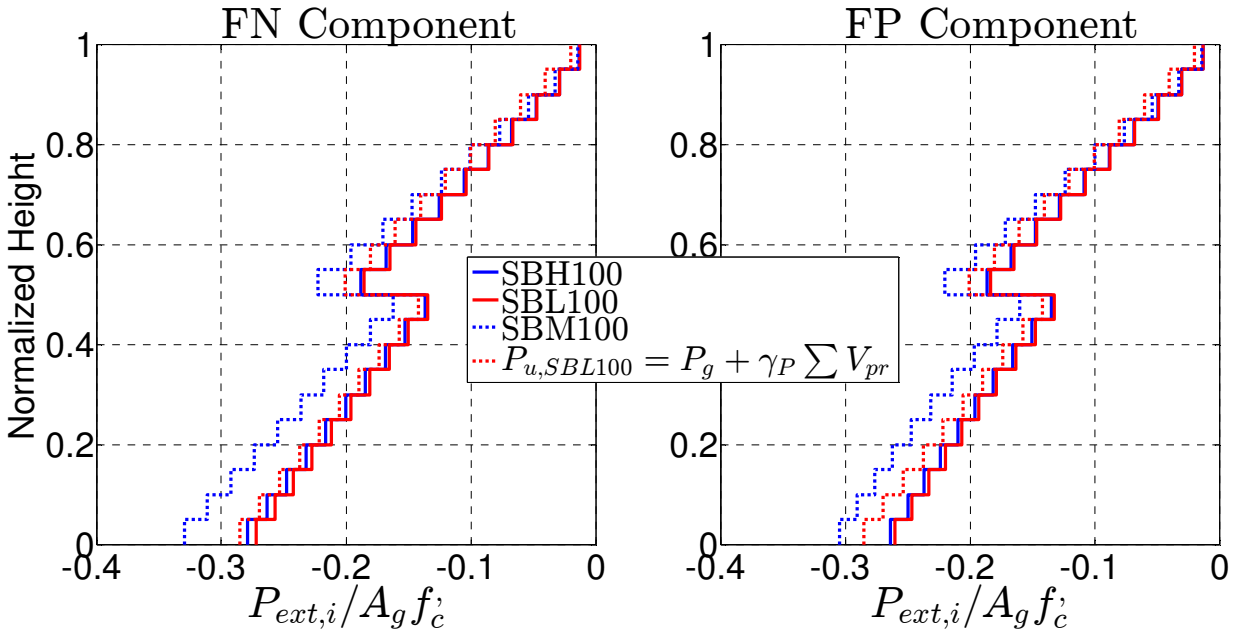

Figure 7.7.25: Exterior Column Compression in Frames SBH100, SBL100, and SBM100

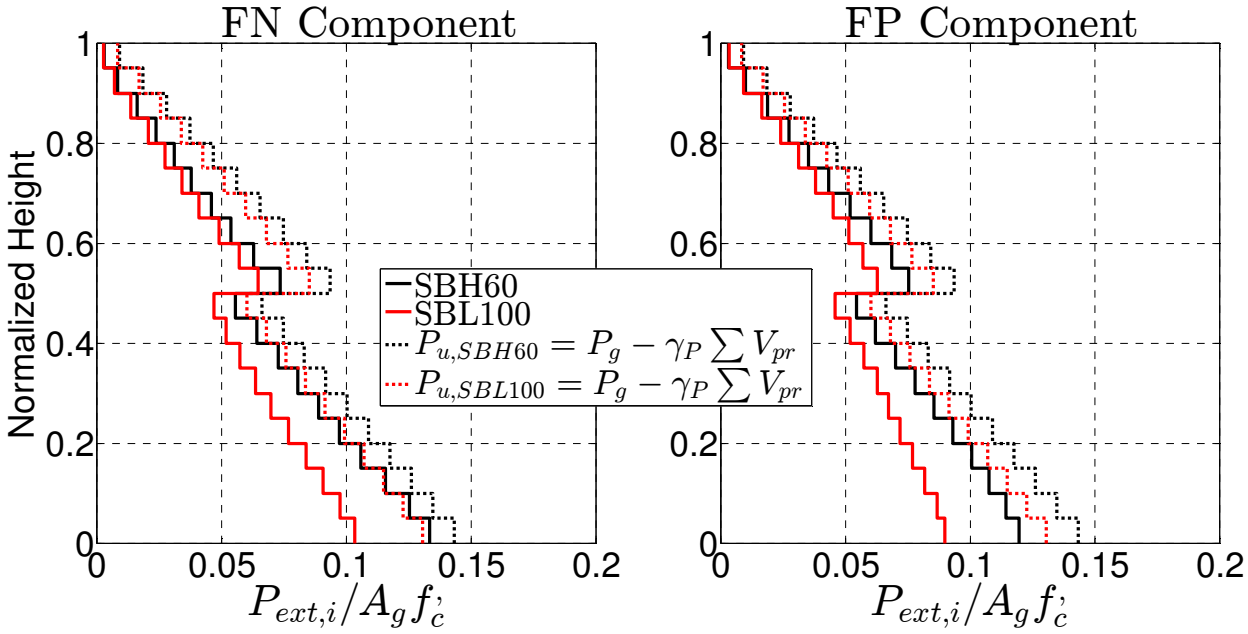

Figure 7.7.26: Exterior Column Tension in Frames SBH60 and SBL100

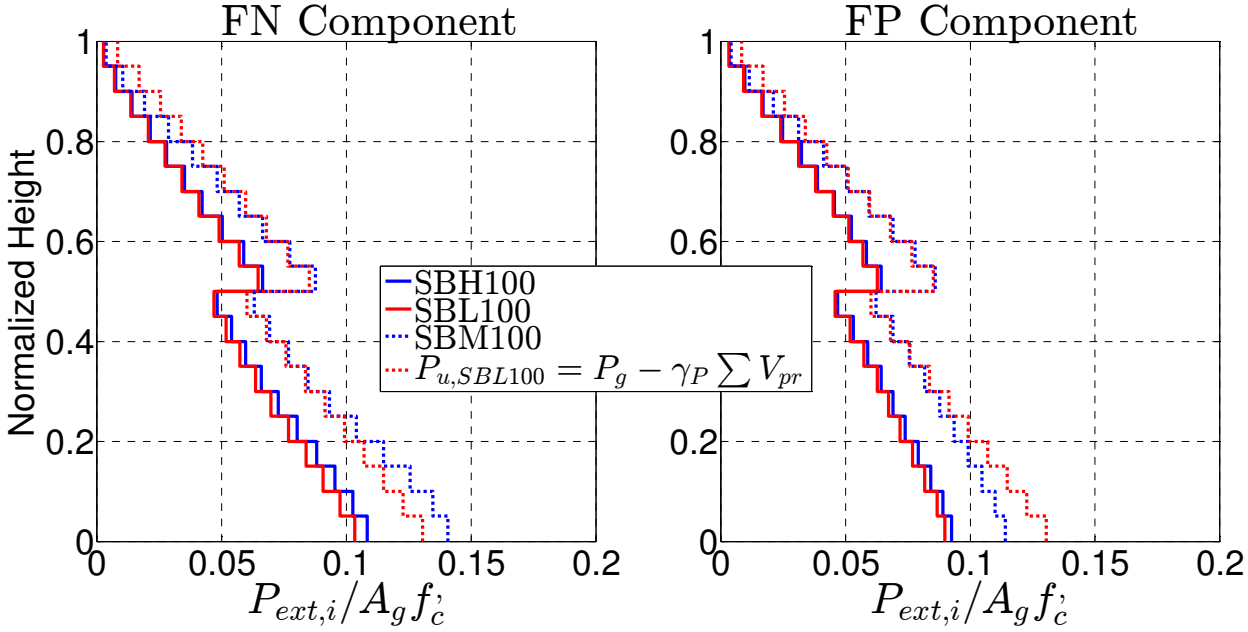

Figure 7.7.27: Exterior Column Tension in Frames SBH100, SBL100, and SBM100

Column shear: Estimation of column shear in design is challenging because the shear is occurring in columns of a frame in which the columns are designed to remain mainly in the linear range of response with primary yielding in the beams. It has been recognized that current methods for approximating design column shear in special moment frames do not always result in conservative estimates of shear forces that columns need to resist (Visnjic et al., 2014; Visnjic, 2014; Moehle, 2014; Moehle and Hooper, 2016). Underestimation of shear demand in columns could lead to column shear failure, which could cascade to more global response deficiencies, possibly including local or global collapse.

According to ACI 318-14, the column design shear force shall be calculated from considering the maximum forces that can be generated at the faces of the joints at each end of the column. These forces shall be calculated using the maximum probable moment strengths, $M_{pr,col}$, at each end of the column associated with the range of factored axial forces, P_u, acting on the column, that is, $V_{u,i} = \sum M_{pr,col,i}/l_{u,i}$. In tall buildings with large columns, this approach is known to result in large overestimation of column shears, and the transverse reinforcement required in some cases might be unfeasible to construct. Recognizing this, 318-14 allows that the column shears need not exceed those calculated from joint strengths based on $M_{pr,beam}$ of the beams framing into the joint. A widespread practice is to assume that the probable moment from the beams is resisted by equal column moments above and below the joint, resulting in column shear $V_{u,i} \approx \sum M_{pr,beam,i}/2l_{u,i}$. In the first story of buildings with fixed-base columns, one of the values in $\sum M_{pr,beam,i}$ is replaced by $M_{pr,col}$ at base of the building. A drawback of determining shears based on the beam moments is that the distribution of column moments above and below any beam-column joint is indeterminate. Studies (e.g., Kelly 1974) show that moment patterns can vary widely during seismic response. As a measure to avoid underestimating column design shear force when it is determined from the beam moments, ACI 318-14 also requires that the column design shear force shall be at least the shear from the controlling load combination determined by (linear) analysis of the structure. This latter provision seldom controls the column design.

Visnjic et al. (2014) and Moehle (2014) proposed that an improved estimate of column design shear can be obtained by amplifying the shear obtained from the linear analysis of the structure. The amplification factors consider system overstrength and dynamic effects. Based on this procedure, design column shears can be computed by:

$$V_u = \omega\Omega_0 V_{MRSA} + V_G \qquad \text{Eq. (10)}$$

where V_G = column shear due to gravity load with combination of $1.0D + 0.25L$
V_{MRSA} = column shear obtained from modal response spectrum analysis
ω = 1.3 as a dynamic amplification factor
Ω_0 = overstrength of the structural system, which can be approximated as

$$\Omega_0 = \frac{\sum M_{pr}}{\sum M_{u,MRSA}} \qquad \text{Eq. (11)}$$

$\sum M_{pr}$ = sum of probable moment strengths of all beam and column plastic hinges in a beam-yielding mechanism. For columns, M_{pr} is estimated assuming axial load corresponding to gravity load of $1.0D + 0.25L$.

$\sum M_{u,MRSA}$ = sum of the moments calculated from modal response spectrum analysis at all beam and column plastic hinge locations of the same beam-yielding mechanism in absence of gravity loads.

Note that column shear in Eq. (10) could also include effects of vertical seismic actions using load combinations of ASCE 7. However, such effects were not represented in the dynamic analyses presented here, so they are not included in the design equation either.

Column shear forces computed by these various approaches are plotted and compared against the average of the column shears from nonlinear dynamic analyses in Figure 7.7.28 and Figure 7.7.29. As expected, $V_{u,i} = \sum M_{pr,col,i}/l_{u,i}$ results in large overestimation of column shears in all cases. $V_{u,i} = \sum M_{pr,beam,i}/2l_{u,i}$ provides a reasonable central approximation of the shears, but underestimation or overestimation in individual stories appear to be unacceptably large. The shear obtained from the controlling load combination determined by linear analysis of the structure V_{MRSA} is well below the shear obtained from nonlinear dynamic analysis, as is typically the case. The last approach of amplifying V_{MRSA} in accordance with Eq. (10) produces the best overall estimate of shear in all exterior, interior, and middle columns. However, it is worth noting that shear in the exterior columns of the first story is underestimated by this method as it does not account for the effects of beam elongation, which pushes the first-story columns outward, thereby increasing the first-story shear (Visnjic et al., 2014; Moehle, 2014).

It can also be observed that the last method slightly overestimates shear in exterior columns for frames SBH100 and SBL100 as these frames are reinforced with higher-grade steel that has lower strain-hardening ratio than that of conventional Grade 60 A706. Hence, the overstrength factor of the structural system is overestimated for these two frames. Nevertheless, the method provides better agreement in shear forces in columns for frame SBM100.

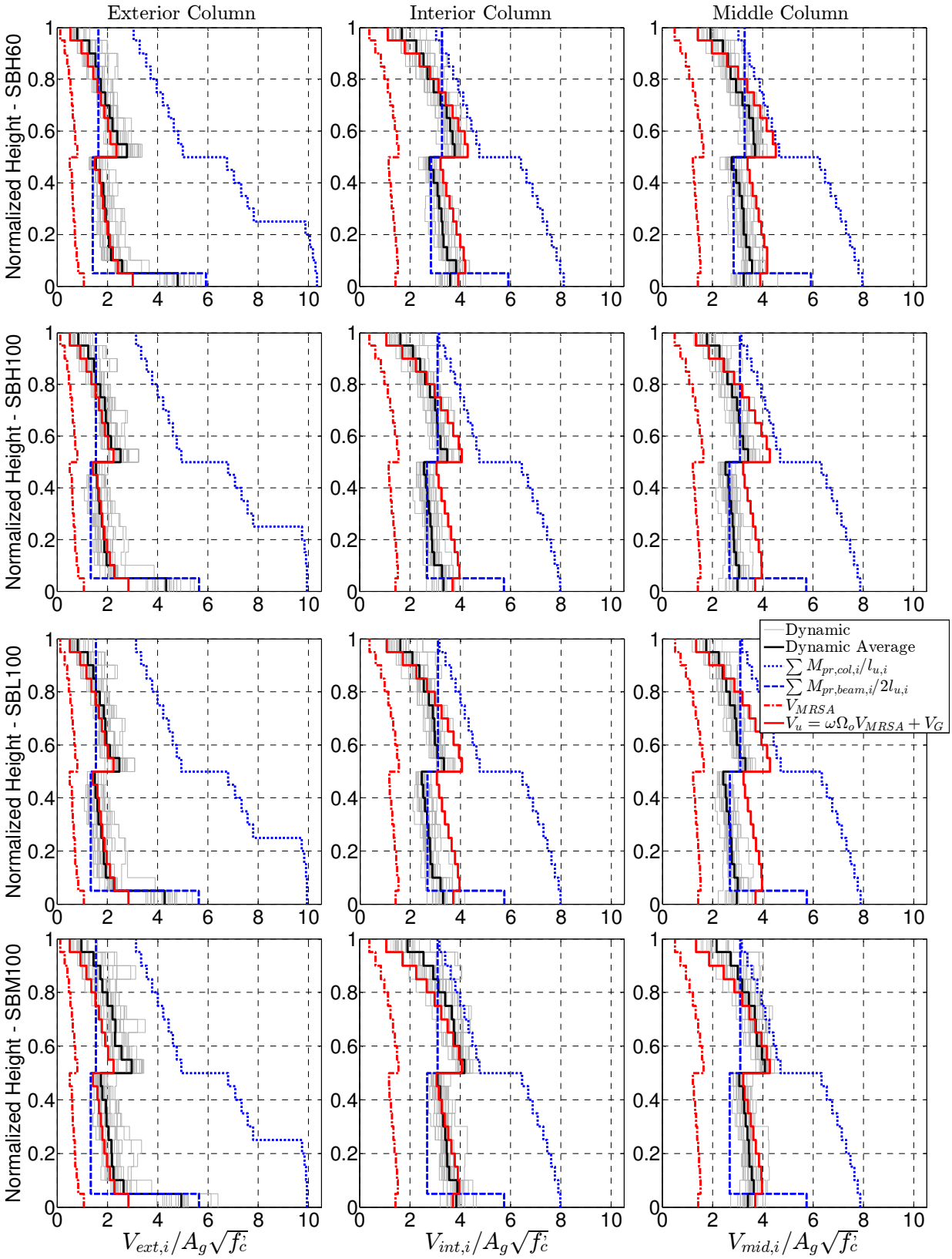

Figure 7.7.28: Column Shear in All Frames – FN Component

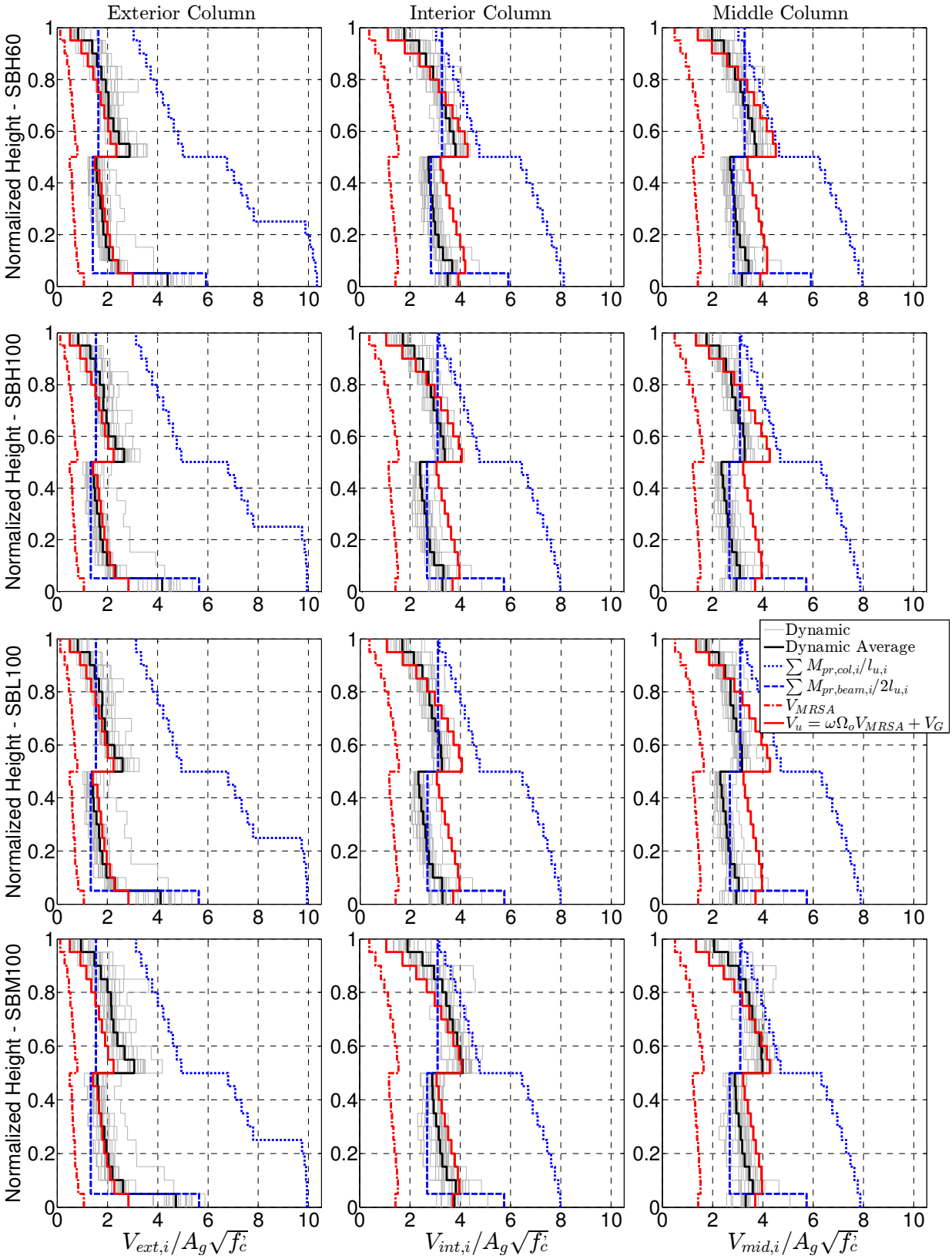

Figure 7.7.29: Column Shear in All Frames – FP Component

In general, the method of amplifying MRSA reasonably estimates shear for exterior columns but overestimates shear for interior and middle columns. Visnjic (2014) discussed an alternative to estimate design shear of all columns in a consistent manner, in which dynamic amplification factor, ω, was reduced from 1.3 to 1.25 and another magnification factor of 1.2 was applied to shear of exterior columns only. Additionally, the method renders inconsistent approximation of column shear on upper half of all frames for all column types due to the effects of higher modes in dynamic response of frame buildings. It has been proposed by Visnjic (2014) to increase column shear of buildings by a shape factor. This shape factor is taken as unity in the bottom half of the building and starts varying linearly from half height to the top of the building, where it is recommended to have value of 1.4 and 1.6 for DE and MCE level of earthquake intensities, respectively.

Also, the column shear computed by MRSA procedure was based on M_{pr} of framing elements with nominal properties of steel reinforcement. According to ACI 318, M_{pr} is calculated assuming elasto-plastic steel stress-strain relation in tension and compression with the yield stress equal to $1.25f_y$ and f_y is the specified yield stress. The factor 1.25 has been intended to account for the actual yield stress and strain-hardening properties of Grade 60 reinforcing steel. From the laboratory tests of beam specimens, it is evident that various strain-hardening properties of different types of reinforcement resulted in different expected moment strengths across test beams although they all provided equivalent yield moment strength (Figure 4.4.5 and Figure 5.2.1 through Figure 5.2.4). Furthermore, OpenSees frame models had steel material models that were calibrated against measured stress-strain relations of longitudinal reinforcement used in laboratory test beams. Therefore, it is justifiable to estimate column shear force using measured steel ultimate strength.

Employing measured ultimate strength of reinforcing steel and proposed procedure by Visnjic (2014) with dynamic amplification factor, magnification factor, and shape factor of 1.0, 1.3, and 1.4, respectively, column shear is computed and compared against results from nonlinear dynamic analyses in Figure 7.7.30 and Figure 7.7.31. It should be noted that these factors are slightly different than those recommended by Visnjic (2014). Overstrength factor, Ω_0, of the structural system in Eq. (11) is still applied to shear calculation as previous MRSA method. Slightly different procedure of estimating column shear than that by Visnjic (2014) is proposed as following steps:

1. Compute column shear of moment frame by elastic MRSA procedure of ASCE 7.
2. Calculate probable moment strength of beams and columns at location of expected plastic hinges in a beam-yielding mechanism. For columns, M_{pr} is estimated assuming axial load corresponding to gravity load of $1.0D + 0.25L$. Expected ultimate strength of steel reinforcement is used.
3. Determine overstrength, Ω_0, of structural system in Eq. (11).
4. Select dynamic amplification factor $A_D = 1.0$

5. Use shape factor on top of building $\Psi_N = 1.4$ and compute Ψ_i:

$$\Psi_i = 1 \quad for\ \frac{h_i}{H} < 0.5$$

$$\Psi_i = 1 + (\Psi_N - 1)\left(\frac{2h_i}{H} - 1\right) \quad for\ \frac{h_i}{H} \geq 0.5$$

6. Interior columns: $V_{u,i} = \Omega_0 A_D \Psi_i V_{MRSA} + V_G$
   Exterior columns: $V_{u,i} = 1.3\Omega_0 A_D \Psi_i V_{MRSA} + V_G$

This approach results in better approximation of shear demand on most columns, and marginally overestimates that for middle columns on upper half stories of frame SBH60 and SBM100 (Figure 7.7.30 and Figure 7.7.31). It is important to acknowledge once again that such approximation of column shear was calculated utilizing measured properties of reinforcing steel. These properties were also used to calibrate steel material models that were implemented in OpenSees frame models.

During the design phase of reinforced concrete constructions, actual material properties are typically unknown. Modeling and analyses of structures are permitted to be done assuming the expected material strengths (TBI, 2016 and LATBSDC, 2017). Consequently, it is proposed in this study that expected material strengths be employed in estimating design column shear for newly designed frame buildings.

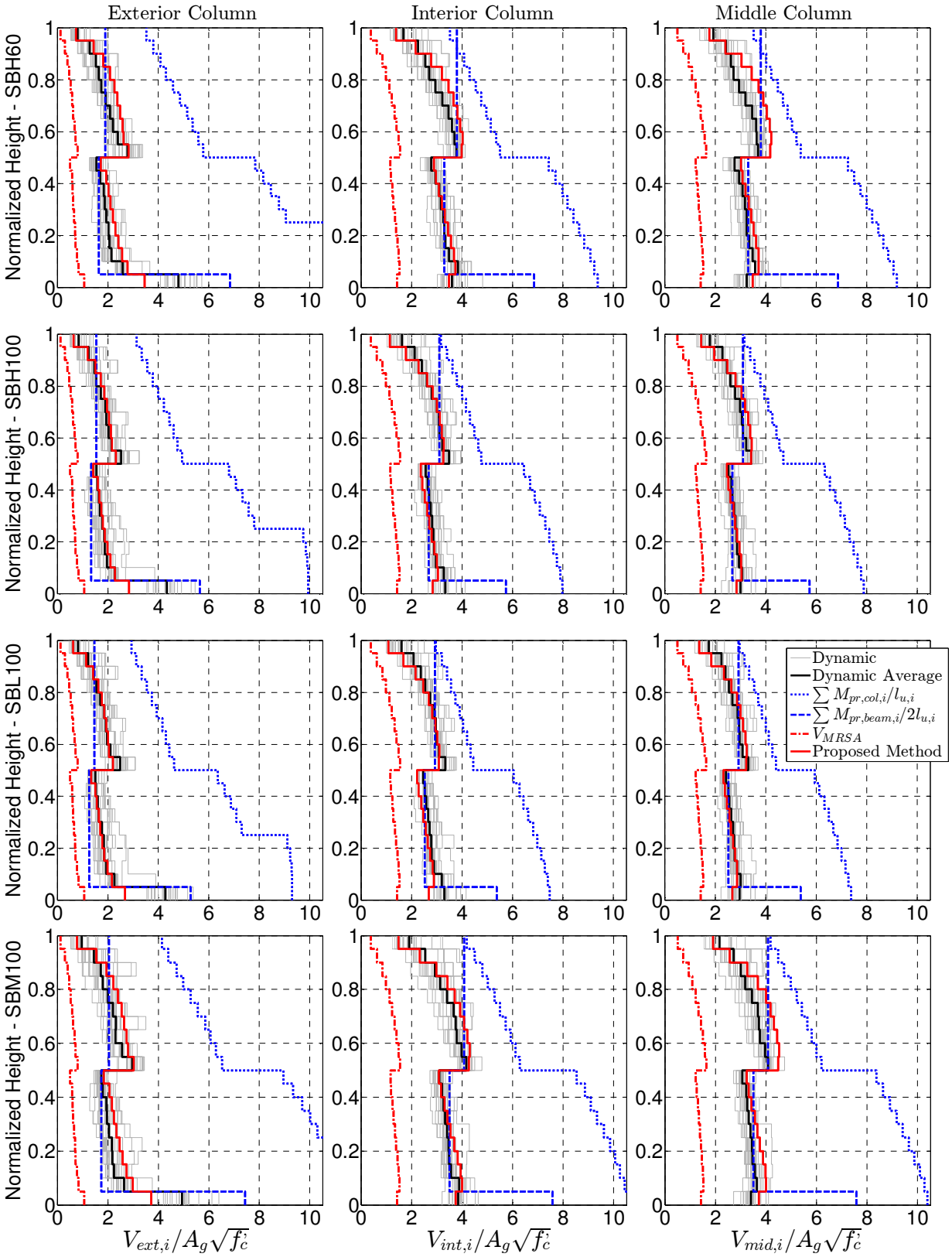

Figure 7.7.30: Column Shear in All Frames – FN Component

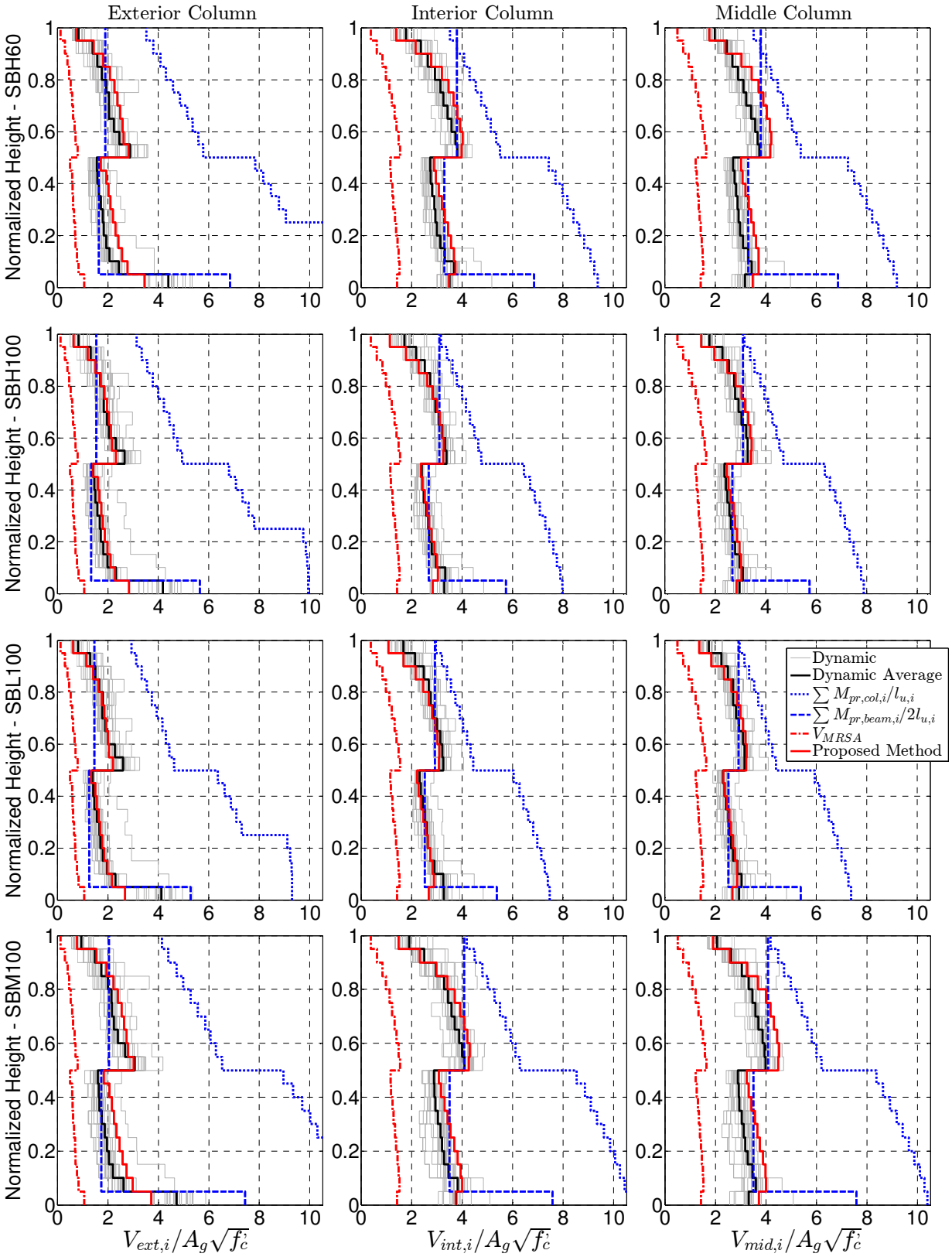

Figure 7.7.31: Column Shear in All Frames – FP Component

CHAPTER 8: LOW-CYCLE FATIGUE DAMAGE

Under earthquake excitation, a building may experience numerous displacement cycles beyond yield. Being a principal source of rotation, beam elements are expected to be subjected to the most severe cyclic deformation demand. The repeated loading may reduce available strain capacity and may cause fracture as a result of low-cycle fatigue. This section uses available data and the results of the calculated building dynamic responses to estimate whether low-cycle fatigue failure should be a consideration in design of frames using high-strength reinforcement.

8.1. LOW-CYCLE FATIGUE MODELS

Existing low-cycle fatigue models are described in Chapter 2. Several models are selected based on similar properties of test specimens, summarized in Table 8.1.1, and plotted in Figure 8.1.1. Among the available models and data, those presented by Ghannoum and Slavin (2016) are based on materials and clear spacing limits ($5d_b$) most similar to those used in the present study. Therefore, they are used to evaluate fatigue response of longitudinal bars in beams of frames with Grade 60 and Grade 100 reinforcement studied in this dissertation. Note, however, that fatigue models for A1035 Grade 100 were not developed at the time of this writing.

As required by ACI 318-14, where Grade 60 reinforcement is used, spacing of the hoops shall not exceed the least of (a) $d/4$, (b) $6d_b$, and (c) 6 inches. For frame model SBH60 with conventional Grade 60 reinforcement, this requirement applies and hoop spacing is governed by (c) 6 inches. In typical beam elements, No. 9 or No. 10 longitudinal bars were used in the design, resulting in transverse reinforcement spacing of approximately $5d_b$. For the other frame models SBH100, SBL100, and SBM100 with high-strength reinforcement, the hoop spacing was based on the recommendation of NIST (2014), which was $5d_b$. Therefore, low-cycle fatigue models provided by Ghannoum and Slavin (2016) for both A706 Grade 60 and Grade 100 tested by $5d_b$ are applicable in the assessment of fatigue performance of longitudinal reinforcement in the archetype frames in this study.

Table 8.1.1: Low-Cycle Fatigue Models

Eq.	Author	Steel type	Grade	Bar Size	Clean Span	M	m
1	Mander et al. (1994)	ASTM A615	40		$6d_b$	0.0795	-0.448
2	Brown & Kunnath (2004)	ASTM A615	60	No. 8	$6d_b$	0.0800	-0.360
3	Hawileh et al. (2010)	ASTM A706	60	No. 6	$6\ in.$	0.0900	-0.409
4	Ghannoum & Slavin (2016)	ASTM A706	60	No. 8	$5d_b$	0.0785	-0.361
5	Ghannoum & Slavin (2016)	ASTM A706	60	No. 8	$6d_b$	0.0772	-0.386

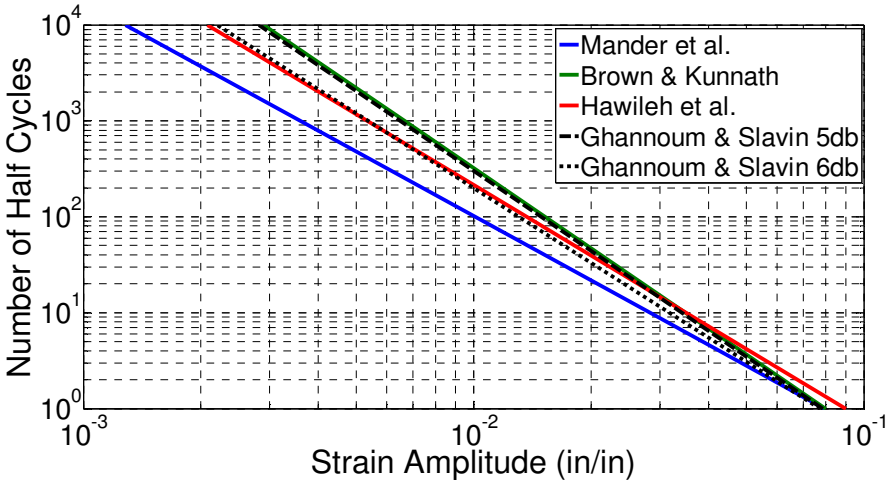

Figure 8.1.1: Fatigue Models for Grade 60 Steel

8.2. RAINFLOW COUNTING METHOD

Matlab function "Rainflow Counting Algorithm" developed by Nieslony (2010) based on rainflow-counting method (ASTM E1049-85, 2005) was applied to the strain response histories to determine the number of cycles and corresponding strain amplitudes used in damage evaluation (the Matlab function can be found on Matlab File Exchange website). The method was tested manually to verify that it was correctly implementing the rainflow-counting method.

As an example, Figure 8.2.1 depicts strain response history of one longitudinal bar over a selected time interval. Local peaks and troughs are determined and plotted in Figure 8.2.2. The number of cycles is determined by applying the "Rainflow Counting Algorithm" to the local peak

strain response history and shown in Figure 8.2.3. The corresponding strain amplitudes are displayed in Table 8.2.1.

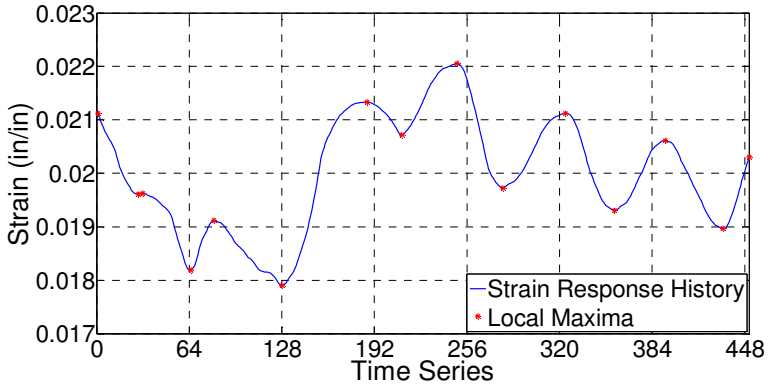

Figure 8.2.1: Example of Strain Response History and Determination of Local Maxima

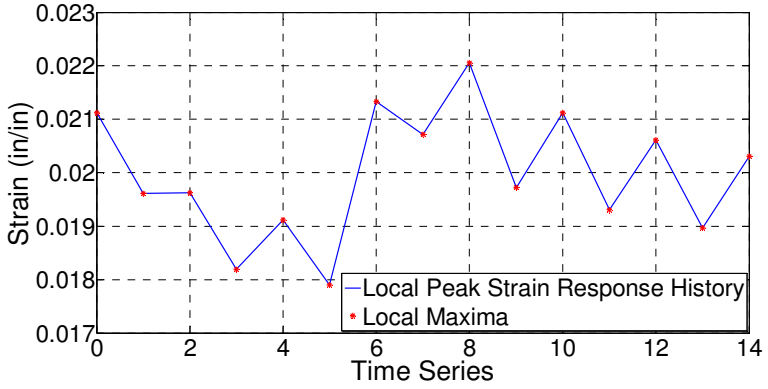

Figure 8.2.2: Local Peak Strain Response History

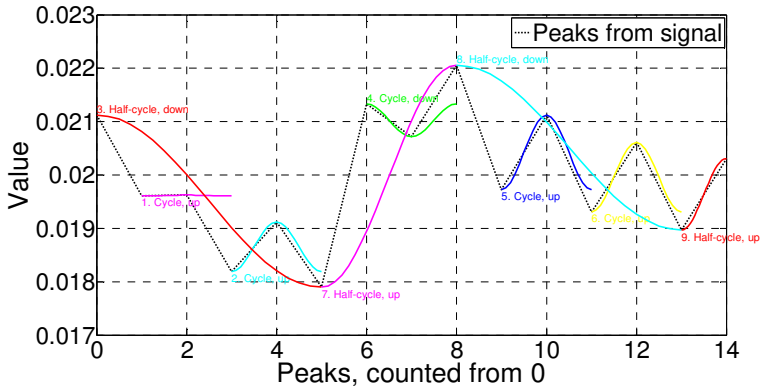

Figure 8.2.3: Rainflow Counting Algorithm (developed by Adam Nieslony)

Table 8.2.1: Output from Rainflow Counting Algorithm (developed by Adam Nieslony)

Cycle	1	2	3	4	5	6	7	8	9
Amplitude	0.0000	0.0005	0.0016	0.0003	0.0007	0.0007	0.0021	0.0015	0.0007
Mean Value	0.0196	0.0187	0.0195	0.0210	0.0204	0.0200	0.0200	0.0205	0.0196
Number of Cycles	1.0	1.0	0.5	1.0	1.0	1.0	0.5	0.5	0.5

8.3. DAMAGE COMPARISON BETWEEN TEST BEAMS AND BEAM MODELS

Strain response of longitudinal reinforcement at the base of test beams and computed by OpenSees models are used to evaluate the validity of low-cycle fatigue models. Figure 8.3.1 displays cyclic strain response of a longitudinal bar of test beam SBL100 measured by strain gauges during testing. Filtered data in this plot were processed using the moving average technique and smoothened to ease subsequent procedures. Peaks and troughs of filtered data are determined and displayed in Figure 8.3.2. The last ascending branch of strain response recorded by the strain gauge might not be accurate and reliable as it had been strained beyond the working strain range of 0.1 (10%). Similar bars had been tested at University of Texas, Austin to develop the low-cycle fatigue model for this type of steel bar. Fracture strain was reported to be 0.098 (9.8%) (Ghannoum and Slavin, 2016). Taking this value to be the maximum strain in the last ascending branch that longitudinal bar of beam SBL100 had ever reached, the cumulative damage of this bar in beam SBL100 is calculated to be 1.02.

Similarly, strain response of a longitudinal bar at the base of the OpenSees beam model is shown in Figure 8.3.3 and compared against that recorded during the test of beam SBL100 in Figure 8.3.4. Although strain of longitudinal bar calculated in OpenSees model for beam SBL100 reached 0.084 at peak, which was less than fracture strain of 0.098, the cumulative damage of steel bar in the beam model is computed to be 1.30, which is about 30% larger than that from the beam test. The discrepancy is substantially due to the strain range between tensile and compressive strains, which, as discussed in Chapter 6 (Section 6.1.f), was not well modeled by the numerical model.

The same overconservatism in evaluating low-cycle fatigue life of longitudinal reinforcement in OpenSees model is observed for the other test beams SBH60 and SBH100. Figure 8.3.5 and Figure 8.3.6 compare measured strain data and calculated strains from the OpenSees models for specimens SBH100 and SBH60, respectively. Damage indices computed for the longitudinal bar in test beam SBH100 and its numerical model are 0.16 and 0.50, respectively. Those for beam SBH60 and corresponding model are 0.04 and 0.17. Therefore, results of low-cycle fatigue characteristics of frame models are expected to be conservative.

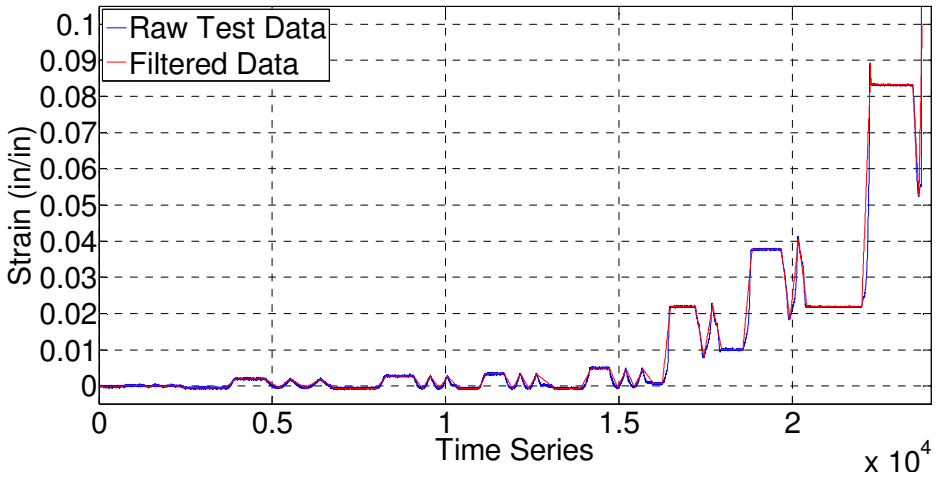

Figure 8.3.1: Strain Response of Longitudinal Bar at Base of Beam SBL100

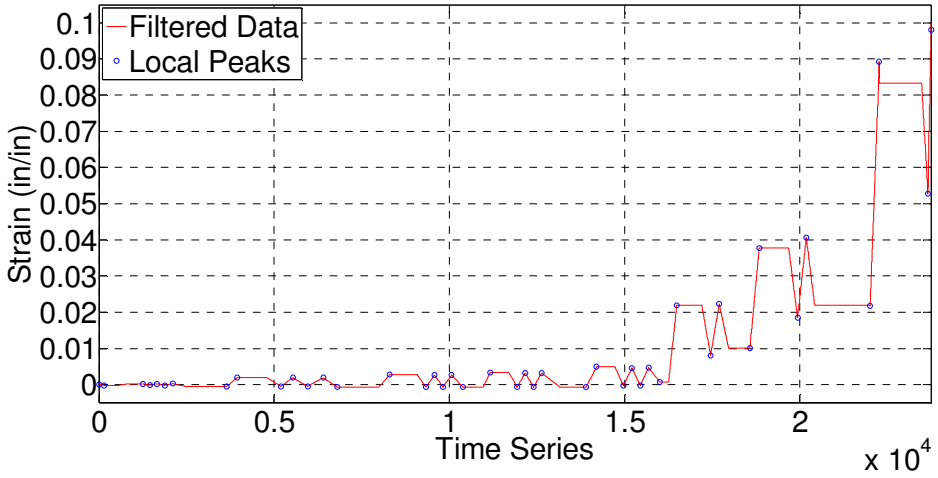

Figure 8.3.2: Filtered Strain Response of Longitudinal Bar at Base of Beam SBL100

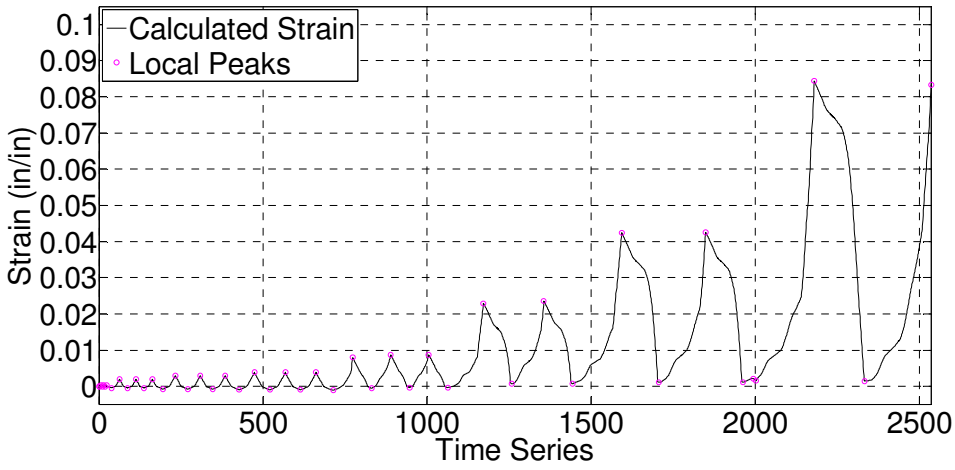

Figure 8.3.3: Strain Response of Longitudinal Bar at Base of OpenSees Model SBL100

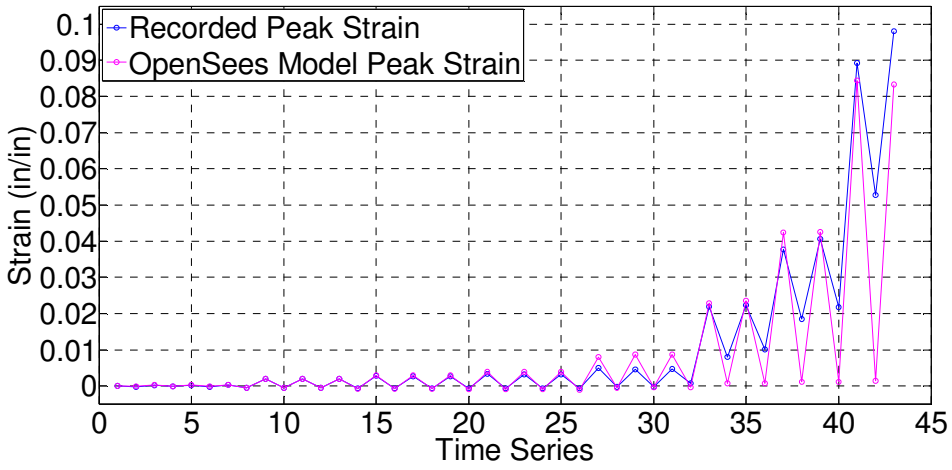

Figure 8.3.4: Strain Response of Longitudinal Bar of Test Beam SBL100 and OpenSees Model

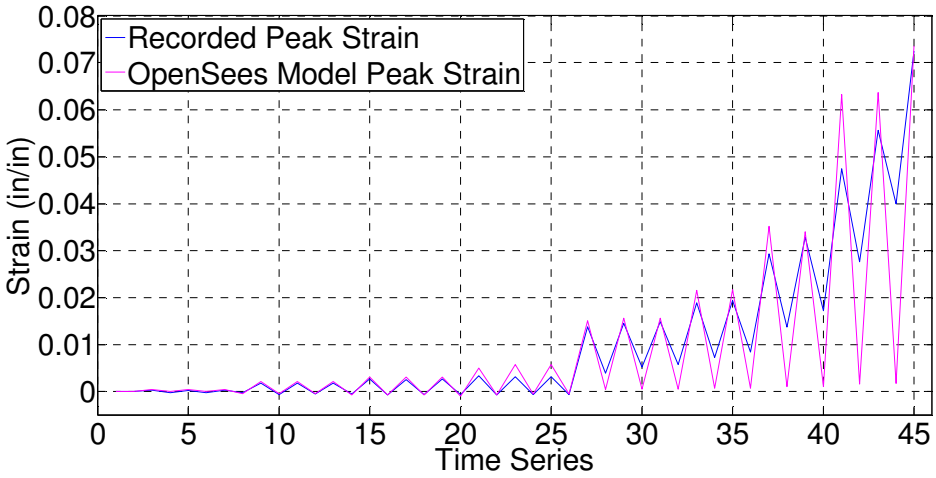

Figure 8.3.5: Strain Response of Longitudinal Bar of Test Beam SBH100 and OpenSees Model

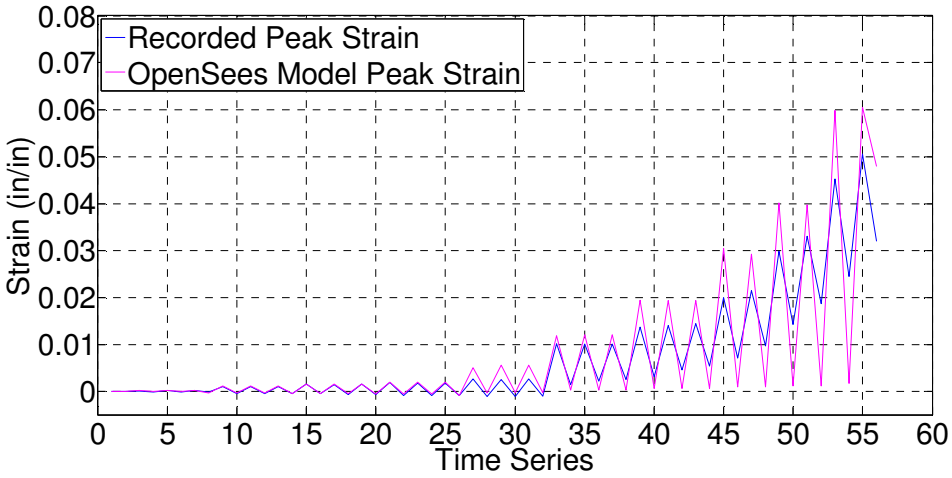

Figure 8.3.6: Strain Response of Longitudinal Bar of Test Beam SBH60 and OpenSees Model

8.4. LOW-CYCLE FATIGUE PERFORMANCE OF FRAME BUILDINGS

For each strain response history calculated from the nonlinear dynamic analyses, the rain-flow counting algorithm is applied to determine the number of cycles and their corresponding strain amplitude. Low-cycle fatigue models proposed by Ghannoum and Slavin (2016) for Grade 60 A706 and Grade 100 at $5d_b$ are applied to total strain range ($total\ strain\ range = 2 \times strain\ amplitude$) for all cycles determined by the rain-flow counting method to find the number of half-cycles associating with fracture of reinforcing bars. The fatigue models are represented by the following expressions.

Grade 60 (SBH60) at $5d_b$: $2N_f = 5.92E \times 10^{-3} \times (total\ strain\ range)^{-2.77}$

Grade 100 (SBH100) at $5d_b$: $2N_f = 8.14E \times 10^{-5} \times (total\ strain\ range)^{-4.06}$

Grade 100 (SBL100) at $5d_b$: $2N_f = 2.60E \times 10^{-6} \times (total\ strain\ range)^{-5.25}$

Subsequently, Miner's rule (Miner, 1945) is adopted to compute and accumulate damage. Damage in half cycle i is given by

$$D_i = \frac{1}{2N_{fi}}$$

Total damage is the linear sum of damage in the individual half cycles

$$D = \sum D_i$$

Strain of the middle longitudinal bars on top and bottom of sections 1 and 5 in all beam elements of frame models SBH60, SBH100, and SBL100 (Chapter 7) calculated from all dynamic analyses were assessed (Figure 8.4.1). Location and index of beam elements in all frame models are as shown in Figure 8.4.2. Figure 8.4.3 through Figure 8.4.10 display the mean low-cycle fatigue damage indices of these longitudinal bars in frames SBH60, SBH100, and SBHL100 under FN and FP component ground motions. Results from individual motions can be found in Appendix B.

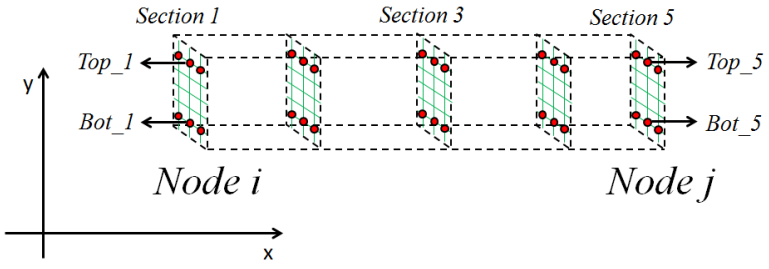

Figure 8.4.1: Locations of Longitudinal Bars Used in Low-Cycle Fatigue Assessment

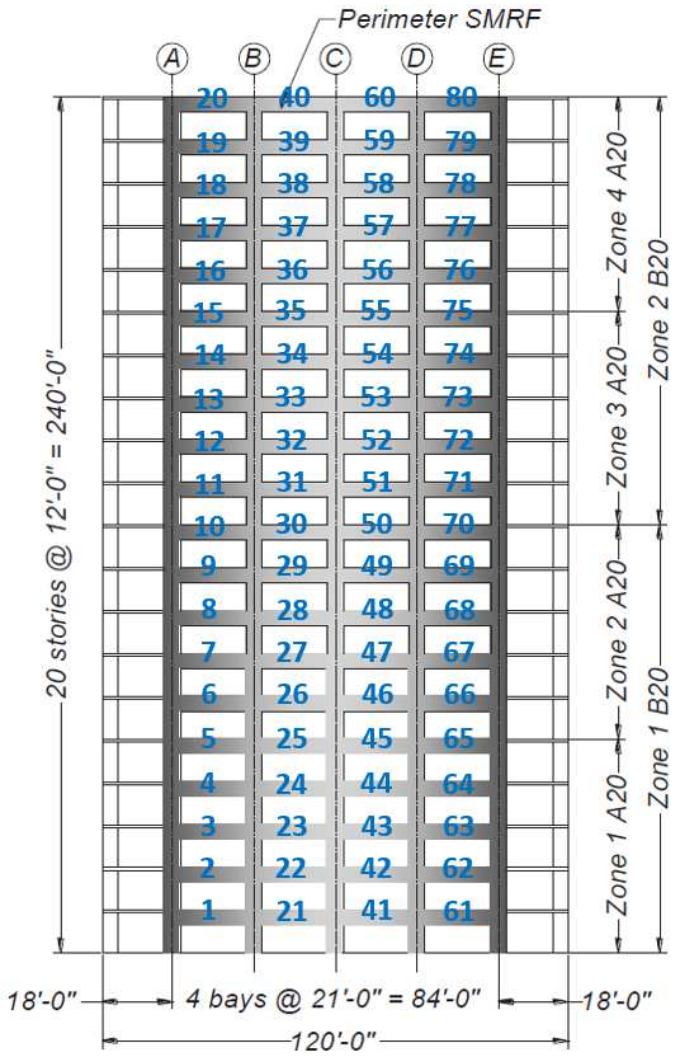

Figure 8.4.2: Location and Designation of Beam Elements in Frame Models

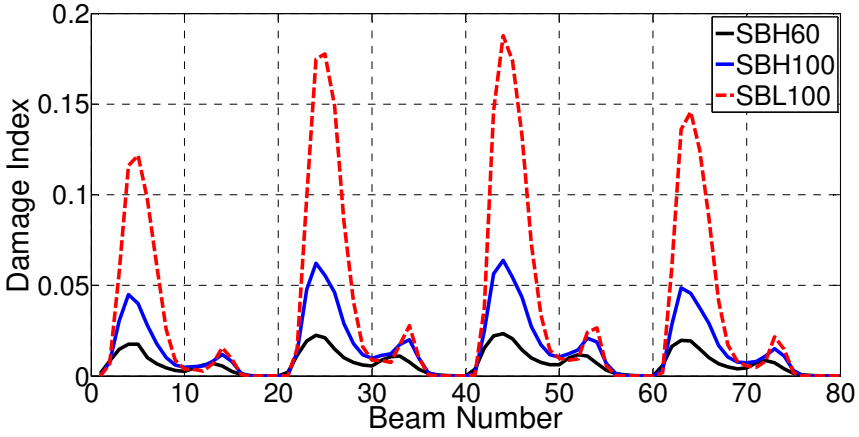

Figure 8.4.3: Mean Low-Cycle Fatigue Damage of Longitudinal Bar Bot_1 in Beams - FN Component

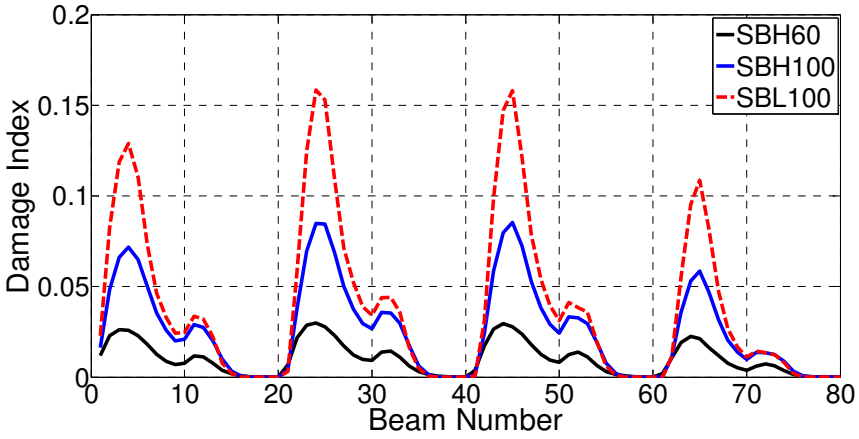

Figure 8.4.4: Mean Low-Cycle Fatigue Damage of Longitudinal Bar Top_1 in Beams - FN Component

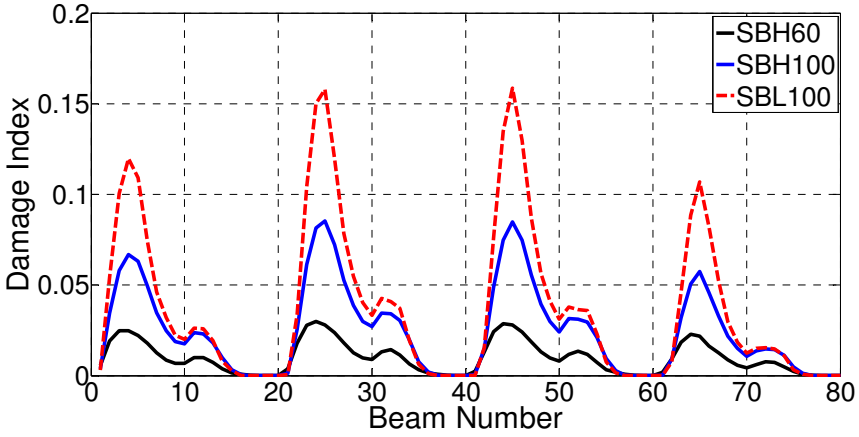

Figure 8.4.5: Mean Low-Cycle Fatigue Damage of Longitudinal Bar Bot_5 in Beams - FN Component

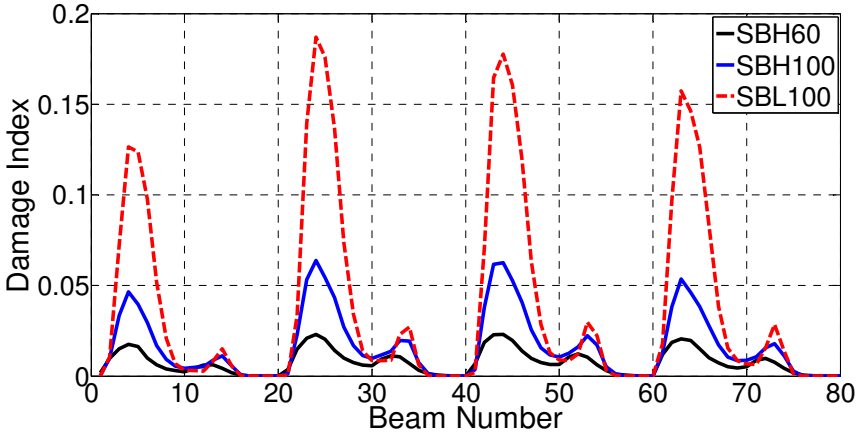

Figure 8.4.6: Mean Low-Cycle Fatigue Damage of Longitudinal Bar Top_5 in Beams - FN Component

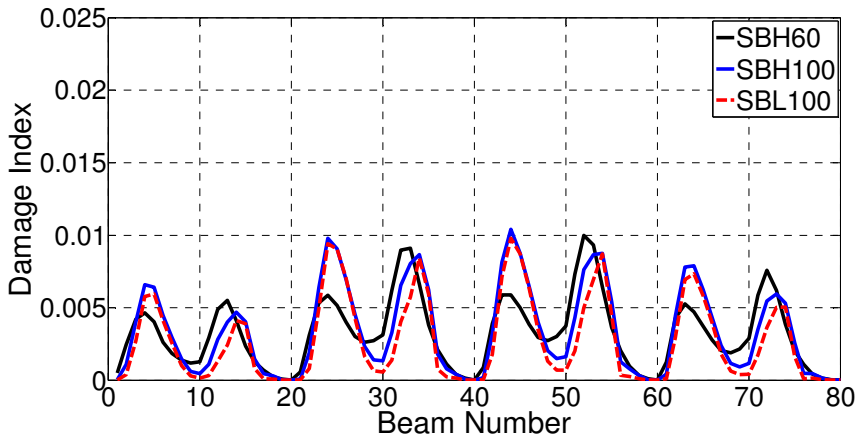

Figure 8.4.7: Mean Low-Cycle Fatigue Damage of Longitudinal Bar Bot_1 in Beams - FP Component

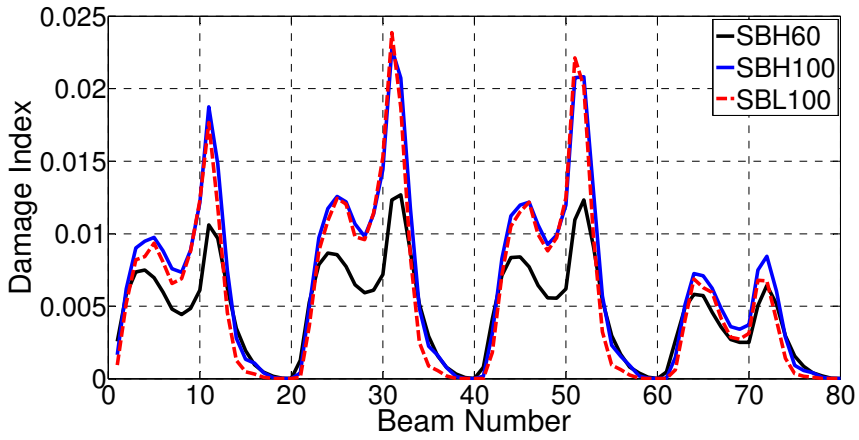

Figure 8.4.8: Mean Low-Cycle Fatigue Damage of Longitudinal Bar Top_1 in Beams - FP Component

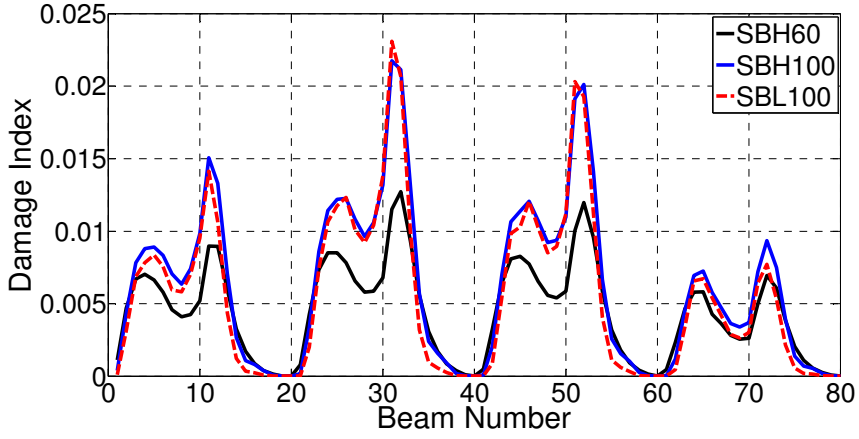

Figure 8.4.9: Mean Low-Cycle Fatigue Damage of Longitudinal Bar Bot_5 in Beams - FP Component

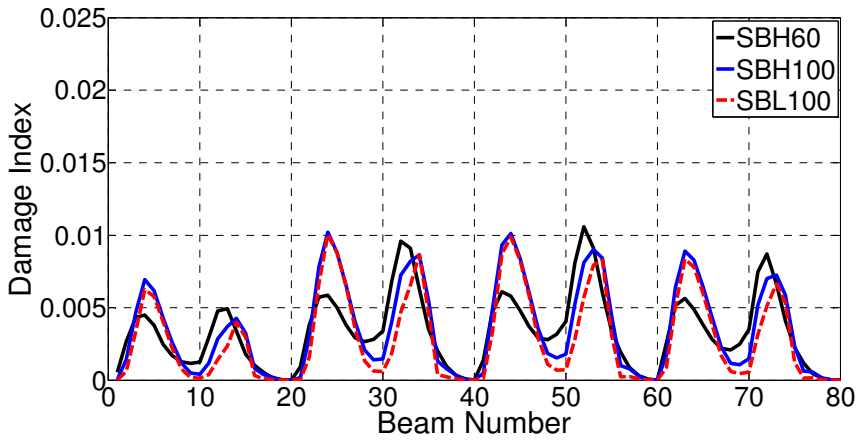

Figure 8.4.10: Mean Low-Cycle Fatigue Damage of Longitudinal Bar Top_5 in Beams - FP Component

In general, longitudinal bars in frame SBH60 attained the least damage while those in frame SBL100 sustained the most damage. This result was expected as frame SBL100 had the largest drift demands. Additionally, Grade 100 with T/Y = 1.17 had the lowest fatigue life among the three types of reinforcing steel bars. However, on the average of all dynamic analyses, the damage indices of all beam elements never exceeded 20%, meaning the chance of longitudinal reinforcement in frame models sustaining low-cycle fatigue failure was relatively small.

It was specifically noticeable that fatigue damage indices for several beam elements in frame SBL100 well exceeded unity when the frame was subjected to ground motions recorded at stations GDLC (GM No. 16) and Duzce (GM No. 18) from the Darfield, New Zealand 2010 and Duzce, Turkey 1999 earthquakes shown in Figure 8.4.11 and Figure 8.4.12, respectively. For example, stress-strain response of longitudinal bar in Beam No. 25 subjected to GM No. 16 is illustrated in Figure 8.4.13. The peak strain demand this steel bar attained was nearly 11%, which was higher than the fracture strain of 9.8% reported by Ghannoum and Slavin (2016) for this Grade 100 T/Y = 1.17 steel. Similar observation was made for other longitudinal bars in frame model SBL100 with fatigue damage indices exceeding unity.

A study of the sensitivity of the low-cycle fatigue model on evaluating fatigue damage of reinforcement was carried out. Scale factors for FN component of GM No. 16 and GM No. 18 were reduced to 1.00 and 1.10, respectively, and frame model SBL100 was analyzed with these reduced ground motions. Figure 8.4.14 and Figure 8.4.15 shows pseudo-acceleration response spectra of two ground motions and the average spectra with different scale factors applied on these two specific ground motions. The reduced spectra still match the target MCE spectrum relatively well. Such small change in scale factor applied on two motions does not result in significant difference of the average spectra.

The smaller scale factors, however, produced apparent drop in peak strain of the longitudinal reinforcement (Figure 8.4.16 and Figure 8.4.17), which consequently reduced low-

cycle fatigue damage indices substantially (Figure 8.4.18 and Figure 8.4.19). This result indicates that the low-cycle fatigue characteristics can be relatively sensitive to the details of the response, especially when strains are close to the fracture strain.

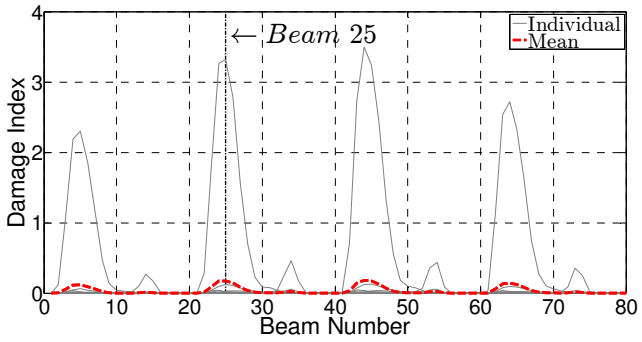

Figure 8.4.11: Fatigue Damage of Bot_1 Bar in Beams of Frame SBL100 - FN Component

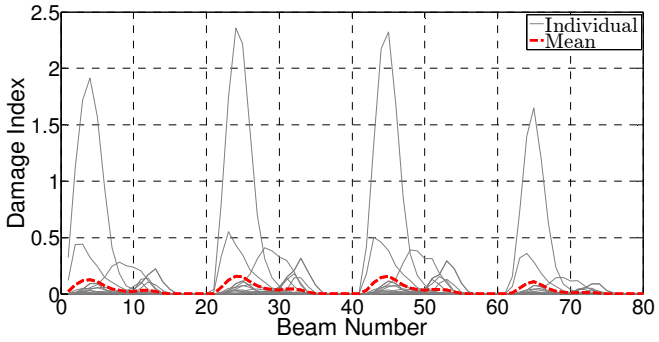

Figure 8.4.12: Fatigue Damage of Top_1 Bar in Beams of Frame SBL100 - FN Component

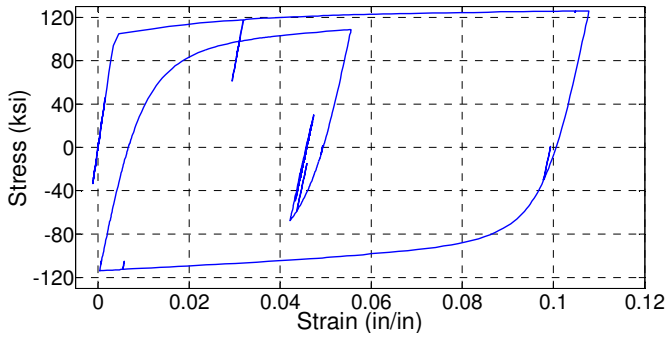

Figure 8.4.13: Stress-Strain Response of Bot_1 Bar in Beam No. 25 of Frame SBL100 under GM No. 16

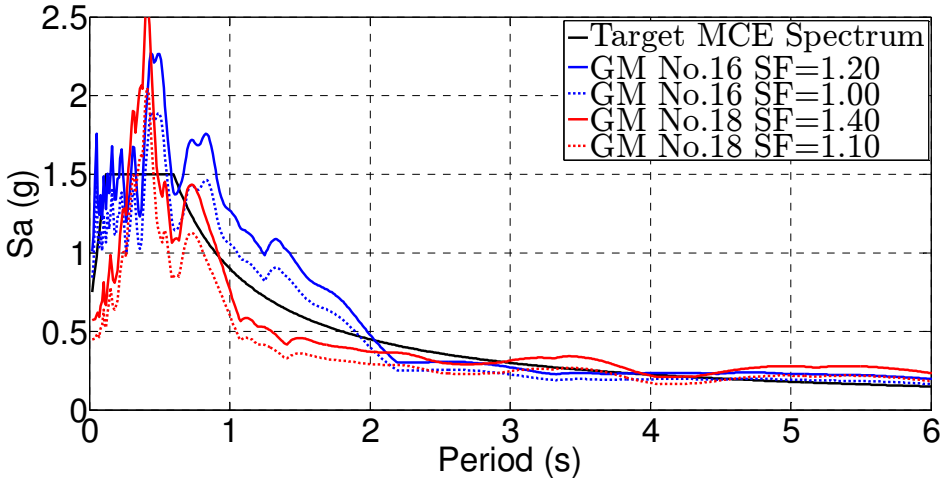

Figure 8.4.14: Pseudo Acceleration Response Spectra of GM No. 16 and No. 18 with Different Scale Factors

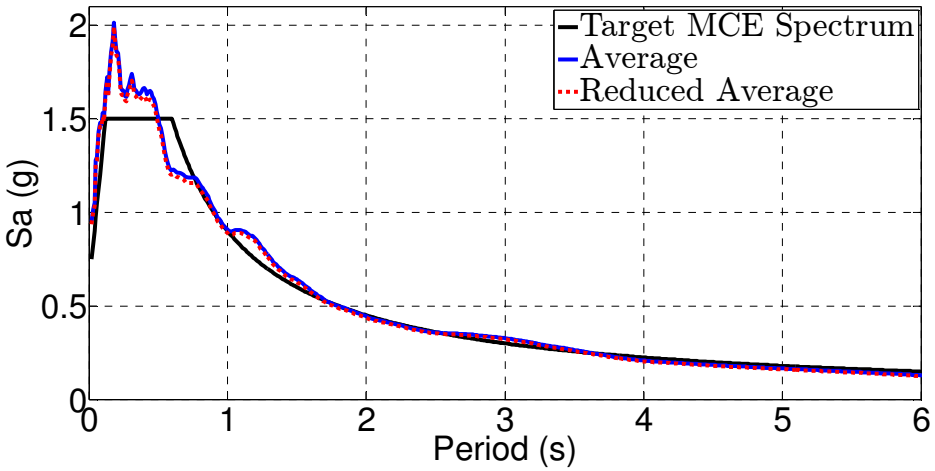

Figure 8.4.15: Average Pseudo Acceleration Response Spectra with Different Scale Factors

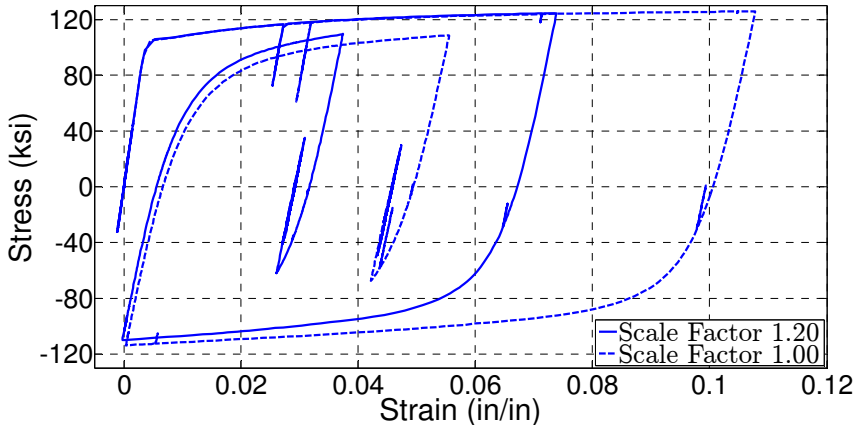

Figure 8.4.16: Stress-Strain Response of Bot_1 Bar in Beam No. 25 of Frame SBL100 under GM No. 16 with Different Scale Factors

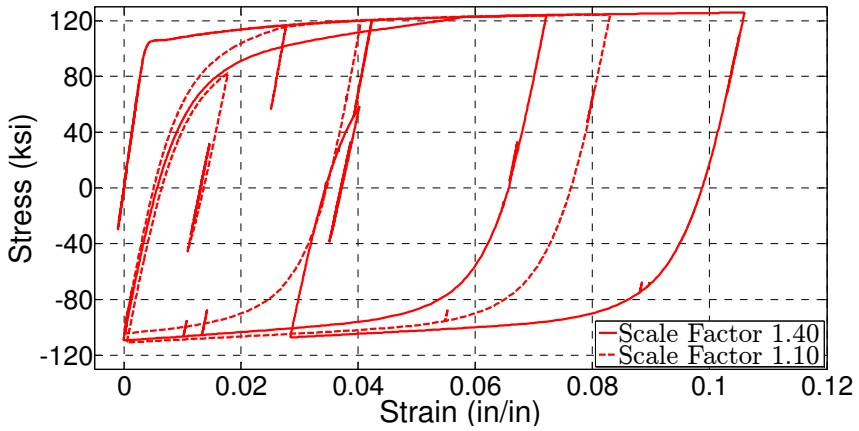

Figure 8.4.17: Stress-Strain Response of Top_1 Bar in Beam No. 25 of Frame SBL100 under GM No. 18 with Different Scale Factors

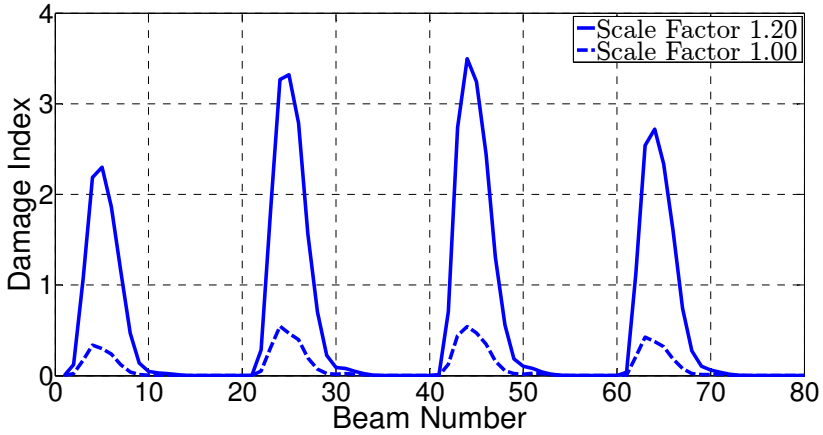

Figure 8.4.18: Fatigue Damage of Bot_1 Bar in Beams of Frame SBL100 Subjected to GM No. 16 with Different Scale Factors - FN Component

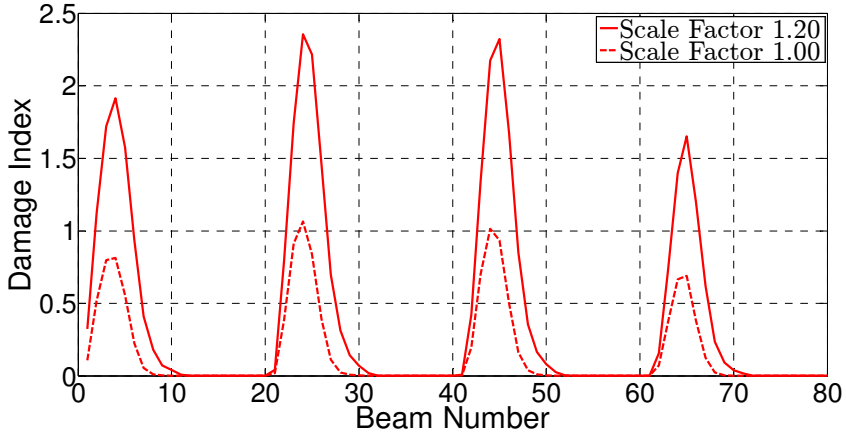

Figure 8.4.19: Fatigue Damage of Top_1 Bar in Beams of Frame SBL100 Subjected to GM No. 18 with Different Scale Factors - FN Component

CHAPTER 9: SUMMARY AND CONCLUSION

The use of higher grade reinforcing steel has the potential benefit of reducing material quantities, thereby leading to reduced reinforcement congestion and reduced construction costs in reinforced concrete construction. Several steel mills in the United States can produce reinforcing steel of grade 100 (nominal yield strength of 100 ksi) and higher. However, at the time of this writing, none of these higher grades can match the benchmark mechanical properties of Grade 60 A706 steel. This raises questions about the performance characteristics of reinforced concrete construction that uses the higher-grade reinforcement.

A research program has been conducted at UC Berkeley in which four reinforced concrete beams were tested in the laboratory. Each beam was reinforced with a different type of reinforcement, including conventional Grade 60 A706, Grade 100 with T/Y = 1.17, Grade 100 with T/Y = 1.26, and Grade 100 A1035. The study investigated stiffness, strength, local bond stress-slip relationships of bars anchored in adjacent concrete sections, spread of plasticity, inelastic rotation capacity, and ultimate failure characteristics.

An analytical study using nonlinear dynamic analysis has also been carried out to investigate the seismic performance of tall reinforced concrete special moment resisting frames using the types of high-strength reinforcement investigated in the laboratory study. Four 20-story concrete moment frames, three reinforced with Grade 100 steel and one with conventional Grade 60 steel, were designed in accordance with ASCE 7-16 and ACI 318-14 at a hypothetical site in San Francisco, California. All four frames had the same dimensions and concrete properties, resulting in identical design drifts. Frames with Grade 100 reinforcement were designed to have reduced amount of reinforcement providing equivalent nominal strength as the frame with Grade 60 reinforcement. Tests carried out as part of this study demonstrate that frames with higher-grade reinforcement had greater strain penetration, resulting in greater slip of reinforcement from connections. Because of this, along with reduced reinforcement ratios, the frames with Grade 100 reinforcement were more flexible than the frame with Grade 60 reinforcement. In addition, many currently available types of Grade 100 reinforcement have lower tensile-to-yield strength ratio and lower uniform elongation compared with Grade 60. Less strain-hardening with higher-strength reinforcement increases strain localization and P-Delta effects. Seismic response of these frame buildings with Grade 100 reinforcement is studied and compared against that of buildings with Grade 60 reinforcement.

KEY FINDINGS:

Based on the limited study reported here, the following key findings are summarized:

Experimental Investigation:

1. All beams reinforced with Grade 100 steel achieved rotation capacity equivalent to that of a beam with conventional Grade 60 A706.
2. Laterally supporting all longitudinal bars at spacing of five (5) times the longitudinal bar diameter provided adequate resistance against bar buckling between hoop sets.
3. Beams SBL100 with Grade 100 T/Y = 1.17 and SBM100 with Grade 100 A1035 both failed by fracture of longitudinal reinforcement. Strain of longitudinal bars in SBL100 was most localized and concentrated at base of the beam, resulting in the highest strain under the same drift among all four specimens.
4. Beams SBH60 and SBH100 both failed by excessive damage of the yielding regions, leading to twisting of the beam about longitudinal axis. Strain in longitudinal bars did not reach the uniform elongation strain capacity.
5. Beams with Grade 100 reinforcement apparently sustained more slip of longitudinal bars out of the anchorage, resulting in more fixed-end rotation, thereby increasing total deformation capacity.
6. To maintain equivalent beam moment strength for all the beams, the beams with Grade 100 reinforcement in this study had reduced longitudinal reinforcement ratio. This effect, combined with increased slip from the anchorage zone, reduced the effective stiffness of the beams with Grade 100 reinforcement compared with the beam with Grade 60 reinforcement.
7. Beam probable moment is affected by the amount of reinforcement material strain-hardening. Beams with lower T/Y had probable moment strength less than that calculated in accordance with ACI 318 procedures, while beams with higher T/Y ratio, especially the beam with ASTM A1035 reinforcement, had probable moment strength higher than that calculated in accordance with ACI 318 procedures.

Nonlinear Dynamic Analysis Study

1. Building frames SBH100, SBL100, and SBM100 with Grade 100 were less stiff than building frame SBH60 with conventional Grade 60 A706. This is because of reduced longitudinal reinforcement area and increased reinforcement slip from anchorages. In relation to this observation, it should be noted that the beam and column gross dimensions were selected to be identical regardless of the selected reinforcement. A widespread practice is to design moment frames such that gross dimensions are controlled by the building code drift limits. By that design practice, gross dimensions cannot be further reduced by using higher grade reinforcement.
2. Frames with higher-grade reinforcement sustained modestly greater drift than that of the frame with Grade 60 steel. SBM100 with Grade 100 A1035 that had round-shaped stress-strain relationship had the largest drift. SBH100 and SBL100 had similar drift despite the difference in reinforcement strain-hardening properties.

3. Story shear envelopes varied for the different frames that were studied. The frames with ASTM A706 Grade 60 reinforcement and ASTM A1035 reinforcement attracted somewhat higher shear, perhaps because of higher material strain-hardening, which increased the member moment strengths.
4. ACI 318-14 procedures for determining column design shear forces produced inconsistent results that, in some cases, were unconservative. An alternative procedure that produces improved estimates is proposed.
5. For the types of Grade 60 and Grade 100 used here, low-cycle fatigue studies indicated that longitudinal reinforcement fracture was unlikely for shaking at levels consistent with MCE_R shaking intensity.

REFERENCE

ACI 318 (1971). *Building Code Requirements for Structural Concrete (ACI 318-71) and Commentary*, American Concrete Institute, Farmington Hills, MI.

ACI 318 (1977). *Building Code Requirements for Structural Concrete (ACI 318-77) and Commentary*, American Concrete Institute, Farmington Hills, MI.

ACI 318 (1983). *Building Code Requirements for Structural Concrete (ACI 318-77) and Commentary*, American Concrete Institute, Farmington Hills, MI.

ACI 318 (2011). *Building Code Requirements for Structural Concrete (ACI 318-11) and Commentary*, American Concrete Institute, Farmington Hills, MI.

ACI 318 (2014). *Building Code Requirements for Structural Concrete (ACI 318-14) and Commentary*, American Concrete Institute, Farmington Hills, MI.

Alath, S., and S.K. Kunnath (1995). "Modeling Inelastic Shear Deformation in RC Beam-Column Joints," *Proceedings of the 10th Conference on Engineering Mechanics*, Part 2 (of 2), Boulder, CO, USA, pp. 822-825.

Anderson, J.C., and W.H. Townsend (1977). "Models for RC Frames with Degrading Stiffness," *ASCE J Struct Division*, Vol. 103, No. 12, pp. 2361-2376.

Aoyama, H., 2001. *Design of Modern Highrise Reinforced Concrete Structures*, Imperial College Press, London, United Kingdom.

Arteta, C.A. (2015). *Seismic Response Assessment of Thin Boundary Elements of Special Concrete Shear Walls*, Doctoral Dissertation, University of California, Berkeley, CA.

ASCE 7 (2016). *Minimum Design Loads for Buildings and Other Structures*, American Society of Civil Engineers, Reston, VA.

ASCE 41 (2013). *Seismic Rehabilitation of Existing Buildings, ASCE/SEI Standard 41-13*, American Society of Civil Engineers, Reston, VA

ASTM A1035 (2016). *Standard Specification of Deformed and Plain, Low-Carbon, Chromium, Steel Bars for Concrete Reinforcement*, ASTM International, West Conshohocken, PA, 8 pp.

ASTM A370 (2014). *Standard Test Methods and Definitions for Mechanical Testing of Steel Products*, ASTM International, 50 pp.

ASTM A431 (1959b). *Specification for High-Strength Deformed Billet-Steel Bars for Concrete Reinforcement with 75,000 psi Minimum Yield Strength*, American Society for Testing and Materials, Philadelphia, Pennsylvania.

ASTM A432 (1959a). *Specification for High-Strength Deformed Billet-Steel Bars for Concrete Reinforcement with 60,000 psi Minimum Yield Strength*, American Society for Testing and Materials, Philadelphia, Pennsylvania.

ASTM A706 (1974). *Standard Specification for Low-Alloy Steel Deformed and Plain Bars for Concrete Reinforcement*, American Society for Testing and Materials, Philadelphia, Pennsylvania.

ASTM A615-09b (2009a). *Standard Specification for Deformed and Plain Carbon-Steel Bars for Concrete Reinforcement*, ASTM International, West Conshohocken, PA, 6 pp.

ASTM A706-09b (2009b). *Standard Specification for Low-Alloy Steel Deformed and Plain Bars for Concrete Reinforcement*, ASTM International, West Conshohocken, PA, 6 pp.

ASTM A706-16 (2009b). *Standard Specification for Deformed and Plain Low-Alloy Steel Bars for Concrete Reinforcement*, ASTM International, West Conshohocken, PA, 7 pp.

ASTM C39 (2012). *Standard Test Method for Compressive Strength of Cylindrical Concrete Specimens*, ASTM International, 8 pp.

ASTM C469 (2010). *Standard Test Method for Static Modulus of Elasticity and Poisson's Ratio of Concrete in Compression*, ASTM International, 5 pp.

ASTM E8 (2016). *Standard Test Methods for Tension Testing of Metallic Materials,* ASTM International, 30 pp.

ATC 115 (2014). *Roadmap for the Use of High-Strength Reinforcement in Reinforced Concrete Design*, ATC-115 Report, Applied Technology Council, Redwood City, California, 197 pp.

Barbosa, A. (2011). *Simplified Vector-Valued Probabilistic Seismic Hazard Analysis and Probabilistic Seismic Demand Analysis: Application to the 13-Story NEHRP Reinforced Concrete Frame-Wall Building Design Example*, Doctoral Dissertation, Department of Structural Engineering, University of California, San Diego, California.

Berry, M.P. (2006). *Performance Modeling Strategies for Modern Reinforced Concrete Bridge Columns*, Doctoral Dissertation, University of Washington, Seattle, WA.

Berry, M.P., D.E. Lehman, and L.N. Lowes (2008). "Lumped-Plasticity Models for Performance Simulation of Bridge Columns," *ACI Structural Journal*, Vol. 105, No. 3, pp. 270-279.

Birely, A. C., Lowes, L. N., and Lehman, D. E. (2012). "Linear Analysis of Concrete Frames Considering Joint Flexibility," *ACI Structural Journal*, v. 109, no. 3, pp. 381-391.

Bournonville, M., J. Dahnke, and D. Darwin (2004). *Statistical Analysis of the Mechanical Properties and Weight of Reinforcing Bars*, SL Report 04-1, Structural Engineering and Material Laboratory, The University of Kansas, Lawrence, KS, 198 pp.

Brown, J., and S.K. Kunnath (2004). "Low-Cycle Fatigue Failure of Reinforcing Steel Bars," *ACI Materials Journal*, Vol. 101, No, 6, pp. 457-466.

Burns, N.H. and C.P. Seiss (1962). *Load Deformation Characteristics of Beam-Column Connections in Reinforced Concrete*, Structural Research Series No. 234, University of Illinois, Urbana, Illinois.

Caifu, Y. (2010). "Development of High-Strength Construction Rebars," *Proceedings*, International Seminar on Production and Application of High Strength Seismic Grade Rebar Containing Vanadium, Central Iron, & Steel Research Institute, Beijing, China.

Chang, G., and J. Mander (1994). *Seismic Energy Based Fatigue Damage Analysis of Bridge Columns: Part I – Evaluation of Seismic Capacity*, NCEER Technical Report 94-006.

Charney, F.A. (2008). "Unintended Consequences of Modeling Damping in Structures," *ASCE Journal of Structural Engineering*, Vol. 134, No. 4, pp. 581-592.

Cheng, M.Y. and M.B. Giduquio (2014). "Cyclic Behavior of Reinforced Concrete Flexural Members Using High-Strength Flexural Reinforcement," *ACI Structural Journal*, Vol. 111, No. 4, pp. 893-902.

Chopra A.K., and F. McKenna (2016). "Modeling Viscous Damping in Nonlinear Response History Analysis of Buildings for Earthquake Excitation," *Earthquake Engineering and Structural Dynamics*, 45:193-211.

Chu, T.C., W.F. Ranson, M.A. Sutton, and W.H. Peters (1985). "Applications of Digital-Image-Correlation Techniques to Experimental Mechanics," *Experimental Mechanics*, 25(3), 232-244.

Coffin, L.F. Jr. (1954)." A Study of the Effect of Cyclic Thermal Stresses on a Ductile Metal," *American Society of Mechanical Engineers*, Vol. 76, pp. 931-950.

El-Metwally, S.E., and W.F.Chen (1998). "Moment-Rotation Modeling of Reinforced Beam-Column Connections," *ACI Structural Journal*, Vol. 85, No. 4, pp. 384-394.

Elmorsi, M., M.R. Kianoush, and W.K. Tso (2000). "Modeling Bond-Slip Deformations in Reinforced Concrete Beam-Column Joints," *Canadian Journal of Civil Engineering*, Vol. 27, No. 3, pp. 490-505.

Elwood, K.J., and M.O. Eberhard (2009). "Effective Stiffness of Reinforced Concrete Columns," *ACI Structural Journal*, Vol. 106, No. 4, pp. 476-484.

Erasmus, L., and N. Pussegoda (1978). "Safe Bend Radii for Deformed Reinforcing Bar to Avoid Failure by Strain Age Embrittlement," *New Zealand Engineering*, Vol. 33, No. 8, pp. 170-177.

FEMA 273 (1997). *NEHRP Guidelines for the Seismic Rehabilitation of Buildings, FEMA-273*, Federal Emergency Management Agency, Washington, D.C.

FEMA 461 (2007). *Interim Testing Protocols for Determining the Seismic Performance Characteristics of Structural and Nonstructural Components*, Federal Emergency Management Agency, Washington, D.C., 138 pp.

Fenwick, R.C., and A. Fong (1979). *The Behaviour of Reinforced Concrete Beams under Cyclic Loading*, University of Auckland, Department of Civil Engineering, Report No. 176, Auckland, New Zealand.

Fenwick, R.C., J.M. Ingham, and P.J.Y. Wuu (1996). "The Performance of Ductile R/C Frames under Seismic Loading," *Proceedings, NZNSEE Technical Conference and AGM*, New Plymouth, New Zealand.

Filippou, F.C., E.P Popov, and V.V. Bertero (1983). *Effects of Bond Deterioration on Hysteretic Behavior of Reinforced Concrete Joints*, Report EERC 83-10, Earthquake Engineering Research Center, University of California, Berkeley.

Fleury, F., J.M. Reynouard, and O. Merabet (2000). "Multicomponent Model of Reinforced Concrete Joints for Cyclic Loading," *Journal of Engineering Mechanics*, Vol. 126, No. 8, pp. 804-811.

Gaston, J.R., and E. Hognestad (1962). "High Strength Bars as Concrete Reinforcement, Part 3 – Tests of Full-Scale Roof Girder," *Journal of the PCA Research and Development Laboratories*, Vol. 4, No. 2, pp. 10-23.

Ghannoum, W. (2007). *Experimental and Analytical Dynamic Collapse Study of a Reinfroced Concrete Frame with Light Transverse Reinforcement*, Doctoral Dissertation, University of California, Berkeley, CA.

Ghanoum, W.M., and J.P. Moehle (2012). "Dynamic Collapse Analysis of a Concrete Frame Sustaining Column Axial Failures," *ACI Structural Journal*, Vol. 109, No. 3, pp. 403-412.

Ghanoum, W.M., and C.M. Slavin (2016). "Low-Cycle Fatigue Performance of High-Strength Steel Reinforcing Bars," *ACI Materials Journal*, Vol. 113, No. 6, pp. 803-814.

Girard, C. and J. Bastien (2002). "Finite-Element Bond-Slip Model for Concrete Columns under Cyclic Loads," Journal of Structural Engineering, Vol. 128, No. 12, pp. 1502-1510.

Hawileh, R., A. Rahman, and H. Tabatabai (2010). "Evaluation of the Low-Cycle Fatigue Life in ASTM A706 and A615 Grade 60 Steel Reinforcing Bars," *Journal of Materials in Civil Engineering*, Vol. 22, No. 1, pp. 65-76.

Haselton, C.B., C.A. Goulet, J. Mitrani-Reiser, J.L. Beck, G.G. Deierlein, K.A. Porter, J.P. Stewart, and E. Taciroglu (2008). *An Assessment to Benchmark the Seismic Performance of a Code-Conforming Reinforced Concrete Moment-Frame Buildings*, Technical Report Peer 2007/2012, Pacific Earthquake Engineering Research Center, Berkeley, CA.

Hognestad, E. (1951*). A Study of Combined Bending and Axial Load in Reinforced Concrete Members*, Bulletin 399, University of Illinois Engineering Experiment Station, Urbana, Ill., 128 pp.

Hognestad, E. (1961). "High Strength Bars as Concrete Reinforcement, Part 1 – Introduction to a Series of Experimental Reports," *Journal of the PCA Research and Development Laboratories*, Vol. 3, No. 3, pp. 23-29.

Hognestad, E. (1962). "High Strength Bars as Concrete Reinforcement, Part 2 – Control of Flexural Cracking," *Journal of the PCA Research and Development Laboratories*, Vol. 4, No. 1, pp. 46-63.

Ibarra L.F., R.A. Medina, and H. Krawinkler (2005). "Hysteretic Models That Incorporate Strength and Stiffness Deterioration," *Earthquake Engineering and Structural Dynamics*, Vol. 34, No. 12, pp. 1489-1511.

Jayaram, N., Lin, T., and Baker, J. W. (2011). "A computationally efficient ground-motion selection algorithm for matching a target response spectrum mean and variance." *Earthquake Spectra*, 27(3), 797-815.

Kaar, P.H., and A.H. Mattock (1963). "High Strength Bars as Concrete Reinforcement, Part 4 – Control of Cracking," *Journal of the PCA Research and Development Laboratories*, Vol. 5, No. 1, pp. 15-38.

Kaar, P.H., and E. Hognestad (1965). "High Strength Bars as Concrete Reinforcement, Part 7 – Control of Cracking in T-Beam Flanges," *Journal of the PCA Research and Development Laboratories*, Vol. 7, No. 1, pp. 42-53.

Kaar, P.H (1966). "High Strength Bars as Concrete Reinforcement, Part 8 – Similitude in Flexural Cracking of T-Beam Flanges," *Journal of the PCA Research and Development Laboratories*, Vol. 8, No. 2, pp. 2-12.

Kabeyasawa, T., Y. Sanada, and M. Maeda (2000), "Effect of Beam Axial Deformation on Column Shear in Reinforced Concrete Beams," *Proceedings, 12 World Conference on Earthquake Engineering*, Auckland, New Zealand.

Kelly, T. (1974). *Some Seismic Design Aspects of Multistorey Concrete Frames*, Master of Engineering Report, University of Canterbury, Christchurch, New Zealand, 163 pp.

Kim, J., J. Stanton, and G. MacRae (2004). "Effect of Beam Growth on Reinforced Concrete Frames," *ASCE Journal of Structural Engineering*, Vol. 130, No. 9, pp. 1333-1342.

Kimura, H., S. Sugano, T. Nagashima and A. Ichikawa (1993). *Seismic Loading Tests of Reinforced Concrete Beams Using High Strength Concrete and High Strength Steel Bars*, Proceedings, 3rd International Symposium of Utilization of High-Strength Concrete, pp. 377-384, Tokyo, Japan.

Koh, S.K., and R.I. Stephens (1991). "Mean Stress Effects on Low Cycle Fatigue for a High Strength Steel," *Fatigue & Fracture of Engineering Materials & Structures*, Vol. 14, No. 4, pp. 413-428.

Kunnath, S., Y. Heo, and L. Mohle, (2009). "Nonlinear Uniaxial Material Model for Reinforcing Steel Bars," *Journal of Structural Engineering*, 135(4): 335-343

LATBSDC (2017). *An Alternative Procedure for Seismic Analysis and Design of Tall Buildings Located in the Los Angeles Region*, Los Angeles Tall Building Structural Design Council, Los Angeles, CA.

Lehman, D.E., and Moehle, J.P. (2000). *Seismic Performance of Well-Confined Concrete Columns*, UCB/PEER 1998/01, Pacific Earthquake Engineering Research Center, Berkeley, California.

Lowes, L.N. (1999). *Finite Element Modeling of Reinforced Concrete Beam-Column Bridge Connections*, Doctoral Dissertation, University of California, Berkeley, CA.

Lowes, L.N., and A. Altoontash (2003). "Modeling Reinforced-Concrete Beam-Column Joints Subjected to Cyclic Loading," *Journal of Structural Engineering*, Vol. 129, No. 12, pp. 1686-1697.

Lu, Y., and M. Panagiotou (2013). "Three-Dimensional Cyclic Beam-Truss Model for Non-Planar Reinforced Concrete Walls," *Journal of Structural Engineering*, Vol. 140, No. 1.

Lu, Y., and G.R. Morris (2017). "Assessment of Three Viscous Damping Methods for Nonlinear History Analysis: Rayleigh with Initial Stiffness, Rayleigh with Tangent Stiffness, and Modal," *Proceedings of 16th World Conference on Earthquake Engineering*, No. 1170, Santiago, Chile

Ma, S-Y.M., V.V. Bertero, and E.P. Popov (1976). *Experimental and Analytical Studies on Hysteretic Behavior of Reinforced Concrete Rectangular and T-Beams*, Report No. UCB/EERC 76/2, University of California, Berkeley, CA, 241 pp.

Mander, J.B., M.J.N. Priestley, and R. Park (1984). *Seismic Design of Bridge Piers*, Report 84-02, Department of Civil Engineering, University of Canterbury, Christchurch, New Zealand.

Mander, J.B., Priestley, M.J.N., and Park, R. (1988a). "Theoretical Stress-Strain Model for Confined Concrete," *Journal of Structural Engineering*, Vol. 114, No. 8, pp. 1804-1826

Mander, J.B., Priestley, M.J.N., and Park, R. (1988b). "Observed Stress-Strain Behavior of Confined Concrete," *Journal of Structural Engineering*, Vol. 114, No. 8, pp. 1827-1849.

Mander, J.B., F.D. Panthaki, and A. Kasalanati (1994). "Low-Cycle Fatigue Behavior of Reinforcing Steel," *Journal of Materials in Civil Engineering*, Vol. 6, No. 4, pp. 453-468.

Manson, S.S. (1953). "Behavior of Materials under Conditions of Thermal Stress," *Heat Transfer Symposium*, University of Michigan Engineering Research Institute, Ann Arbor, Michigan.

McKenna, F., Fenves, G.L., Scott, M.H., and Jeremic, B., 2000. Open System for Earthquake Engineering Simulation (OpenSees) [software]. Pacific Earthquake Engineering Research Center, University of California, Berkeley, CA. http://opensees.berkeley.edu

Miner, M.A. (1945). "Cumulative Damage in Fatigue," *Journal of Applied Mechanics*, Vol. 12, pp. A159-A164.

MMFX Technologies Corporation (2012). *Material Properties and Design Considerations MMFX$_2$ (ASTM A1035/AASHTO MP18)*, MMFX Product Information, December 2012, 36 pp.

Moehle, J.P., and J.D. Hooper (2016). *Seismic Design of Reinforced Concrete Special Moment Frames: A Guide for Practicing Engineers, Second Edition*, NEHRP Seismic Design Technical Brief No. 1, NIST GCR 16-917-40, National Institute of Standards and Technology, Gaithersburg, MD.

Moehle, J. P. (2014). *Seismic Design of Reinforced Concrete Buildings*, Mc Graw-Hill Education, New York, 760 pp.

Neuenhofer, A., and Filippou, F.C. (1997). "Evaluation of Nonlinear Frame Finite-Element Models." *Journal of Structural Engineering*, 123(7), 958-966

Nieslony, A. (2010). *Rainflow Counting Algorithm*, retrieved from Mathworks File Exchange: https://mathworks.com/matlabcentral/fileexchange/3026-rainflow-counting-algorithm

NIST (2014). *Use of High-Strength Reinforcement in Earthquake-Resistant Concrete Structures*, GCR 14-917-30, prepared by the NEHRP Consultants Joint Venture, a partnership of the Applied Technology Council and the Consortium for Universities for Research in Earthquake Engineering, for the National Institute of Standards and Technology, Gaithersburg, Maryland, 231 pp.

Open System for Earthquake Engineering Simulation (OpenSees) 2012-2014. http://opensees.berkeley.edu/.

Otani, S. (1974). "Inelastic Analysis of R/C Frame Structures," *Journal of the Structural Division, ASCE*, Vol. 100, pp. 1433-1449.

Panagiotou, M., J.I. Restrepo, and J. Conte (2011). "Shake-table Test of a Full-Scale 7-Story Building Slice, Phase 1: Rectangular Wall," *Journal of Structural Engineering*, Vol. 137, No. 6, pp. 691-704.

Park, R., and T. Paulay (1975). *Reinforced Concrete Structures*, Wiley Interscience, New York, NY, 769 pp.

PEER 2014, Ground Motion Database. http://peer.berkeley.edu/ngawest2/databases/

Pfister, J.F., and E. Hognestad (1964). "High Strength Bars as Concrete Reinforcement, Part 6 – Fatigue Tests," *Journal of the PCA Research and Development Laboratories*, Vol. 6, No. 1, pp. 65-84.

Pfister, J.F., and A.H. Mattock (1963). "High Strength Bars as Concrete Reinforcement, Part 5 – Lapped Splices in Concentrically Loaded Columns," *Journal of the PCA Research and Development Laboratories*, Vol. 5, No. 2, pp. 27-40.

Pfund. S.J. (2012). *Cyclic Response of Concrete Beams Reinforced with ASTM A1035 Grade-120 Steel Bars*, M.S. Thesis, The Pennsylvania State University, University Park, Pennsylvania.

Priestley, M.J.N., and R. Park (1987). "Strength and Ductility of Concrete Bridge Columns under Seismic Loading," *ACI Structural Journal*, Vol. 84, No. 1, pp. 61-76.

Qi, X., and S.J. Pantazopoulou (1991). "Response of RC Frame under Lateral Loads," *ASCE Journal of Structural Engineering*, Vol. 117, No. 4, pp.1167-1188.

Ramberg, W., and W.R. Osgood (1943). *Description of Stress-Strain Curves by Three Parameter*, Technical Note No. 902, National Advisory Committee for Aeronautics, Washington DC.

Rautenberg, J.M. (2011). *Drift Capacity of Concrete Columns Reinforced with High Strength Steel*, Doctoral Dissertation, Purdue University, West Lafayette, Indiana.

Rautenberg, J.M., and S. Pujol (2012). "Numerical Estimates of the Seismic Response of Building Structures Reinforced with High-Strength Steel," *ACI SP 293-3*, American Concrete Institute, Farmington Hills, MI, pp. 35-44.

Rautenberg, J.M., S. Pujol, H. Tavallali, and A. Lepage (2013). "Drift Capacity of Concrete Columns Reinforced with High-Strength Steel," *ACI Structural Journal*, Vol. 110, No. 2, pp. 307-317.

Razvi, S., and M. Saatcioglu (1999). "Confinement Model for High-Strength Concrete," *Journal of Structural Engineering*, Vol. 125, No. 3, pp. 281-289.

Restrepo-Posada, J.I., L. Dodd, R. Park, and N. Cooke (1994). "Variables Affecting Cyclic Behavior of Reinforcing Steel," *Journal of Structural Engineering*, Vol. 120, No. 11, pp. 3178-3196

Richart, F.E., and R.L. Brown (1934). *An Investigation of Reinforced Concrete Columns: A Report of an Investigation*, The Engineering Experiment Station, University of Illinois, in cooperation with the American Concrete Institute, University of Illinois, Urbana, Illinois.

Scott, M.H., and Fenves G. 2006. "Plastic Hinge Integration Methods for Force-Based Beam-Column Elements," *Journal of Structural Engineering*, Vol. 132, No. 2, pp. 244-252.

Sezen, H., and E.J. Setzler (2008). "Reinforcement Slip in Reinforced Concrete Columns," *ACI Structural Journal*, Vol. 105, No. 3, pp. 280-289.

Sezen, H., and J.P. Moehle (2006). "Seismic Tests of Concrete Columns with Light Transverse Reinforcement," *ACI Structural Journal*, Vol. 103, No. 6, pp. 842-849.

Sokoli, D., A. Limantono, and W. M. Ghannoum (2017). *Defining Structurally Acceptable Properties of High-Strength Steel Bars through Material and Column Testing - Part II: Column Testing Report*, Research Grant Agreement #05-14, Charles Pankow Foundation, Vancouver, WA, 219 pp.

Sokoli, D. and W.M. Ghannoum (2016). "High-Strength Reinforcement in Columns under High Shear Stresses," *ACI Structural Journal*, Vol. 113, No. 3, pp. 605-614.

Sugano, S., T. Nagashima, H. Kimura and A. Ichikawa (1990). "Experimental Study on High-Strength Concrete Beams Using High-Strength Main Bars," *Proceedings of the Japan Concrete Institute*, Vol. 12, No. 2, pp. 215-220.

Tavallali, H., A. Lepage, J.M. Rautenberg and S. Pujol (2014). "Concrete Beams Reinforced with High-Stregnth Steel Subjected to Displacement Reversals," *ACI Structural Journal*, Vol. 111, No. 5, pp. 1037-1047.

TBI (2016). *Seimic Design Guidelines for Tall Buildings*, Report No. 2016/09, Pacific Earthquake Engineering Research Center, University of California, Berkeley, CA, 140 pp.

Todeschini, C.E., A.C. Bianchini, and C.E. Kesler (1964). "Behavior of Concrete Columns Reinforced with High Strength Steels," *ACI Journal*, Vol. 61, No. 6, pp. 701-715.

Visnjic, T., M. Panagiotou, and J.P. Moehle (2012). *Seismic Response of Four 20-Story Tall Reinforced Concrete Special Moment Resisting Frames Designed with Current Code Provisions*, UCB/SEMM Report No. 2012/02, Department of Civil and Environmental Engineering, University of California, Berkeley, CA.

Visnjic, T. (2014). *Design Considerations for Earthquake-Resistant Reinforced Concrete Special Moment Frames*, Doctoral Dissertation, University of California, Berkeley, CA.

Visnjic, T., M. Panagiotou, and J.P. Moehle (2014). "Seismic Response of 20-Story Tall Reinforced Concrete Special Moment Resisting Frames Designed with Current Code Provisions," *Earthquake Spectra*, doi: http://dx.doi.org/10.1193/082112EQS267M.

XTRACT (2009). XTRACT, version 3.0.8. TRC/Imbsen Software Systems, http://www.imbsen.com/xtract.htm.

Zhao, J., and S. Sritharan (2007). "Modeling of Strain penetration Effects in Fiber-Based Analysis of Reinforced Concrete Structures," *ACI Structural Journal*, 104(2), pp. 133-141.

APPENDIX A. DESCRIPTION OF LABORATORY TESTS

CONSTRUCTION OF TEST SPECIMENS

All specimen formworks were laid down horizontally on the lab floor during construction (Figure A-2). Reinforcement cages were fabricated on the side and placed onto the form by crane. Concrete was cast into forms using a pump truck. Cast specimens were then covered by wet burlaps and plastic sheets. Concrete cylinders were also made from the same concrete at the same time that specimen casting was done. These concrete cylinders were covered with plastic sheet and later tested for representative concrete strength of test specimens.

Actual dimensions of test specimens are described and summarized in Figure A-8 and Table A-1. Actual material properties including concrete and reinforcing steel are presented in material section.

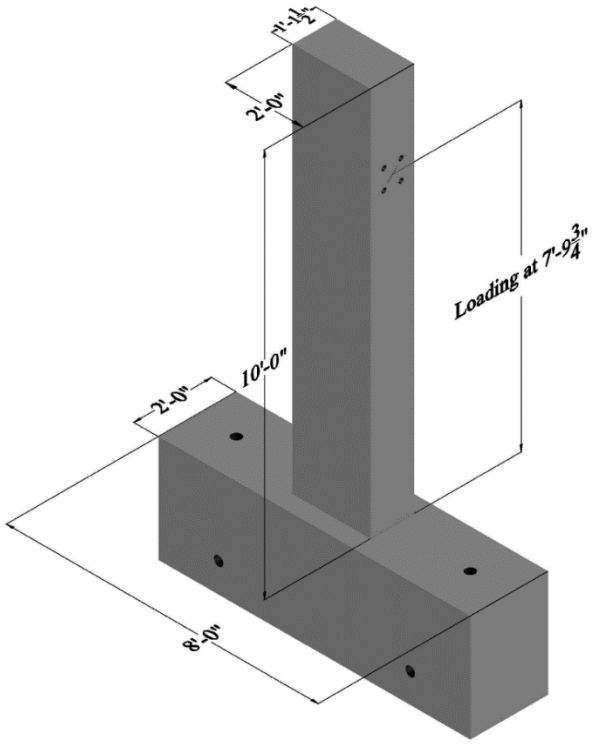

Figure A-1: Geometry and Dimensions of Test Beam Designs

Figure A-2: Construction of Test Specimens – Formwork

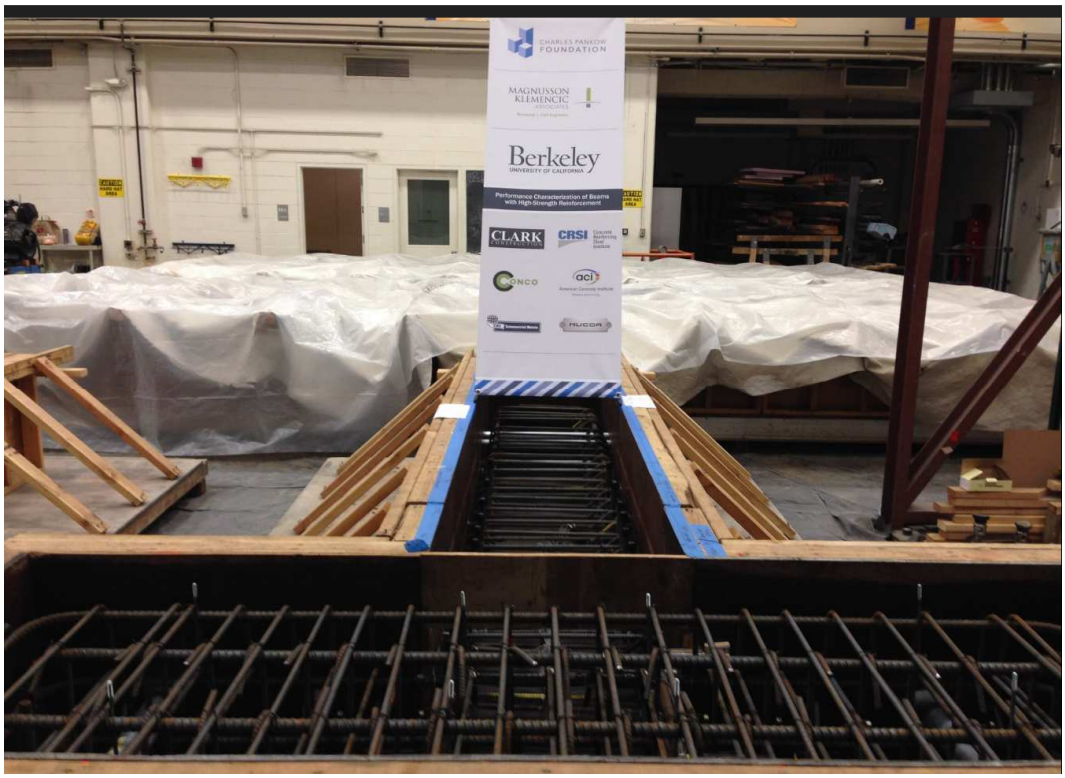

Figure A-3: Construction of Test Specimens - Reinforcement Cage

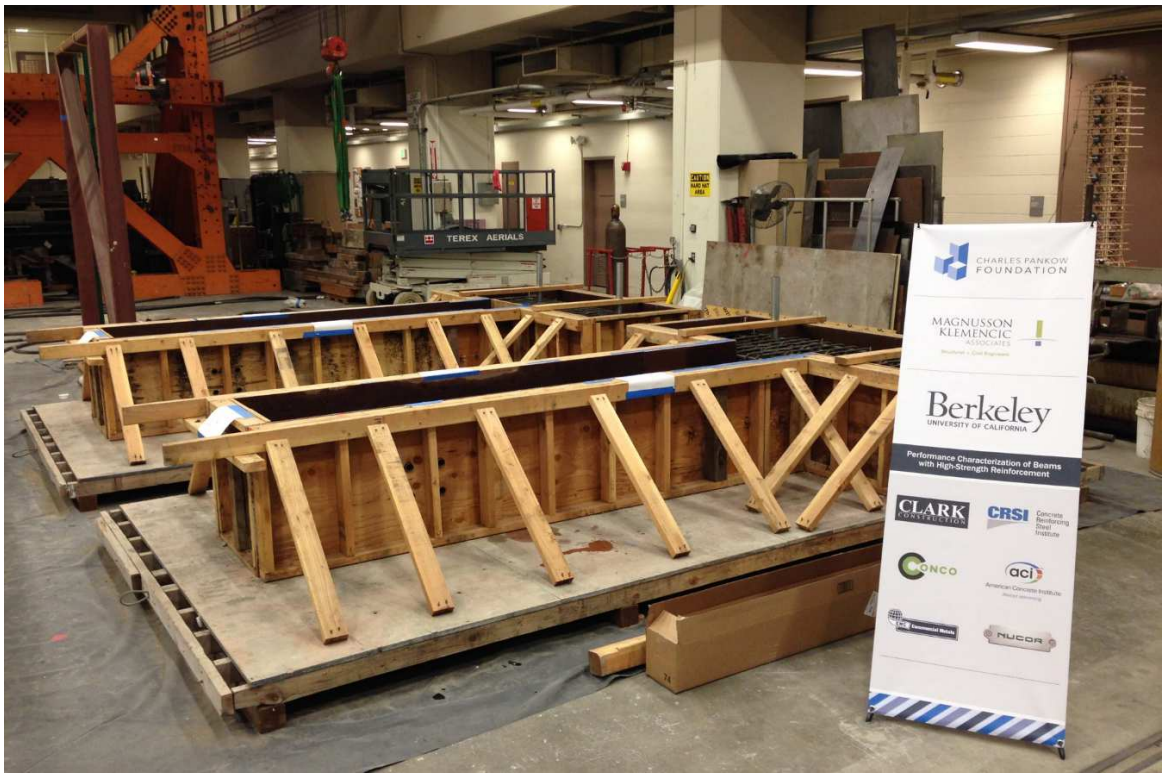

Figure A-4: Construction of Test Specimens - Before Concrete Casting

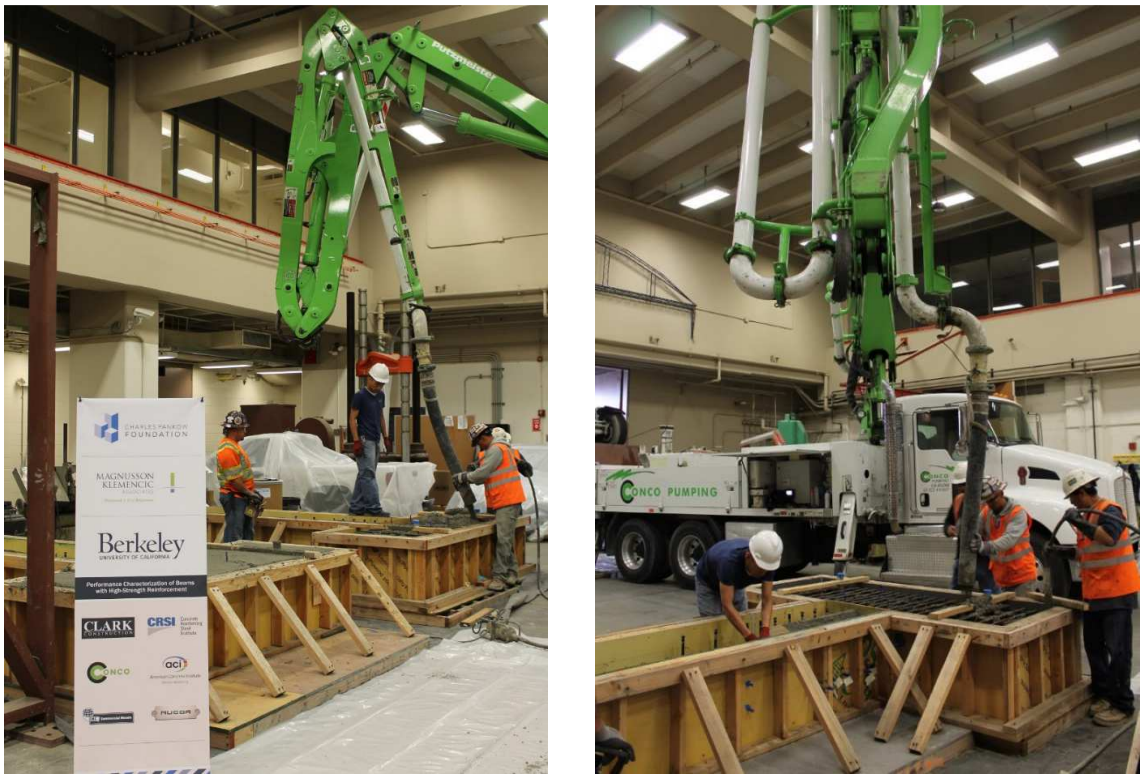

Figure A-5: Construction of Test Specimens - Concrete Casting

Figure A-6: Casting Concrete Cylinders

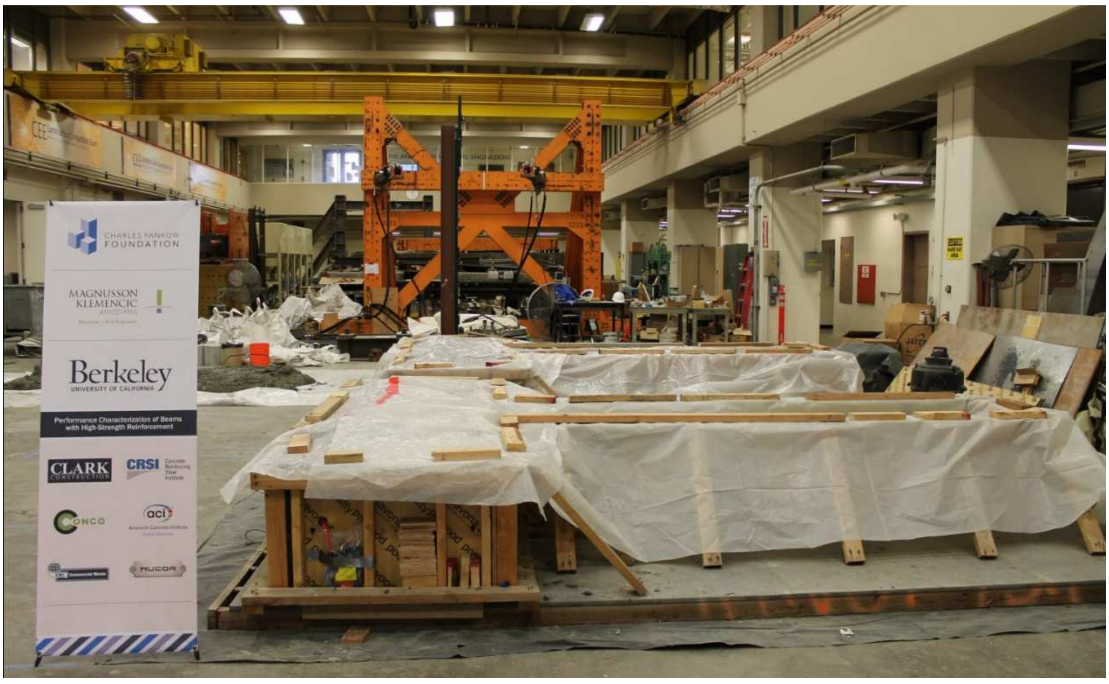

Figure A-7: Construction of Test Specimens - Curing of Specimens

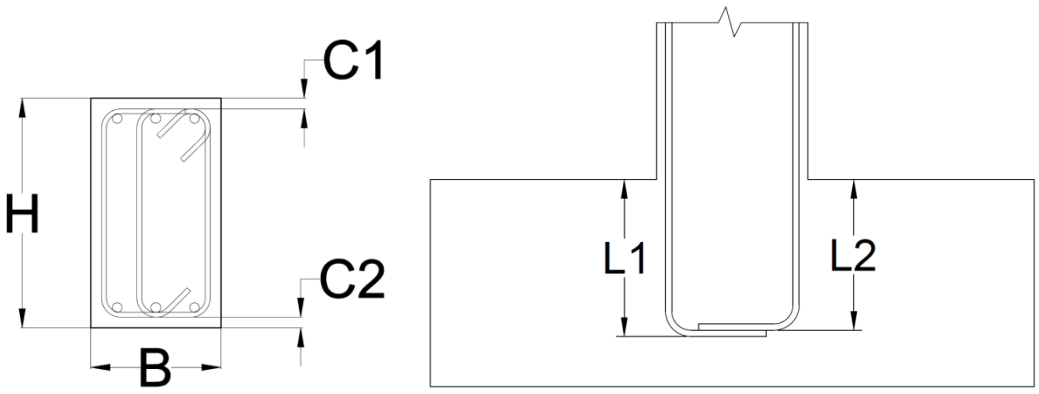

Figure A-8: Typical Dimensions of Test Specimens

Table A-1: Actual Measured Dimensions of Test Specimens

	SBL100	**SBH100**	**SBM100**	**SBH60**
H (in.)	24	24.125	24.25	24
B (in.)	13.5	13.5	13.5	13.5
C1 (in.)	1.5	1.375	1.25	1.0
C2 (in.)	1.5	1.375	1.25	1.5
L1 (in.)	24	24.75	25	24
L2 (in.)	23.5	23.75	24	23

TEST APPARATUS

Cured specimens were oriented vertically and anchored down on the strong floor of the laboratory (Figure A-9 through Figure A-11). Since each hole on the strong floor has capacity of only 100 kips under tension, two large W-section steel beams were used to grab onto three holes on each side of test beam, resulting in total of 450 kips on each side (post-tensioning the middle hole was actually squeezing concrete block and the floor, a peak post-tensioning force of 250 kips was allowed to be applied). The anchorage force on both sides together created large enough friction on the interface between test specimen and laboratory floor to resist sliding caused by applied lateral load on top of the beam.

Two actuators were used to apply reverse cyclic lateral load on the specimen. Each of actuators formed an angle of about sixty (60) degrees with the horizontal steel beam on the reaction frame and was connected to the specimen through a loading fixture in order to restrain accidental out-of-plane bending of the specimen during test.

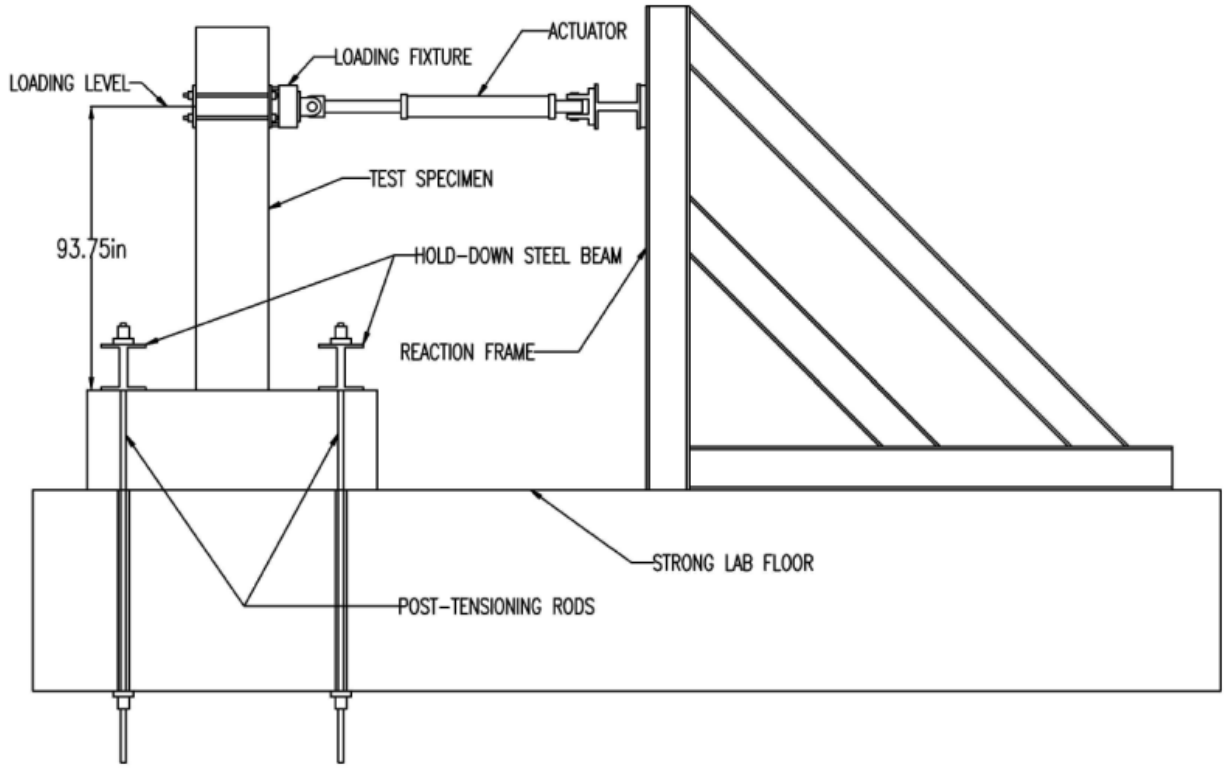

Figure A-9: Schematic Test Setup – Elevation View

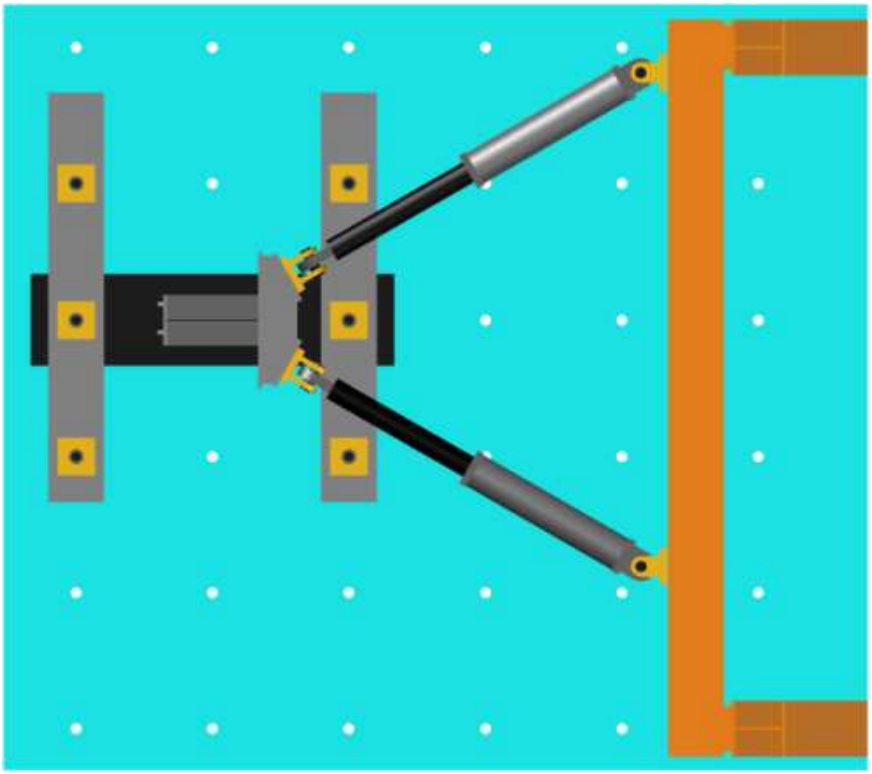

Figure A-10: Schematic Test Setup – Top View

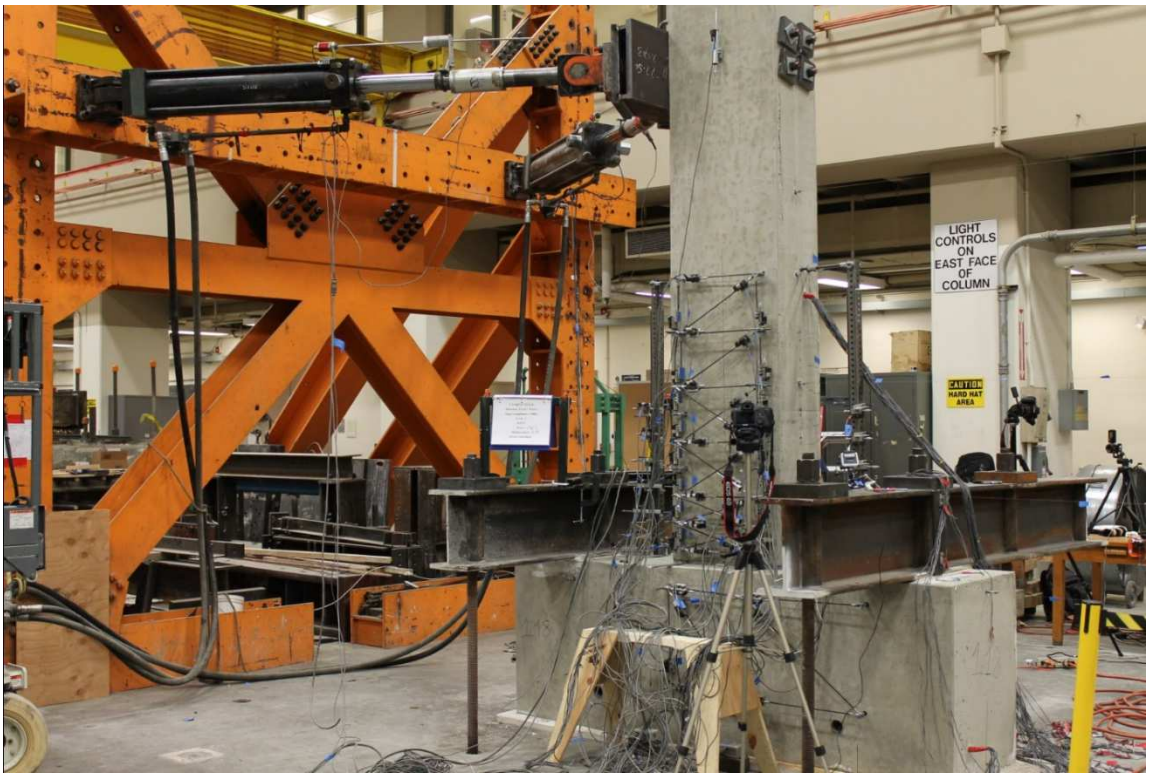

Figure A-11: General Test Setup

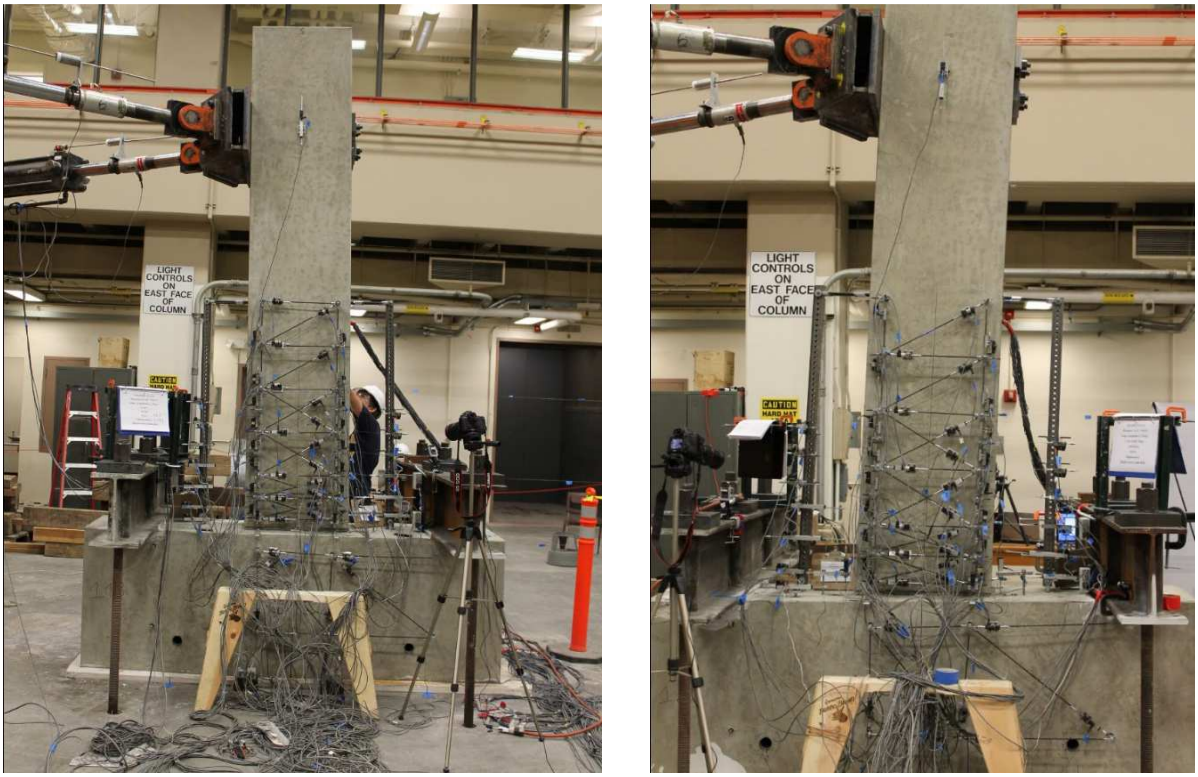

Figure A-12: During Test - Left: Specimen SBL100 - Right: Specimen SBH100

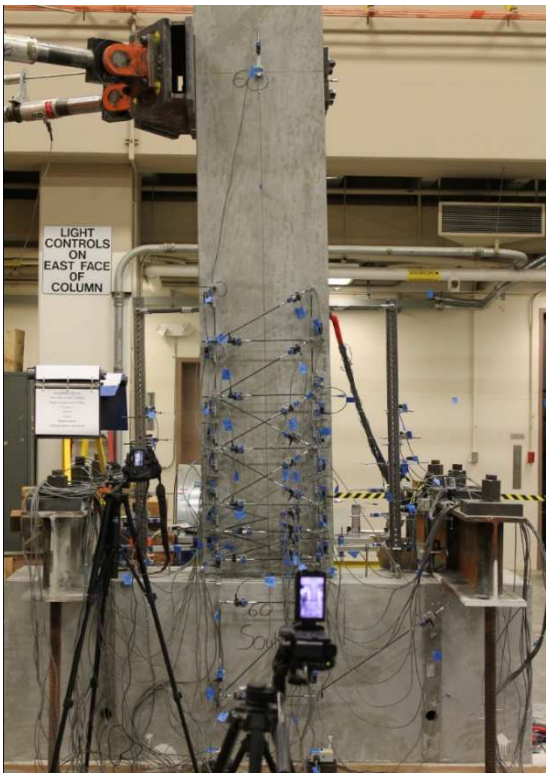

Figure A-13: During Test - Left: Specimen SBH60 - Right: Specimen SBM100

MATERIALS

Concrete

Normal-weight concrete with specified compressive strength of 5 ksi and six-inch slump was used for all beam specimens and their foundation blocks. Materials used in mix design are presented in Table A-2.

Table A-2: Concrete Mix Design Materials

Material	Description	Design Quantity	Actual Quantity*
Cement	ASTM C150	547 lbs/yd^3	548 lbs/yd^3
Coarse Aggregate	ASTM C33 #67	1675 lbs/yd^3	1662 lbs/yd^3
Fine Aggregate	ASTM C33	1424 lbs/yd^3	1393 lbs/yd^3
Fly Ash	ASTM C618 Class F	97 lbs/yd^3	98 lbs/yd^3
Water	ASTM C1602	34 gals/yd^3	31 gals/yd^3

*: Actual quantities were taken from concrete batch cast for specimens in 2nd phase. These quantities varied slightly for specimens in 1st phase.

Plastic cylinders with six-inch diameter and twelve-inch height were used to prepare concrete cylinders during casting. These cylinders were covered by plastic sheets to keep the same curing conditions as concrete in beam specimens. They were then tested for compressive strength at 7, 14, 21, 28 days, and day of beam testing.

All concrete cylinders were removed from plastic molds and capped at both ends with sulfur-capping compound prior to compression test to minimize stress concentration, and ensure uniform loading. The loading procedure had two phases. In the first phase, which was intended to determine modulus of elasticity of concrete following ASTM C469/C469M-10 standards, cylinders were compressed to approximately 40% of the crushing load, which was estimated by testing one sacrificial sample to failure. The loading rate was about 25 kips per minute for this phase. The cylinders were then unloaded close to zero, and reloaded in compression again until a slight drop or plateau of load resistance was observed, indicating initiation of crushing of concrete cylinders. The second phase of testing to determine compressive strength was performed per ASTM C39/C39M-12 standards, and the loading rate was approximately 60 kips per minute. Figure A-14 displays typical concrete stress-strain curves. A summary of concrete strength and moduli is presented in Table A-3.

.

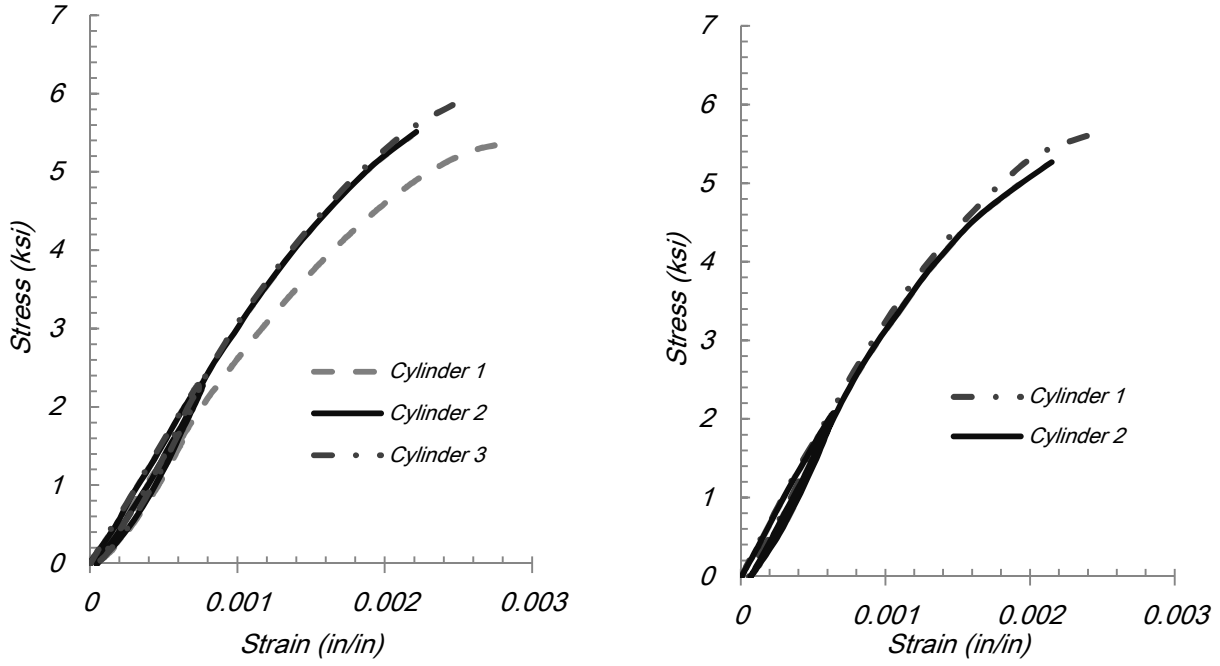

Figure A-14: Compressive Stress-Strain Relationships of Concrete Cylinders: Left – Test Day of SBH60 Beam; and Right – Test Day of SHM100 Beam

Table A-3: Summary of Compressive Strength of Concrete Cylinders

		Cylinder 1	Cylinder 2	Cylinder 3	Average	Modulus
SBL100	7 days	2.74	2.74	2.71	2.73	
	14 days	3.33	3.44	3.32	3.36	
	21 days	3.60	3.49	3.58	3.56	
	28 days	3.61	3.65	3.92	3.73	
	Day of test	5.06	5.09	5.16	5.10	NA
SBH100	7 days	2.74	2.74	2.71	2.73	
	14 days	3.33	3.44	3.32	3.36	
	21 days	3.60	3.49	3.58	3.56	
	28 days	3.61	3.65	3.92	3.73	
	Day of test	4.91	5.00	5.10	5.00	NA
SBM100	7 days	3.87	4.04	3.96	3.96	
	14 days	4.79	5.05	4.90	4.91	
	21 days	5.22	5.01	5.01	5.08	
	28 days	5.23	5.11	5.34	5.24	
	Day of test	5.31	5.51	5.60	5.47	3500
SBH60	7 days	4.13	4.10	4.12	4.12	
	14 days	5.08	4.89	4.94	4.77	
	21 days	5.46	5.26	5.30	5.34	
	28 days	5.26	5.36	5.63	5.41	
	Day of test	5.87	5.69	5.42	5.66	3200

Note: All units are in ksi.

Reinforcing Steel

Four test beams in research program were reinforced with four different types of steel reinforcement (Figure A-15). Steel bars used in Beam SBL100 were Nominal Grade 100 produced by quenching and tempering, while those in Beam SBH100 were also of the same grade and manufactured mainly through micro-alloying. Reinforcement in Beam SBM100 was classified as Grade 100 as well with properties satisfying ASTM A1035 specifications. This type of steel was a low-carbon steel and produced under controlled-rolling process. The last beam specimen was reinforced with conventional Grade 60 ASTM A706 steel.

Coupon specimens were taken from the same batch of longitudinal reinforcement used in each test beam and tested under monotonic loading in tension to determine mechanical properties. These monotonic tension tests were conducted following ASTM A370 standards. Important mechanical properties of reinforcing steel were determined by methods specified in ASTM E8/E8M.

Figure A-17 shows a typical stress-strain relation of one No. 8 Nominal Grade 100 used in Beam SBH100 obtained from monotonic test with 8-inch gauge length. Yield stress was obtained by the 0.2% offset method (Figure A-18). This method was also applied to find yield stress of Grade 100 steel bars used in Beam SBM100 that had no distinct yield plateau in stress-strain relation. Onset and slope of strain-hardening were determined graphically on stress-strain curve (Figure A-19). By observation, x-coordinate of the blue line defined strain at onset of strain-hardening. Meanwhile, slope of the red line was calibrated such that it represented the slope of strain-hardening. Uniform elongation was determined by taking the average of strains, at which stress was 0.5% of the magnitude of the peak stress value (Figure A-20). Figure A-21 and Figure A-22 display typical stress-strain relations of all longitudinal and transverse reinforcement, respectively, used in all beam specimens. And Table A-4 presents their important mechanical properties.

Figure A-15: Longitudinal Steel Used in Test Specimens - Left to Right: SBL100, SBH100, SBM100, SBH60

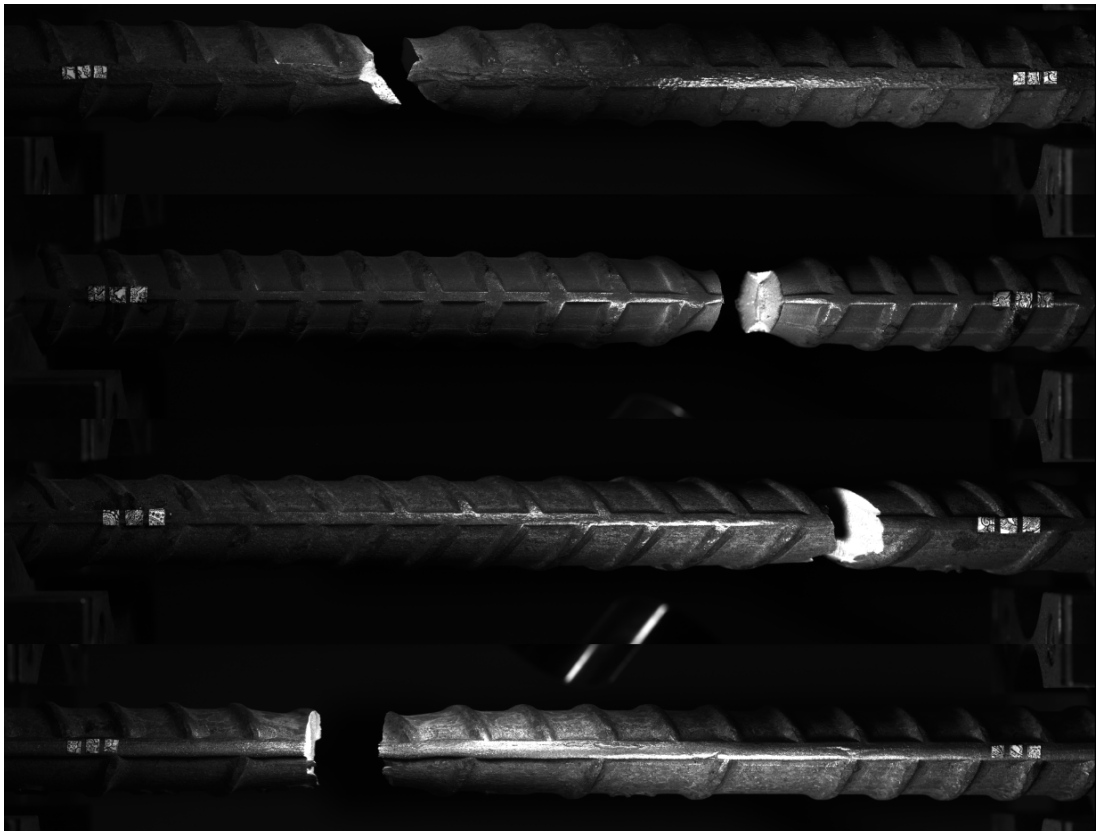

Figure A-16: Typical Photograph from DIC System in Bar Tests – From Top Down: A706 Gr. 60, Gr. 100 A1035, Gr. 100 with T/Y = 1.17, and Gr. 100 with T/Y = 1.26.

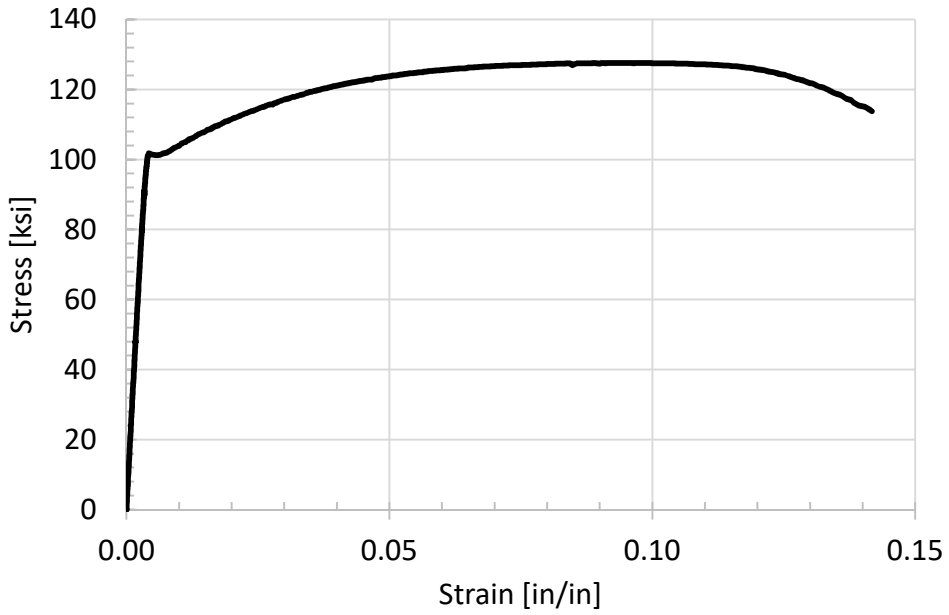

Figure A-17: Typical Stress-Strain Relationship of No. 8 Nominal Grade 100 with T/Y = 1.26 in Beam SBH10

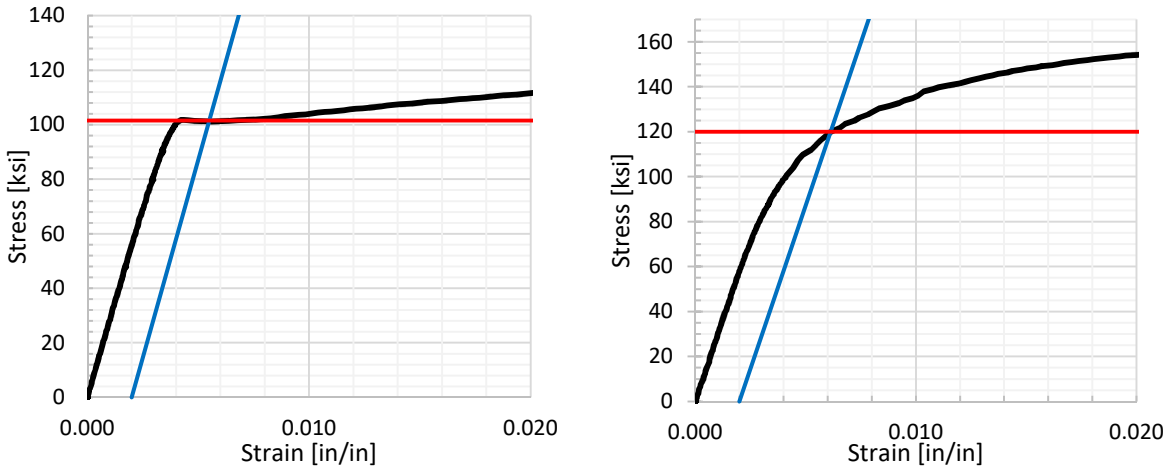

Figure A-18: Yield Strength Determination by 0.2%-Offset Method – Left: Grade 100 T/Y = 1.26 – Right: Grade 100 A1035

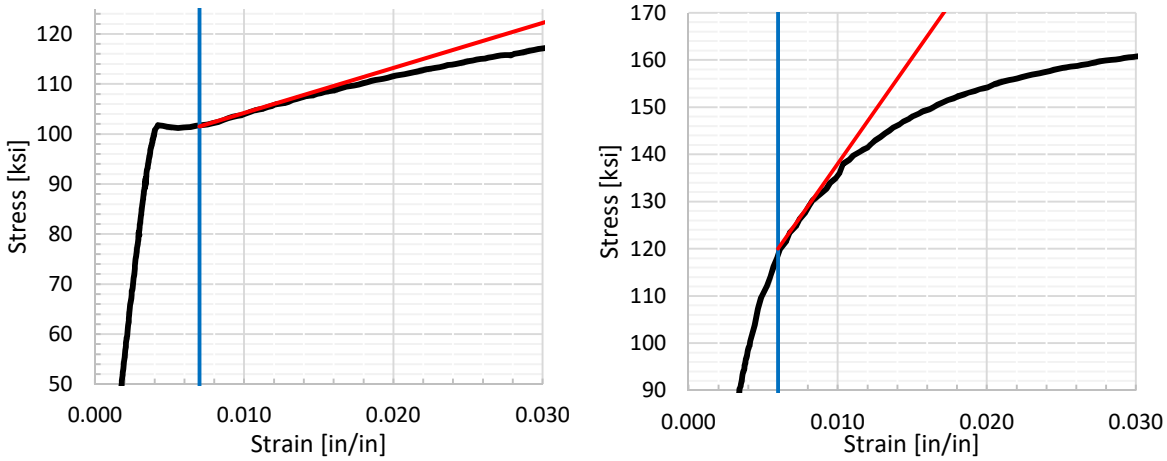

Figure A-19: Onset and Slope of Strain-Hardening – Left: Grade 100 T/Y = 1.26 – Right: Grade 100 A1035

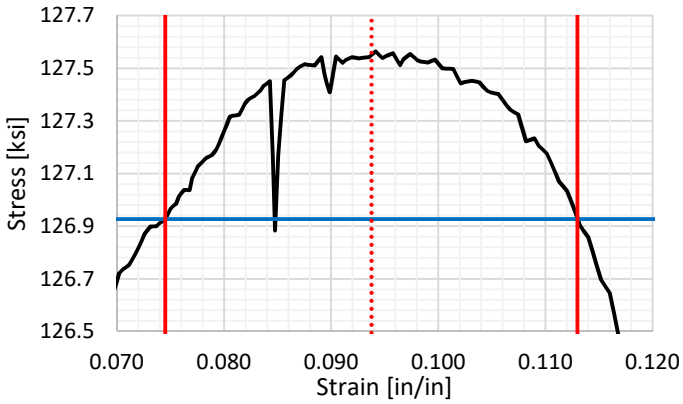

Figure A-20: Determination of Uniform Elongation by Plateau within 0.5% of Magnitude of Peak Force

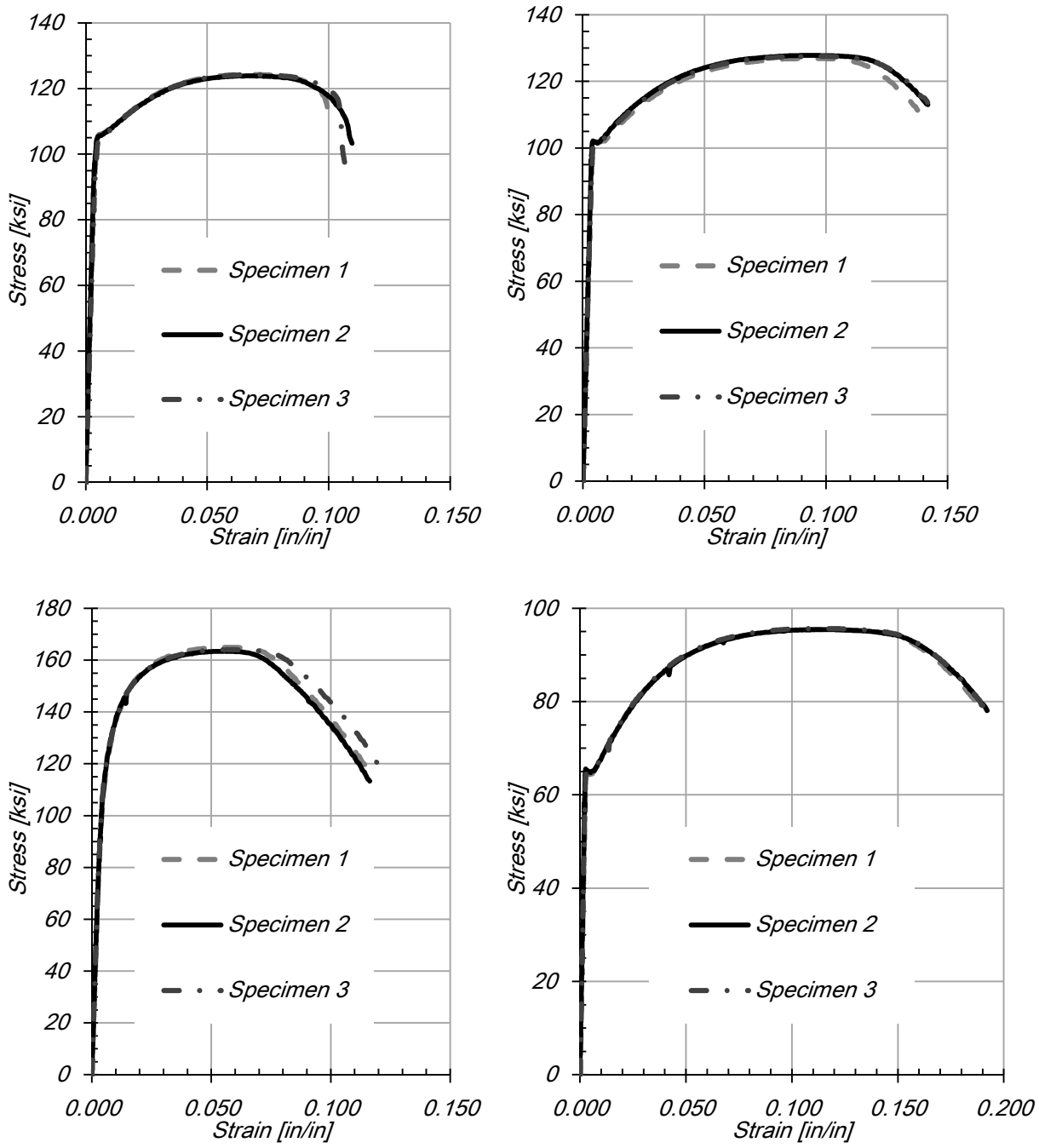

Figure A-21: Tension Stress-Strain Relationship of Longitudinal Steel Coupon Tests: Top Left: No. 8 Bars Used in Beam SBL100; Top Right: No. 8 Bars Used in Beam SBH100; Bottom Left: No. 8 Bars Used in Beam SBM100; Bottom Right: No. 9 Bars Used in Beam SBH60

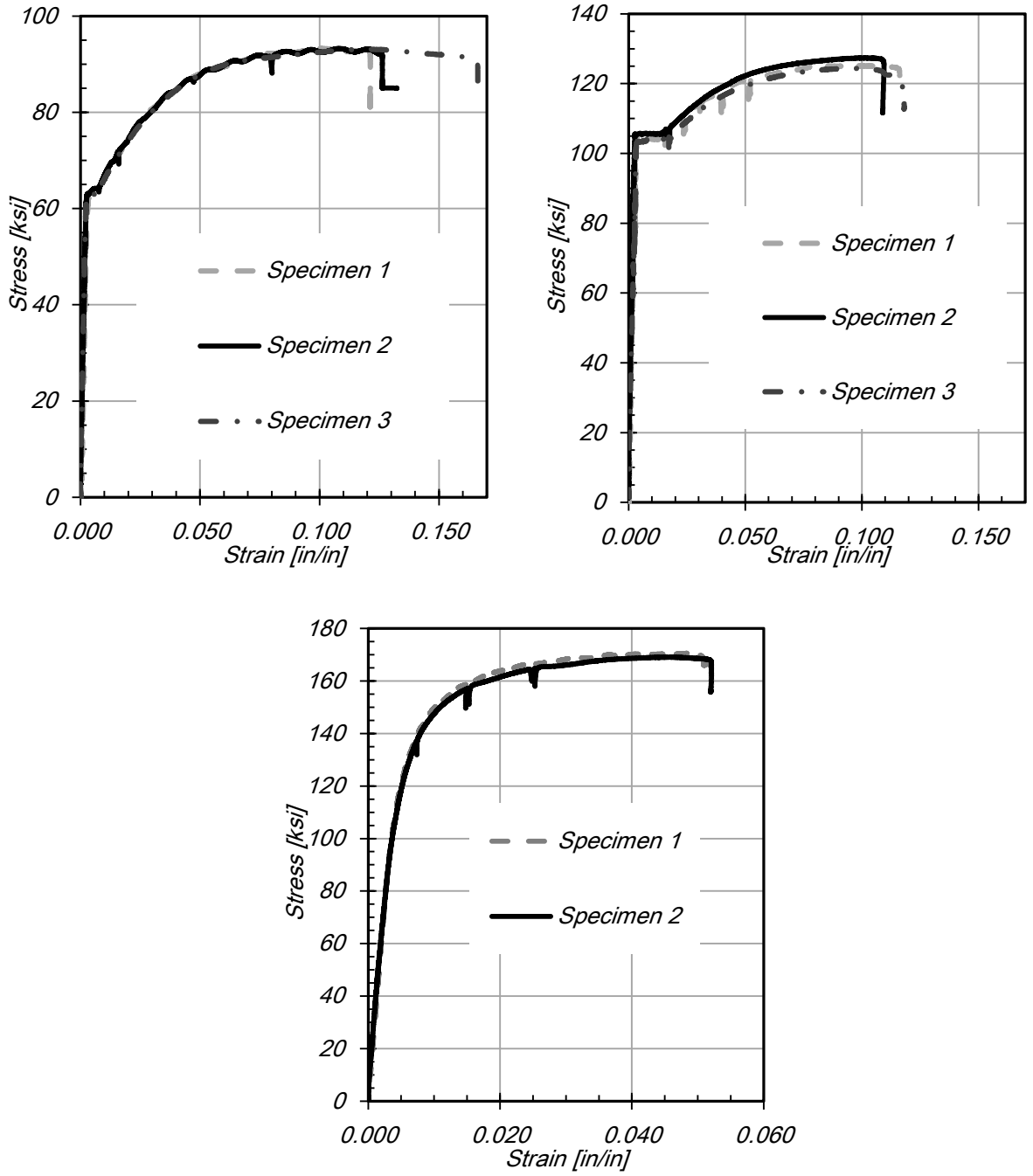

Figure A-22: Tension Stress-Strain Relationship of Transverse Steel Coupon Tests: Top Left: No. 4 Bars Used in Beam SBH60; Top Right: No. 4 Bars Used in Beam SBH100 and SBL100; Bottom: No. 4 Bars Used in Beam SBM100

Table A-4: Mechanical Properties of Reinforcement

Specimen	Yield Strength (ksi)	Tensile Strength (ksi)	Tensile-to-Yield Strength Ratio (T/Y)	Strain at Onset of Strain-Hardening	Slope of Strain-Hardening (ksi)	Uniform Elongation
Longitudinal Reinforcement						
SBL100	106.0	123.9	1.17	0.007	600	0.068
SBH100	101.5	127.6	1.26	0.007	900	0.094
SBM100	120.0	165.0	1.38	0.0024	4500	0.056
SBH60	64.5	95.5	1.48	0.006	950	0.114
Transverse Reinforcement						
SBL100	102.0	127.4	1.25	0.015	750	0.097
SBH100	102.0	127.4	1.25	0.015	750	0.097
SBM100	130.0	169.0	1.30	0.0034	5000	0.044
SBH60	62.5	93.2	1.49	0.006	950	0.119

TEST INSTRUMENTATION AND DATA ACQUISITION SYSTEMS

Interior (Strain gauges)

Strain gauges were installed onto reinforcing bars as interior instrumentation. Typical locations of these strain gauges are shown in Figure A-23. These strain gauges were installed to measure strain primarily along middle longitudinal bars on both sides of beam, hoops and crossties, and along anchorage length of middle longitudinal bars.

Strain gauges used were Tokyo Measuring Instruments Laboratory Co., Ltd. Model YLFA-5-5LT. These gauges are designed for measurements of large strains up to 15-20%. All gauges were 0.2-in. long and 0.08-in. wide. Detailed information can be found on manufacturer's website (www.tml.jp). To attach the strain gauges to the rebar, the rebar was smoothed, prepped with an acid, base, and alcohol, and then the gauges were glued to the bar with CN-Y adhesive. After the glue had cured, gauges were coated with wax, SB tape, and epoxy to protect them during casting. Care was taken to ensure these layered materials took up as little area as possible at each location on the surface of the bar. SB tape and CN-Y adhesive are manufactured by Tokyo Measuring Instruments Laboratory Co., Ltd.

Exterior (Displacement transducers)

Exterior instrumentation included displacement transducers set up to measure global deflection and local deformations along test specimen length (Figure A-25).

String potentiometers used to measure global displacements were Celesco Model PT 101-0015-111-110 (Figure A-24). Detailed information can be found website (www.stringpots.ca). In all cases, sensors with a 15-in. stroke length were used. In cases where sensors had to be placed more than 15 in. from the point on the specimen they measured, thin braided-steel wires were used to extend from the point of placement to the point of measurement. This was done because accuracy is related to stroke length, so it was undesirable to use instruments with greater extension capacity.

Linearly Varying Displacement Transducers (LVDTs) were attached onto the specimen at various locations to measure local deformations (flexural, shear, and dilation deformations), longitudinal bar buckling, slip, beam base sliding relative to concrete foundation, and beam elongation. Linear transducers used to measure both local and global displacements were Novotechnik Models TRS-0025, TRS-0050, and TRS-0100 (Figure A-24). Detailed information can be found on http://www.novotechnik.com. In the case of local displacements, instruments were affixed near the surface of each beam using eyelets on threaded rods that allowed them to rotate without distorting their line of measurement. Where the instrument bore on a concrete surface, a thin sheet of metal was epoxied to the concrete to prevent distortion due to the uneven surface.

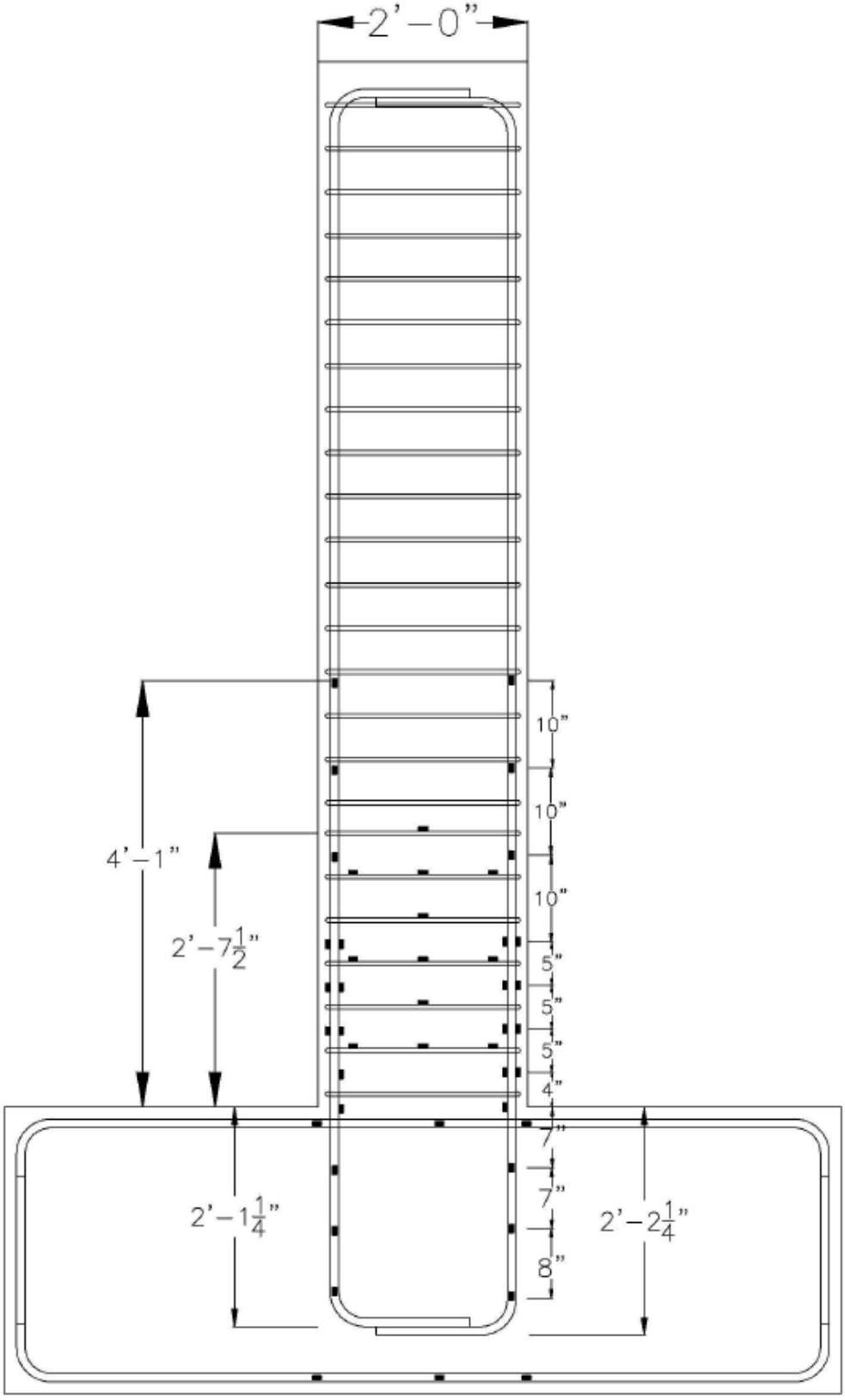

Figure A-23: Interior Instrumentation – Strain Gauges

Figure A-24: Typical Displacement Transducers Used in Tests. Left: String Potentiometer for Global Deflection Measurement; Right: Novotechnik Used to Measure Local Deformations

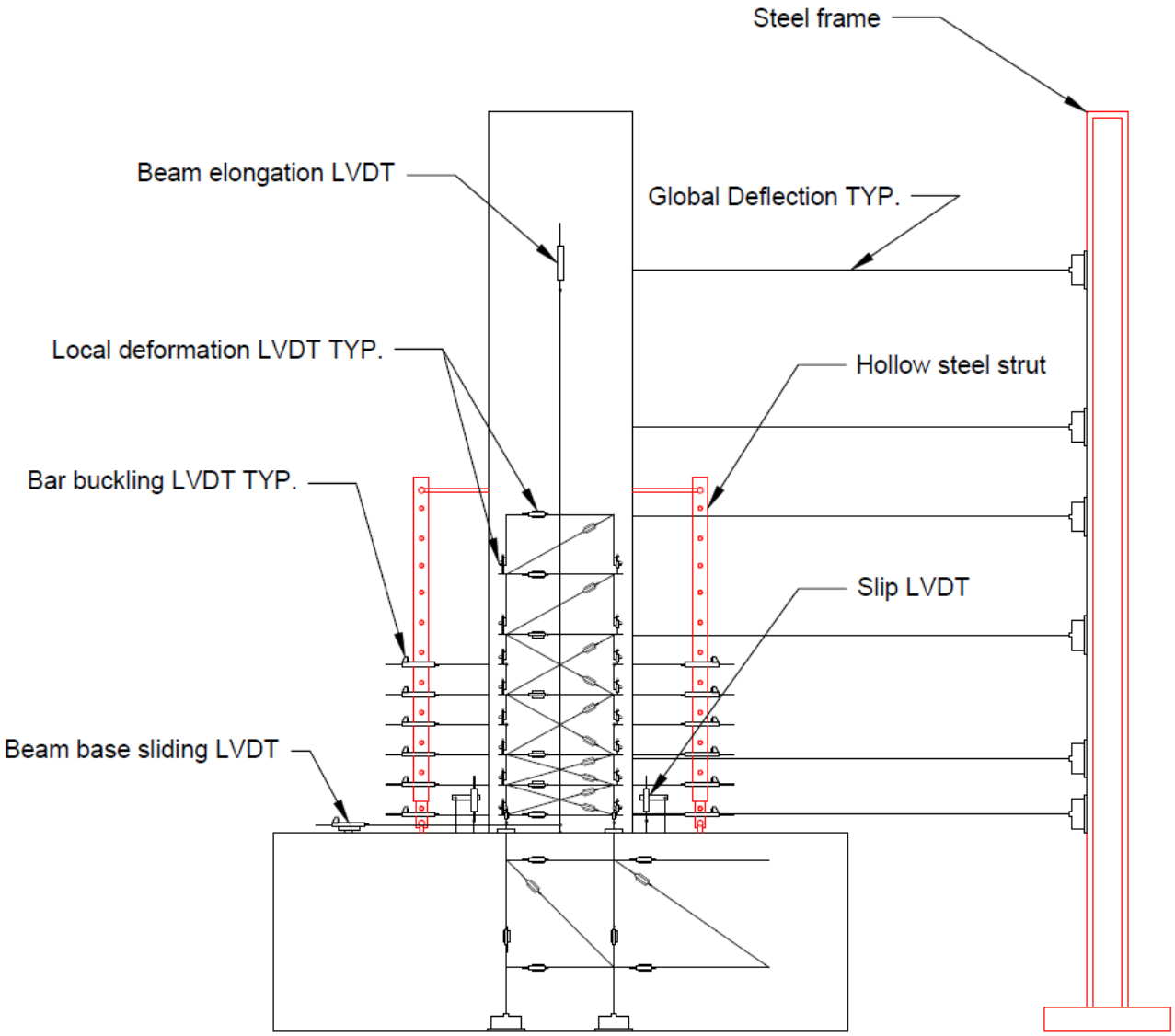

Figure A-25: Schematic Drawing of Exterior Instrumentations

Instrumentation for measuring slip of reinforcement:

As shown in Figure A-25, Figure A-33, & Figure A-34, slip of longitudinal reinforcement out of anchorage is measured by two LVDTs that are connected to two threaded rods attached to reinforcement at base of beams. These two threaded steel rods are brass-brazed onto the reinforcement. The brass-brazing procedure is described as followings:

1. At the location of interest (base of beam), the longitudinal reinforcement is surface cleaned by steel-wire brush (Figure A-26).
2. Heating chemical is applied on the cleaned surface of reinforcement and threaded rod (Figure A-28).
3. Both cleaned surface of reinforcement and threaded rod are heated up to approximately 900-degree Fahrenheit using a torch (Figure A-29). At the same time, a thin rod of brass material is also heated under the same torch and melted.
4. Threaded rod is brought into contact with reinforcement and melted brass material is applied in between to bond the threaded rod onto reinforcement.
5. Heat is removed and a strong connection between threaded rod and reinforcement is formed as melted brass material cools off (Figure A-30).

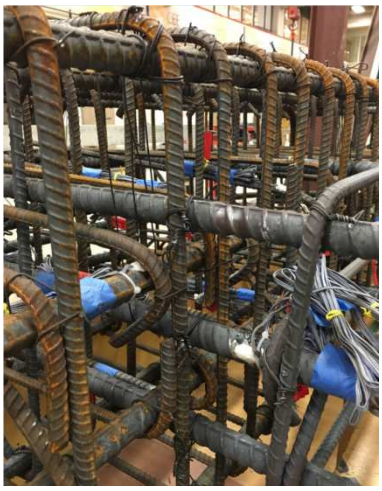

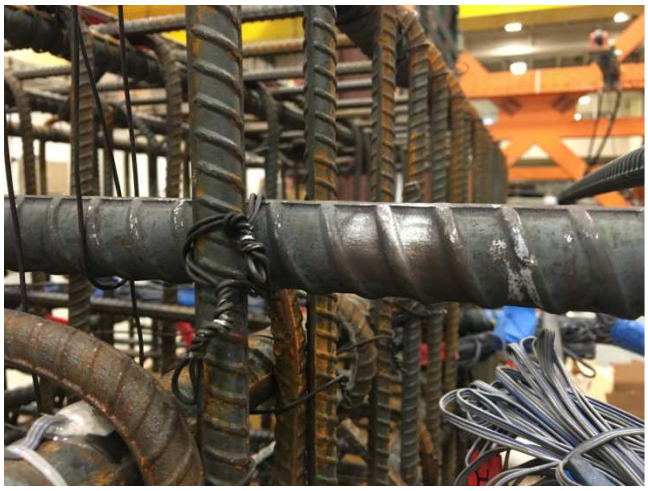

Figure A-26: Brass-Brazing Procedure - Step 1: Surface Clean

Figure A-27: Brass-Brazing Procedure - Placement of Threaded Rod

Figure A-28: Brass-Brazing Procedure - Step 2: Application of Heating Chemical

Figure A-29: Brass-Brazing Procedure - Step 3: Heating by Torch

Figure A-30: Brass-Brazing Procedure - Step 5: Removal of Heat and Formation of Bond

This brass-brazing technique is used to attach the threaded rods onto reinforcement for measuring slip of steel bars out of anchorage in specimens SBH60, SBH100, and SBL100 with conventional Grade 60 A706, Grade 100 T/Y = 1.17, and Grade 100 T/Y = 1.26, respectively. This technique has been tested in the laboratory and shown that it does not alter the mechanical properties of these steel types.

Steel specimens are taken from the same batch of reinforcement used in construction of beams SBH60, SBH100, SBL100, and SBM100. A threaded rod is attached on each specimen by brass-brazing technique. All steel coupons are then tested under cyclic loading in tension for ten cycles in Universal Testing Machine. Figure A-31 displays the setup of one of these tests. Another set of four steel specimens from the same batches are also tested under similar loading conditions. These coupons are plain with no procedure performed on. The force-strain relations of steel specimens that is Nominal Grade 100 T/Y = 1.26 used in beam SBH100 are shown in Figure A-32. Both plain specimen and the one with threaded rod attached on using brass-brazing technique have similar mechanical properties including low-cycle fatigue. The other Grade 100 T/Y = 1.17 and conventional Grade 60 A706 reinforcing steel specimens with brass-brazing procedure performed on also behave similarly with same mechanical properties as corresponding plain ones.

Brass-brazing procedure, however, causes premature fracture of Grade 100 A1035 reinforcement. Therefore, Digital Image Correlation (DIC) technique (Chu et al., 1985) is used instead to measure slip of longitudinal bars in test of beam SBM100. More details on DIC techniques can be found in Arteta (2015).

In the test of specimen SBM100, two small notches are created in concrete at base of test beam to expose the surface of longitudinal reinforcement (Figure A-35). The exposed surface is cleaned, painted white, and black dots are printed on with random patterns. The region is shined with LED flash light and high-resolution cameras are used to take pictures of the region every ten

seconds during the beam tests. The first pictures taken prior to test serve as initial state of measurement. Subsequent pictures are taken and analyzed using computer software Optecal to obtain displacement field of subsets of speckle, which is also the slip of reinforcement out of anchorage (Figure A-36 & Figure A-37).

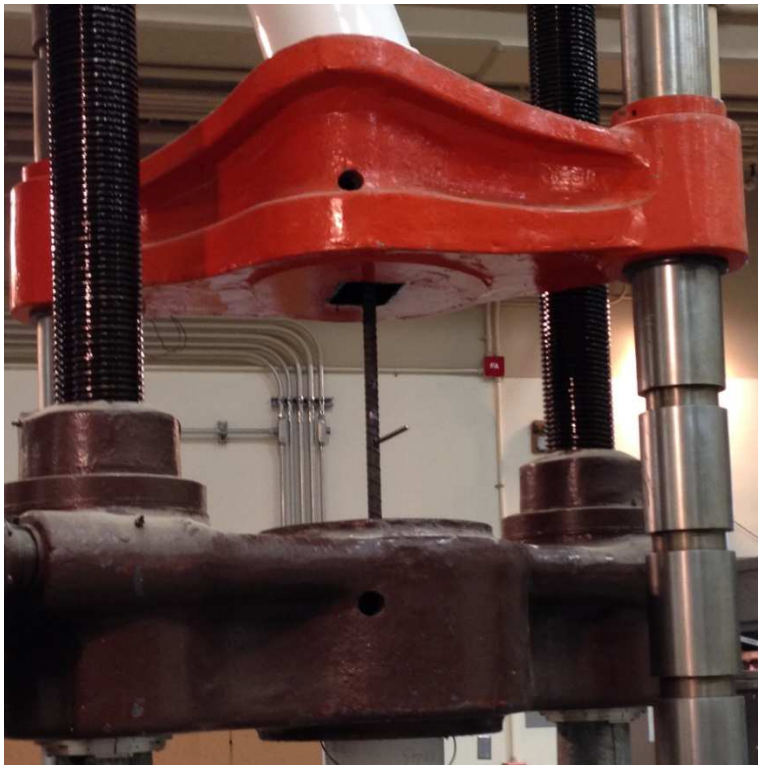

Figure A-31: Test Setup of Steel Specimen with Brass-Brazing - Nominal Grade 100 T/Y = 1.26

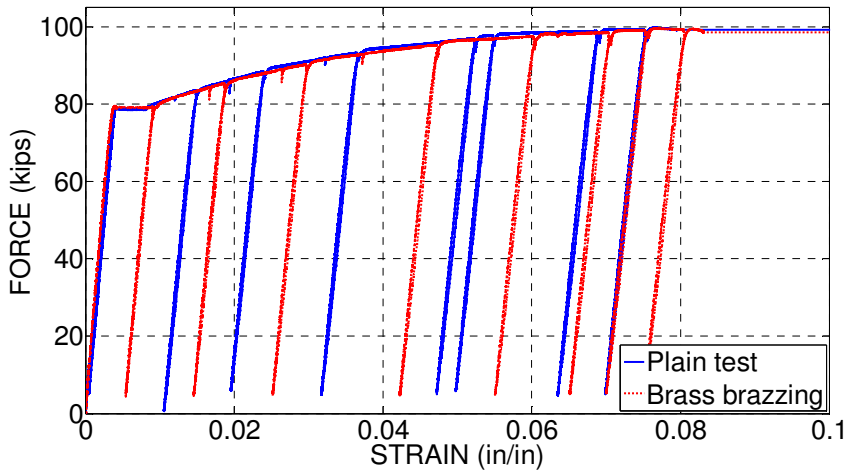

Figure A-32: Stress-Strain Relations of Steel Specimen - Nominal Grade 100 T/Y = 1.26

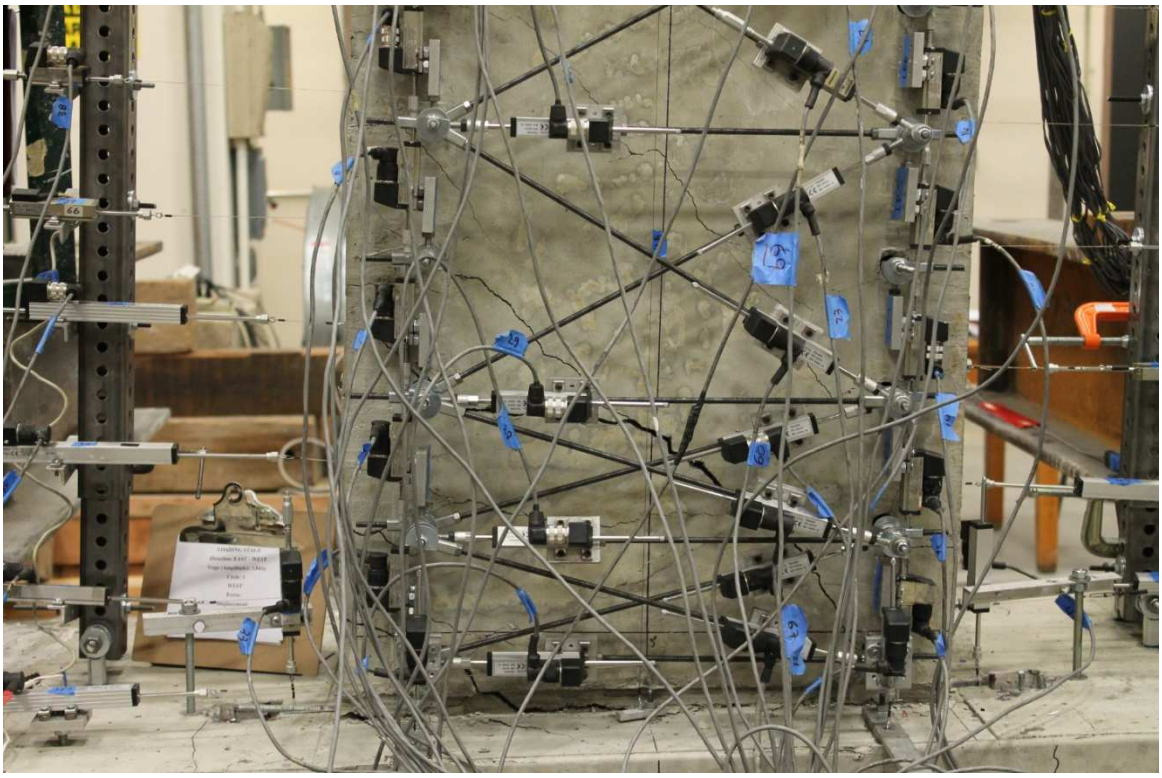

Figure A-33: General Instrumentation for Measuring Slip by Brass-Brazed Threaded Rods

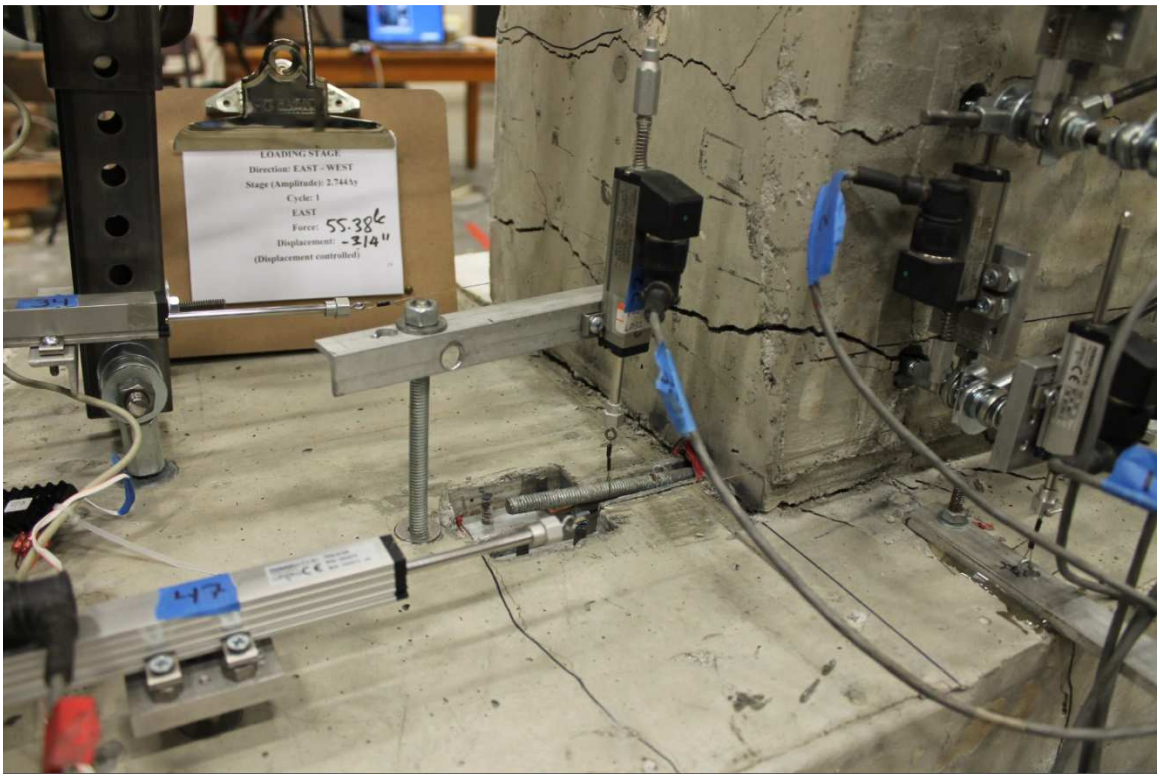

Figure A-34: General Instrumentation for Measuring Slip by Brass-Brazed Threaded Rods

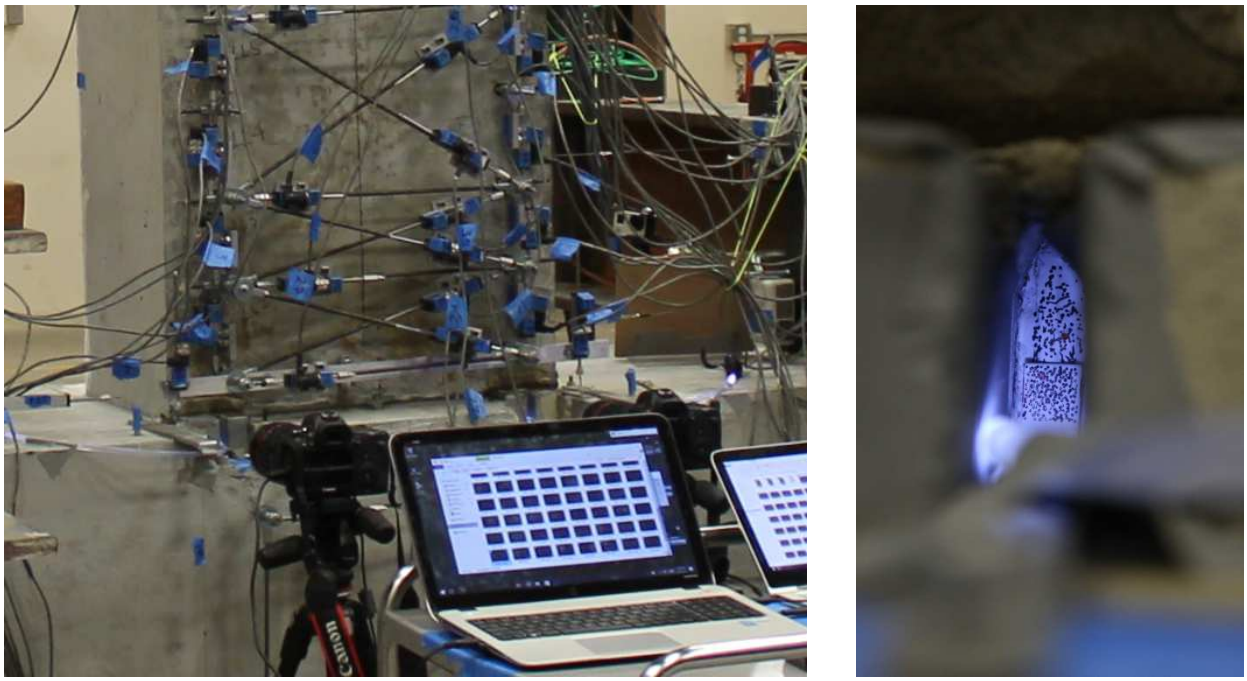

Figure A-35: General Instrumentation for Measuring Slip by Digital Image Correlation (DIC)

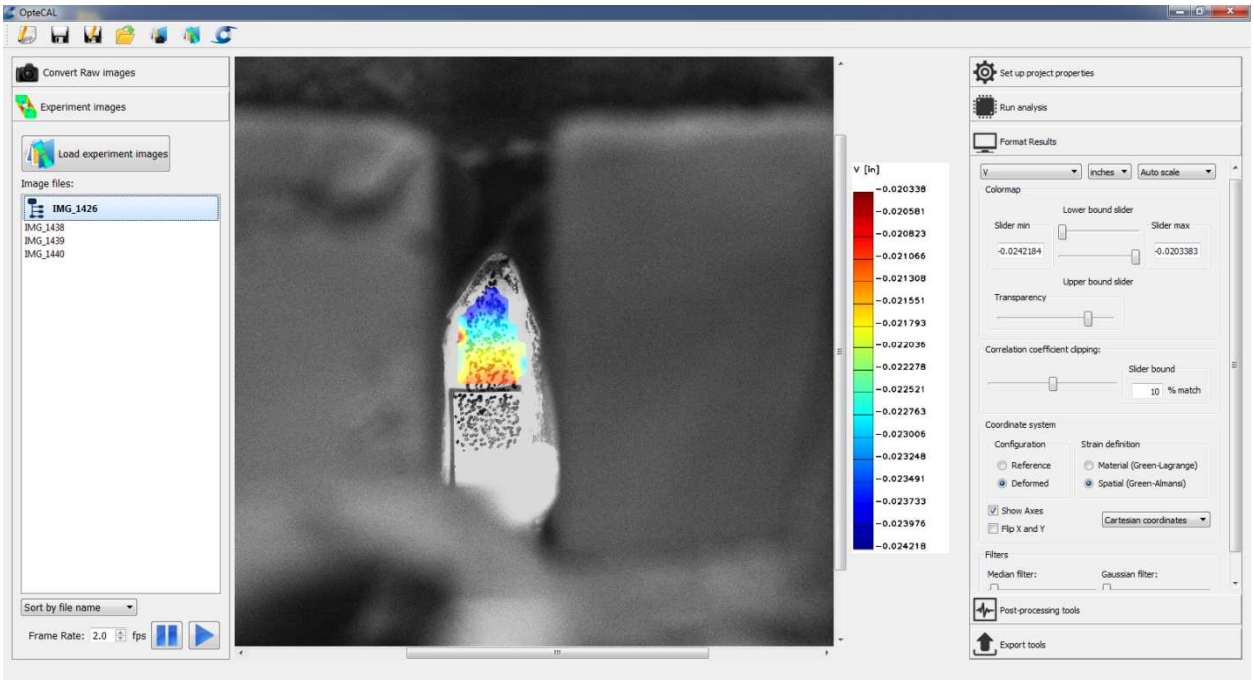

Figure A-36: Data Reduction of DIC

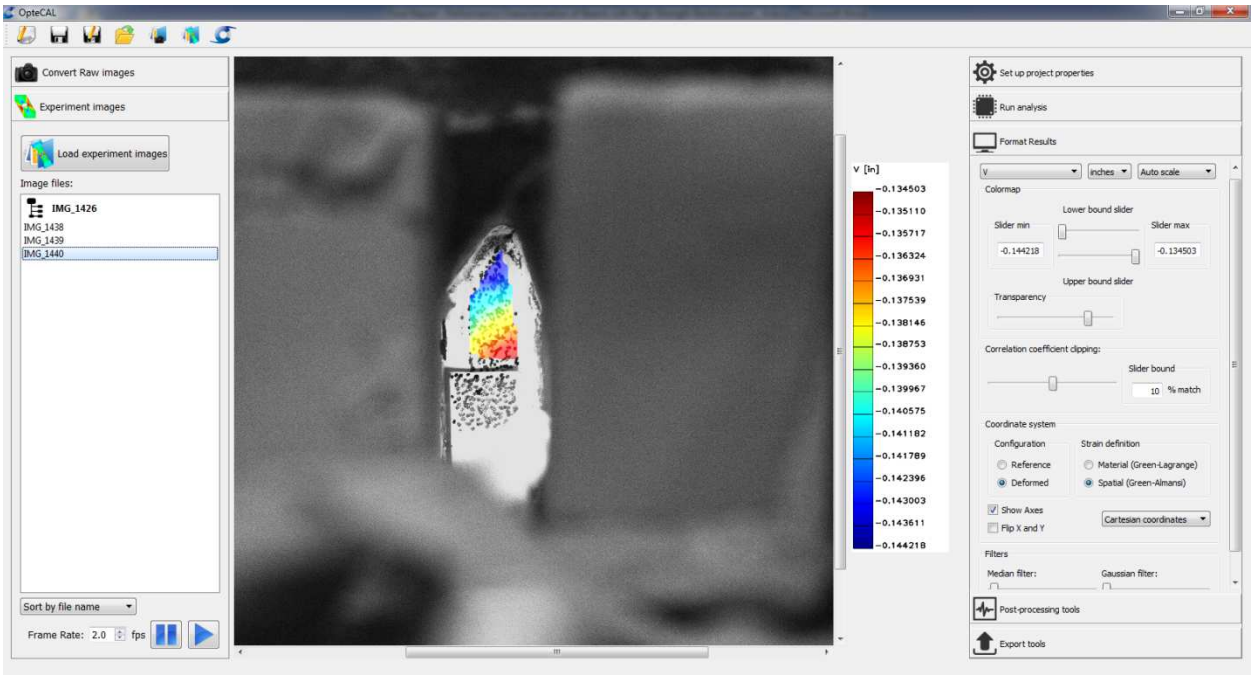

Figure A-37: Data Reduction of DIC

Data Acquisition System

The data acquisition control system enclosure was Pacific Instruments Model 6000 (Figure A-38). Detailed information can be found on http://www.pacificinstruments.com. The data acquisition system control system input/output modules were Pacific Instruments Model 6035, 8-Channel Strain/Bridge Transducer Amplifier-Filter-Digitizer. These modules are particularly suited to strain gauges.

Figure A-38: Left: Data Acquisition System; Right: Analog I/O Modules

TEST PROCEDURES

The loading history to impose on test specimens was developed based on recommendations of FEMA 461 (FEMA, 2007). It consists of two major loading types: load controlled, and displacement controlled. The details are described as below.

Load-controlled cycles:

Lateral load was applied to the specimens using two actuators that were controlled by magnitude of applied load from the beginning of test up to yielding point, which was defined as the amount of force needed to apply on top of the specimen to cause the first longitudinal reinforcement to yield. Load-controlled was chosen for these loading cycles because the magnitudes of load to result in cracking, yielding, and intermediate stages between cracking and yielding on the specimens could be estimated relatively accurately. The corresponding tip displacements resulted from these pre-determined magnitudes of lateral force were measured during test. Accordingly, tip displacement at yield point was measured and used to compute following magnitudes of displacement to be applied to specimens in later displacement-controlled loading cycles. For each magnitude of force, three cycles of loading were applied.

Displacement-controlled cycles:

From measured yield displacement, magnitudes of displacement to be applied onto the top of specimens in displacement-controlled loading cycles were computed by multiplying the displacement of previous cycle by a factor of 1.4 as suggested by FEMA 461. For the pre-determined displacement amplitudes that result in top drift ratio less than 2%, three cycles of loading were applied, while for those resulting in top drift ratio larger than 2%, only two cycles were imposed.

Table A-5 shows the loading sequence of the tests on Beams SBL100, SBH100, and SBM100 while Table A-6 displays that on Beam SBH60. Figure A-39 illustrates the time history of top drift ratio measured or applied onto the beam.

For each loading amplitude of either force- or displacement-controlled, the test beams were loaded from initial position to the peak in East direction first, followed by another peak in the West direction, and one cycle was completed by loading the beam back to initial position. The test was stopped for marking cracks when the specimen was loaded to the peak on the East, and West direction of the first cycle, and the end of loading cycles (either second or third) when the pre-determined applied load or displacement became zero.

Table A-5: Loading Protocol for Beams with Nominal Grade 100 Reinforcement

Loading Stage	Number of Cycles	Loading Type
Cracking Force	3	Force-Controlled
0.60Fy	3	Force-Controlled
0.84Fy	3	Force-Controlled
1.00Fy	3	Force-Controlled
1.40Δy	3	Displacement-Controlled
1.96Δy	2	Displacement-Controlled
2.74Δy	2	Displacement-Controlled
3.84Δy	2	Displacement-Controlled
5.38Δy	2	Displacement-Controlled

Table A-6: Loading protocol for Beam with Grade 60 A706 Reinforcement

Loading Stage	Number of Cycles	Loading Type
Cracking Force	3	Force-Controlled
0.60Fy	3	Force-Controlled
0.84Fy	3	Force-Controlled
1.00Fy	3	Force-Controlled
1.40Δy	3	Displacement-Controlled
1.96Δy	3	Displacement-Controlled
2.74Δy	3	Displacement-Controlled
3.84Δy	2	Displacement-Controlled
5.38Δy	2	Displacement-Controlled
7.53Δy	2	Displacement-Controlled

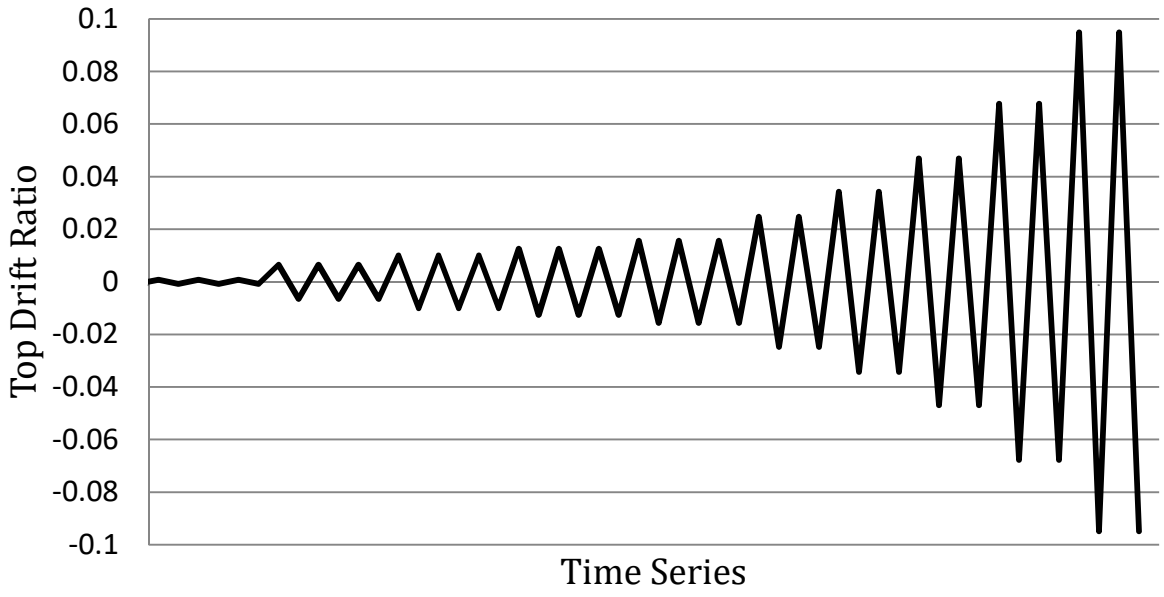

Figure A-39: Loading History

DATA REDUCTION

Global deflection was measured by wire potentiometer (Figure A-40). Lateral force was measured by load cells attached on two actuators that were used to apply force on test specimens. The total force was the sum of the force measured by two load cells projected on direction of loading.

Local deformation was measured by LVDT's. From a truss system of LVDT's as shown in Figure A-40, total deformation was computed from measurement of local deformation based on principle of virtual force:

$$F_v \Delta_r = \sum_{i=1}^{n} f_{i,v} \Delta L_{i,r}$$

where: F_v = virtual force applied horizontally at 52.5 inches above base of beam

Δ_r = real horizontal deflection of interest at 52.5 inches above base of beam

$f_{i,v}$ = virtual internal force in each truss member caused by virtual force F_v

$\Delta L_{i,r}$ = real deformation in each truss member or the change in length of each LVDT in truss system

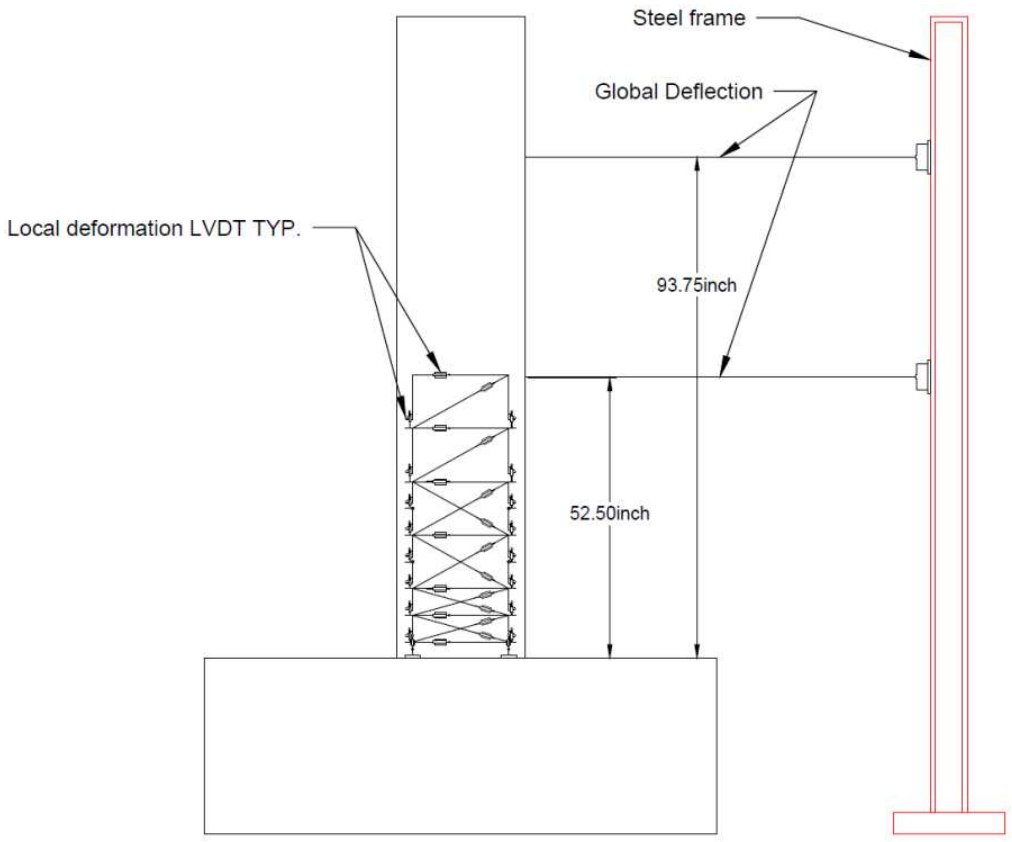

Figure A-40: Instrumentation Scheme for Measuring of Global Deflection and Local Deformation.

Flexural deformation is then defined by contribution of longitudinal truss members (or LVDT's) and shear deformation is that of diagonal and transverse members. The bottom two longitudinal LVDT's measure both flexural deformation and slip of longitudinal reinforcement out of anchorage. Therefore, another set of LVDT's was used to measure slip of reinforcement separately (Figure A-41) and decoupled from bottom two LVDT's in truss system to obtain flexural deformation.

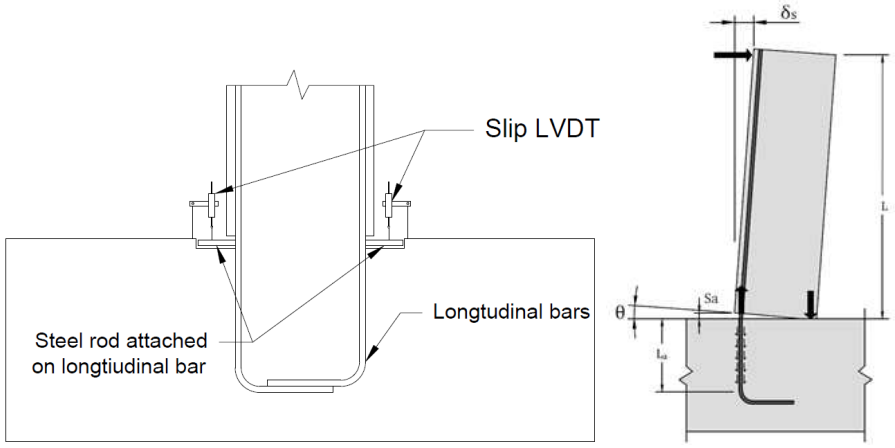

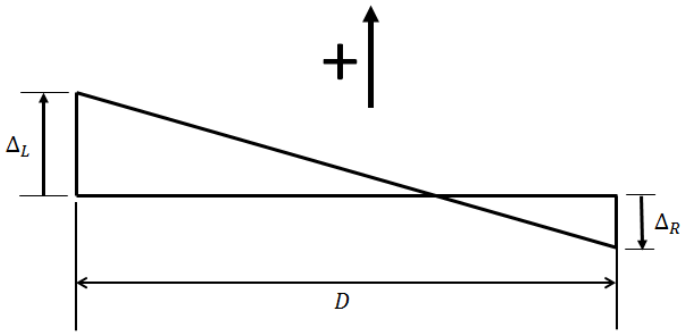

Figure A-41: Instrumentation of Slip Measurement and Computation of Slip Deformation.

Deformation due to slip was then computed by:

$$\delta_s = L\frac{\Delta_L - \Delta_R}{D}$$

where: L = length of test beam from base to loading point
D = distance between two slip LVDTs
Δ_L = change in length of LVDT on the left of beam
Δ_R = change in length of LVDT on the right of beam

All flexural, shear, and slip deformations were calculated from measurement of LVDT's truss system up to location of 52.5 inches above base of beam. Deformation of the remaining section of beam up to tip was computed based on elastic theory of mechanics.

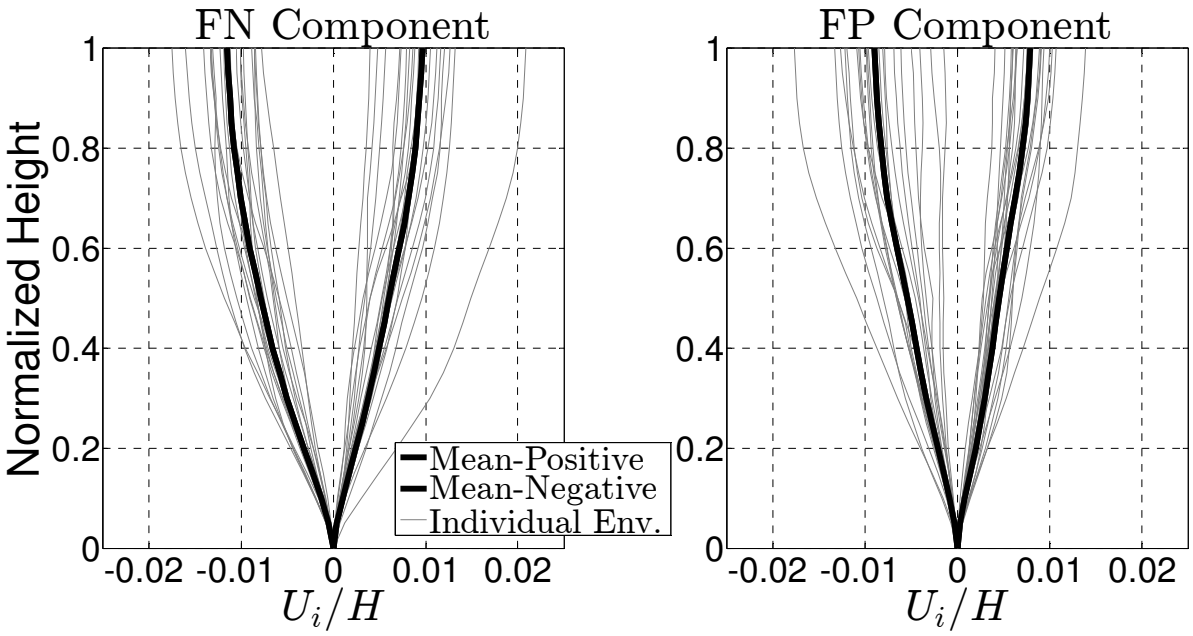

Figure B-1: Drift Envelopes for Frame SBH60 – Left: FN Component – Right: FP Component

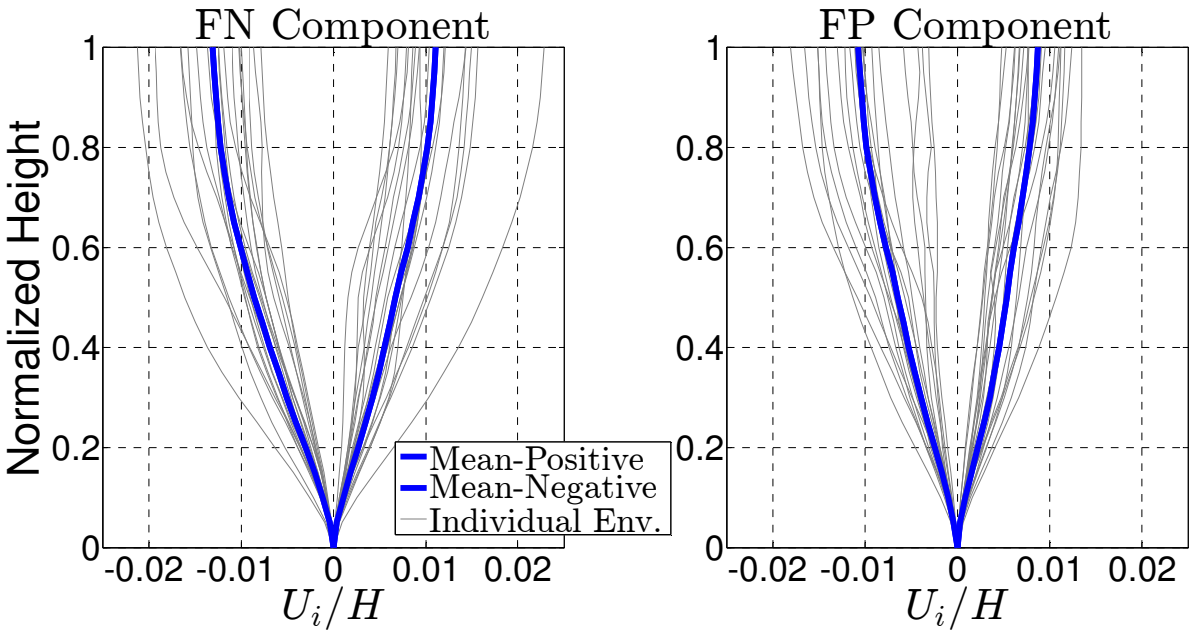

Figure B-2: Drift Envelopes for Frame SBH100 – Left: FN Component – Right: FP Component

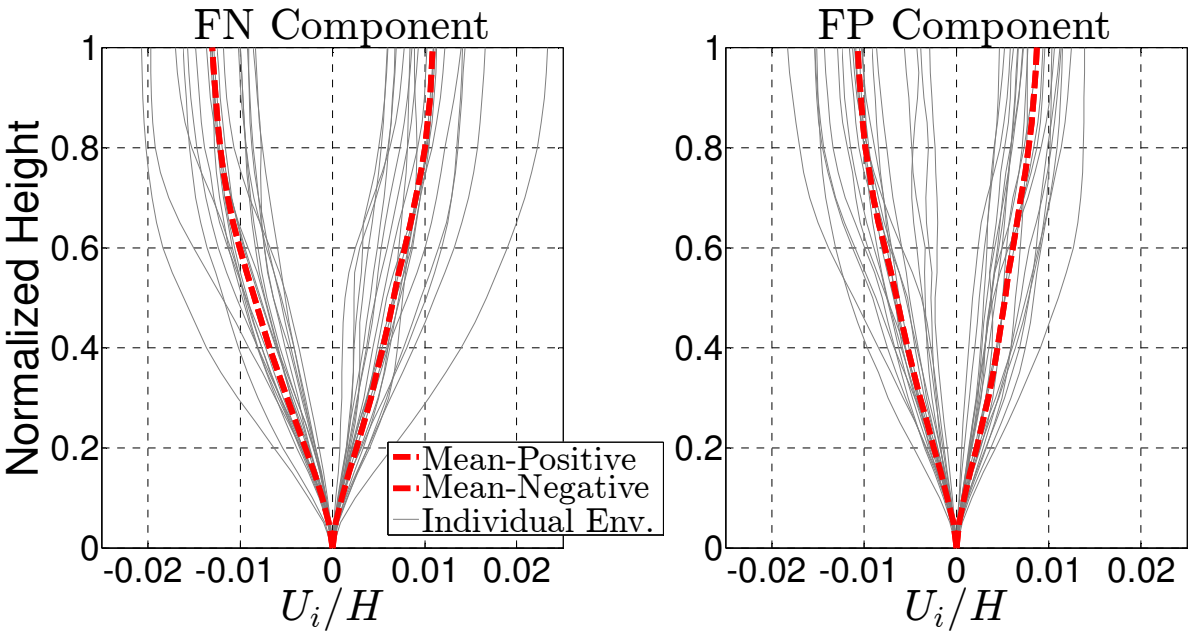

Figure B-3: Drift Envelopes for Frame SBL100 – Left: FN Component – Right: FP Component

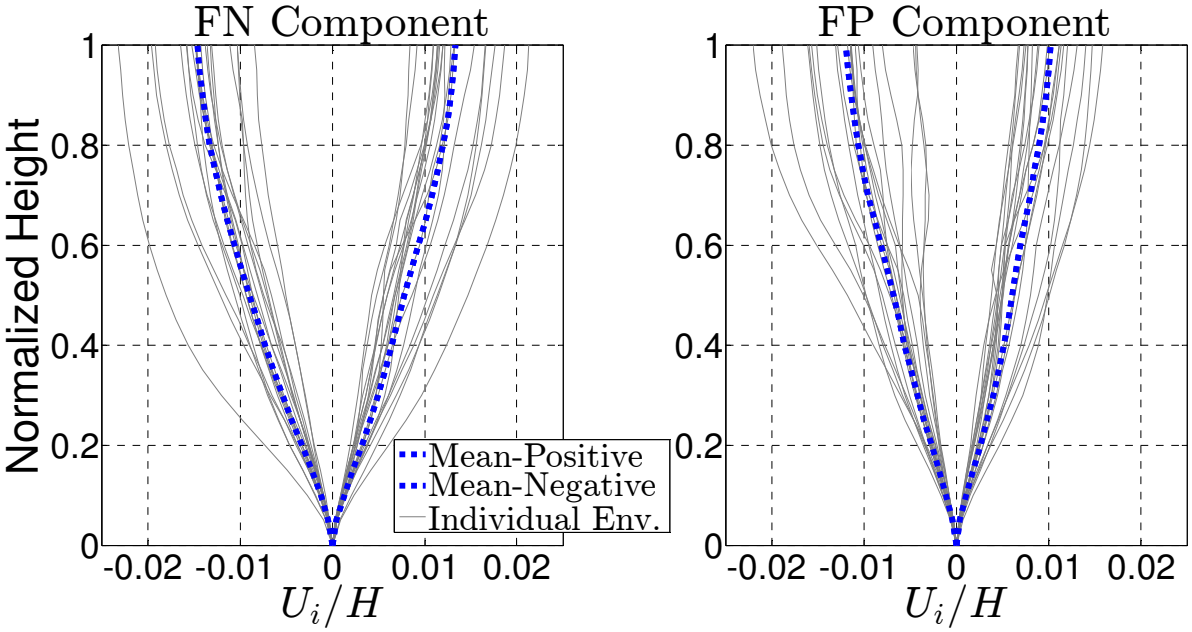

Figure B-4: Drift Envelopes for Frame SBM100 – Left: FN Component – Right: FP Component

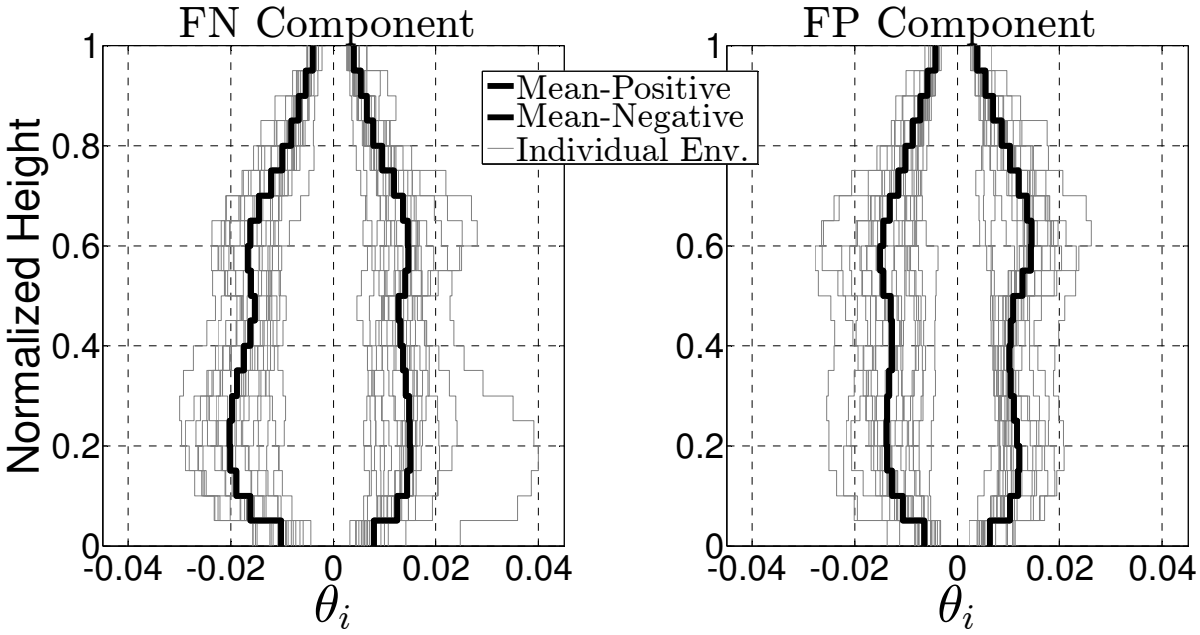

Figure B-5: Story Drift Envelopes for Frame SBH60 – Left: FN Component – Right: FP Component

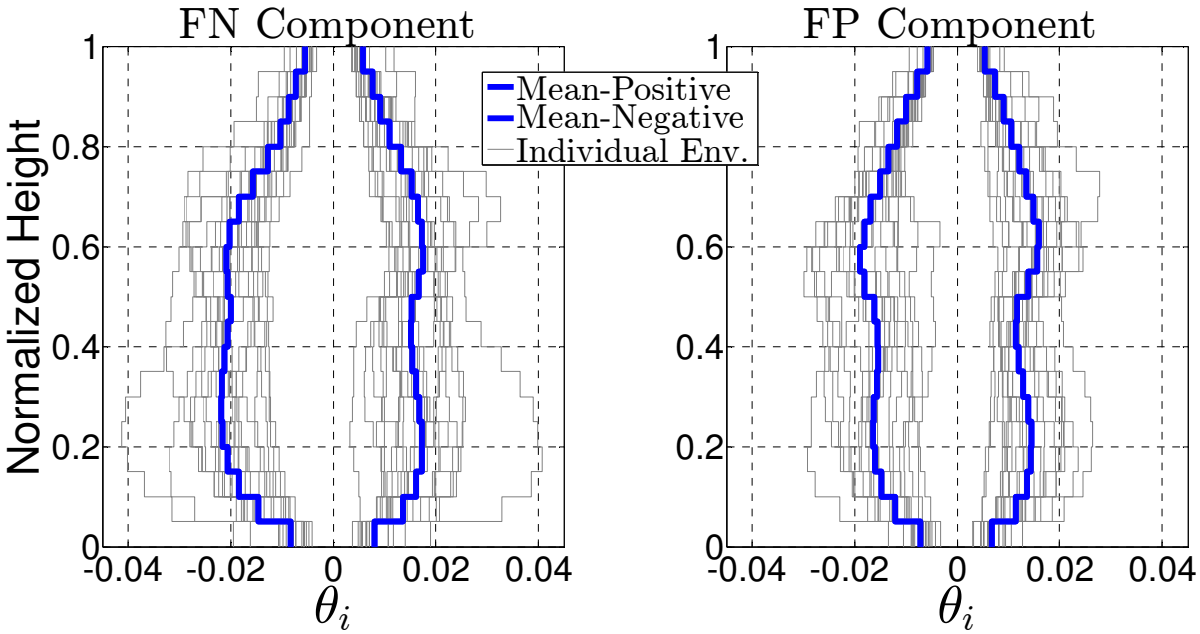

Figure B-6: Story Drift Envelopes for Frame SBH100 – Left: FN Component – Right: FP Component

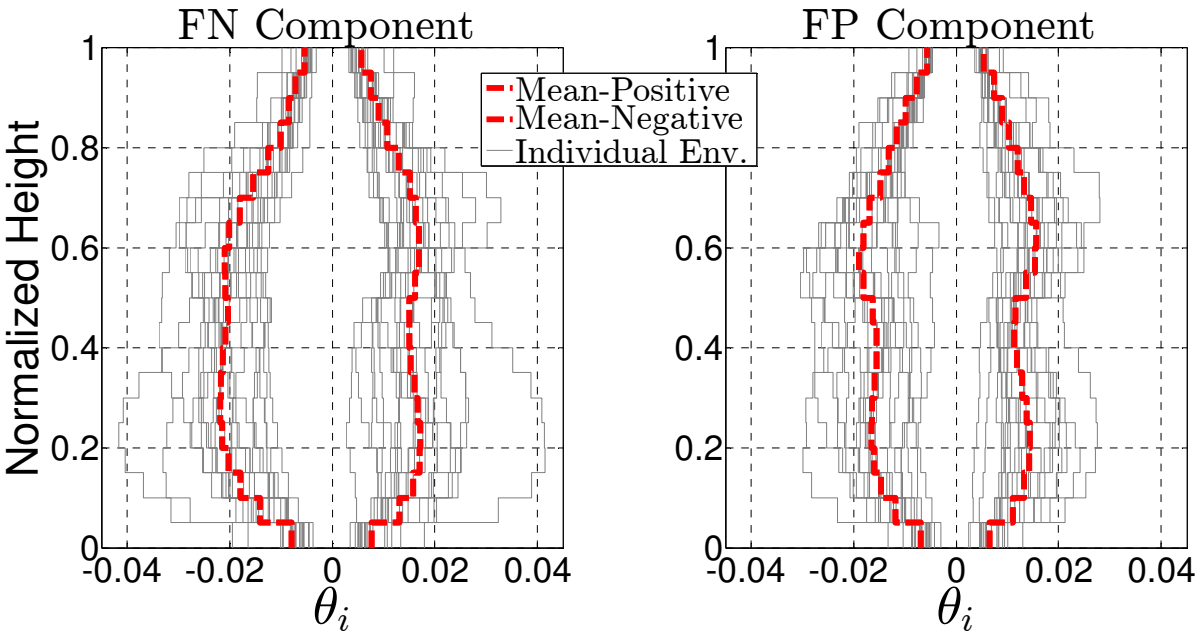

Figure B-7: Story Drift Envelopes for Frame SBL100 – Left: FN Component – Right: FP Component

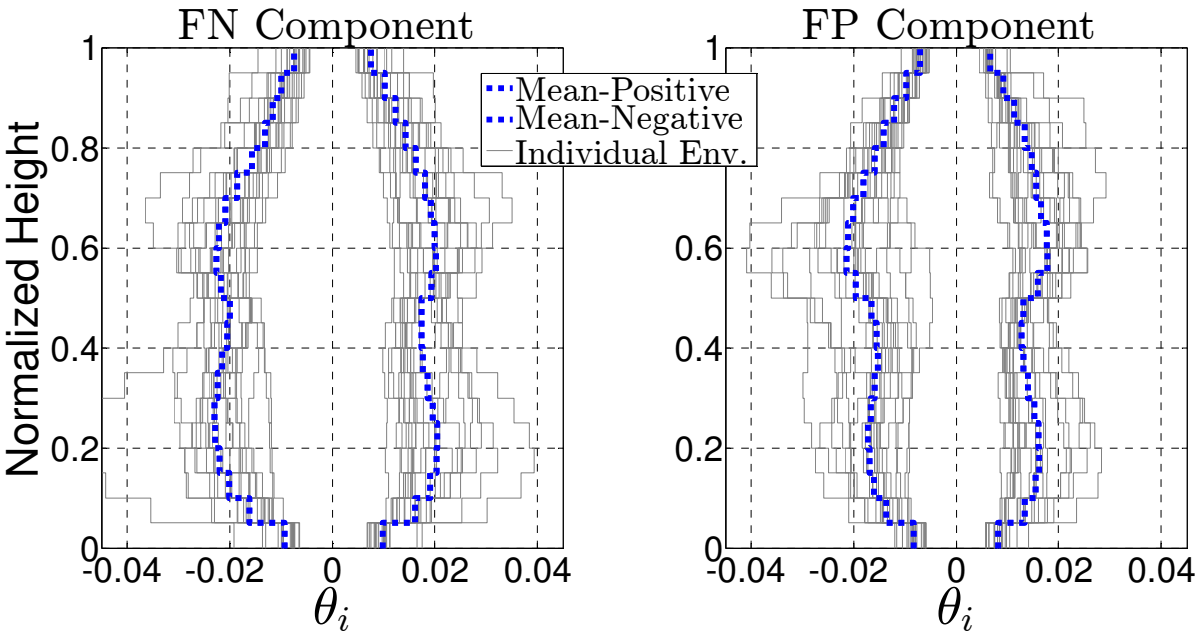

Figure B-8: Story Drift Envelopes for Frame SBM100 – Left: FN Component – Right: FP Component

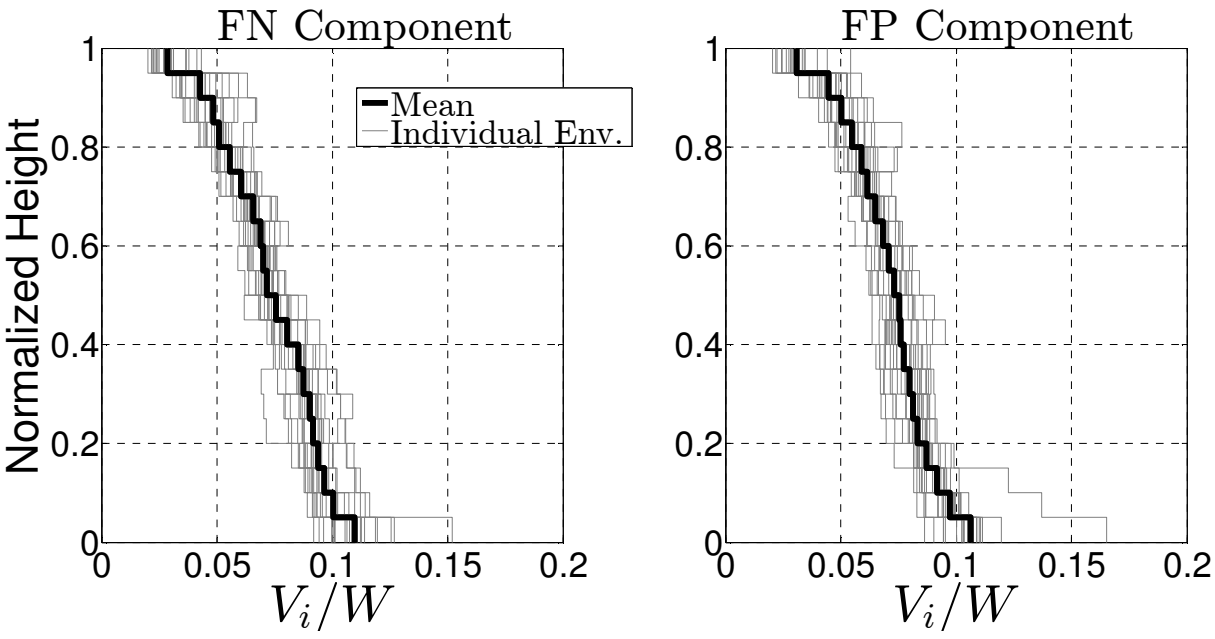

Figure B-9: Story Shear Envelopes for Frame SBH60 – Left: FN Component – Right: FP Component

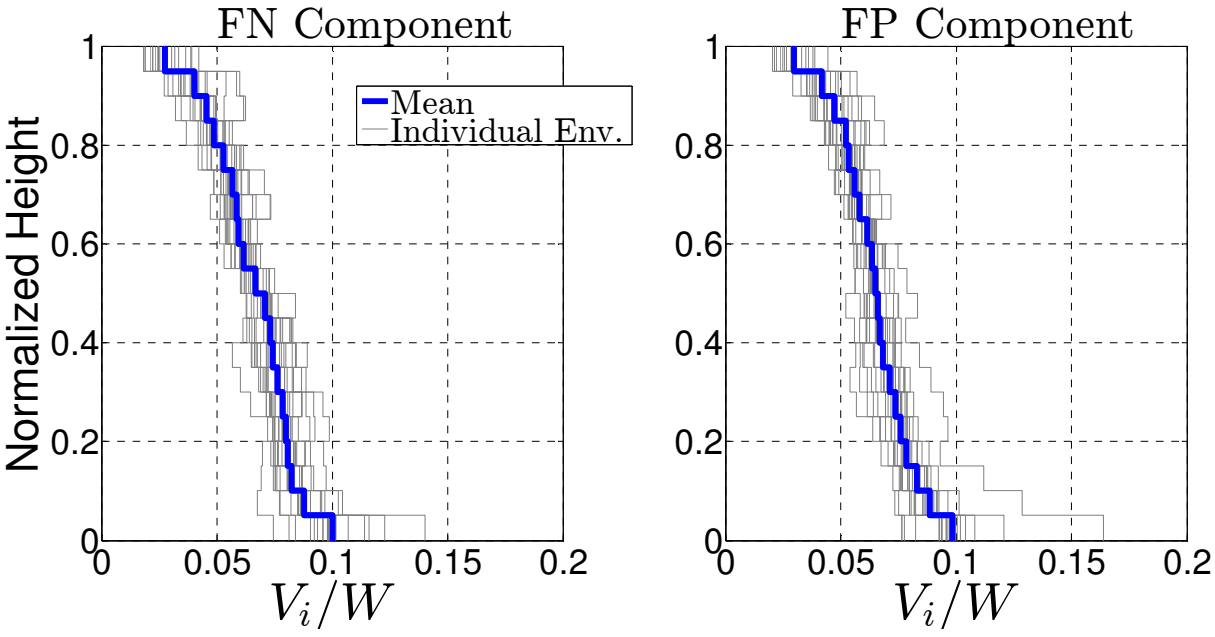

Figure B-10: Story Shear Envelopes for Frame SBH100 – Left: FN Component – Right: FP Component

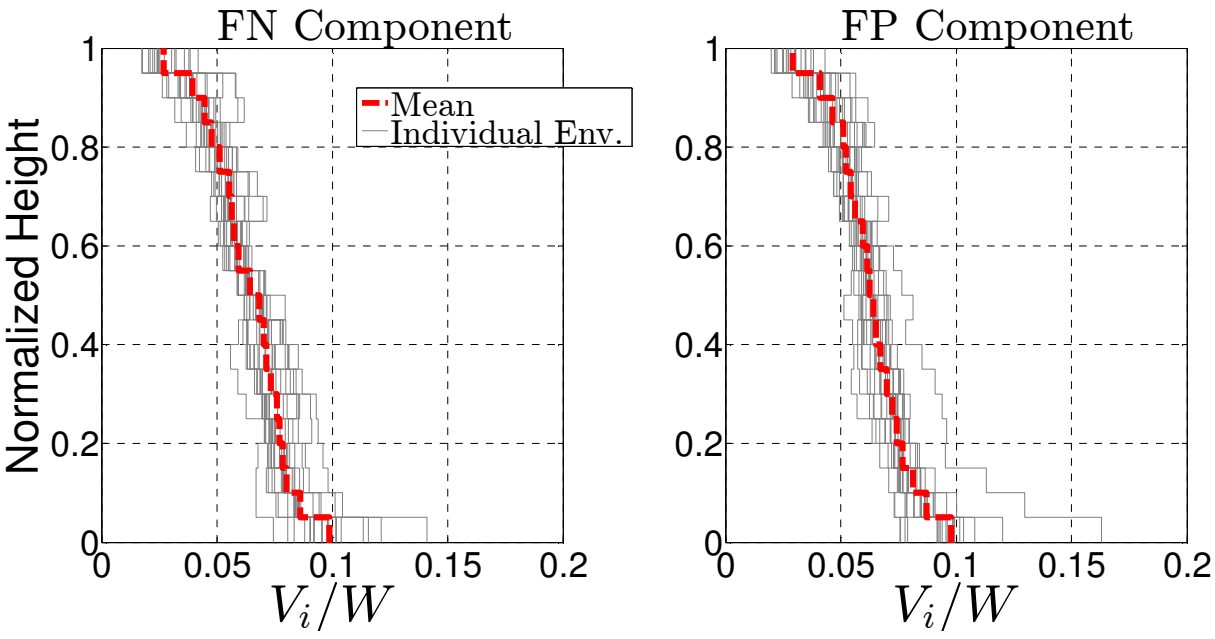

Figure B-11: Story Shear Envelopes for Frame SBL100 – Left: FN Component – Right: FP Component

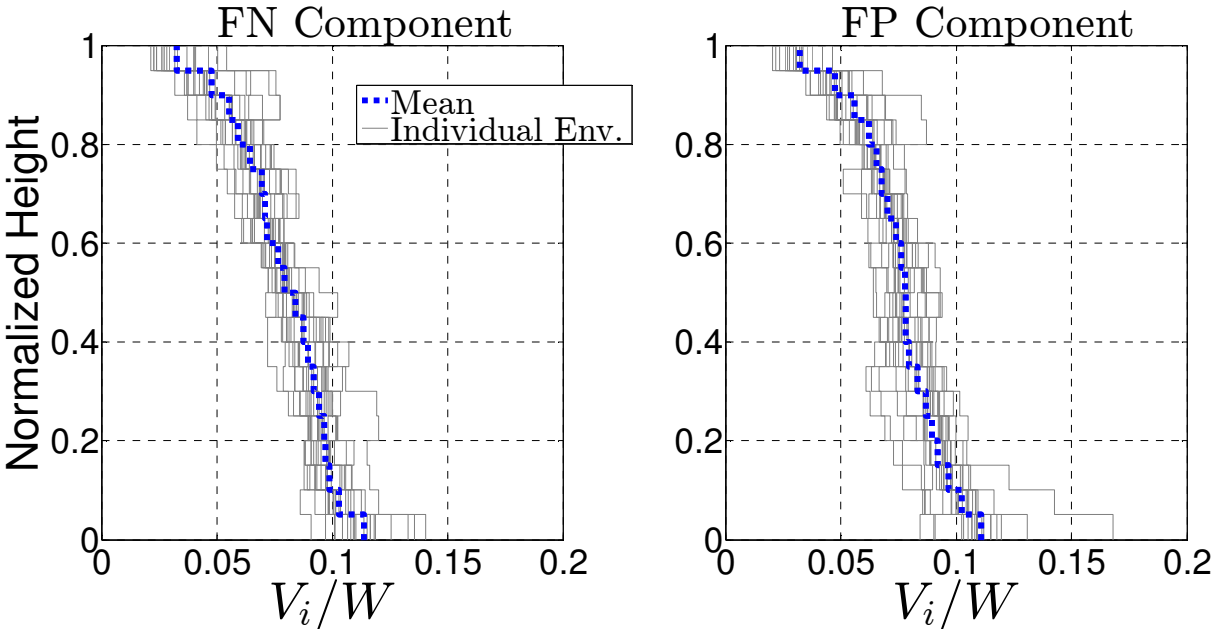

Figure B-12: Story Shear Envelopes for Frame SBM100 – Left: FN Component – Right: FP Component

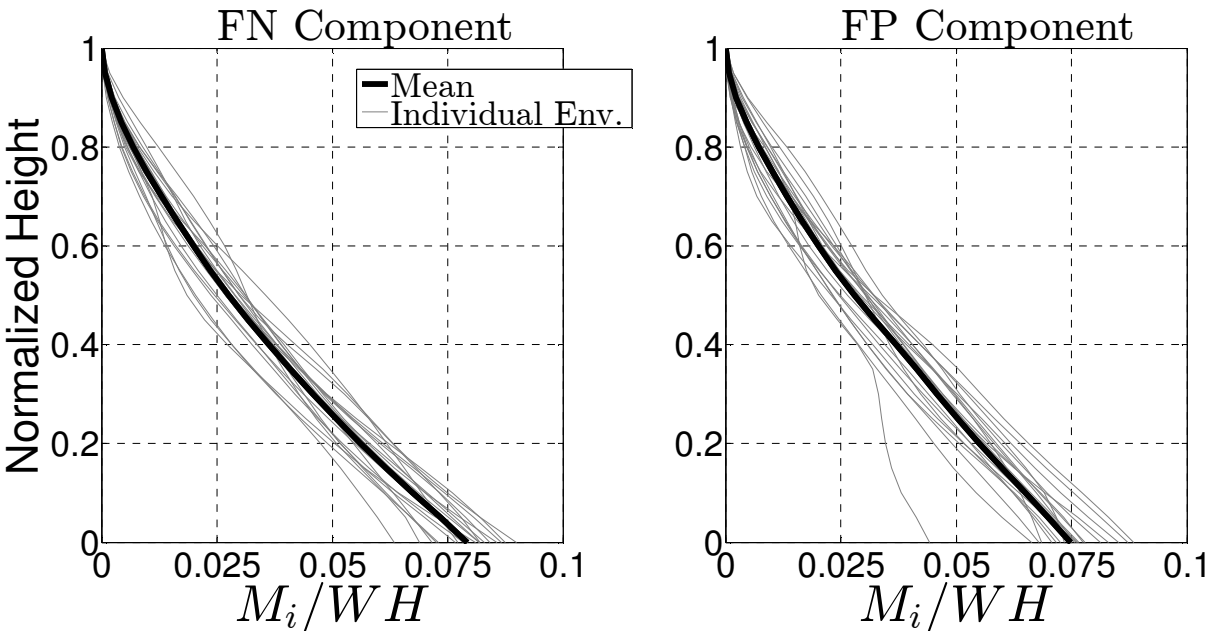

Figure B-13: Story Moment Envelopes for Frame SBH60 – Left: FN Component – Right: FP Component

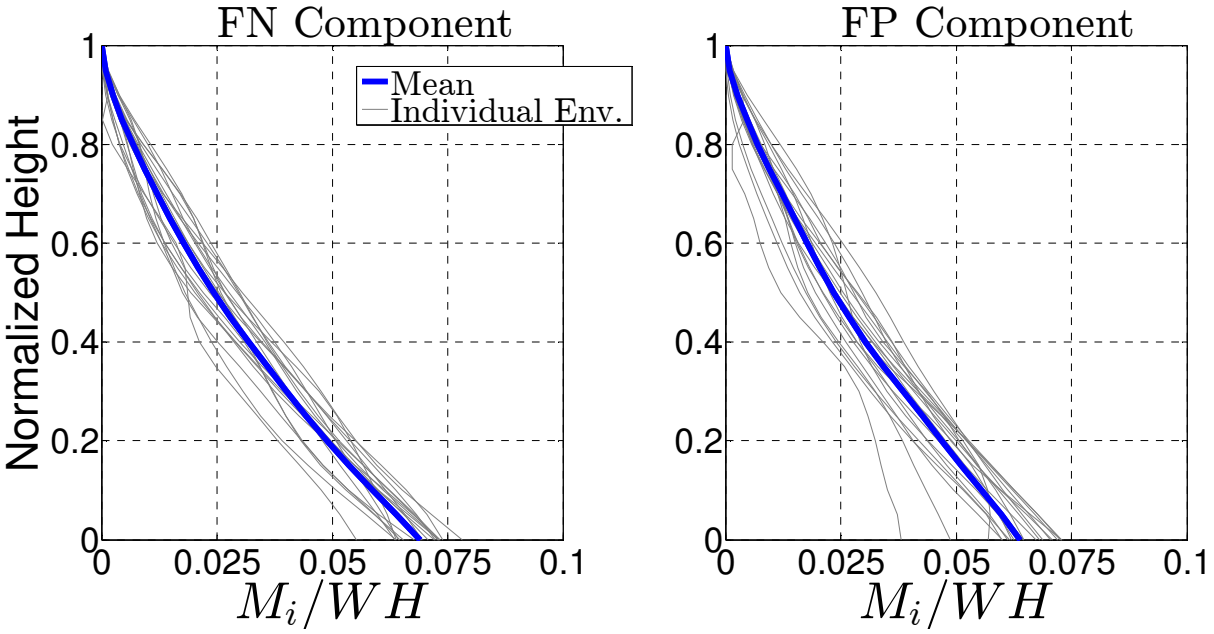

Figure B-14: Story Moment Envelopes for Frame SBH100 – Left: FN Component – Right: FP Component

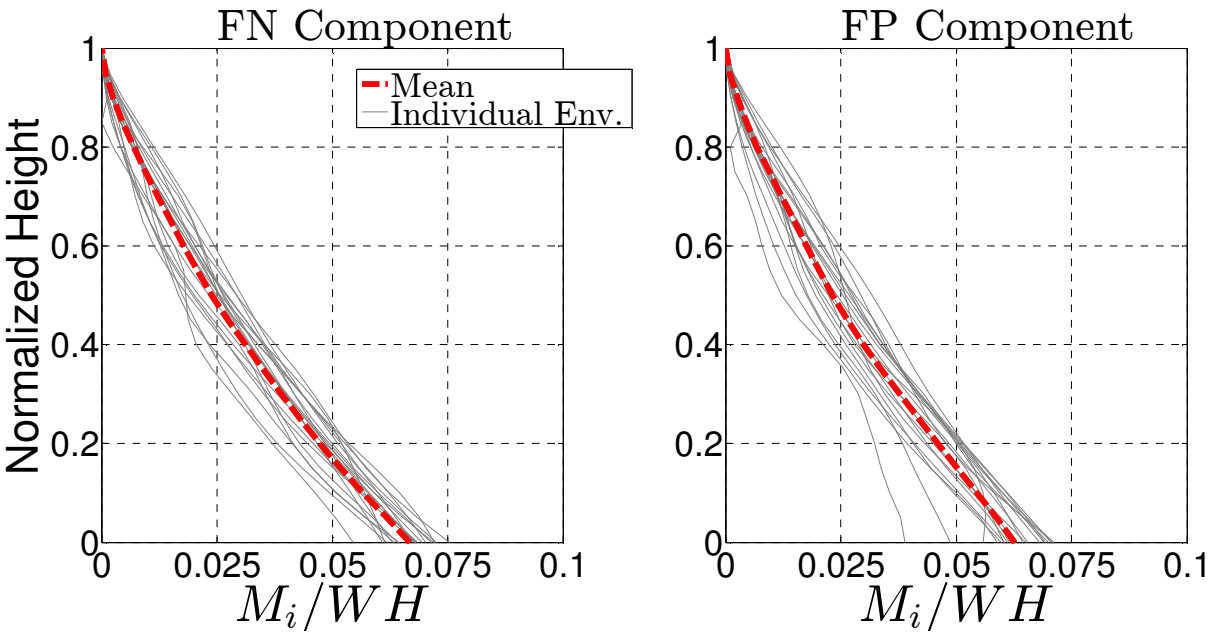

Figure B-15: Story Moment Envelopes for Frame SBL100 – Left: FN Component – Right: FP Component

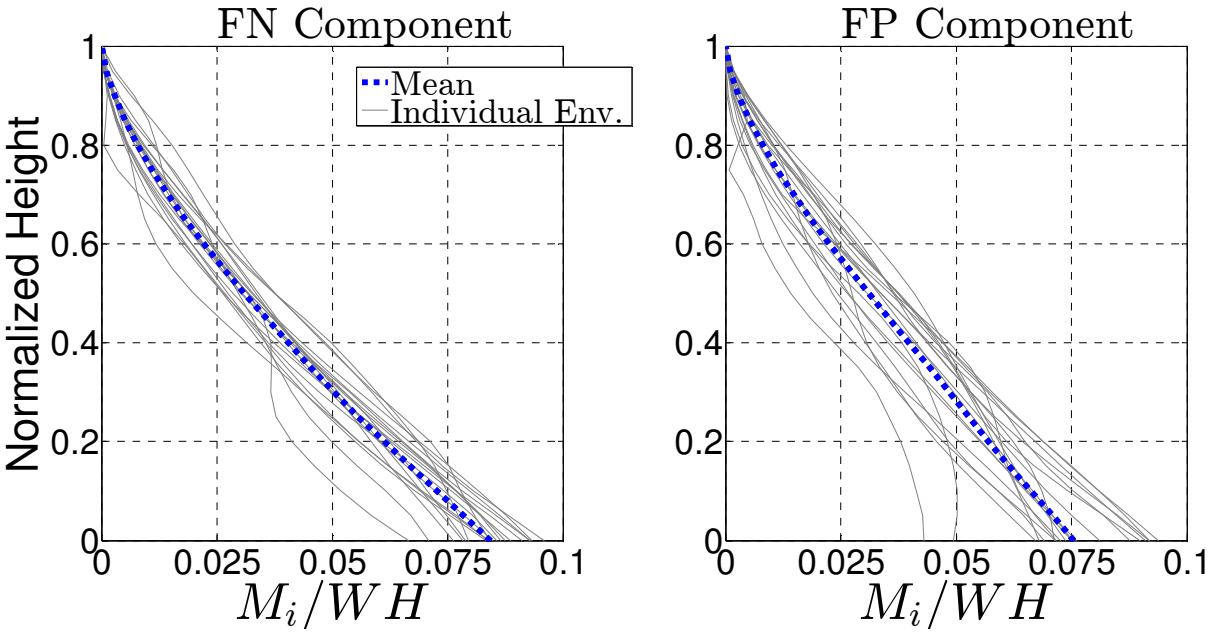

Figure B-16: Story Moment Envelopes for Frame SBM100 – Left: FN Component – Right: FP Component

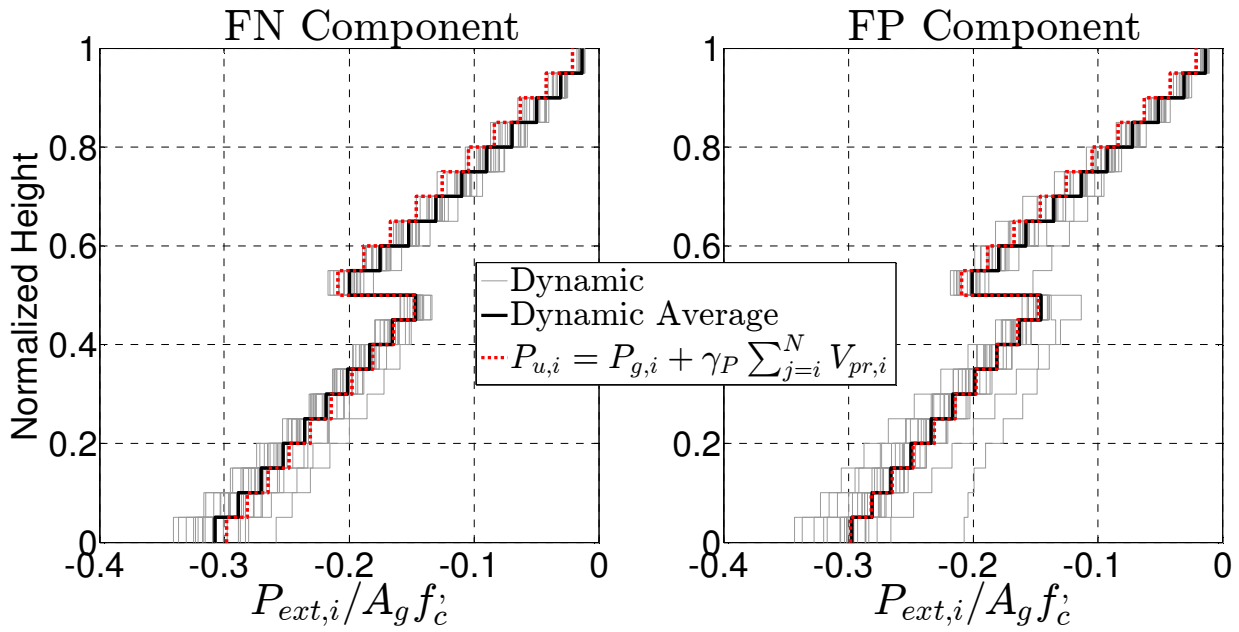

Figure B-17: Exterior Column Compression in Frame SBH60 – Left: FN Component – Right: FP Component

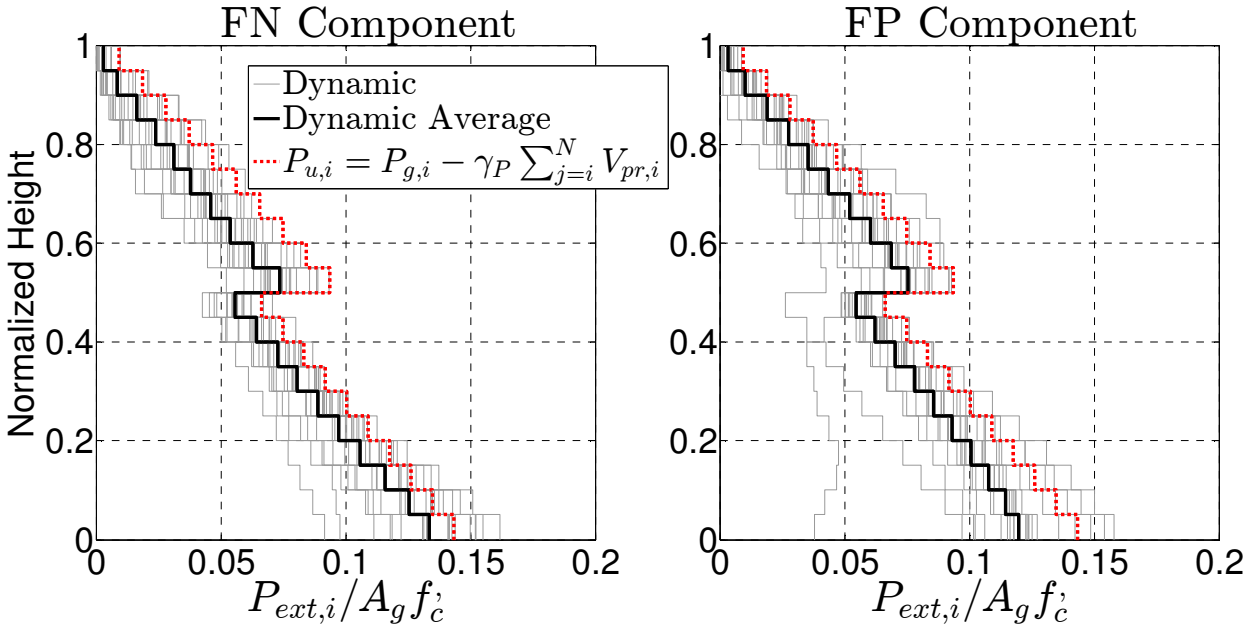

Figure B-18: Exterior Column Tension in Frame SBH60 – Left: FN Component – Right: FP Component

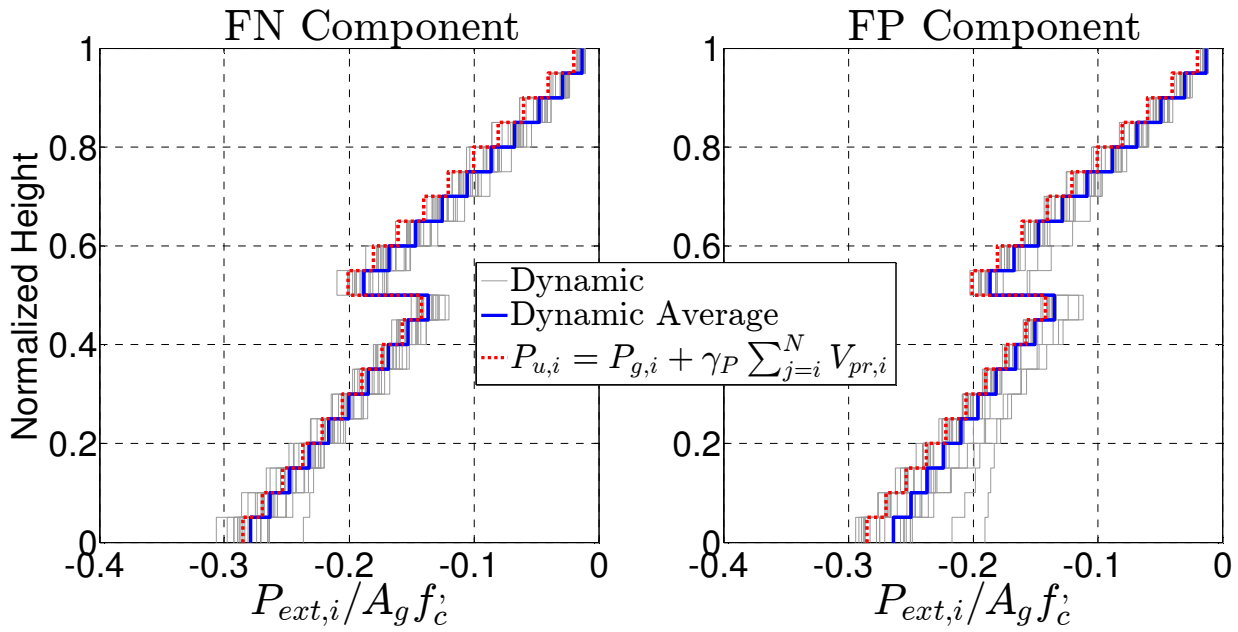

Figure B-19: Exterior Column Compression in Frame SBH100 – Left: FN Component – Right: FP Component

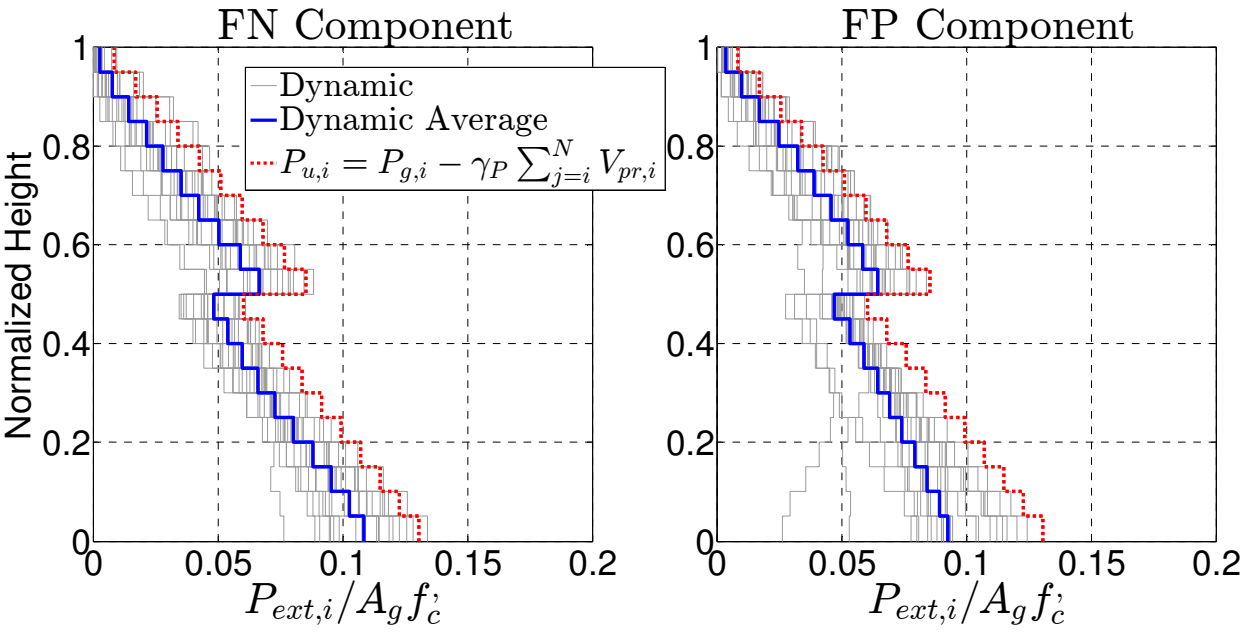

Figure B-20: Exterior Column Tension in Frame SBH100 – Left: FN Component – Right: FP Component

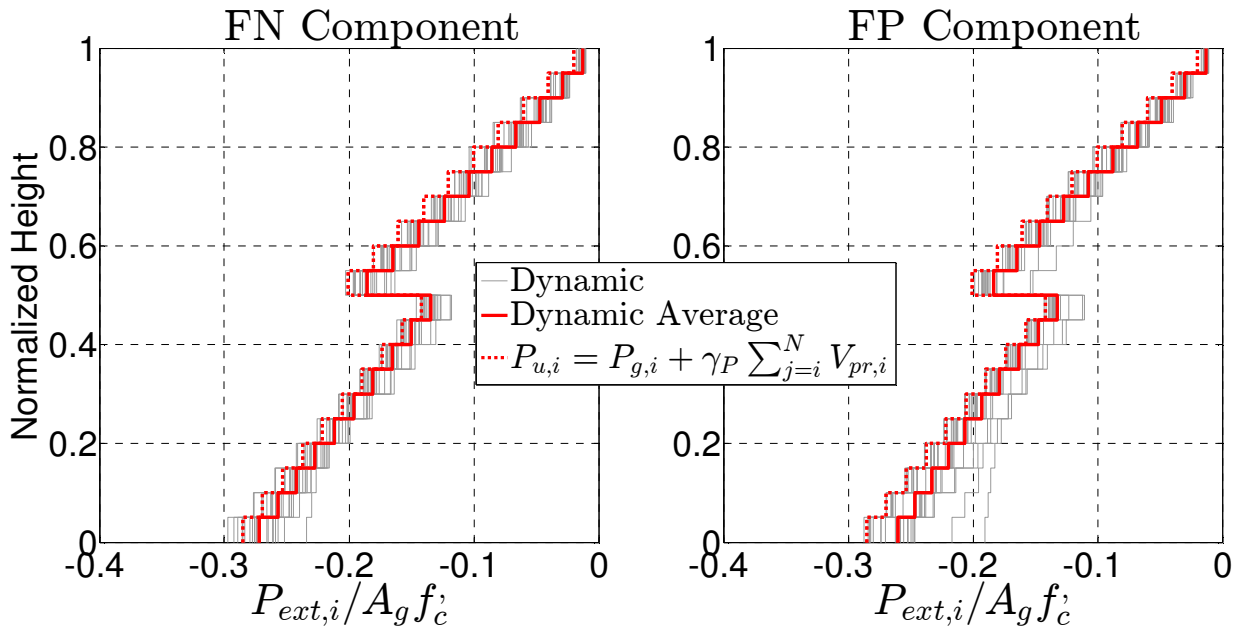

Figure B-21: Exterior Column Compression in Frame SBL100 – Left: FN Component – Right: FP Component

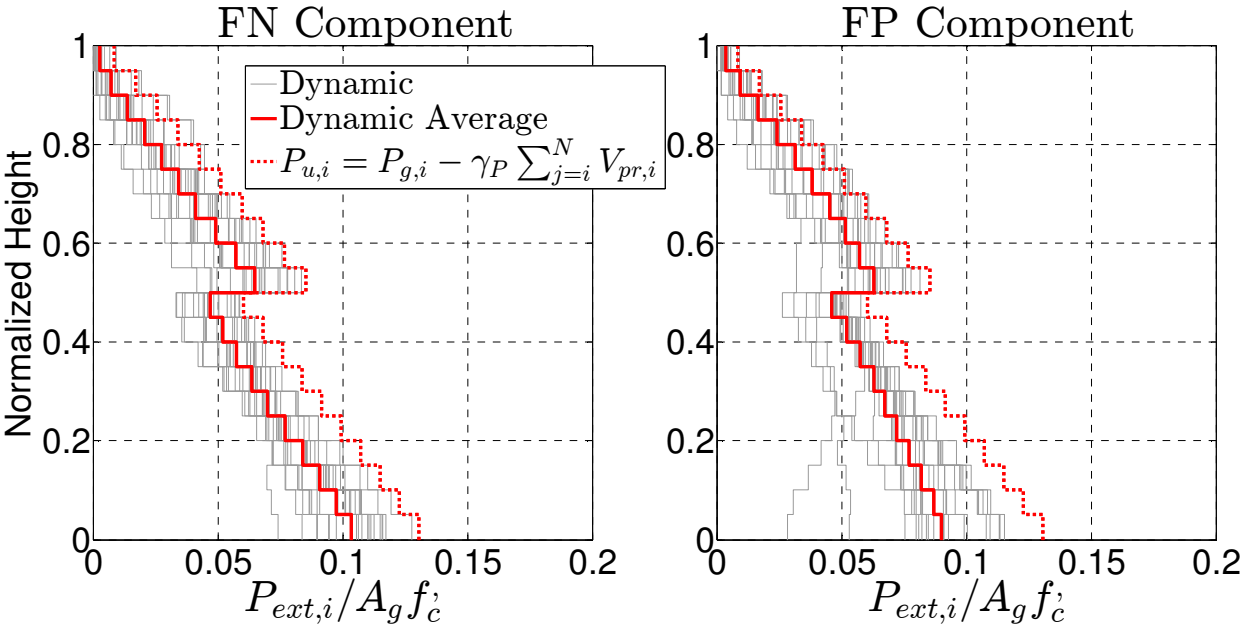

Figure B-22: Exterior Column Tension in Frame SBL100 – Left: FN Component – Right: FP Component

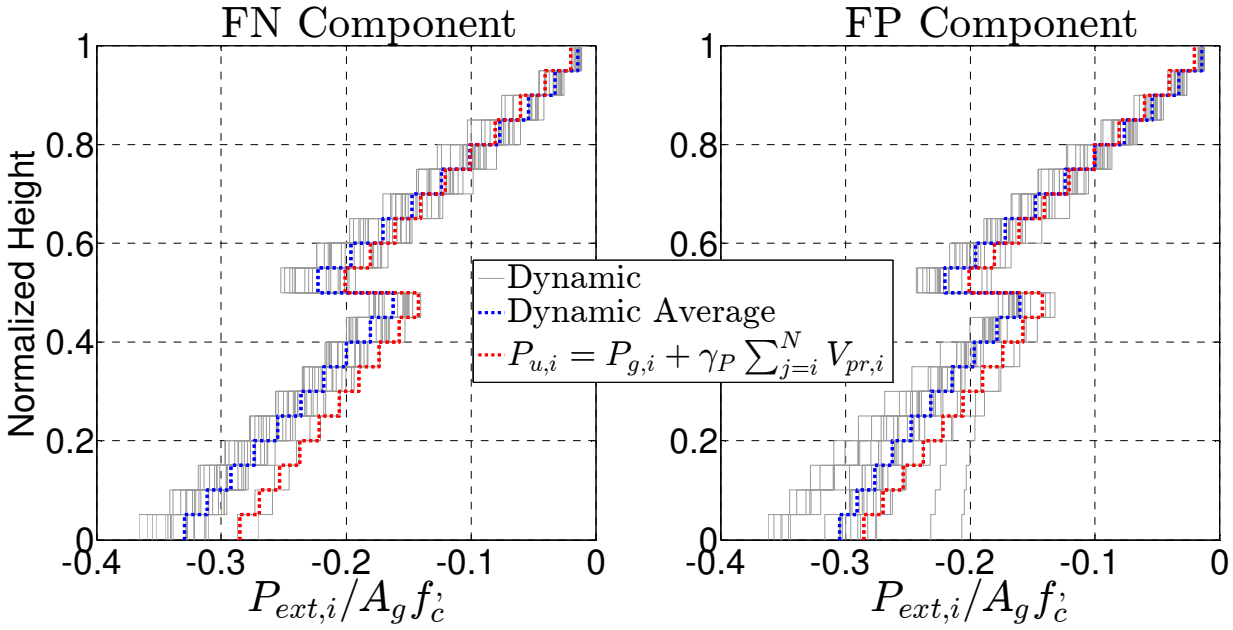

Figure B-23: Exterior Column Compression in Frame SBM100 – Left: FN Component – Right: FP Component

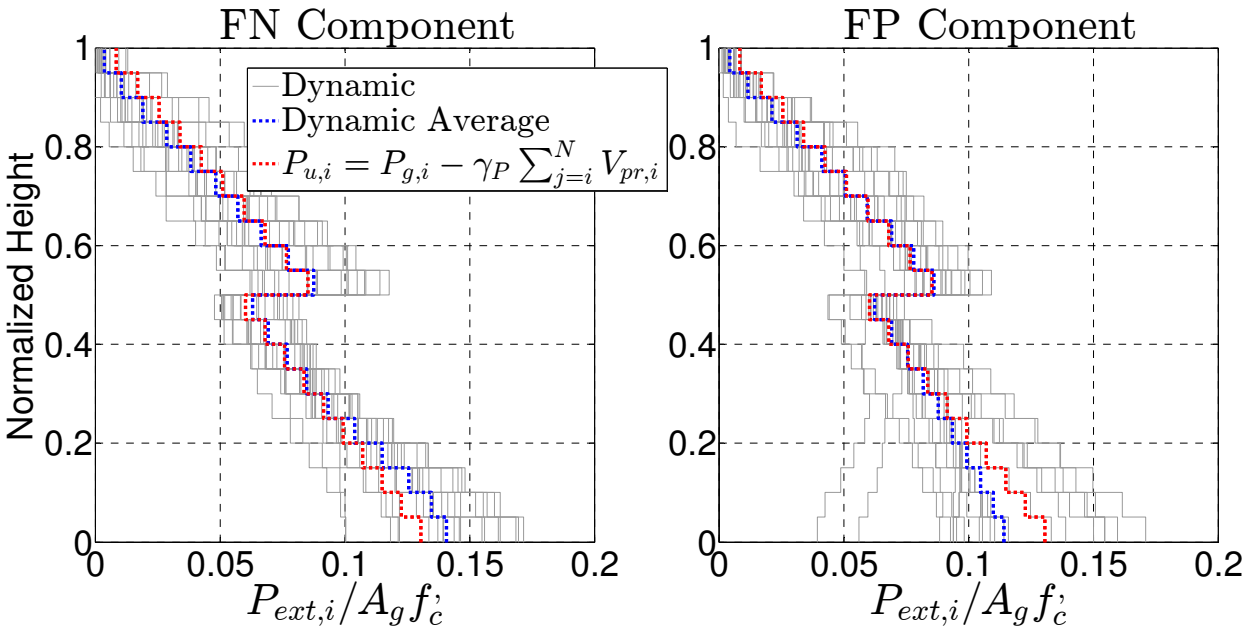

Figure B-24: Exterior Column Tension in Frame SBM100 – Left: FN Component – Right: FP Component

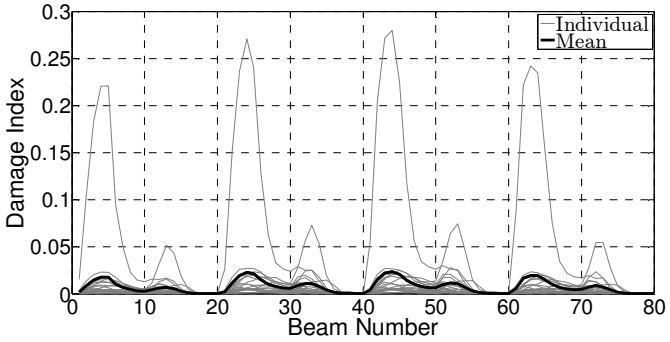

Figure B-25: Fatigue Damage of Bot_1 Bar in Beams of Frame SBH60 - FN Component

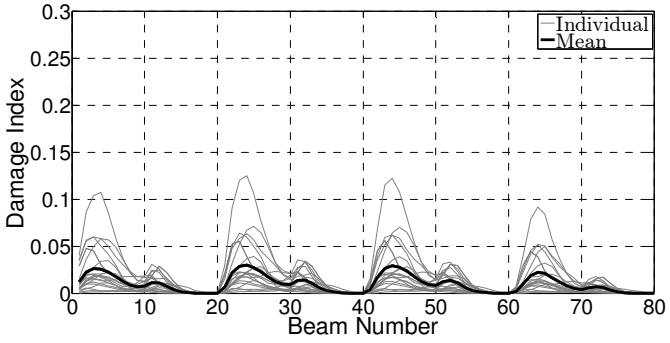

Figure B-26: Fatigue Damage of Top_1 Bar in Beams of Frame SBH60 - FN Component

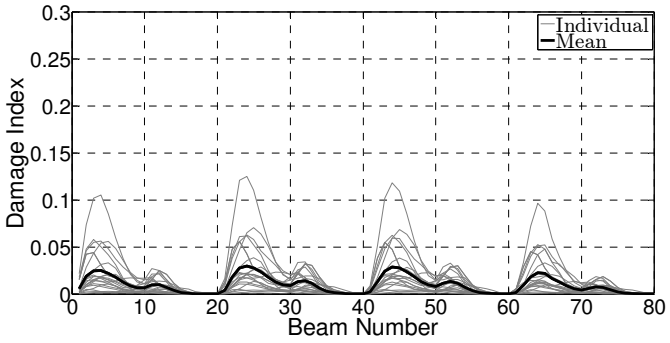

Figure B-27: Fatigue Damage of Bot_5 Bar in Beams of Frame SBH60 - FN Component

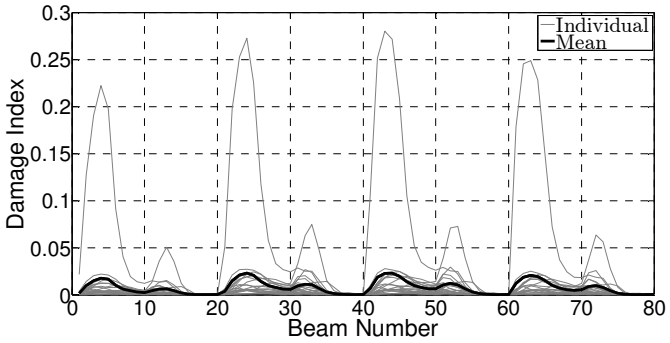

Figure B-28: Fatigue Damage of Top_5 Bar in Beams of Frame SBH60 - FN Component

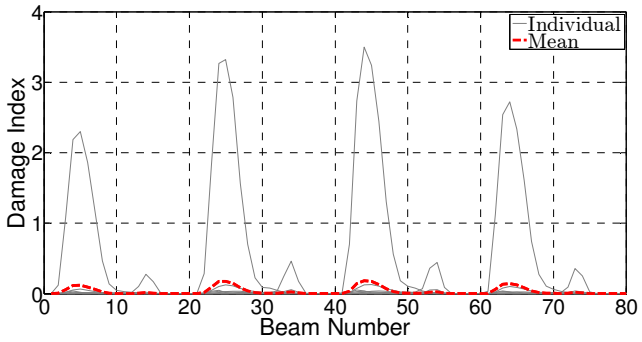

Figure B-29: Fatigue Damage of Bot_1 Bar in Beams of Frame SBL100 - FN Component

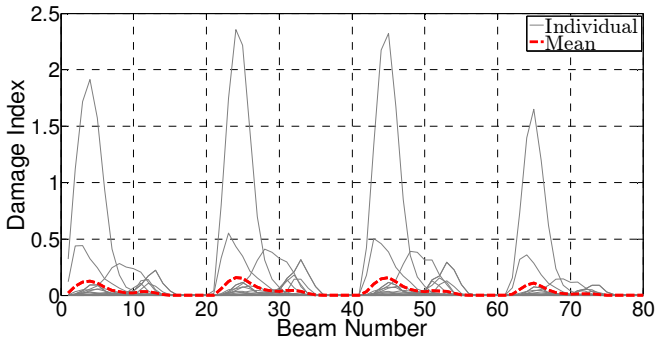

Figure B-30: Fatigue Damage of Top_1 Bar in Beams of Frame SBL100 - FN Component

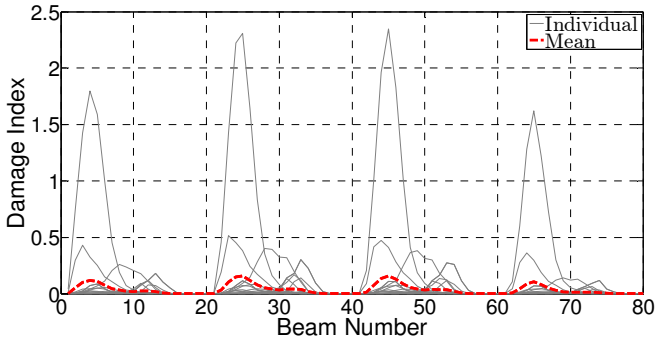

Figure B-31: Fatigue Damage of Bot_5 Bar in Beams of Frame SBL100 - FN Component

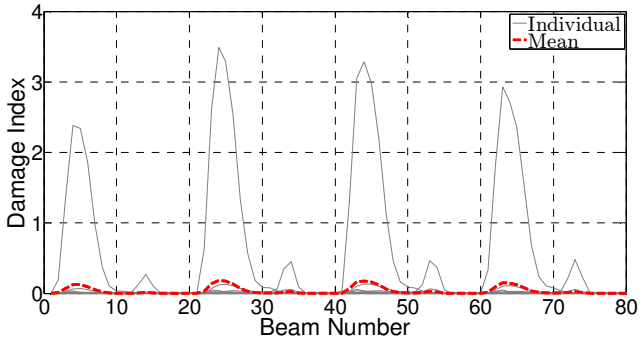

Figure B-32: Fatigue Damage of Top_5 Bar in Beams of Frame SBL100 - FN Component

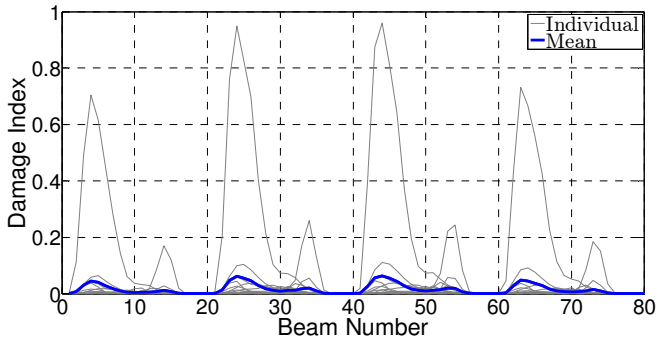

Figure B-33: Fatigue Damage of Bot_1 Bar in Beams of Frame SBH100 - FN Component

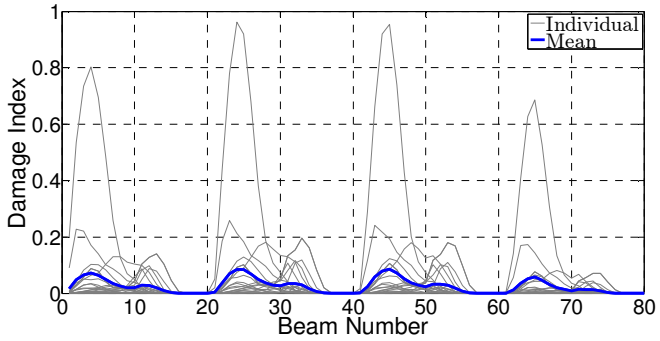

Figure B-34: Fatigue Damage of Top_1 Bar in Beams of Frame SBH100 - FN Component

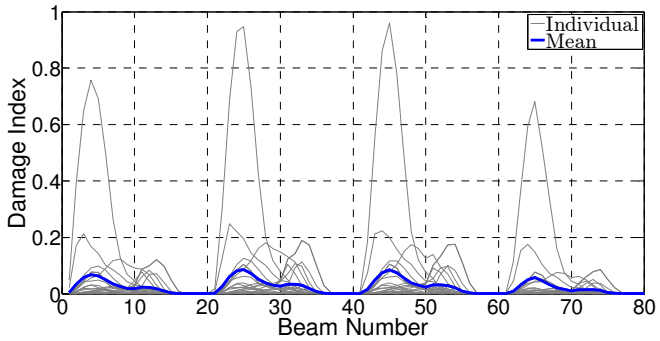

Figure B-35: Fatigue Damage of Bot_5 Bar in Beams of Frame SBH100 - FN Component

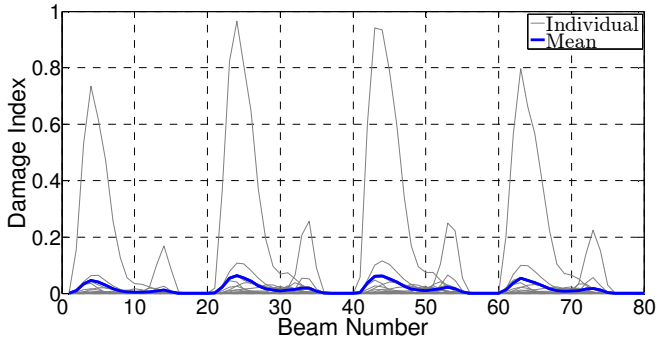

Figure B-36: Fatigue Damage of Top_5 Bar in Beams of Frame SBH100 - FN Component

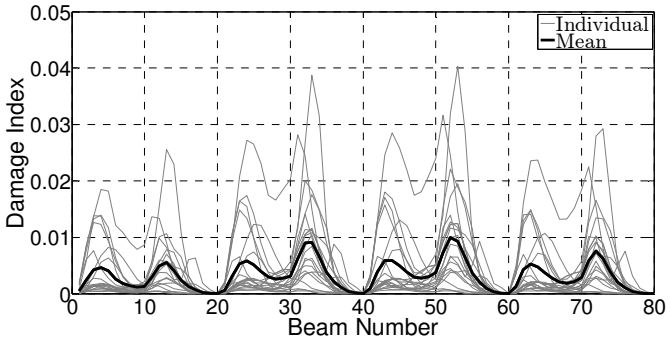

Figure B-37: Fatigue Damage of Bot_1 Bar in Beams of Frame SBH60 - FP Component

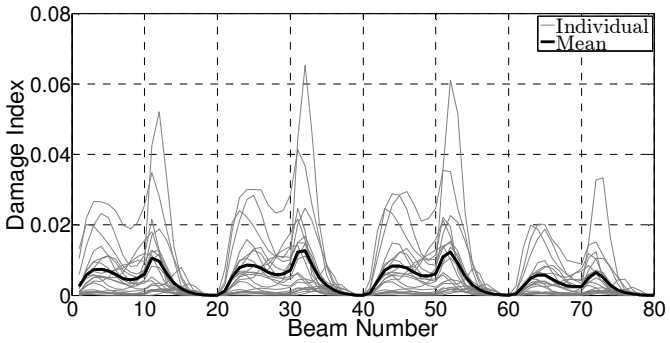

Figure B-38: Fatigue Damage of Top_1 Bar in Beams of Frame SBH60 - FP Component

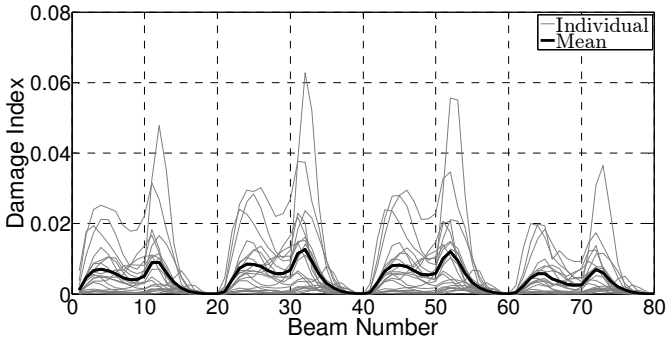

Figure B-39: Fatigue Damage of Bot_5 Bar in Beams of Frame SBH60 - FP Component

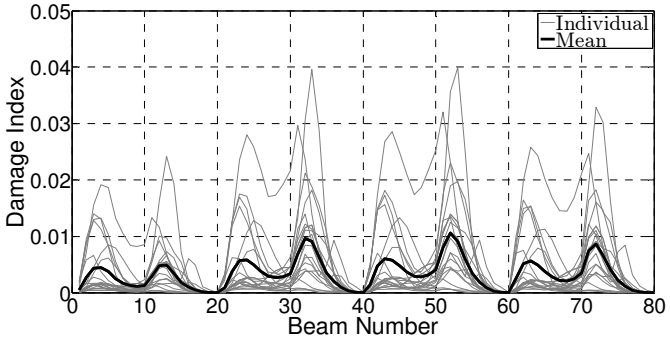

Figure B-40: Fatigue Damage of Top_5 Bar in Beams of Frame SBH60 - FP Component

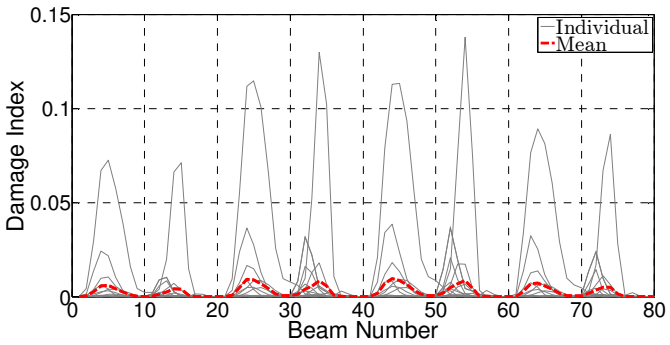

Figure B-41: Fatigue Damage of Bot_1 Bar in Beams of Frame SBL100 - FP Component

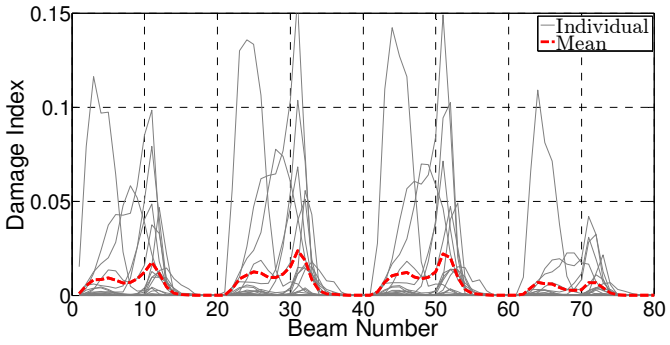

Figure B-42: Fatigue Damage of Top_1 Bar in Beams of Frame SBL100 - FP Component

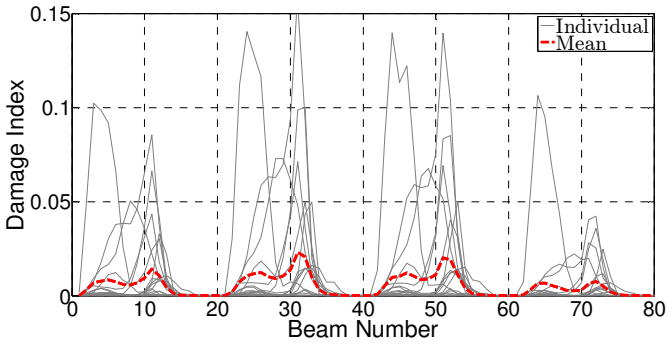

Figure B-43: Fatigue Damage of Bot_5 Bar in Beams of Frame SBL100 - FP Component

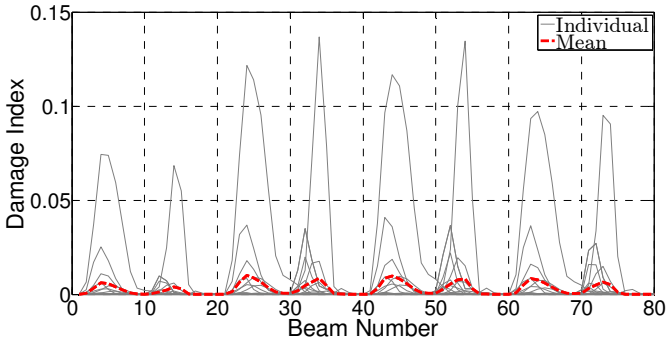

Figure B-44: Fatigue Damage of Top_5 Bar in Beams of Frame SBL100 - FP Component

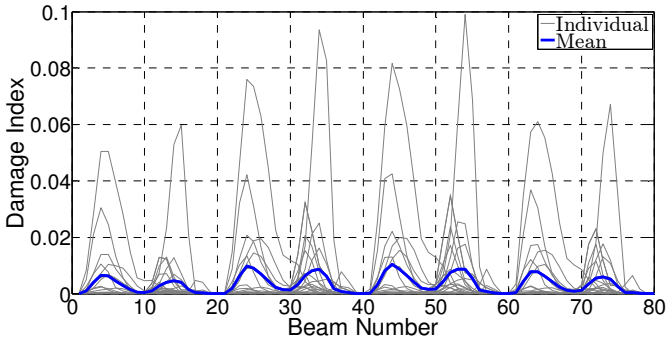

Figure B-45: Fatigue Damage of Bot_1 Bar in Beams of Frame SBH100 - FP Component

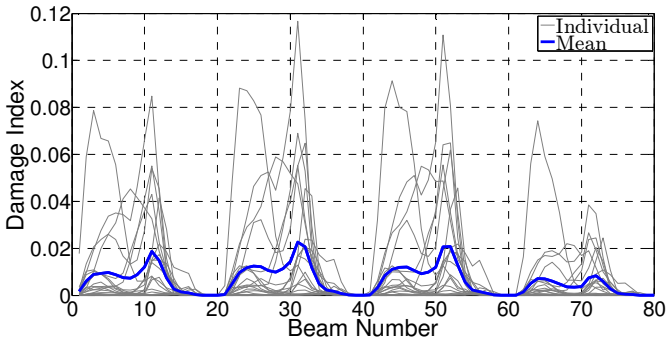

Figure B-46: Fatigue Damage of Top_1 Bar in Beams of Frame SBH100 - FP Component

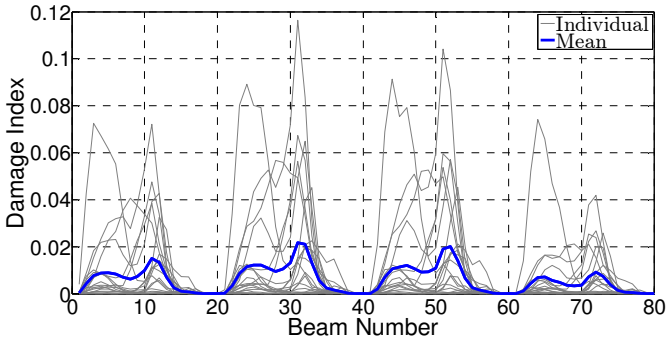

Figure B-47: Fatigue Damage of Bot_5 Bar in Beams of Frame SBH100 - FP Component

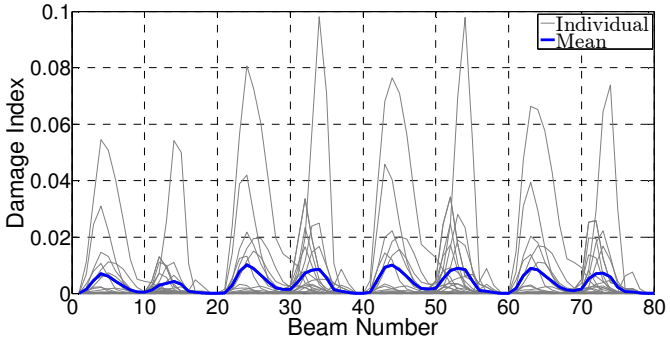

Figure B-48: Fatigue Damage of Top_5 Bar in Beams of Frame SBH100 - FP Component

APPENDIX C. LABORATORY TEST DATA

MEASURED CRACK WIDTHS

Crack widths were measured during pauses in each loading amplitude as described in Test Procedures section and presented in details here. In each figure, the left, middle, and right pictures display measured cracked widths when the test specimens were loaded to the West, East directions, and at the end of loading cycle (original position), respectively.

Specimen SBH60

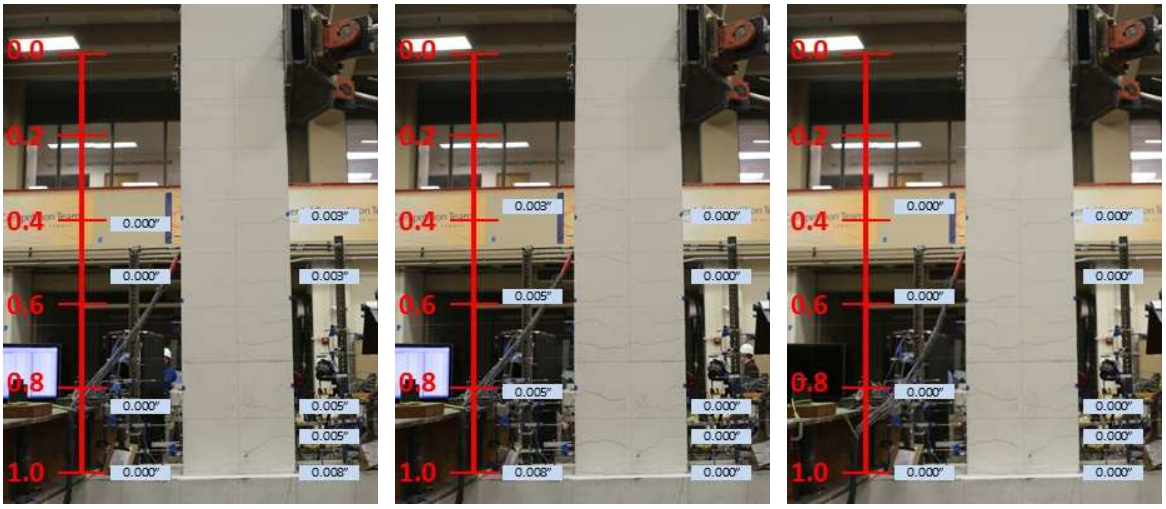

Figure C-1: Measured Crack Widths at Drift Ratio of 0.35% – Specimen SBH60

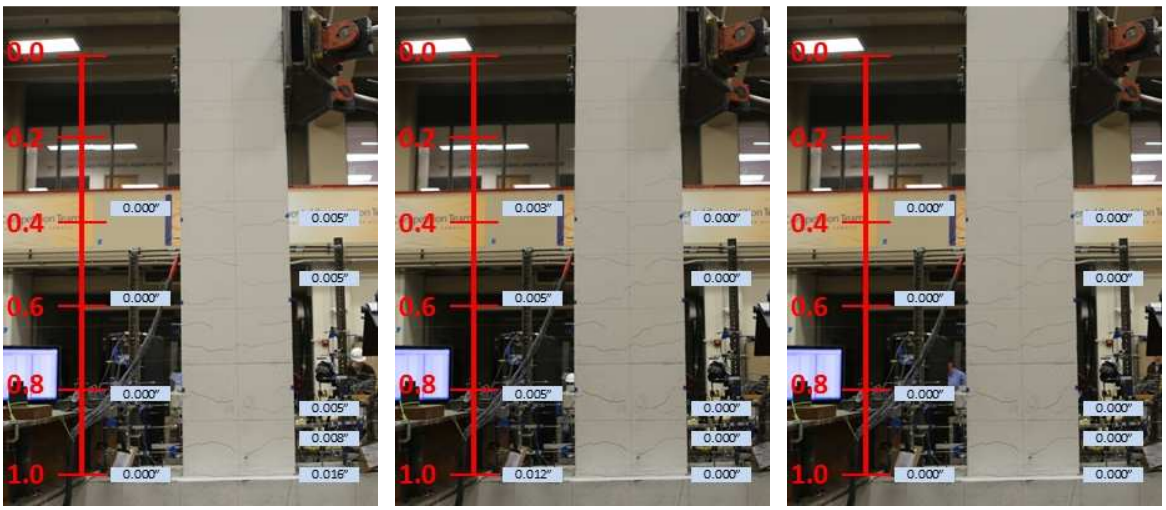

Figure C-2: Measured Crack Widths at Drift Ratio of 0.5% – Specimen SBH60

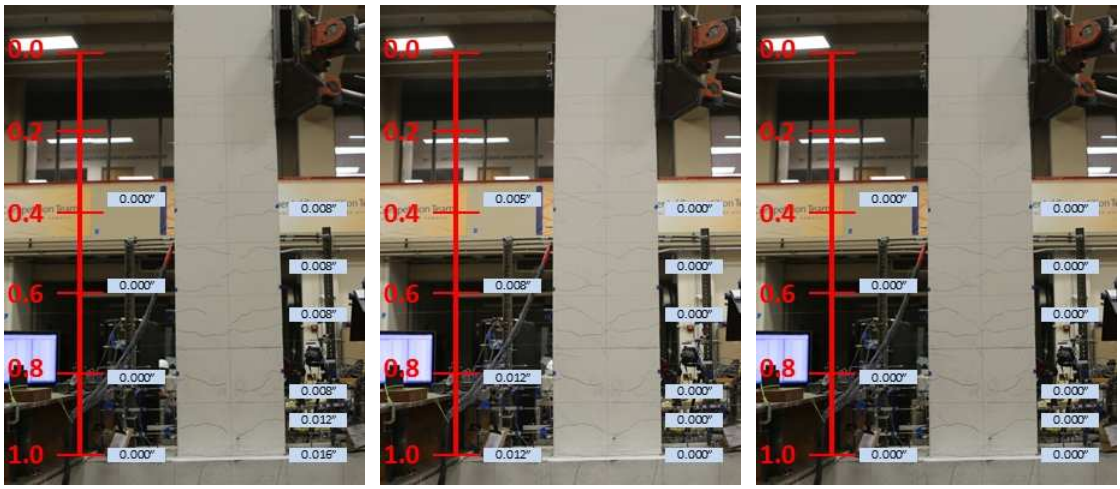

Figure C-3: Measured Crack Widths at Drift Ratio of 0.6% – Specimen SBH60

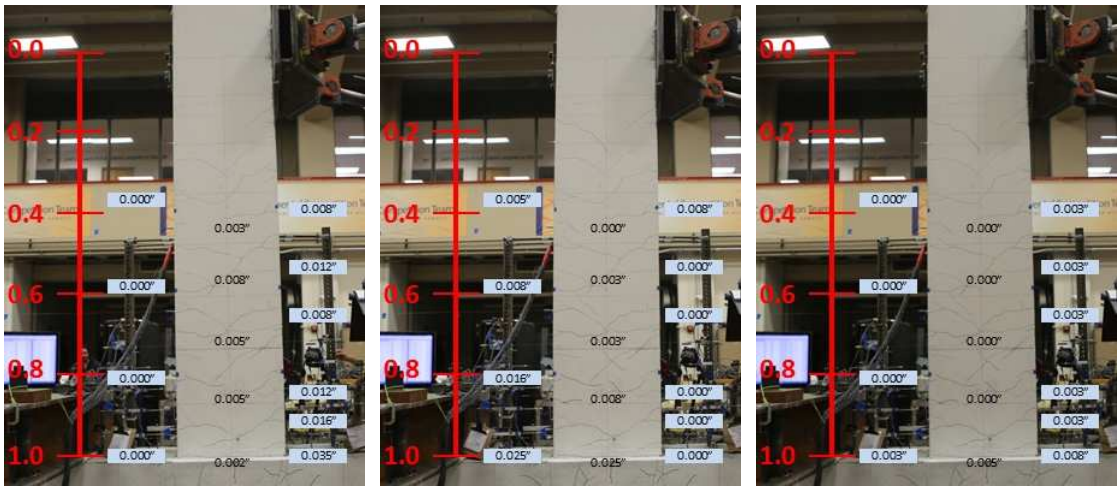

Figure C-4: Measured Crack Widths at Drift Ratio of 0.9% – Specimen SBH60

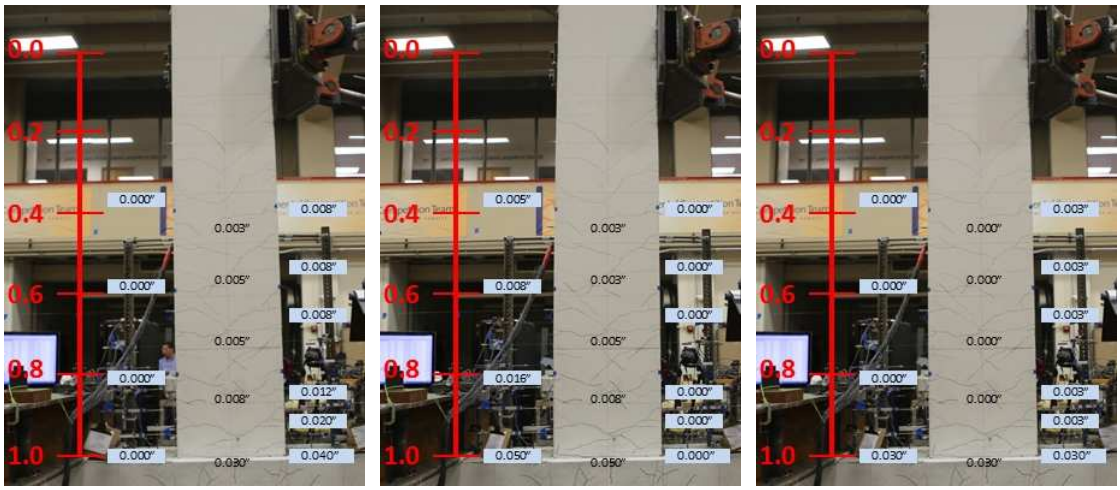

Figure C-5: Measured Crack Widths at Drift Ratio of 1.25% – Specimen SBH60

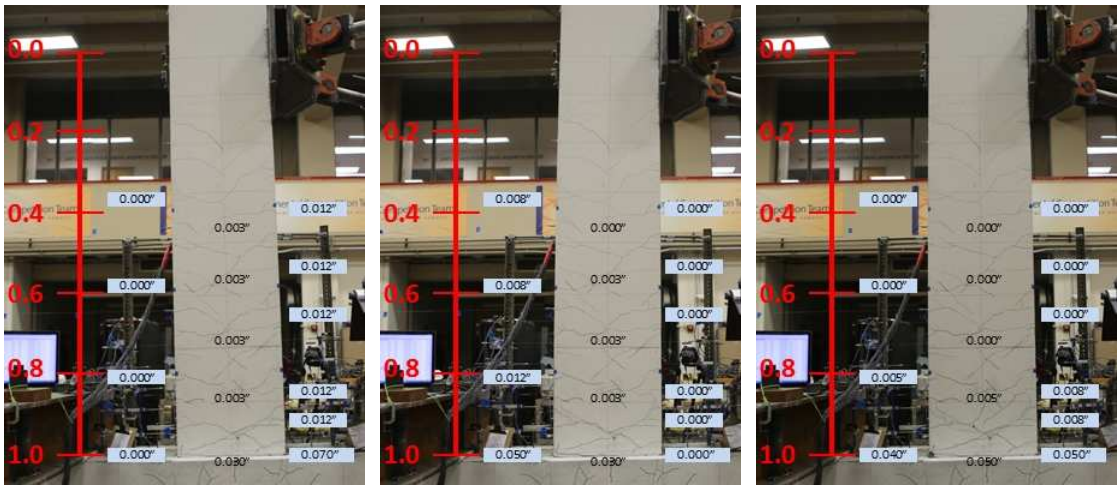

Figure C-6: Measured Crack Widths at Drift Ratio of 1.75% – Specimen SBH60

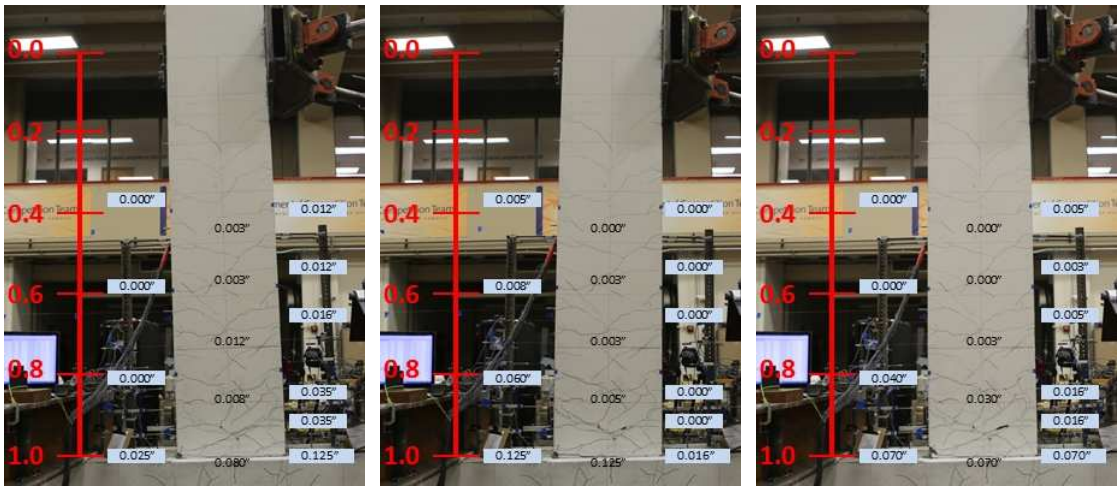

Figure C-7: Measured Crack Widths at Drift Ratio of 2.45% – Specimen SBH60

Figure C-8: Measured Crack Widths at Drift Ratio of 3.45% – Specimen SBH60

Specimen SBH100

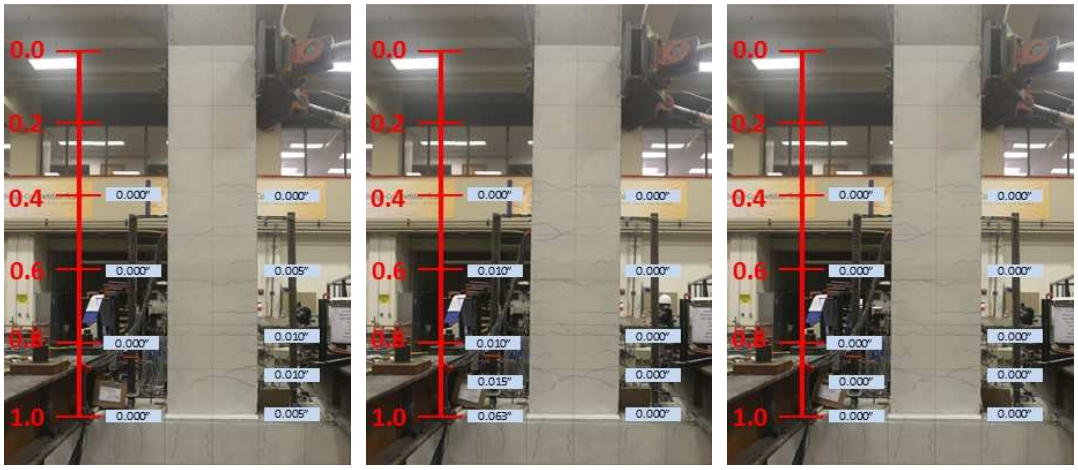

Figure C-9: Measured Crack Widths at Drift Ratio of 0.6% – Specimen SBH100

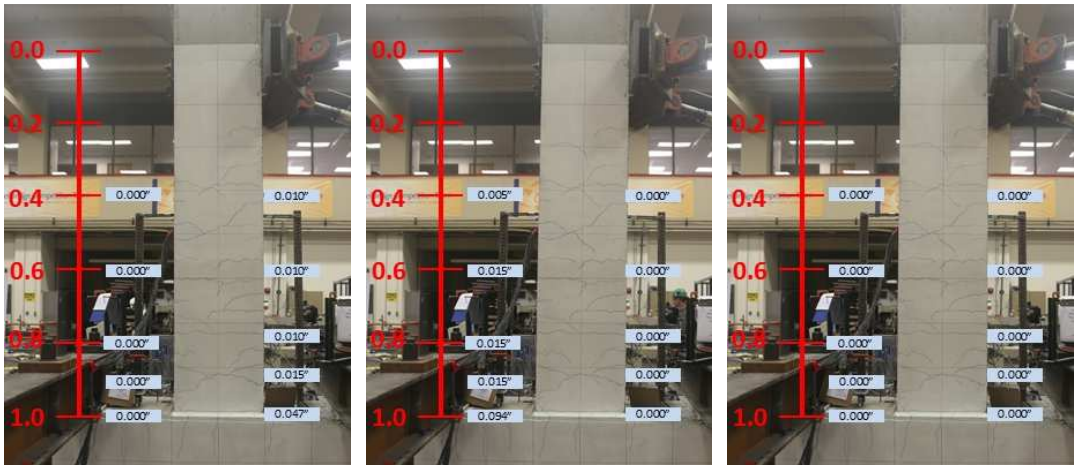

Figure C-10: Measured Crack Widths at Drift Ratio of 0.9% – Specimen SBH100

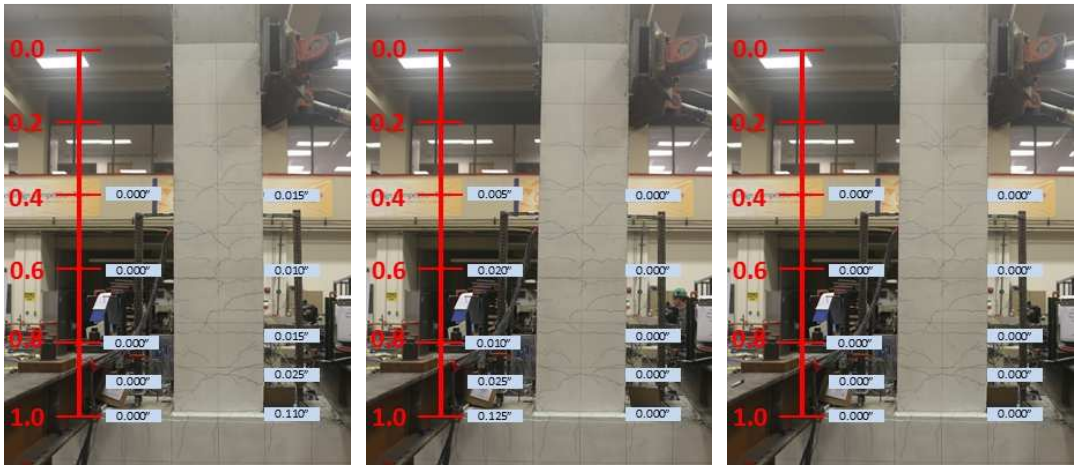

Figure C-11: Measured Crack Widths at Drift Ratio of 1.25% – Specimen SBH100

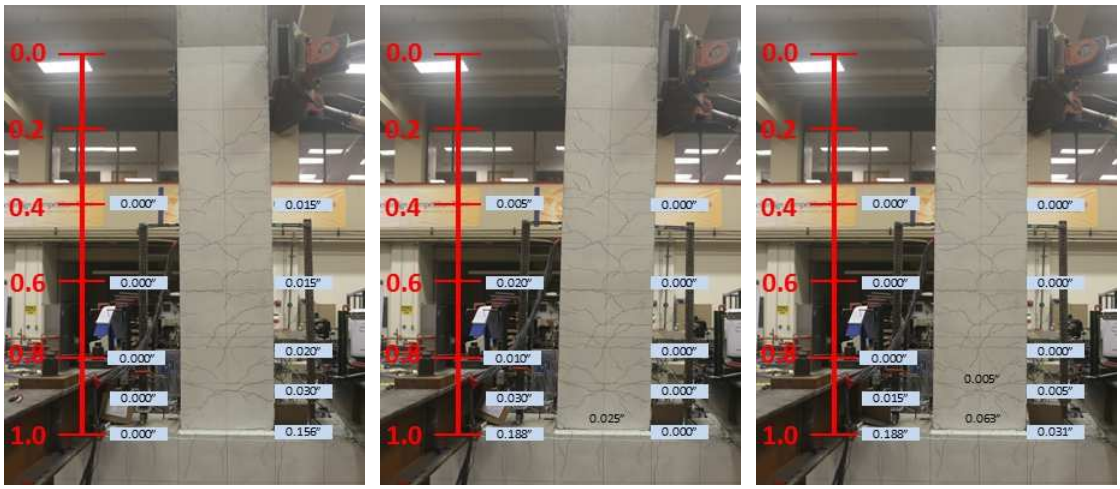

Figure C-12: Measured Crack Widths at Drift Ratio of 1.75% – Specimen SBH100

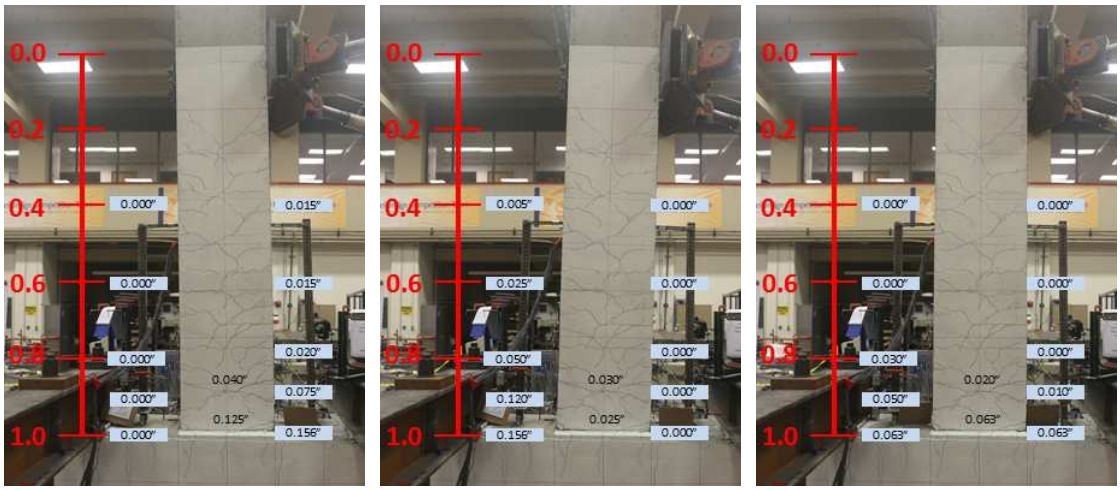

Figure C-13: Measured Crack Widths at Drift Ratio of 2.45% – Specimen SBH100

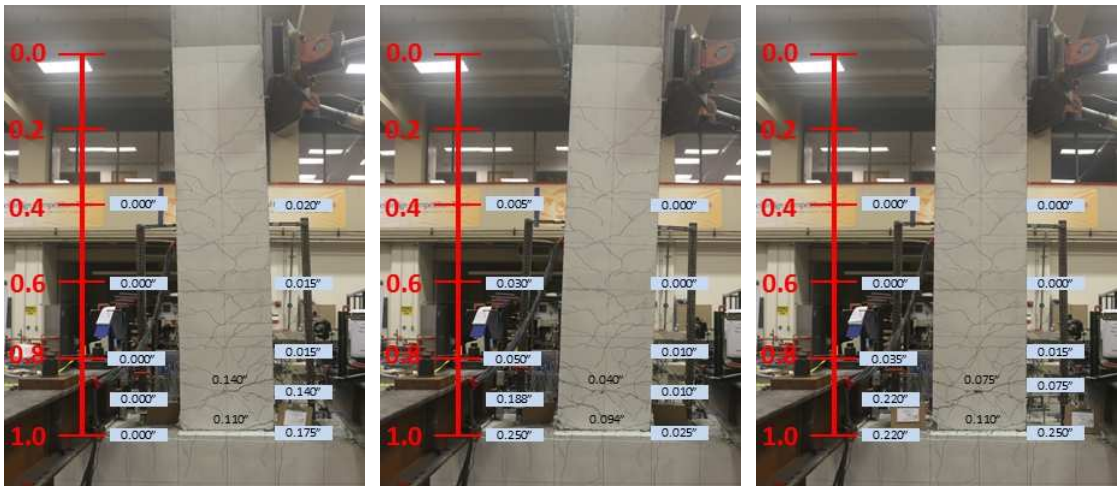

Figure C-14: Measured Crack Widths at Drift Ratio of 3.45% – Specimen SBH100

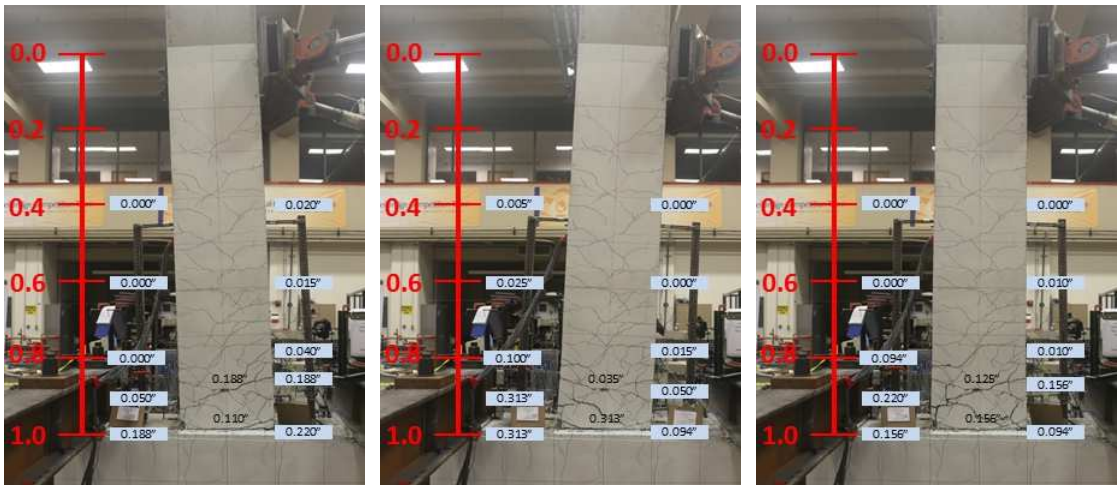

Figure C-15: Measured Crack Widths at Drift Ratio of 4.85% – Specimen SBH100

Specimen SBL100

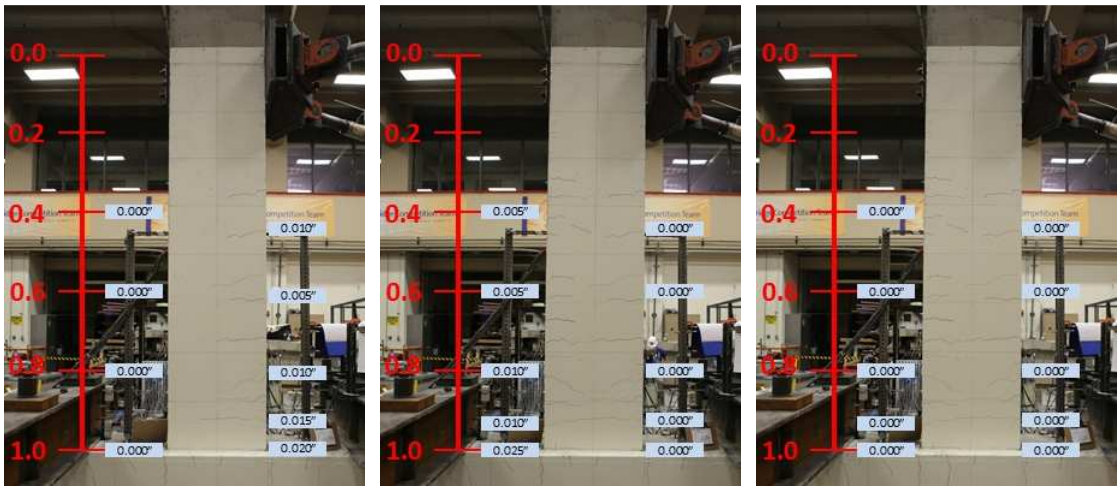

Figure C-16: Measured Crack Widths at Drift Ratio of 0.6% – Specimen SBL100

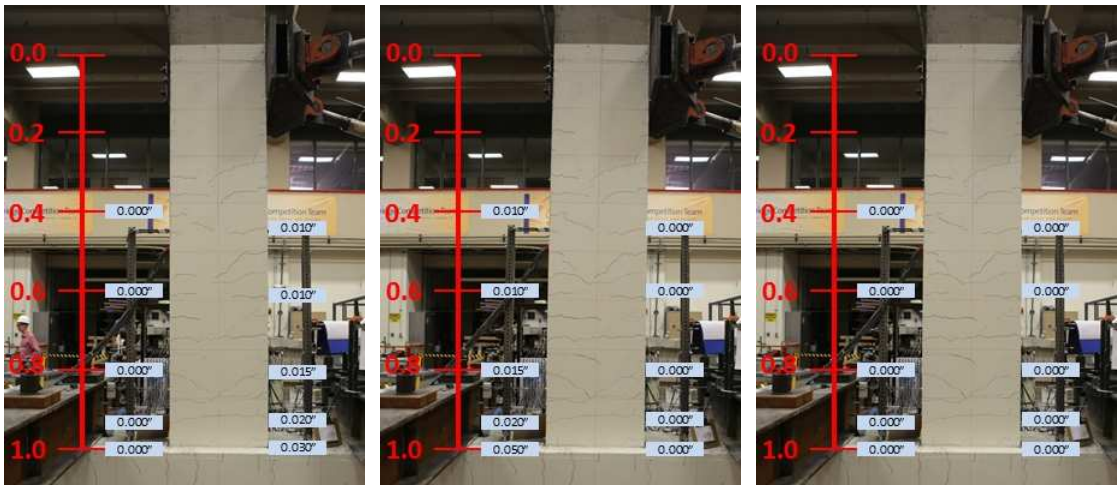

Figure C-17: Measured Crack Widths at Drift Ratio of 0.9% – Specimen SBL100

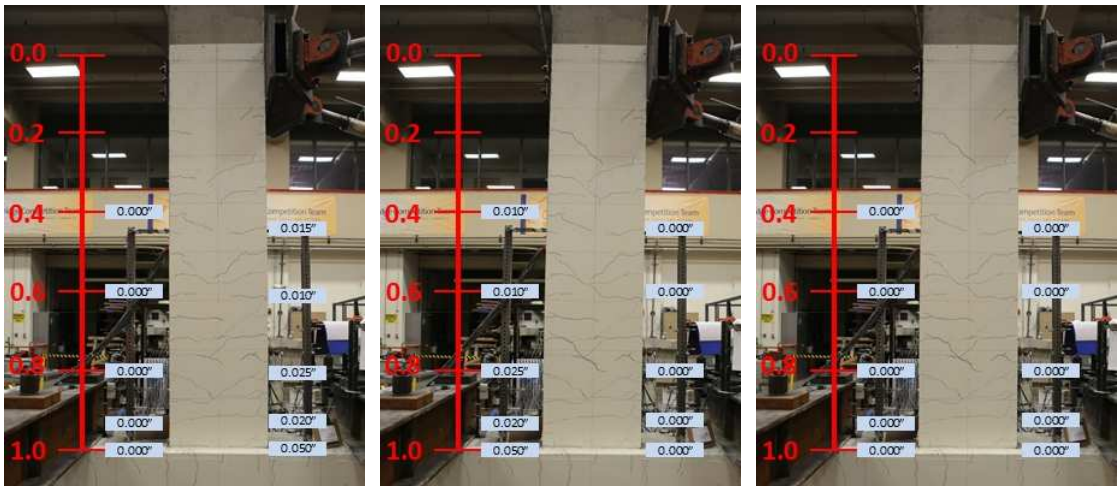

Figure C-18: Measured Crack Widths at Drift Ratio of 1.25% – Specimen SBL100

Figure C-19: Measured Crack Widths at Drift Ratio of 1.75% – Specimen SBL100

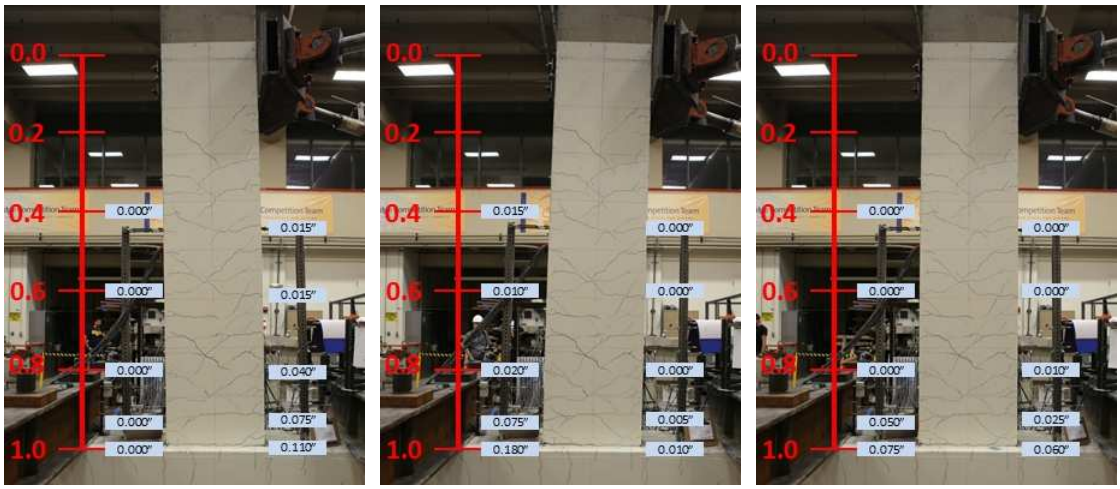

Figure C-20: Measured Crack Widths at Drift Ratio of 2.45% – Specimen SBL100

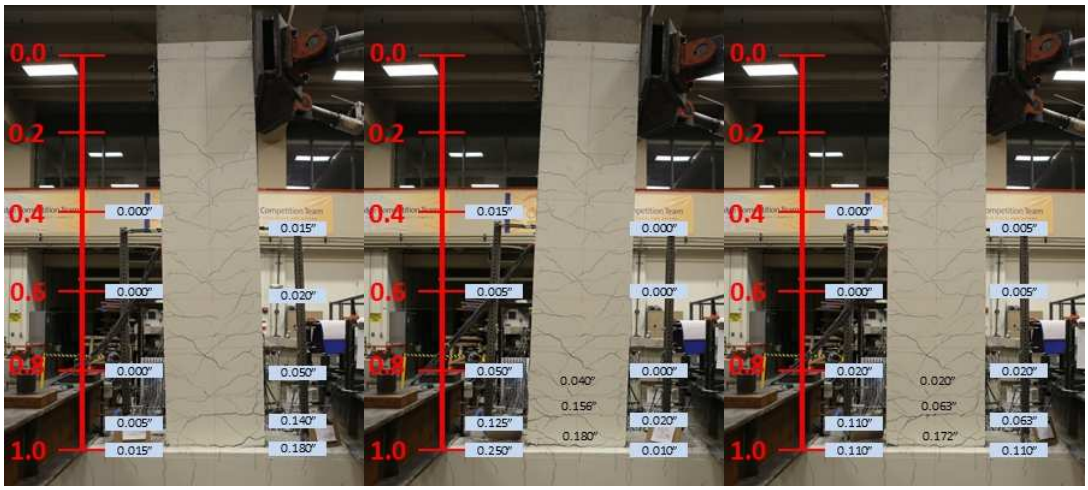

Figure C-21: Measured Crack Widths at Drift Ratio of 3.45% – Specimen SBL100

Figure C-22: Measured Crack Widths at Drift Ratio of 4.85% – Specimen SBL100

Specimen SBM100

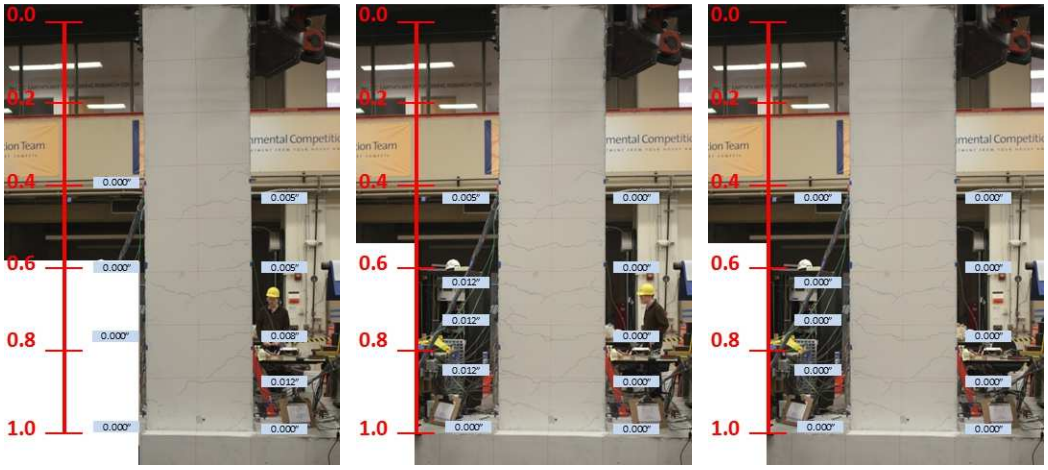

Figure C-23: Measured Crack Widths at Drift Ratio of 0.6% – Specimen SBM100

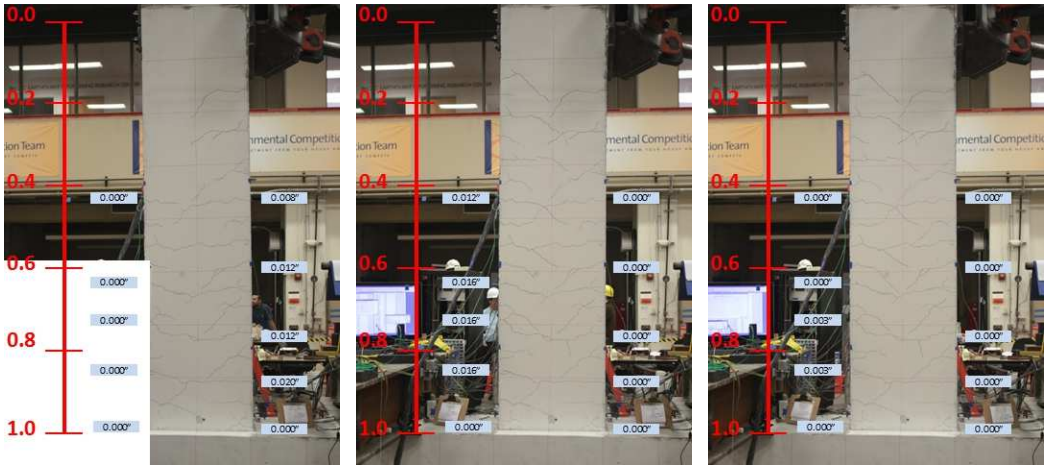

Figure C-24: Measured Crack Widths at Drift Ratio of 0.9% – Specimen SBM100

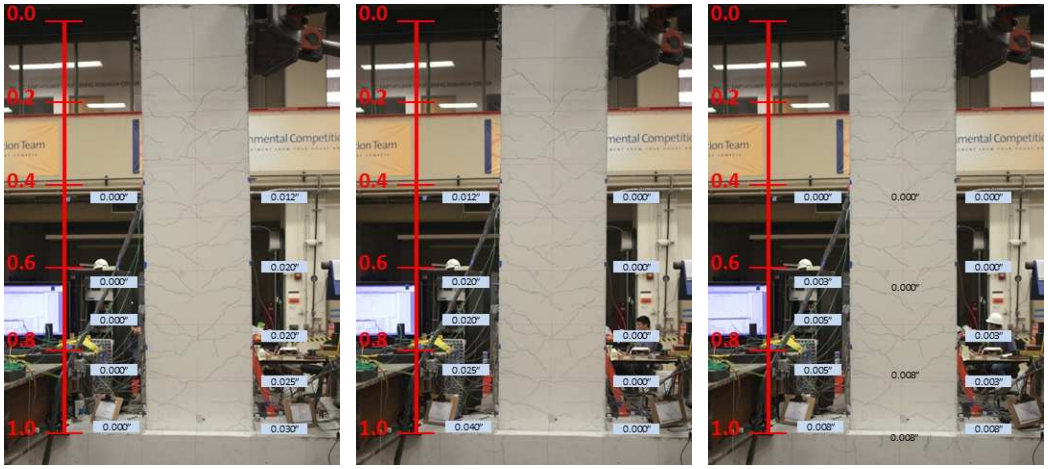

Figure C-25: Measured Crack Widths at Drift Ratio of 1.25% – Specimen SBM100

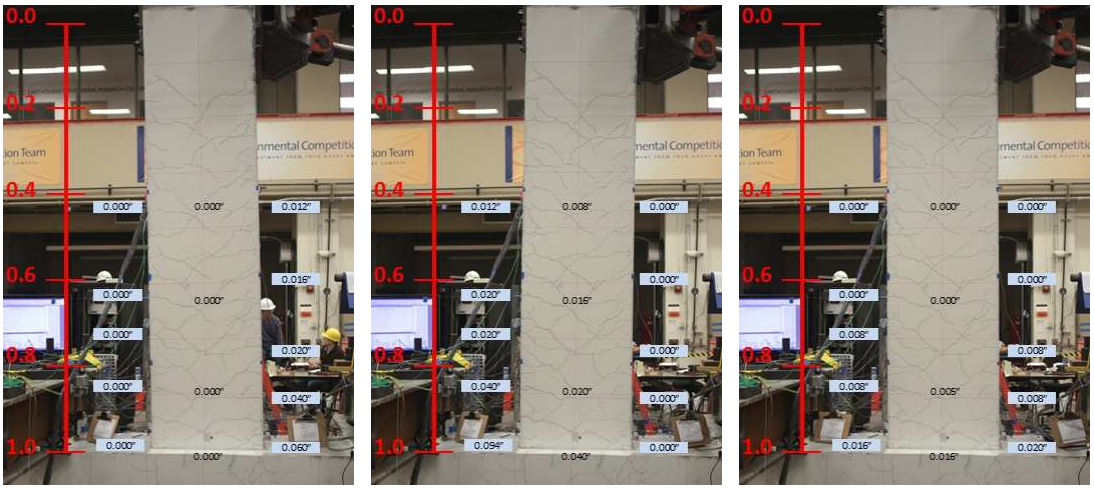

Figure C-26: Measured Crack Widths at Drift Ratio of 1.75% – Specimen SBM100

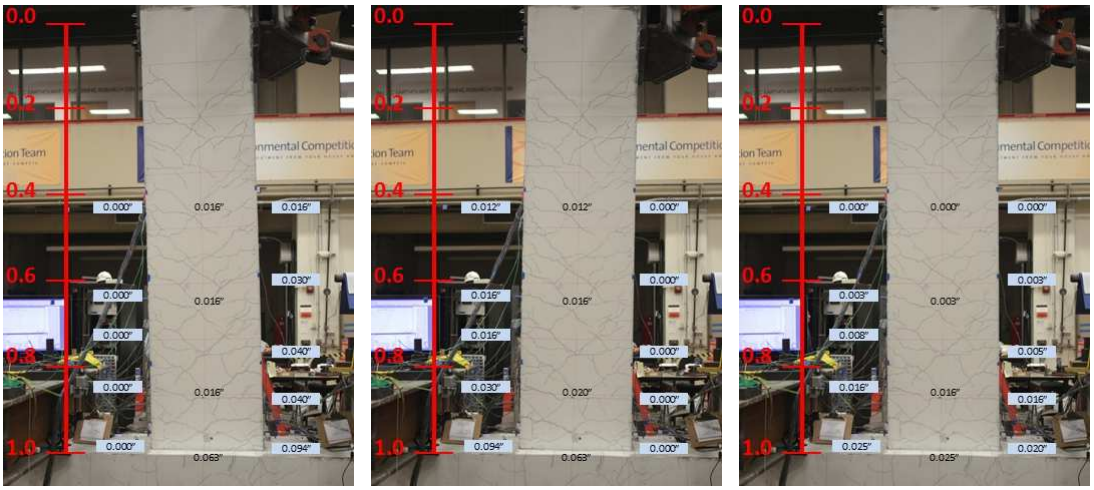

Figure C-27: Measured Crack Widths at Drift Ratio of 2.45% – Specimen SBM100

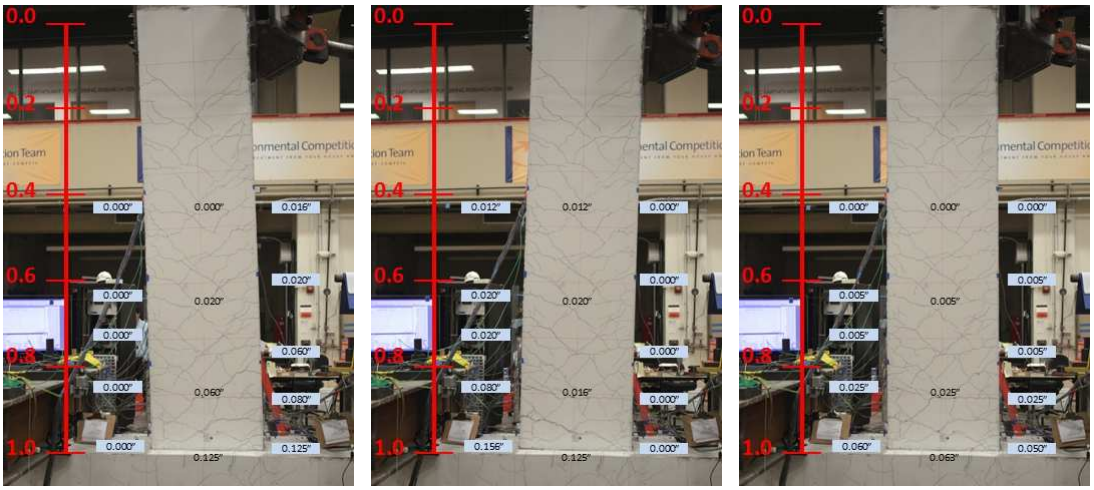

Figure C-28: Measured Crack Widths at Drift Ratio of 3.45% – Specimen SBM100

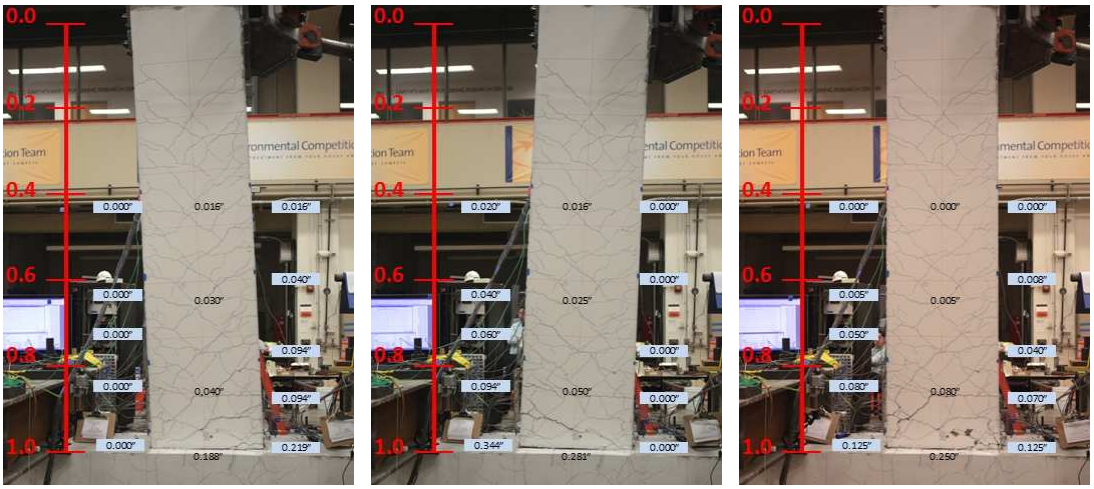

Figure C-29: Measured Crack Widths at Drift Ratio of 4.85% – Specimen SBM100

STRAIN DATA

Strain was measured by strain gauges installed along the length of longitudinal reinforcement in test specimens including extension length anchored in concrete block. Several strain gauges with measured peak strain less than yield strain had certain amount of noise in recording. Therefore, their measured data was filtered by moving-average technique. Some peculiar strain data toward the end of the test shown below was due to malfunctioning or breaking of those gauges. The red line plotted with constant zero value indicates the gauge was broken early in the test and no data was measured. Typical location of strain gauges installed on longitudinal reinforcement is depicted in Figure C-30.

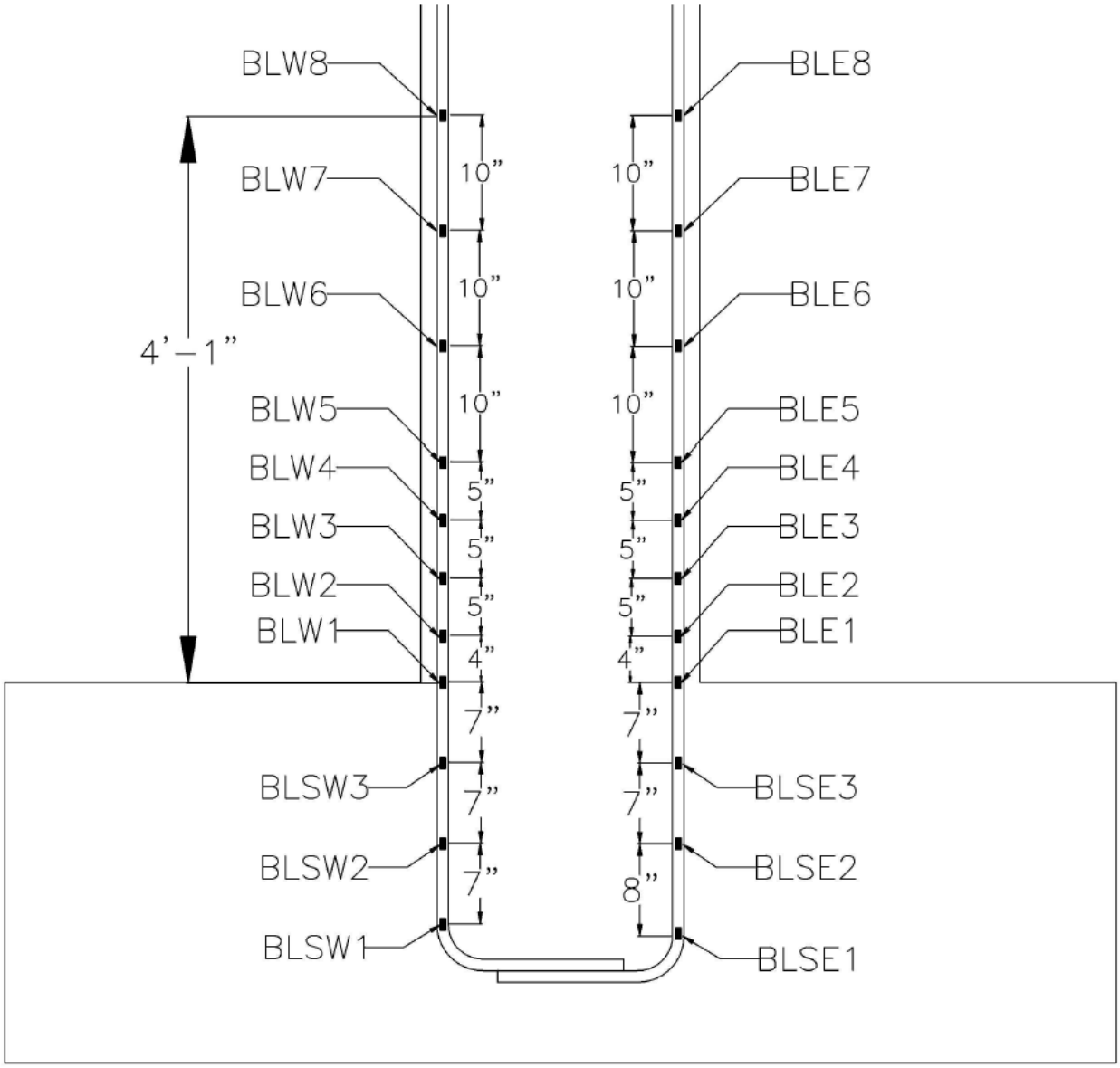

Figure C-30: Layout of Strain Gauges on Longitudinal Reinforcement

Specimen SBH60

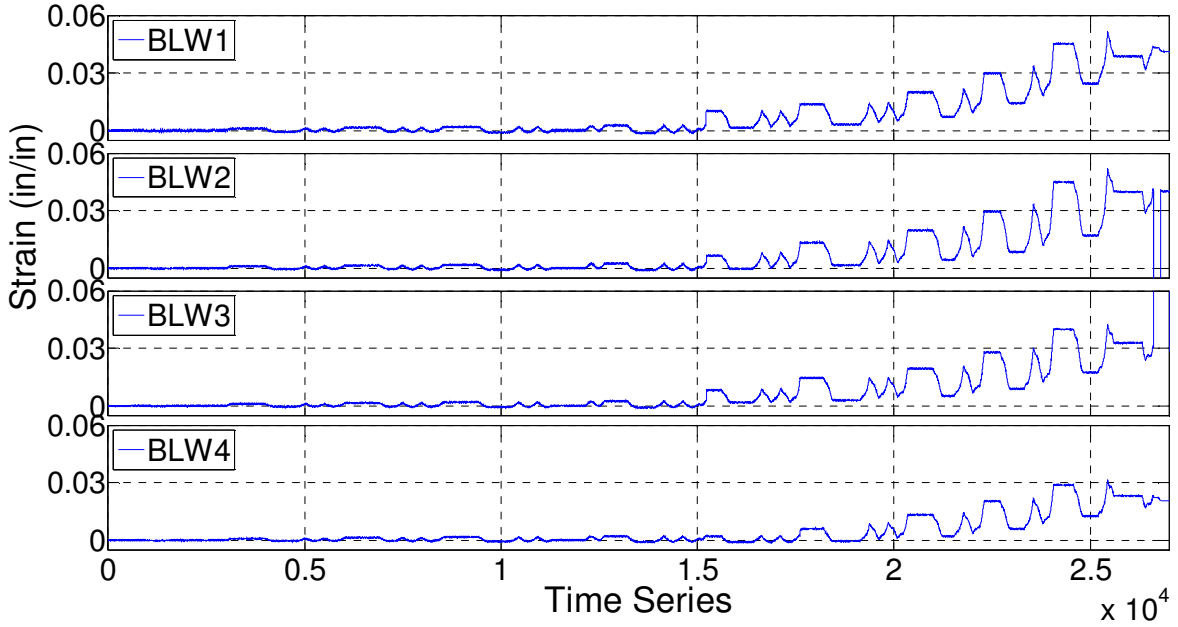

Figure C-31: Strain Response Histories of Middle Longitudinal Bar on the West Side of Beam SBH60

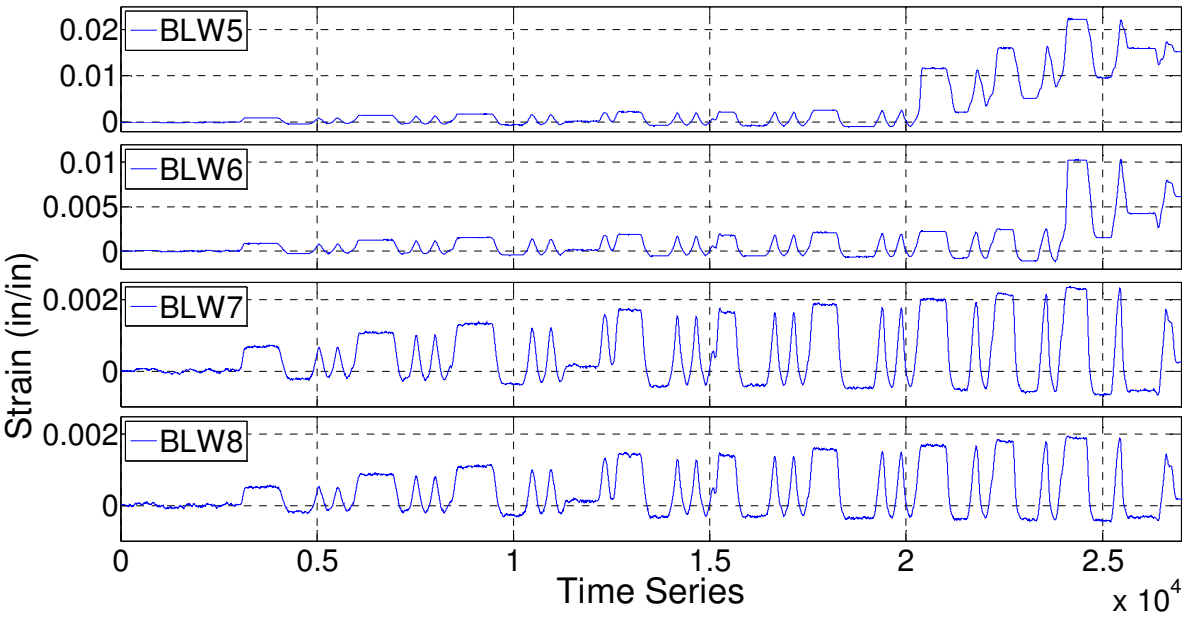

Figure C-32: Strain Response Histories of Middle Longitudinal Bar on the West Side of Beam SBH60

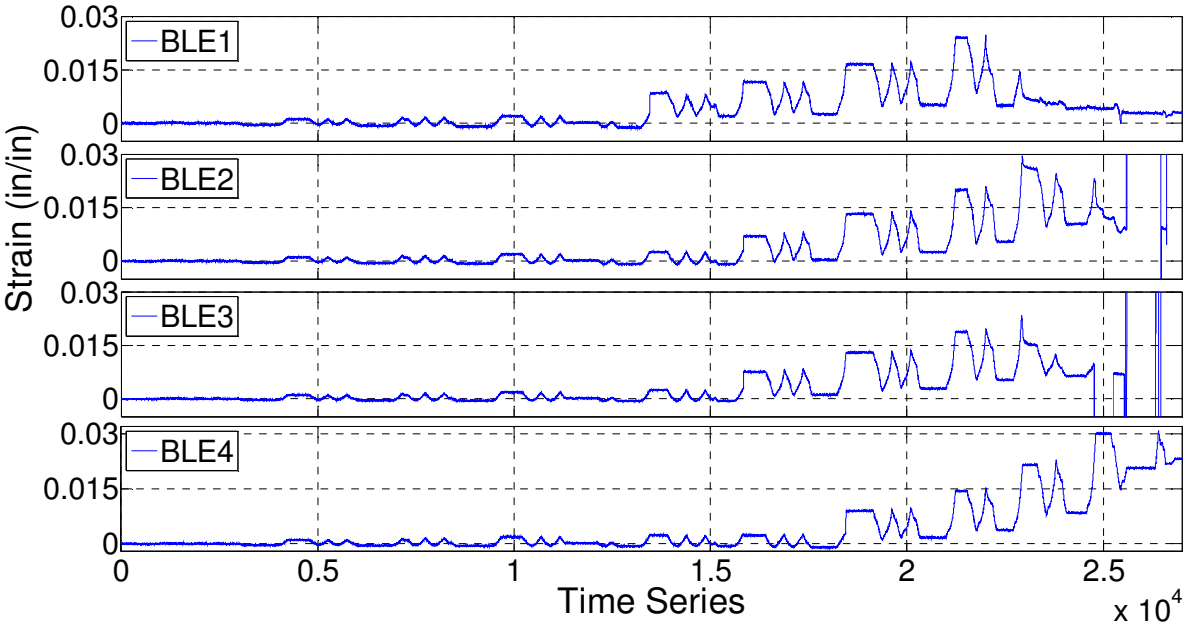

Figure C-33: Strain Response Histories of Middle Longitudinal Bar on the East Side of Beam SBH60

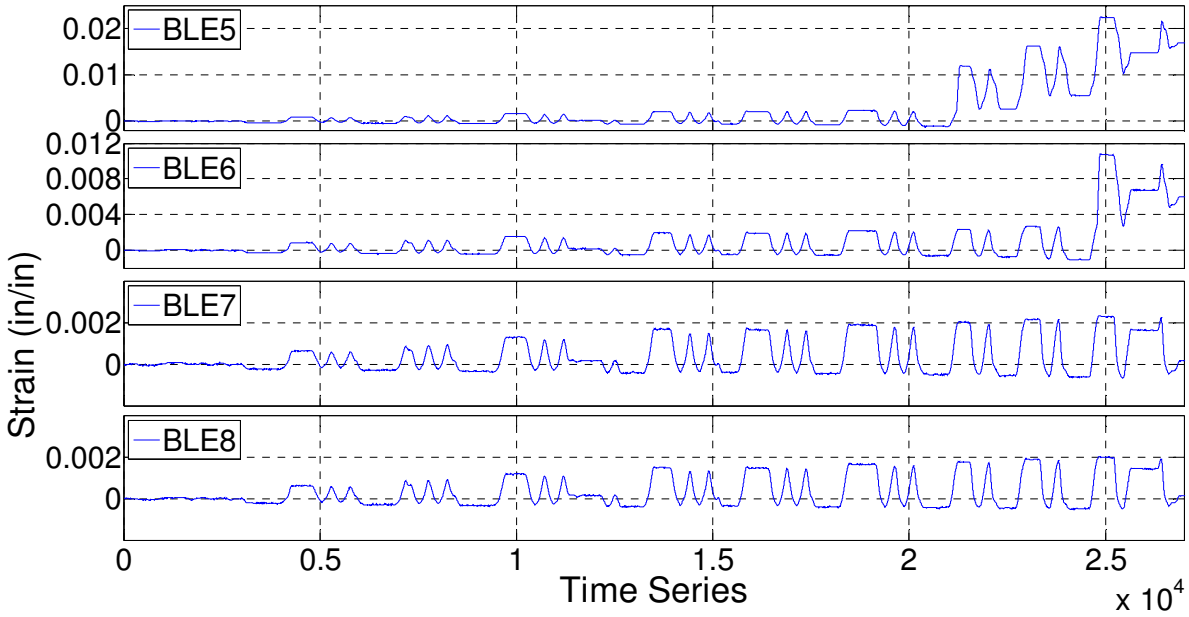

Figure C-34: Strain Response Histories of Middle Longitudinal Bar on the East Side of Beam SBH60

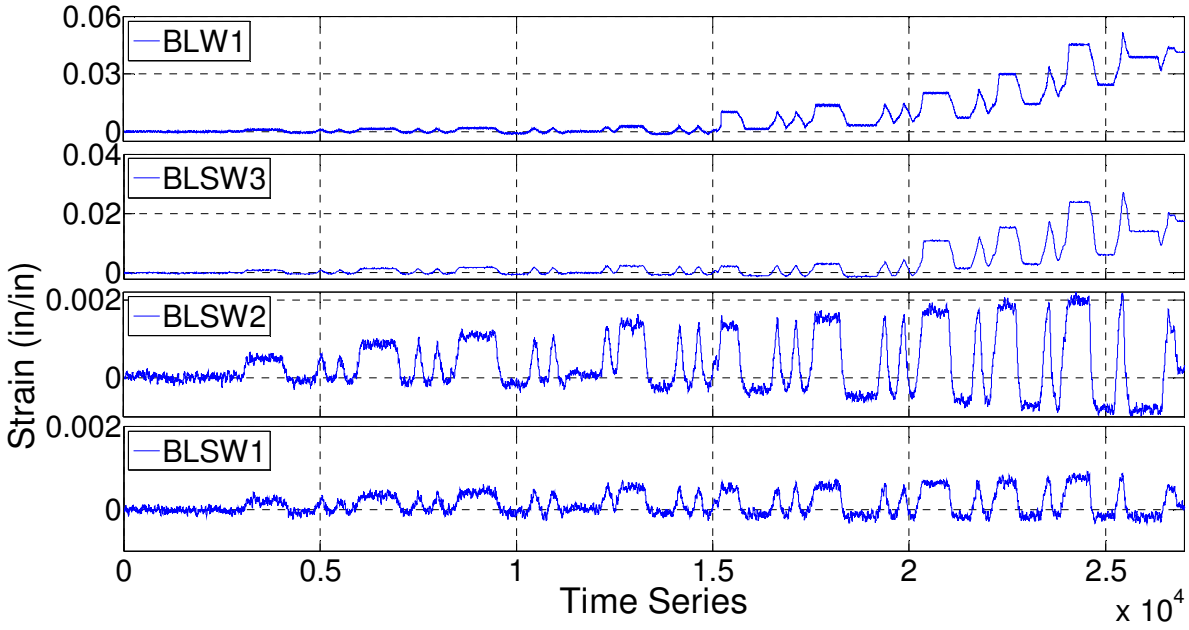

Figure C-35: Strain Response Histories of Middle Longitudinal Bar in Anchorage Zone on the West Side of Beam SBH60

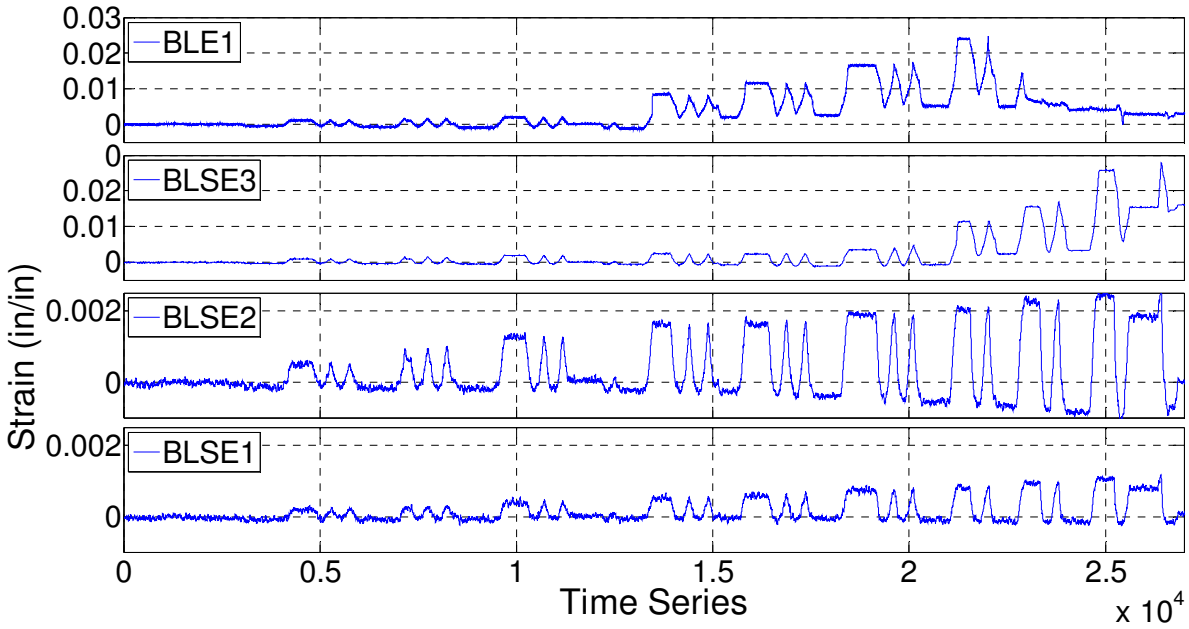

Figure C-36: Strain Response Histories of Middle Longitudinal Bar in Anchorage Zone on the East Side of Beam SBH60

Specimen SBH100

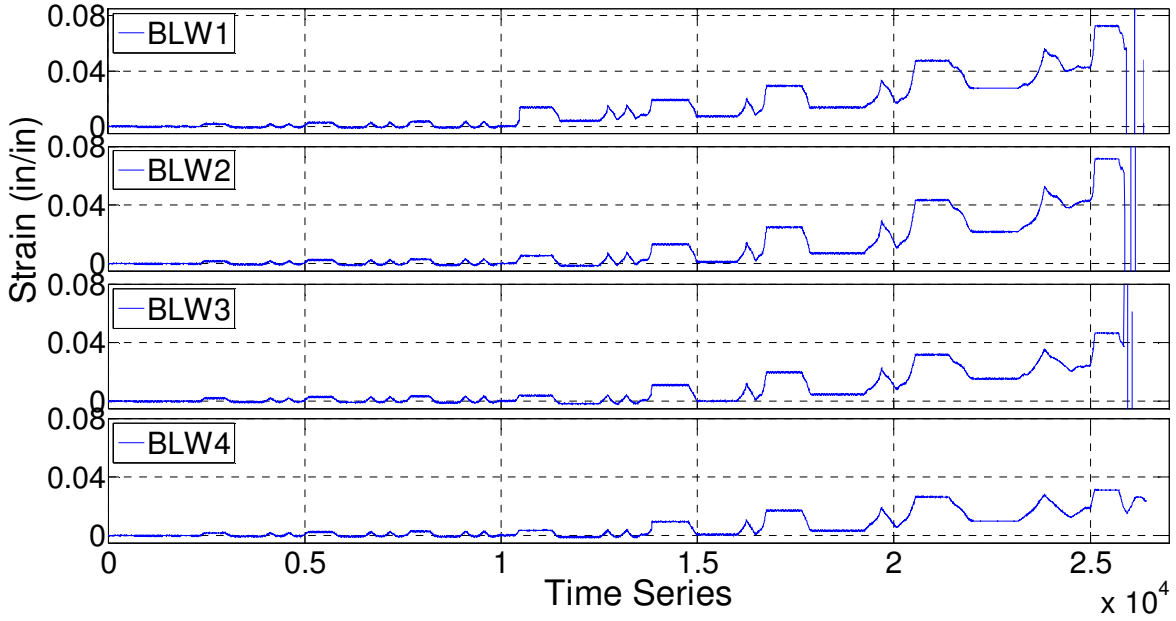

Figure C-37: Strain Response Histories of Middle Longitudinal Bar on the West Side of Beam SBH100

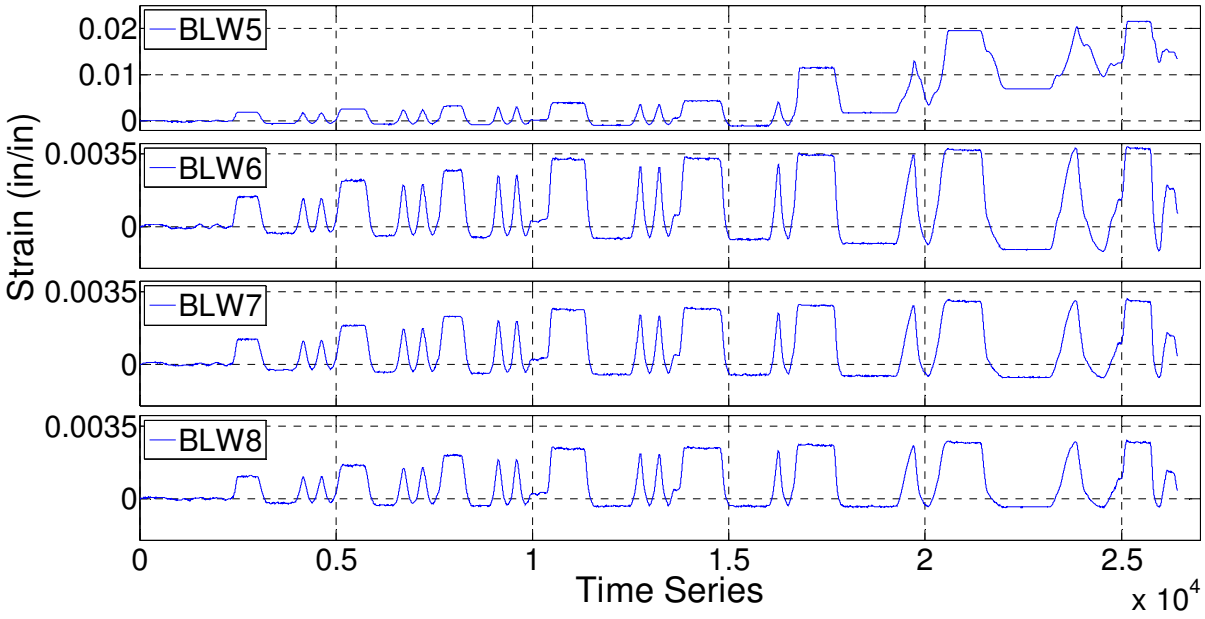

Figure C-38: Strain Response Histories of Middle Longitudinal Bar on the West Side of Beam SBH100

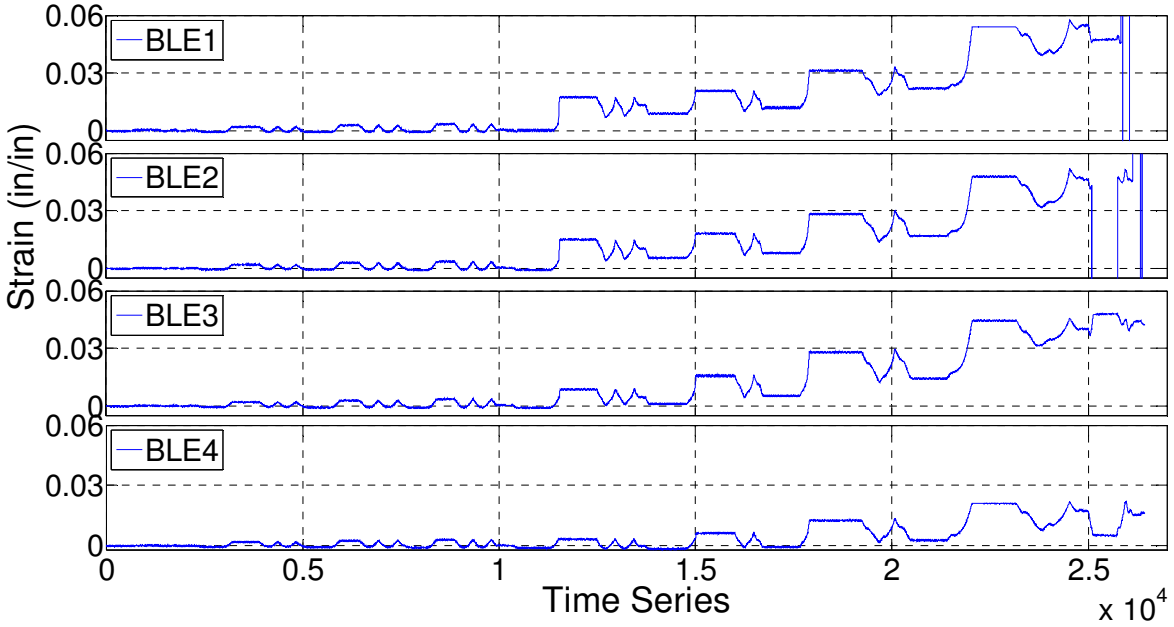

Figure C-39: Strain Response Histories of Middle Longitudinal Bar on the East Side of Beam SBH100

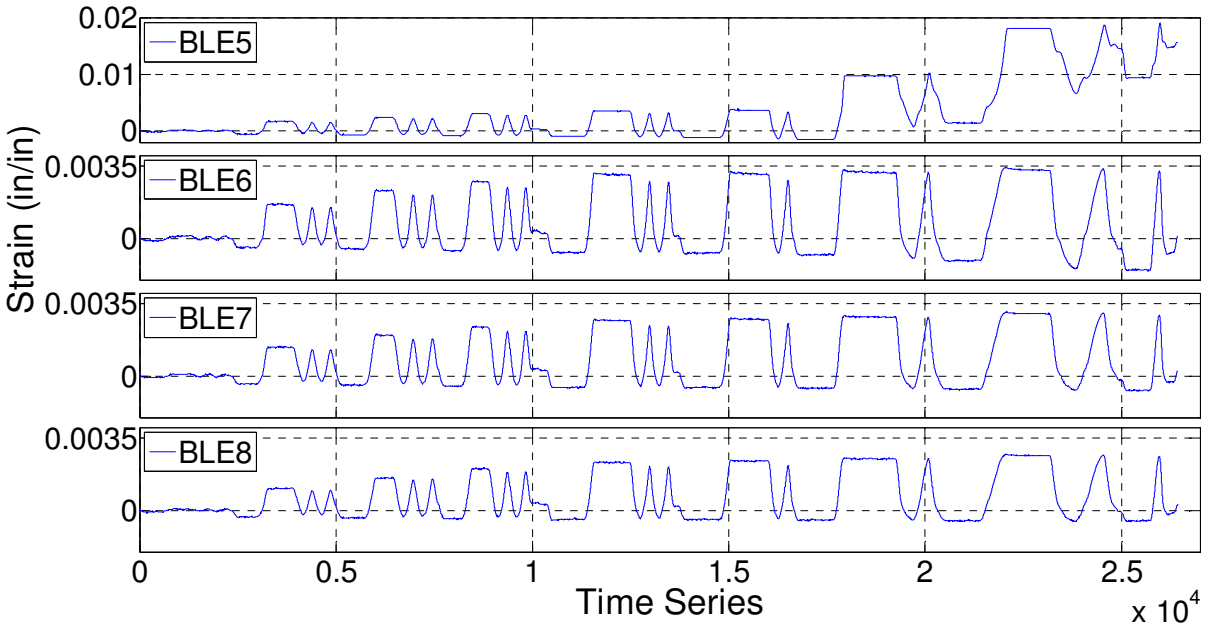

Figure C-40: Strain Response Histories of Middle Longitudinal Bar on the East Side of Beam SBH100

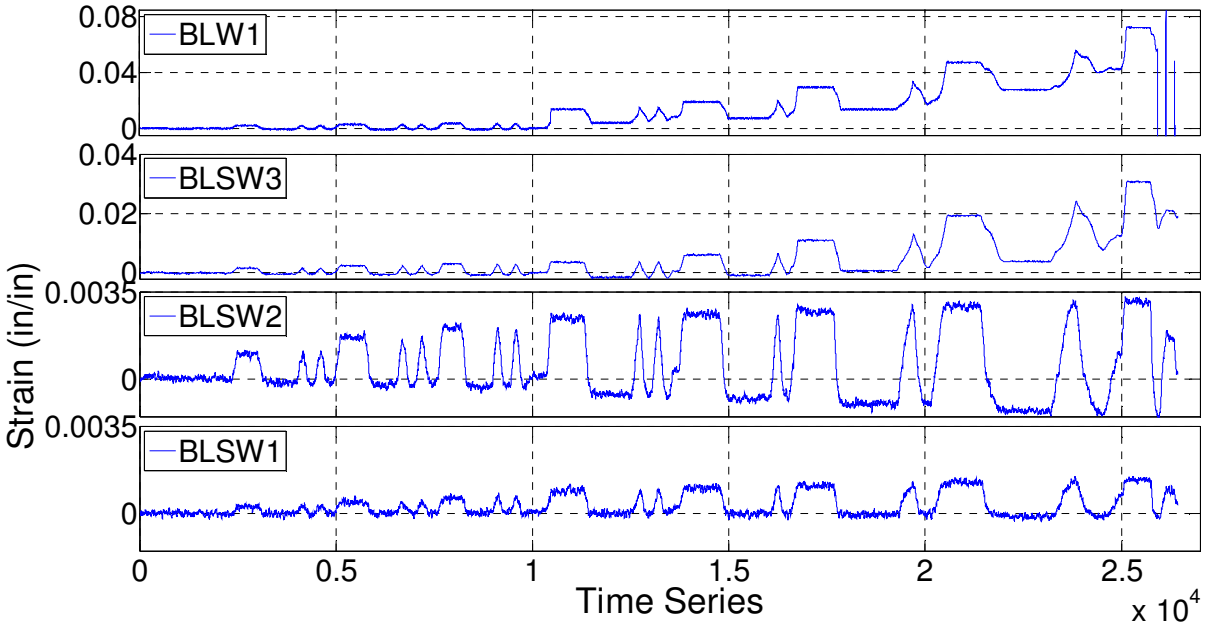

Figure C-41: Strain Response Histories of Middle Longitudinal Bar in Anchorage Zone on the West Side of Beam SBH100

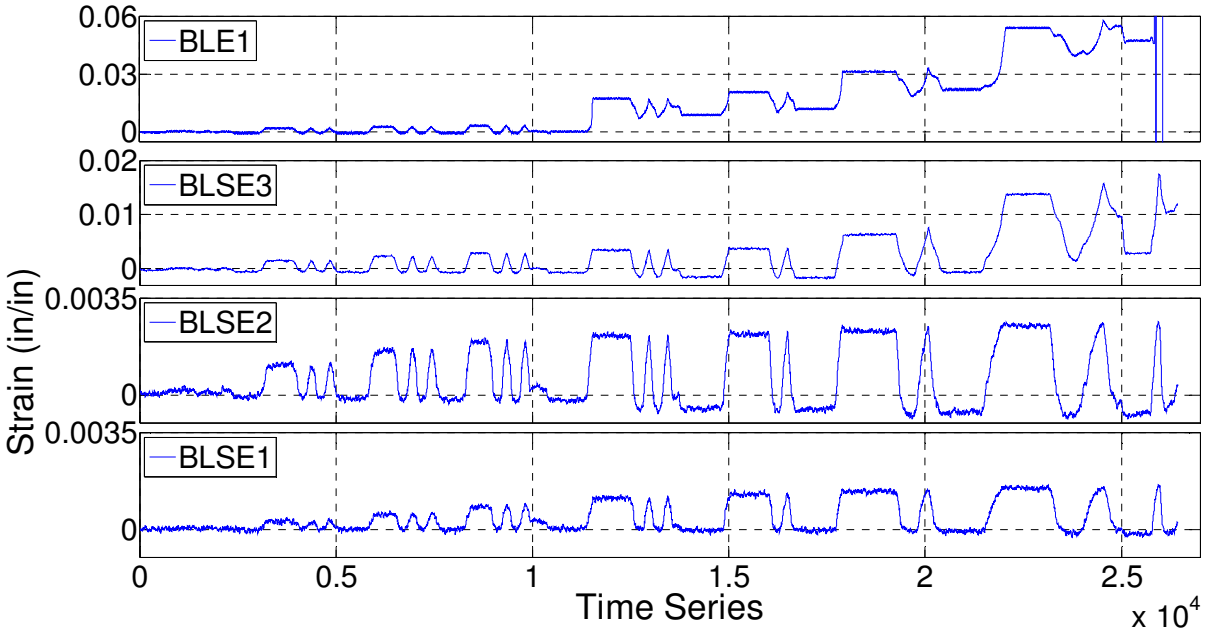

Figure C-42: Strain Response Histories of Middle Longitudinal Bar in Anchorage Zone on the East Side of Beam SBH100

Specimen SBL100

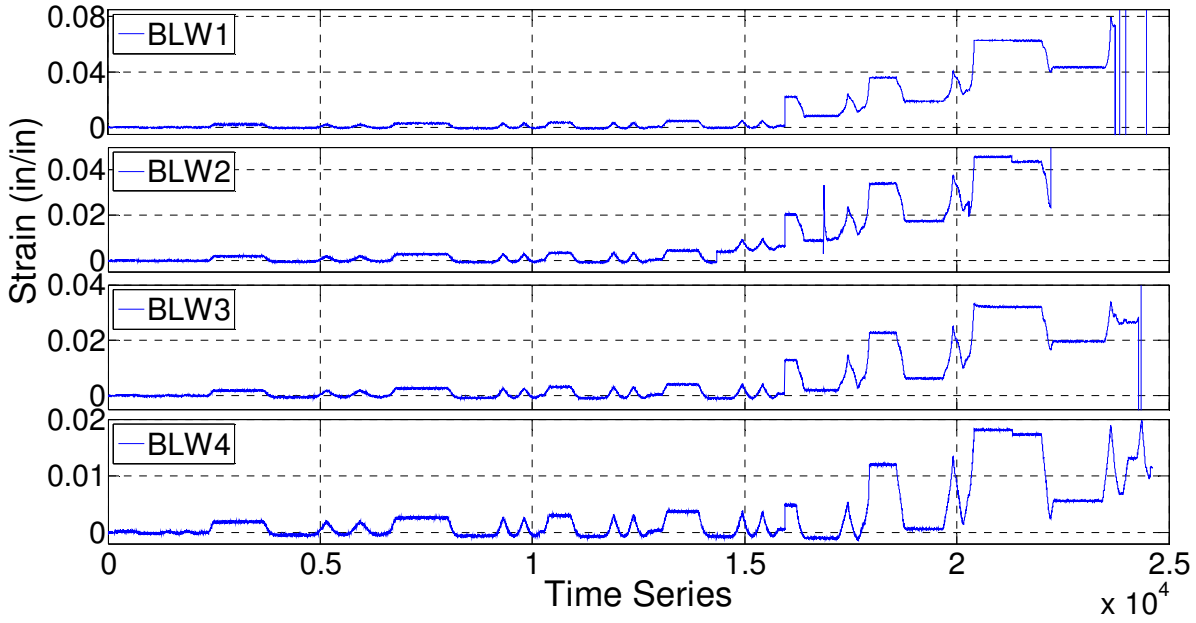

Figure C-43: Strain Response Histories of Middle Longitudinal Bar on the West Side of Beam SBL100

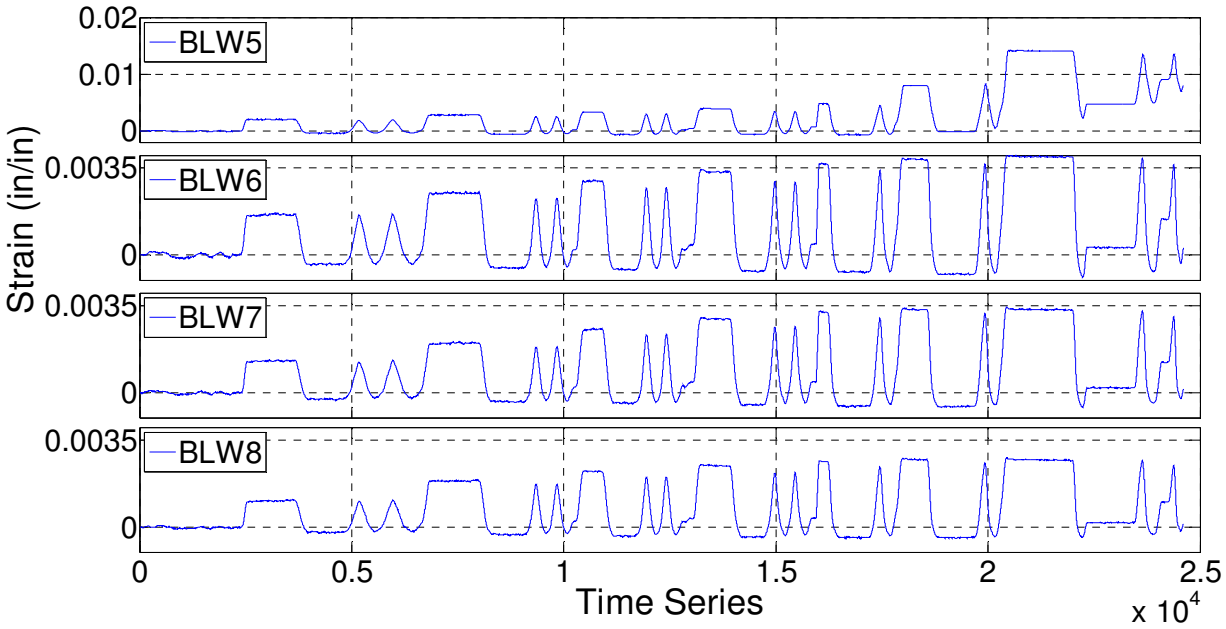

Figure C-44: Strain Response Histories of Middle Longitudinal Bar on the West Side of Beam SBL100

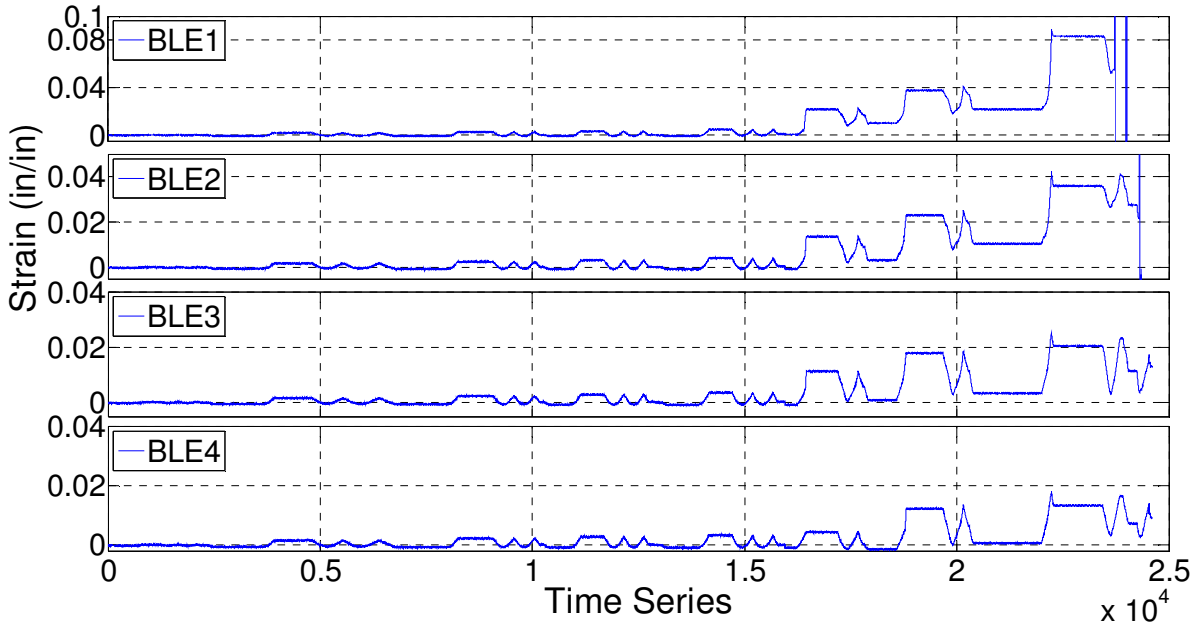

Figure C-45: Strain Response Histories of Middle Longitudinal Bar on the East Side of Beam SBL100

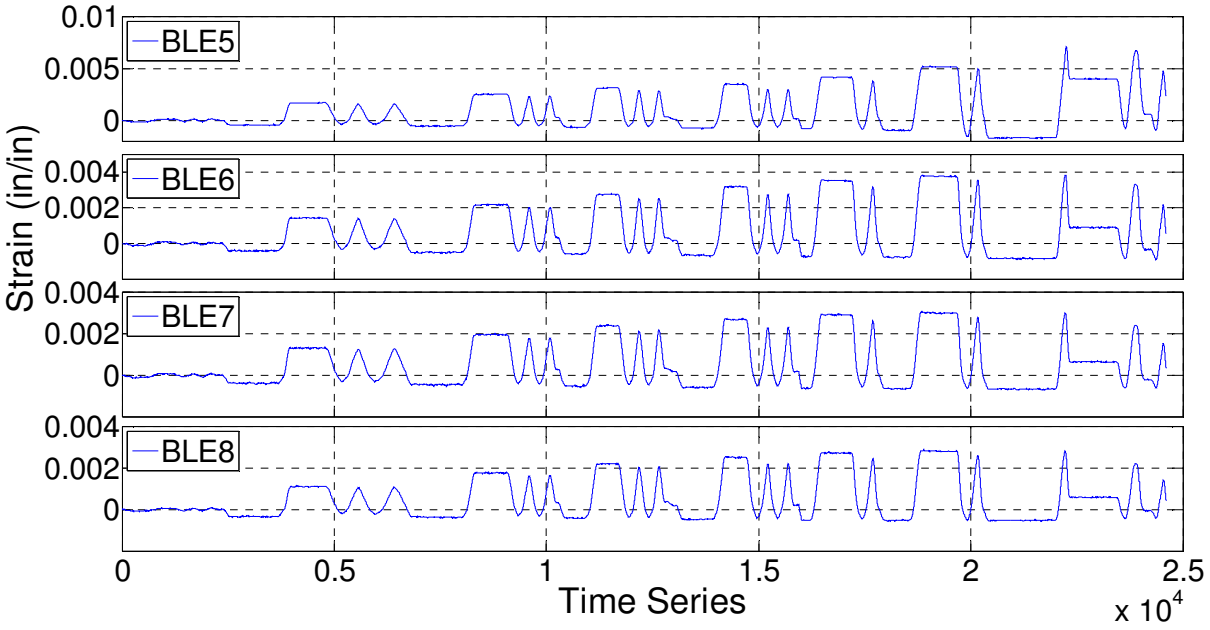

Figure C-46: Strain Response Histories of Middle Longitudinal Bar on the East Side of Beam SBL100

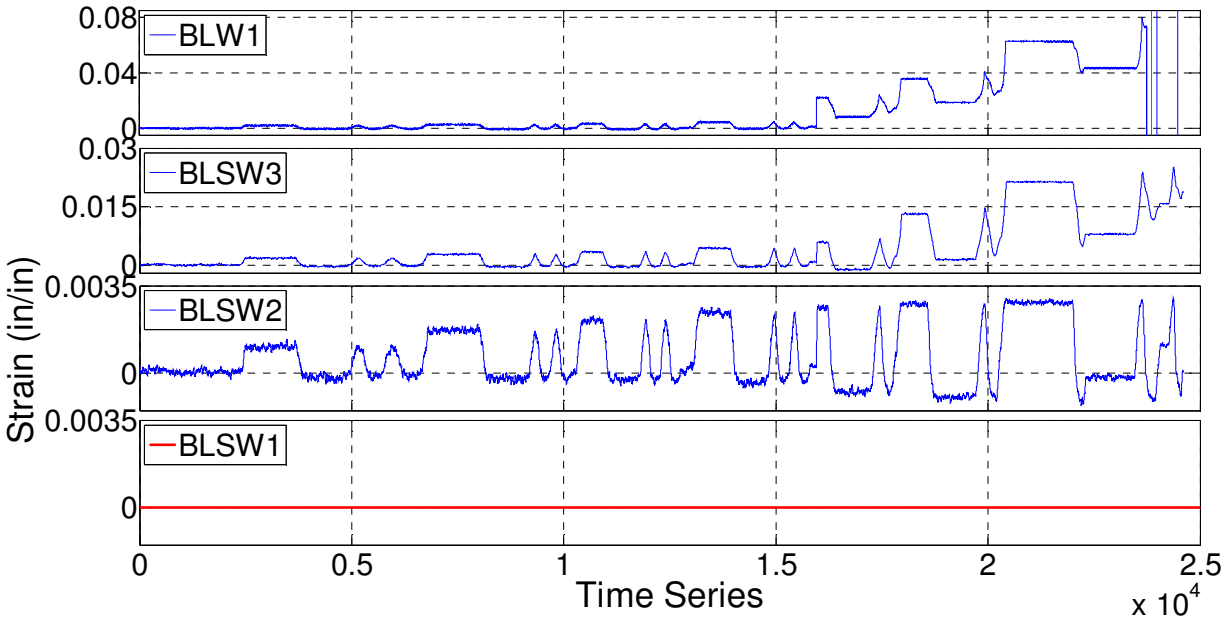

Figure C-47: Strain Response Histories of Middle Longitudinal Bar in Anchorage Zone on the West Side of Beam SBL100

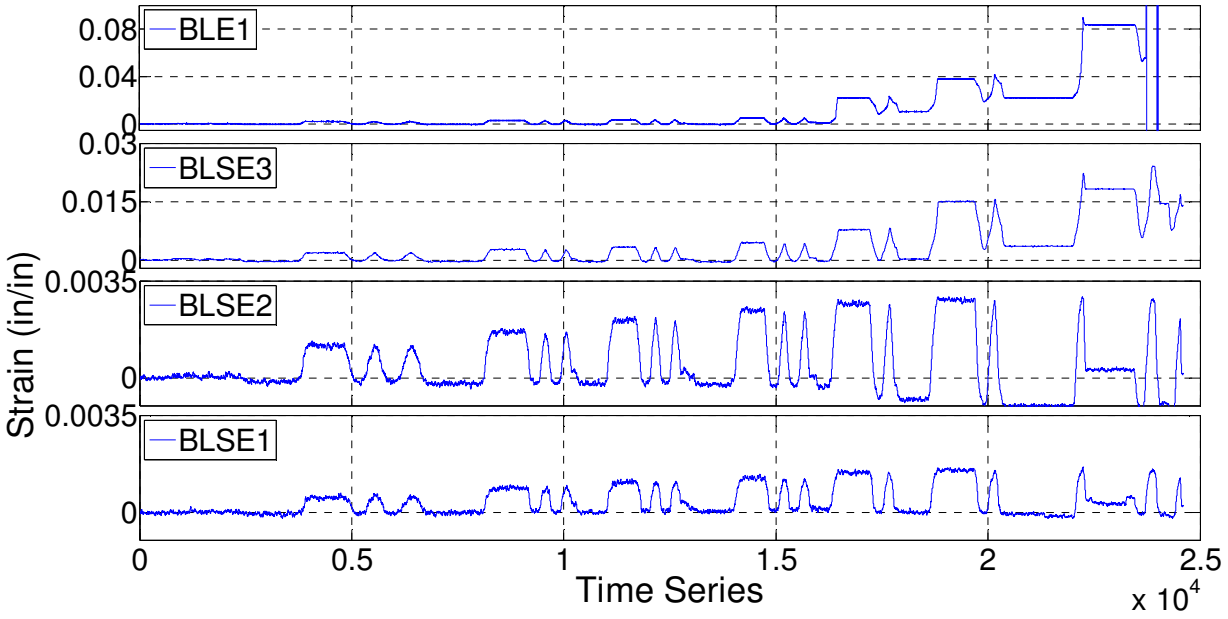

Figure C-48: Strain Response Histories of Middle Longitudinal Bar in Anchorage Zone on the East Side of Beam SBL100

Specimen SBM100

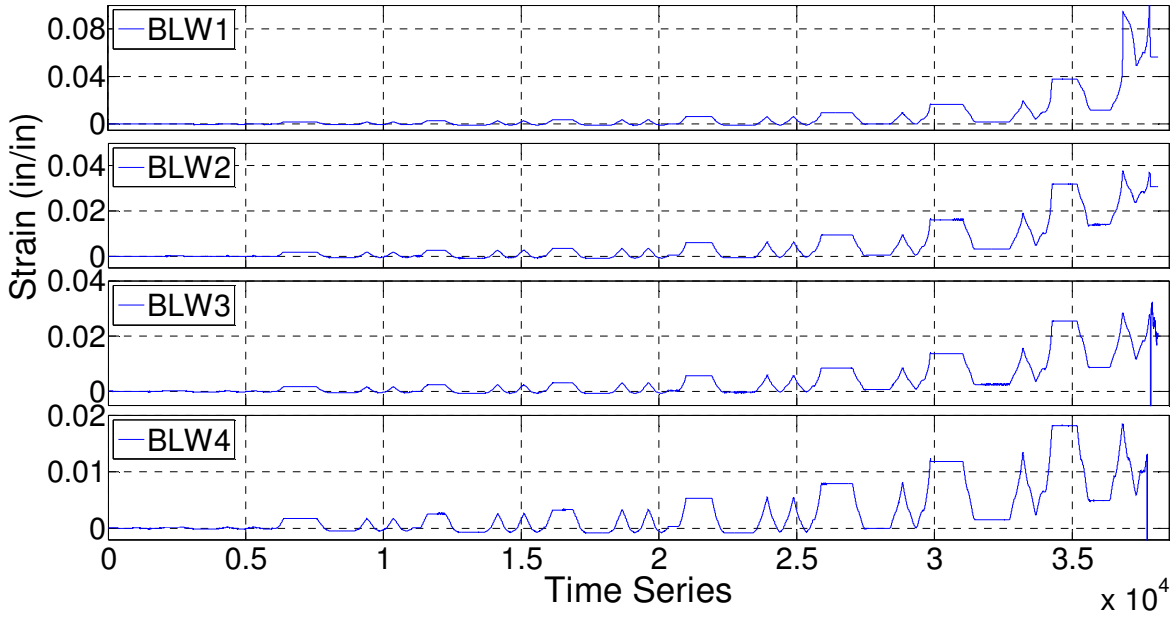

Figure C-49: Strain Response Histories of Middle Longitudinal Bar on the West Side of Beam SBM100

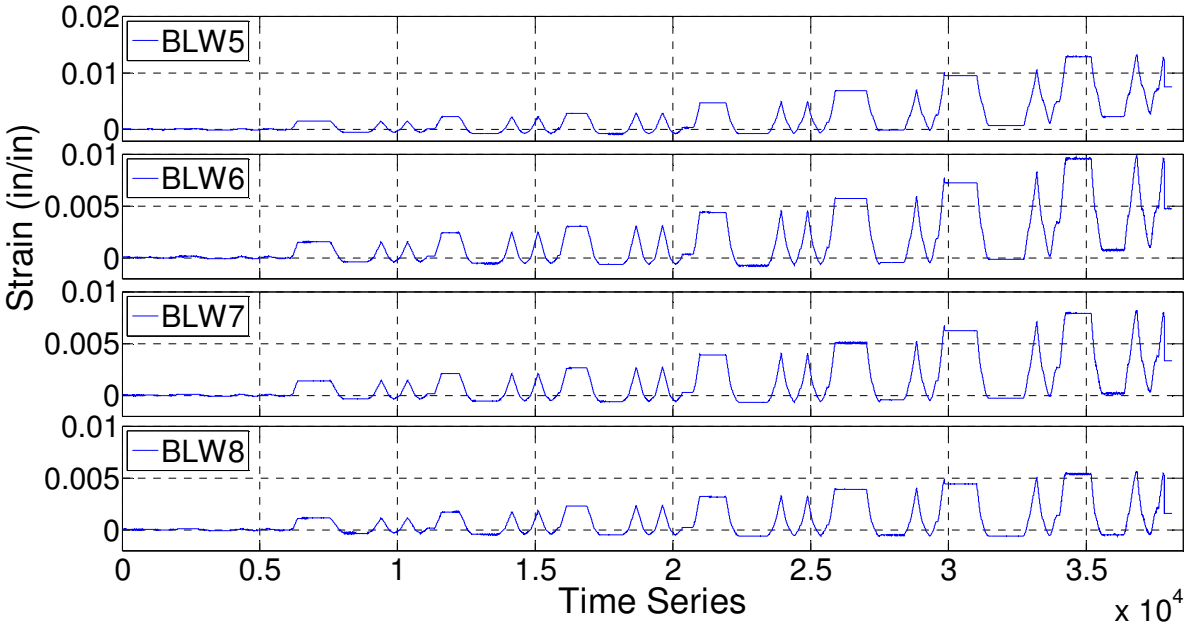

Figure C-50: Strain Response Histories of Middle Longitudinal Bar on the West Side of Beam SBM100

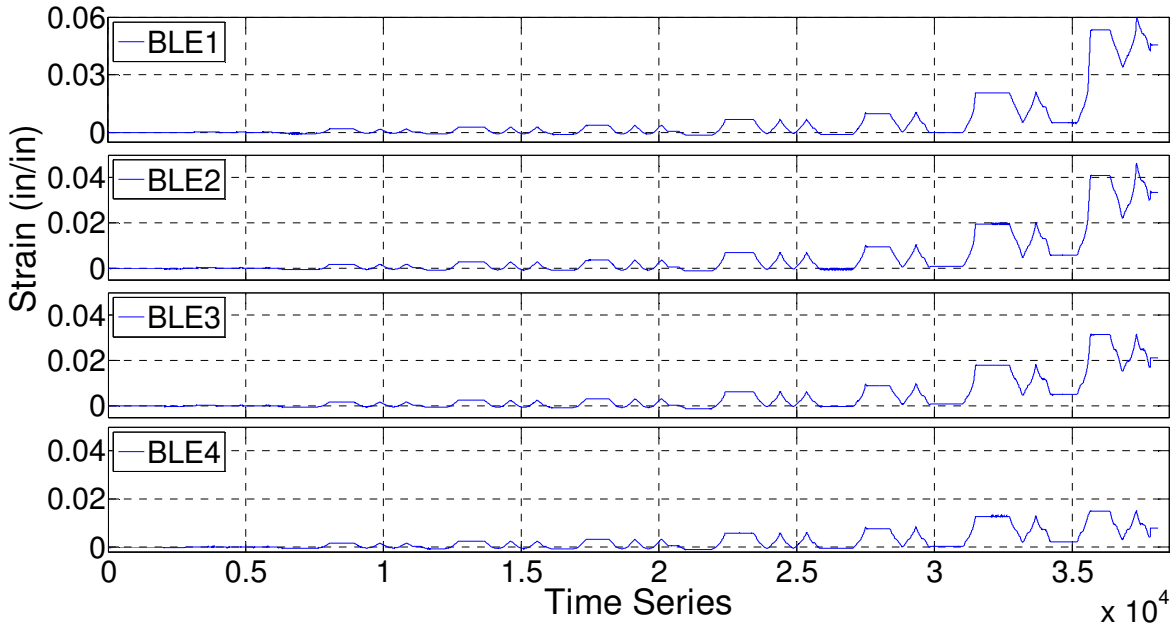

Figure C-51: Strain Response Histories of Middle Longitudinal Bar on the East Side of Beam SBM100

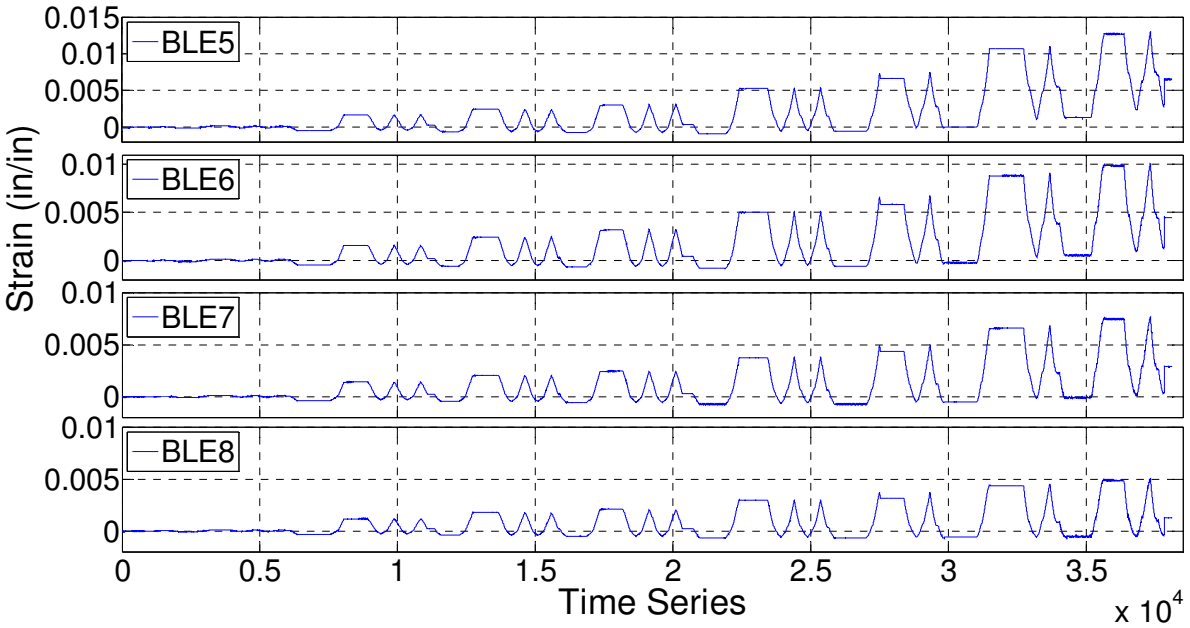

Figure C-52: Strain Response Histories of Middle Longitudinal Bar on the East Side of Beam SBM100

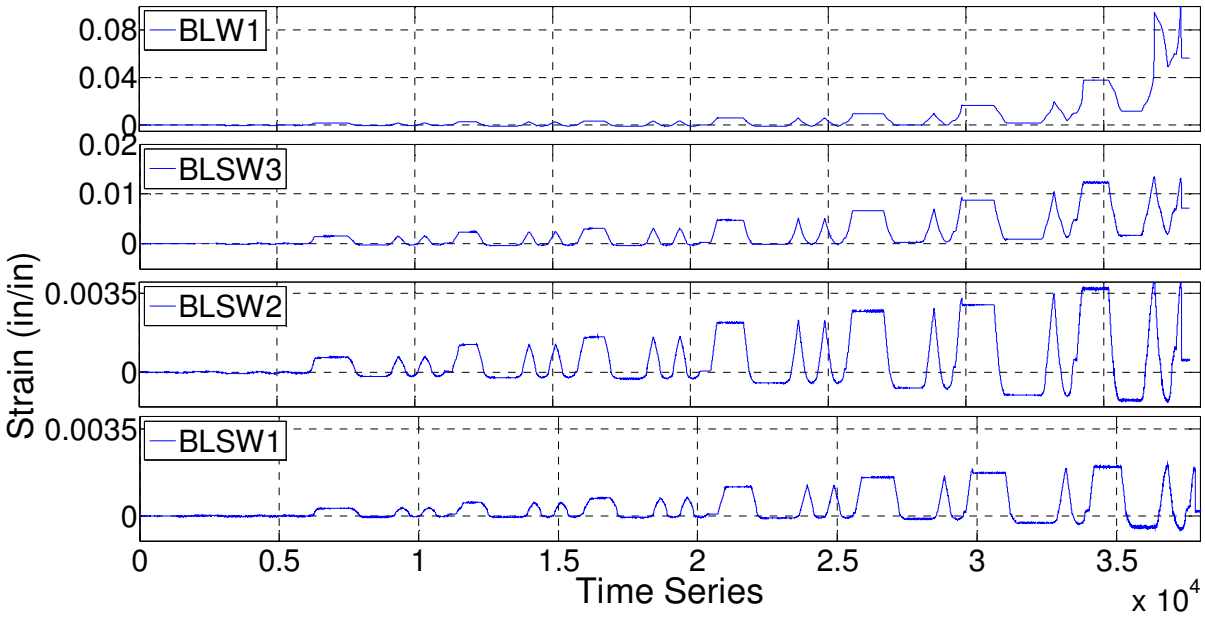

Figure C-53: Strain Response Histories of Middle Longitudinal Bar in Anchorage Zone on the West Side of Beam SBM100

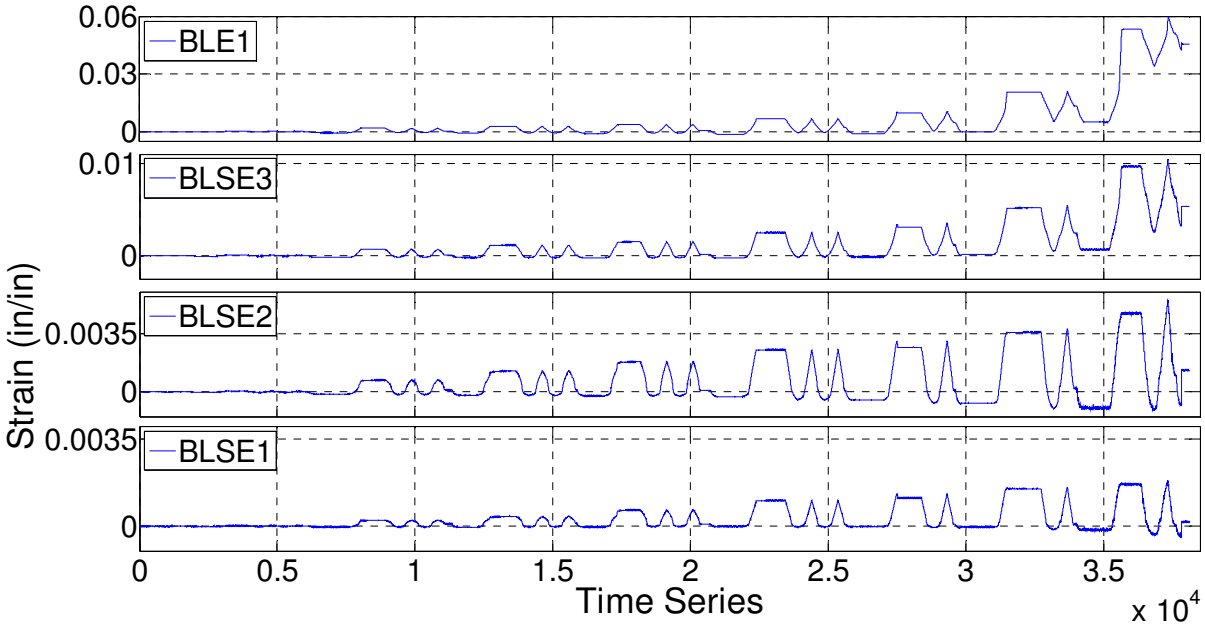

Figure C-54: Strain Response Histories of Middle Longitudinal Bar in Anchorage Zone on the East Side of Beam SBM100